SEMI-ANNUAL REPORT

(for January – June 1996)

Contract Number NAS5–31363

OCEAN OBSERVATIONS WITH EOS/MODIS:

Algorithm Development and Post Launch Studies

Howard R. Gordon
University of Miami
Department of Physics
Coral Gables, FL 33124

(Submitted July 15, 1996)

Semi-Annual Report (1 January – 30 June 1996) NAS5–31363

Preamble

As in earlier reports, we will continue to break our effort into seven distinct units:

- Atmospheric Correction Algorithm Development
- Whitecap Correction Algorithm
- In-water Radiance Distribution
- Residual Instrument Polarization
- Direct Sun Glint Correction
- Pre-launch Atmospheric Correction Validation
- Detached Coccolith Algorithm and Post-launch Studies

This separation has been logical thus far; however, as launch of AM-1 approaches, it must be recognized that many of these activities will shift emphasis from algorithm development to validation. For example, the second, third, and sixth will become almost totally validation-focussed activities in the post-launch era, providing the core of our experimental validation effort. Work under the first bullet will continue into the post-launch time frame, but will be driven in large part by algorithm deficiencies revealed as a result of validation activities.

We will continue to use the above format for CY96 and CY97.

Abstract

Several significant accomplishments were made during the present reporting period.

- We have completed our basic study of using the 1.38 μm MODIS band for removal of the effects of thin cirrus clouds and stratospheric aerosol. The results suggest that it should be possible to correct imagery for thin cirrus clouds with optical thicknesses as large as 0.5 to 1.0.

- We have acquired reflectance data for oceanic whitecaps during a cruise on the *RV Malcolm Baldrige* in the Gulf of Mexico. The reflectance spectrum of whitecaps was found to be similar to that for breaking waves in the surf zone measured by *Frouin, Schwindling and Deschamps* [1996].

- We installed a CIMEL sun photometer at Fort Jefferson on the Dry Tortugas off Key West in the Gulf of Mexico. The instrument has yielded a continuous stream of data since February. It shows that the aerosol optical thickness at 669 nm is often < 0.1 in winter. This suggests that the Southern Gulf of Mexico will be an excellent winter site for vicarious calibration.

- We completed a study of the effect of vicarious calibration, i.e., the accuracy with which the radiance at the top of the atmosphere (TOA) can be predicted from measurement of the sky radiance at the bottom of the atmosphere (BOA). The results suggest that the neglect of polarization in the aerosol optical property inversion algorithm and in the prediction code for the TOA radiances is the largest error associated with the radiative transfer process. Overall, the study showed that the accuracy of the TOA radiance prediction is now limited by the radiometric calibration error in the sky radiometer.

- W.M. Balch participated in two cruises (March and June) in the Gulf of Maine, a region of known dense populations of coccolithophore blooms. Considerable coccolith light scattering data were obtained with a flow-through instrument, along with data relating to calcite concentration and the rate of calcite production.

Semi-Annual Report (1 January – 30 June 1996) NAS5–31363

1. Atmospheric Correction Algorithm Development.

a. Task Objectives:

During CY 1996 there are four objectives under this task:

(i) Complete development of an algorithm module for removing the effects of stratospheric aerosol and/or cirrus clouds from MODIS imagery over the oceans.

(ii) Conduct research on the effects of strongly absorbing aerosols, and their vertical structure, on the existing atmospheric correction algorithm. Use the results of this research to develop a strategy for their removal.

(iii) Develop a detailed model of the diffuse transmittance of the atmosphere and the manner in which it is influenced by the angular distribution of subsurface upwelling spectral radiance. Add a module for this to the atmospheric correction algorithm.

(iv) Investigate the effects of ignoring the polarization of the atmospheric light field on the performance of the proposed atmospheric correction algorithm.

b. Work Accomplished:

A comprehensive report on the present status of the MODIS atmospheric correction algorithm was prepared for the Aerosol Remote Sensing and Atmospheric Correction Workshop (sponsored by NASA/EOS). This was submitted to the *Journal of Geophysical Research.* A revised version is included in this report as Appendix 1. Several references to this Appendix are made in this report.

(i) Considerable progress was made regarding the influence of stratospheric aerosols on atmospheric correction, and the possibility of using the 1380 nm MODIS band for removing their effects. A paper has been prepared and submitted to *Applied Optics.* The paper is included in this report as Appendix 2. In Appendix 2 it is demonstrated that it should possible to perform a correction for cirrus clouds having optical thicknesses approaching unity. More work is required, however, to implement the algorithm.

(ii) As demonstrated in Appendix 1, strongly absorbing aerosols present a serious problem for atmospheric correction. The nature of the problem is two fold: (1) in contrast to weakly-absorbing aerosols, when the aerosol is strongly absorbing its distribution in altitude becomes very important; and (2) the technique of distinguishing aerosol type through examination of the spectral variation of the radiance in the near infrared, used by the correction algorithm, cannot distinguish between weakly-absorbing and strongly-absorbing aerosols. During this reporting period, we have tried to quantify the effect of the vertical structure, and to find ways in which to distinguish weakly- and strongly-absorbing aerosols.

One revealing simulation study was a series of computations in which the strongly-absorbing aerosol (the *Shettle and Fenn* [1979] Urban aerosol model at relative humidity 80% – U80) was confined to thin layer near the surface, as assumed in the correction algorithm, and then to layers 1 km thick progressively moved higher and higher in the atmosphere. Figure 1–1 provides examples of the variation of the radiance at the top of the atmosphere for as a function of the altitude of the 1-km thick layer. In the figure, θ_0 is the solar zenith angle, and the viewing is either at the center of the edge of the MODIS scan. Z_{top} is the height of the top of the 1-km thick aerosol layer. When $Z_{\mathrm{top}} = 0$ the aerosol is confined to a thin layer at the surface. The decrease in the radiance at the top of the atmosphere as the altitude of the layer increases is remarkably large at 443 nm where the contribution from molecular scattering is large. No such decrease is seen when the aerosol is nonabsorbing.

The radiances used to generate Figure 1–1 were used as pseudo data and introduced into the correction algorithm. The correction algorithm employed a set of candidate aerosol models having strong absorption (U80 was *not* among the set), i.e., it was assumed that somehow the fact that the aerosol was strongly absorbing had already been determined. The resulting errors in the retrieved water-leaving reflectance ($\Delta\rho$) as a function of the height of the aerosol layer for several MODIS bands and viewing-solar geometries are presented in Figure 1–2.

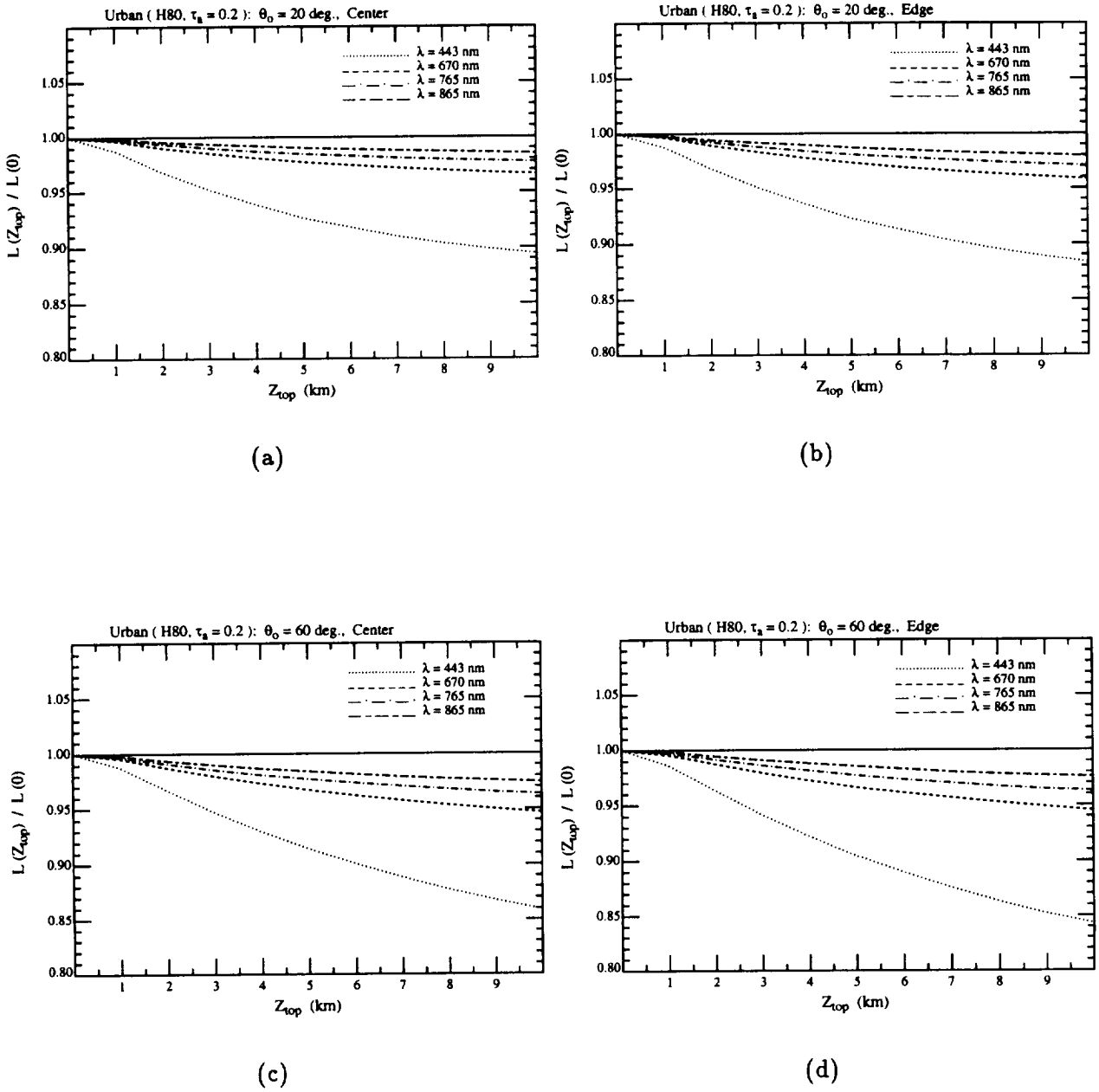

Figure 1–1. Ratios of radiances for the U80 aerosol in a 1 km thick layer with the top at Z_{top}. (a) $\theta_0 = 20°$, viewing at center; (b) $\theta_0 = 20°$, viewing at edge; (c) $\theta_0 = 60°$, viewing at center; (d) $\theta_0 = 60°$, viewing at edge.

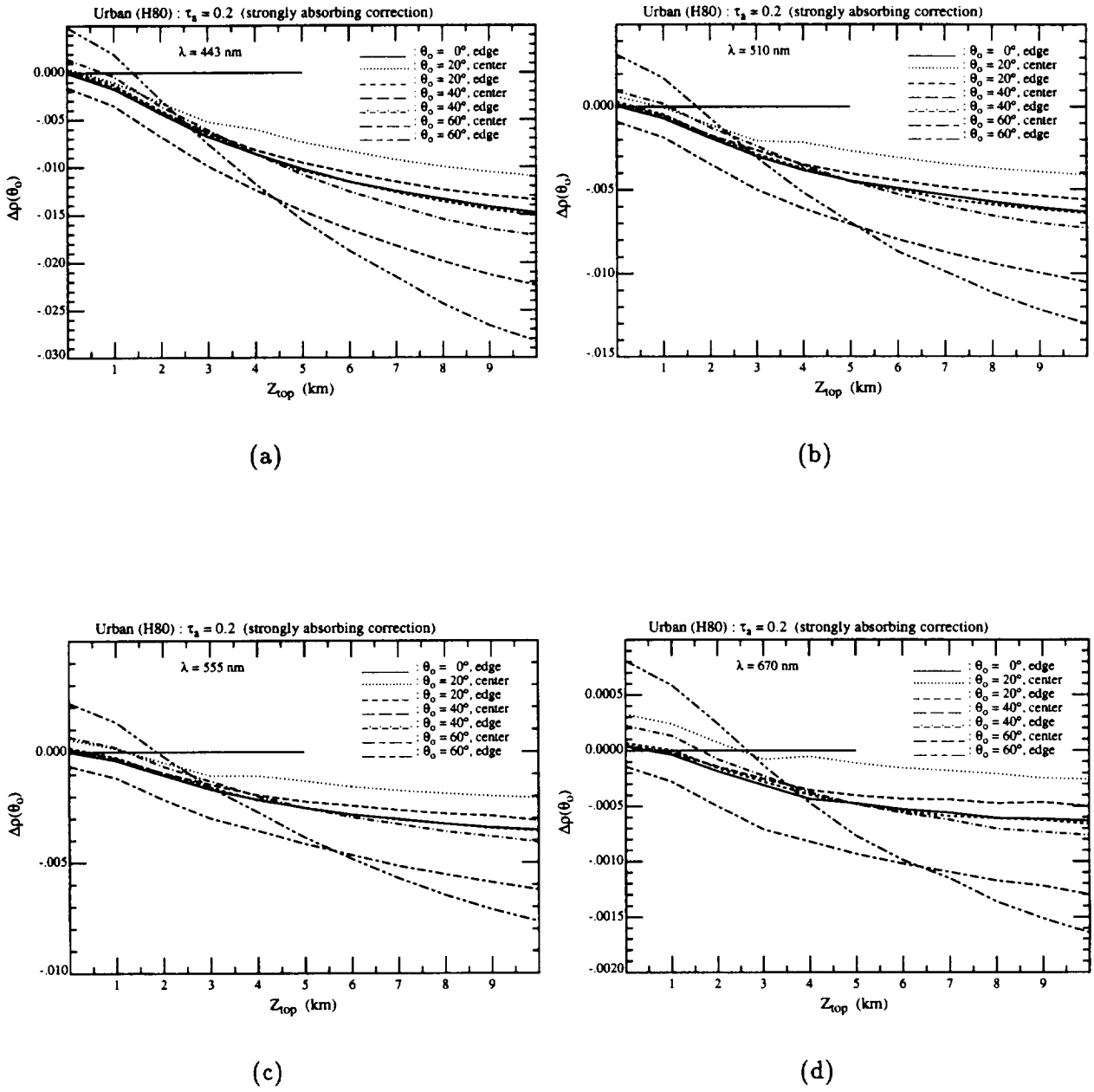

Figure 1–2. Vertical structure effects on the retrieval errors for U80 using strongly-absorbing aerosols as candidates: (a) $\lambda = 443$ nm, (b) $\lambda = 510$ nm, (c) $\lambda = 555$ nm, (d) $\lambda = 670$ nm.

The goal of atmospheric correction is $|\Delta\rho| < 0.002$ at 443 nm. If the aerosol is at the surface or uniformly distributed in a layer 1 km above the surface ($Z_{\mathbf{top}} = 1$), the algorithm meets the accuracy goal; however, if it is in a 1-km thick layer the top of which is 2 km or higher above the surface ($Z_{\mathbf{top}} \geq 2$ in Figure 1–2) the algorithm fails to meet the goal. This suggests that

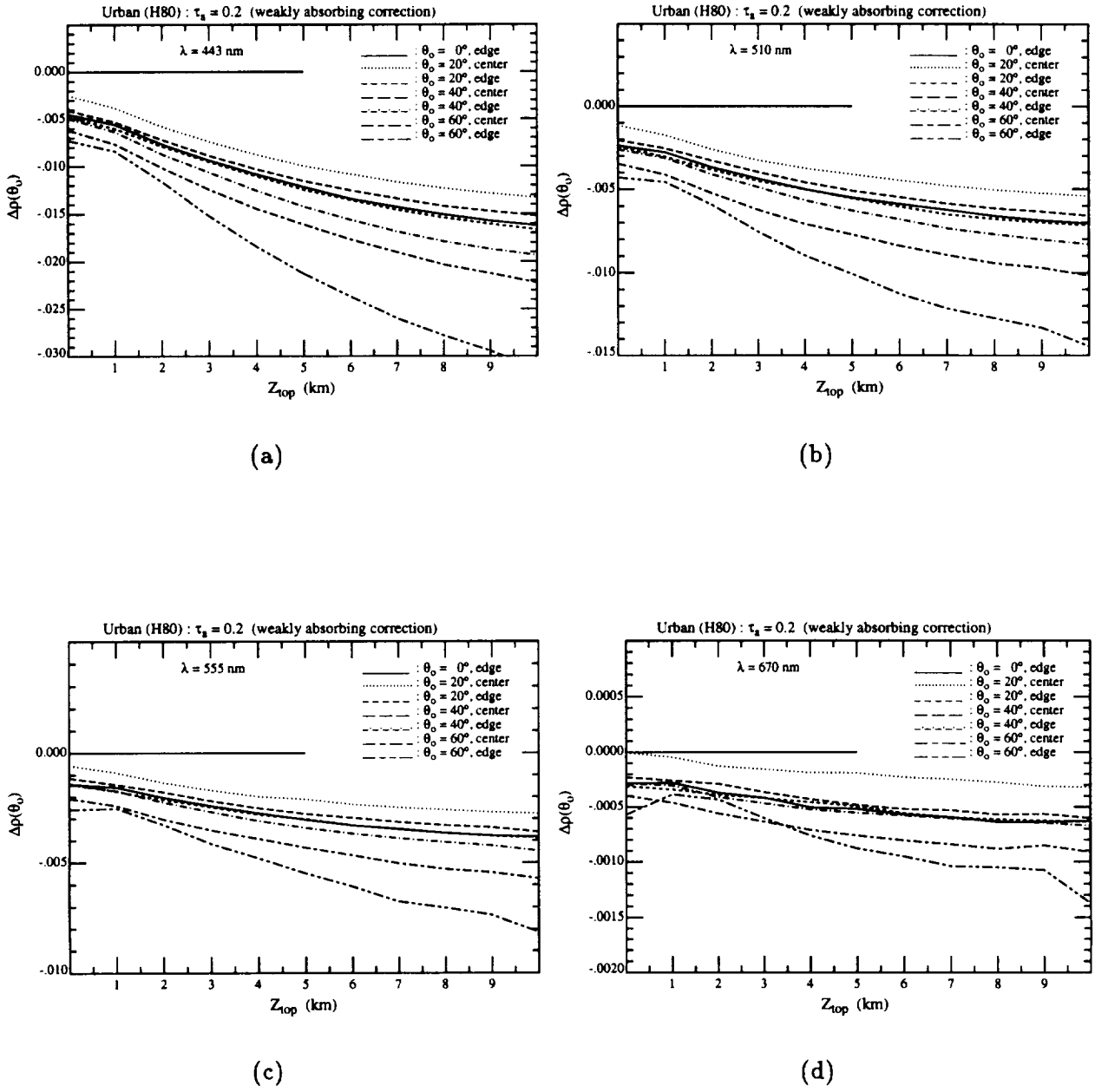

Figure 1–3. Vertical structure effects on the retrieval errors for U80 using weakly-absorbing aerosols as candidates: (a) $\lambda = 443$ nm, (b) $\lambda = 510$ nm, (c) $\lambda = 555$ nm, (d) $\lambda = 670$ nm.

the vertical placement of the absorbing aerosol must be known to within ± 1 km. Earlier studies (Appendix 1), in which the same aerosol was uniformly mixed from the surface to an arbitrary altitude, also suggested that the thickness of the layer had to be known to within ± 1 km. These results indicate that when strongly absorbing aerosols are present, e.g., urban pollution or desert

dust transported over the oceans, atmospheric correction will require that the candidates aerosol models also include candidate vertical distributions as well as aerosol types. This will considerably complicate the algorithm in such cases, and underscores the importance of a climatology of aerosol vertical distribution for oceanic regions influenced by strongly absorbing aerosols.

The result described above assumed that the presence of the strongly absorbing aerosol was not in doubt; however, at this time we have no method of detecting their presence. Figure 1–3 provides the results for the same simulations as in Figure 1–2 but with the normal (weakly-absorbing) aerosol models used as candidates, i.e., assuming that the presence of the strong absorption was not determined. Clearly, the results are poorer than those in Figure 1–2, possessing a negative-error bias. Thus, it is as necessary to know that the aerosol absorbs strongly as it is to know the vertical distribution.

We are examining several possibilities for detecting the presence of strongly-absorbing aerosols. One method we have tried for detecting the presence of strong absorption was examination of the atmospheric correction error at 670 nm. In this band, the water-leaving reflectance is generally low $\sim$ 0.0005 to 0.001 in Case 1 waters (it was assumed to be zero in the CZCS atmospheric correction algorithm). The results in Figure 1–3 suggest that if the aerosol is strongly absorbing the water-leaving reflectance at 670 nm will have a negative bias of $\sim$ 0.0005. Thus, if atmospheric correction yields a negative water-leaving radiance at 670 nm, it would be a sure indication of a correction problem. However, as the error is of the same order as the actual water-leaving reflectance at 670 nm, such a test will not always be valid, i.e., there will be false negatives, situations in which the aerosol strongly absorbs, but the retrieved water-leaving radiance at 670 will be positive.

Another possible way of attempting to detect absorbing aerosols, in particular desert dust, is to examine the behavior of the radiance reflected from the ocean-atmosphere system in the short-wave infrared (SWIR). In Appendix 1 (Section 4.2) it is suggested that the variation of the aerosol component of the reflectance from the NIR to the SWIR is significantly different for aerosols possessing refractive indices and size distributions representative of Saharan dust when compared

to nonabsorbing aerosols. This is shown in Figure 1-4 which provides the atmospheric correction ε parameter defined according to

$$\varepsilon(\lambda, 865) = \frac{\rho_{as}(\lambda)}{\rho_{as}(865)},$$

where $\rho_{as}(\lambda)$ is the aerosol contribution to the ocean-atmosphere reflectance at a wavelength λ, for several aerosol size distributions. Note that the value of ε decreases more rapidly into the SWIR

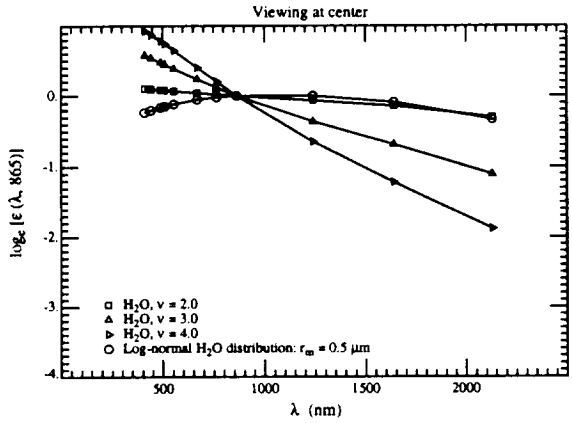

Figure 1-4a. $\varepsilon(\lambda, 865)$ for nadir viewing with $\theta_0 = 60°$ for the Haze C models composed of liquid water.

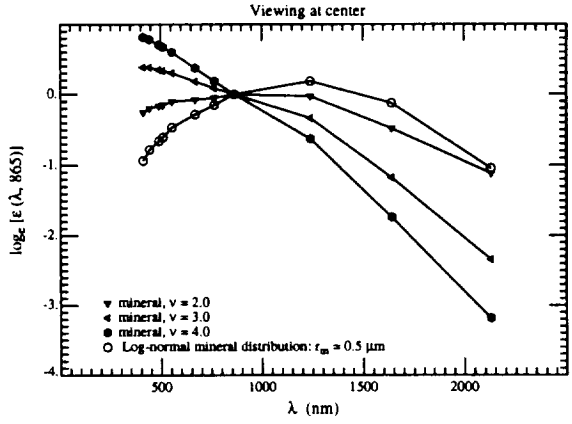

Figure 1-4b. $\varepsilon(\lambda, 865)$ for nadir viewing with $\theta_0 = 60°$ for the Haze C models composed of absorbing minerals.

for the Saharan dust compared with a similar sized aerosol possessing the refractive index of water. The source of this decrease appears to be a significant decrease in the real part of the refractive index of the dust. If this decrease is correct, the fact the dust particles are nonspherical would probably only minimally influence the sensitivity of this method of detection.

Although such a method would likely be limited to Saharan dust (assuming the modeled index of refraction is correct) we have performed simulations aimed at determining whether the single scattering approximation could be used to implement a discrimination algorithm based on this idea in a simple manner. If we ignore multiple scattering in the aerosol contribution, then ε is approximated by

$$\varepsilon_{\mathbf{Approx}}(\lambda, 865) = \frac{\rho_t(\lambda) - \rho_r(\lambda)}{\rho_t(865) - \rho_r(865)}, \quad (1)$$

where ρ_t is the total reflectance of the ocean-atmosphere system, and ρ_r is the contribution due to Rayleigh scattering. Figure 1-5 compares the value of $\varepsilon_{\mathbf{Approx}}(\lambda, 865)$ using this equation with the

true value for the Log-normal (largest $\tau_a(\lambda)$ in the SWIR) model in Figure 1–4 and for aerosol optical thicknesses $\tau_a(865)$ of 0.3 and 0.4. Clearly, Eq. (1) provides an excellent approximation to $\varepsilon(\lambda, 865)$ in the NIR and SWIR for even large aerosol optical thicknesses. Thus, it appears that the SWIR could be used in a simple manner to distinguish Saharan dust from nonabsorbing maritime aerosols

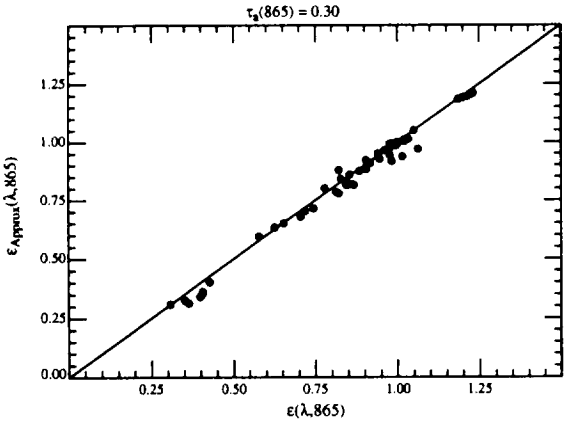

Figure 1–5a. Comparison between $\varepsilon(\lambda, 865)$ and $\varepsilon_{Approx}(\lambda, 865)$ for several viewing geometries with $\tau_a = 0.30$.

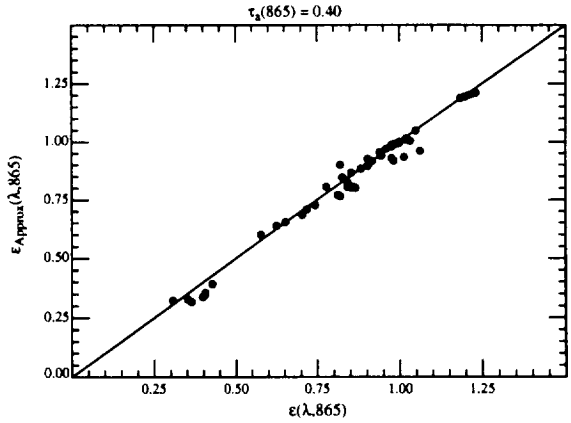

Figure 1–5a. Comparison between $\varepsilon(\lambda, 865)$ and $\varepsilon_{Approx}(\lambda, 865)$ for several viewing geometries with $\tau_a = 0.40$.

by extrapolating and $\varepsilon_{\mathbf{Approx}}(865, 865)$ and $\varepsilon_{\mathbf{Approx}}(1260, 865)$ to find $\varepsilon_{\mathbf{Extrapolated}}(2130, 865)$. If $\varepsilon_{\mathbf{Extrapolated}}(2130, 865) \gtrsim 2\varepsilon_{\mathbf{Approx}}(2130, 865)$, it would indicate the presence of Saharan dust.

Finally, we are examining a new concept for distinguishing absorbing aerosols, in which a bio-optical radiance model, e.g., *Gordon et al.* [1988], is used to predict the water-leaving reflectance as a function of λ and pigment concentration (C). The value of C and the aerosol optical depth at 865 nm are then varied to provide $\rho_t(\lambda)$ for each aerosol model. The values of C, $\tau_a(865)$ and the aerosol model which yield the best fit (in an RMS sense) to the measured $\rho_t(\lambda)$ are taken to be correct. Initial tests suggest that this may work well for low C, e.g., $\lesssim 0.5$ mg/m^3. The algorithm is very slow and probably could not be applied on a pixel-by-pixel basis; however, it may be possible to apply it on a regional basis.

(iii) The basic correction algorithm yields the product of the diffuse transmittance t and the water-leaving reflectance ρ_w. However, t depends on the angular distribution of ρ_w. If ρ_w were uniform, t would be easy to compute, and this approximation has always been employed in the past.

In a series of papers Morel and Gentili [*Morel and Gentili*, 1991; *Morel and Gentili*, 1993] studied theoretically the bidirectional effects as a function of the sun-viewing geometry and the pigment concentration. Their simulations suggest that, although the bidirectional effects nearly cancel in the estimation of the pigment concentration using radiance ratios, ρ_w can depend significantly on the solar and viewing angles. (Our major task number 3, a study of the in-water radiance distribution, experimentally addresses this problem.)

In this reporting period, we initiated a study to understand the effect of bidirectional effects on the diffuse transmittance t. Through the use of the reciprocity principle, we were able to develop a simplified method of computing t, given the upward radiance distribution with direction just beneath the sea surface. Although the study has only just begun, it appears that the difference between t (the correct diffuse transmittance) and t^* (the diffuse transmittance computed by assuming the subsurface upward radiance is uniform) is typically $\lesssim 4\%$, and is a relatively weak function of the aerosol optical thickness. Thus, considering the error likely to result from the removal of the aerosol path radiance, it appears that in the blue t can be replaced by t^*, except in waters with low pigment concentrations, e.g., $\lesssim 0.5$ mg/m^3.

(iv) We have performed no new numerical experiments concerning the effect of ignoring polarization in preparation of the aerosol reflectance look up tables. Rather, we now include polarization in most of our simulations, e.g., those provided in Figures 1–1, 1–2, and 1–3. Our results thus implicitly contain the polarization effect. We do not plan any more polarization-specific studies.

c. Data/Analysis/Interpretation: See item **b** above.

d. Anticipated Future Actions:

(i) We must now develop a strategy for implementation of the cirrus cloud/stratospheric aerosol correction into the existing atmospheric correction algorithm. Specific issues include (1) the phase function to be used for the cirrus clouds, (2) the details of making two passes through the correction algorithm, (3) removal of the effect of water vapor above the clouds, and (4) preparation of the required tables. These will be addressed during the remainder of this calendar year with the goal

of answering all of the questions; however, actual preparation of the required look up tables will not begin until CY 1997.

(ii) We will continue the study with the goal of having a conceptual algorithm (or candidate algorithms) by the end of CY 1996. As our work has shown that a knowledge of the vertical distribution of the aerosol is critical, if it is strongly absorbing, we will begin procurement of a micro pulse lidar (MPL) system for use at sea on validation cruises, and from an island (likely Barbados) in the Saharan dust zone, to begin to compile a climatology of the vertical distribution required to adopt candidate distributions for use in this area.

(iii) We will develop a set of lookup tables for t^* to be used with the individual aerosol models. This will be coded and a module will be added to the correction algorithm utilizing these tables. We will attempt to devise a simple method of modifying t^* to form t at least for low pigment concentrations. This will require a model of the subsurface BRDF.

(iv) We will continue to use our vector radiative transfer code to generate pseudo test data; however, specific studies of the effect of polarization on atmospheric correction are being discontinued.

Additional task for CY96: We will initiate a study to determine the efficacy of the present atmospheric correction algorithm on removal of the aerosol effect from the measurement of the fluorescence line height (MOD 20).

e. Problems/Corrective Actions:

(i) None.

(ii) None.

(iii) None.

(iv) None.

(v) None.

f. Publications:

H.R. Gordon, Atmospheric Correction of Ocean Color Imagery in the Earth Observing System Era, Revised to *Journal of Geophysical Research, Atmospheres.*

H.R. Gordon, T. Zhang, F. He, and K. Ding, Effects of stratospheric aerosols and thin cirrus clouds on atmospheric correction of ocean color imagery: Simulations, Submitted to *Applied Optics.*

2. Whitecap Correction Algorithm (with K.J. Voss).

a. Task Objectives:

As described in earlier reports, a whitecap radiometer system has been built and tested to provide a database for developing and validating the whitecap correction algorithm, as well as for providing an estimation of the whitecap contribution to the water-leaving radiance during the post-launch validation phase. The database includes spectral information as well as variables associated with the formation and occurrence of whitecaps such as wind speed and air/sea temperature.

b. Work Accomplished:

The software for data acquisition has been modified in order to increase observation time during whitecap events and GPS data, UTC time is updated less often (at 30 second intervals). The 6 channel upwelling radiometer, downwelling irradiance collector (deck cell) and air/water temperature, wind speed and direction are now acquired at $\sim$ 7 samples per second. The video image from the TV camera mounted along side the radiometer to visually observe the water surface during data acquisition is also time/date stamped at the higher rate. This higher acquisition rate provides spectral information on a whitecap as it passes through its various stages of growth and decay. However, it should be noted that tracking a particular part of a whitecap is rare as the speed and direction in which the ship moves is rarely the same speed and direction in which a whitecap moves over the water surface.

From 29 March to 18 April 1996 the whitecap radiometer system was deployed on the NOAA ship *RV Malcolm Baldrige* on a cruise from Miami to a test location in the Gulf of Mexico, approximately 70 miles off shore from Cedar Key (Florida) in the Apalachicola Bay. The location provided relatively warm waters (16°-17°C) with a number of cold fronts moving off the mainland. These fronts usually lasted a couple of days bringing strong winds (sometimes as high as 18 m/s) and lowering the air temperature to about 12°C. The occurrence of an unstable atmosphere and good winds provided an interesting spectral whitewater data set.

Analysis software using Matlab has been developed to provide spectral reflectance values of different whitewater types, ranging from fresh thick foam as the waves begins to break to thin residual streaks and patches just before the whitewater is absorbed back into the ocean. In addition, software to estimate the effective augmented spectral reflectance of these different whitewater types and the total augmented spectral reflectance on the water leaving radiance for particular sea state conditions has been developed.

Although the effect of whitecaps on useful satellite data is generally restricted to their occurrence in cloud free regions and with data acquired around solar noon, whitecap events during this cruise were measured under a greater variety of sky conditions and times during the day to take full advantage of ship time. This combination of various solar zenith angles and overcast, diffuse to patchy, and clear sky conditions, pushes the capability of the radiometer/deck cell relationship, established from laboratory calibration, in providing true reflectance measurements under all these conditions. Performance characterization of the radiometer and deck cell calibrations for conditions similar to that experienced during the cruise is being quantified in terms of both the angular response of the calibration reflectance plaque and the cosine collector of the deck cell under various lighting conditions.

c. Data/Analysis/Interpretation

An example of two whitecaps passing under the radiometer is shown in Figure 2–1. The 96 consecutive samples shown below are acquired over a period of $\sim$ 15 seconds. In this example a large whitecap suddenly breaks in view of the radiometer with thick white foam (sample point 11) reaching a peak reflectance of $\sim$ 55%. Six traces are plotted representing the six radiometer channels (410, 440, 510, 550, 670 and 860 nm). The lower trace corresponds to the 860 nm reflectance. The thick foam is temporarily replaced by a region of submerged bubbles and less thick foam ($\sim$ sample points 13, 14, 15) and some thick foam comes into view again at sample point 17. At sample point 20 and 21 a thin layer of foam passes followed by the decaying thicker foam to about sample point 35. Sample points from about 35 to 55 show the reflectance of thinning residual foam. From 60 to about 75 the reflectance of the foam free water surface is shown and is suddenly followed by another

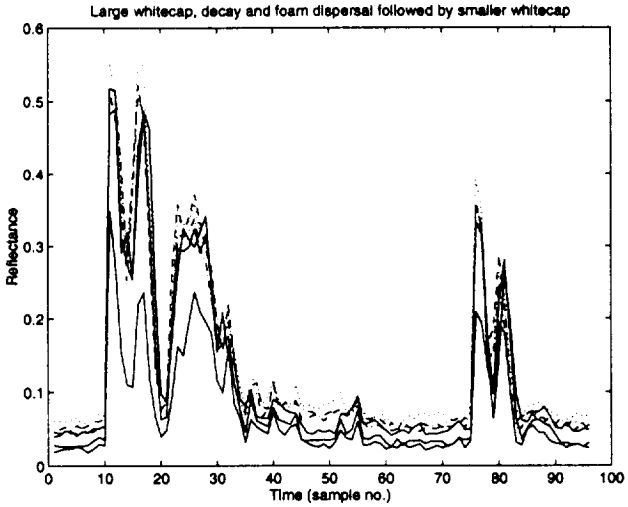

Figure 2–1. An $\sim$ 15 second record of the reflectance of two whitecaps passing within the field of view of the radiometer. The lowest line corresponds to 860 nm.

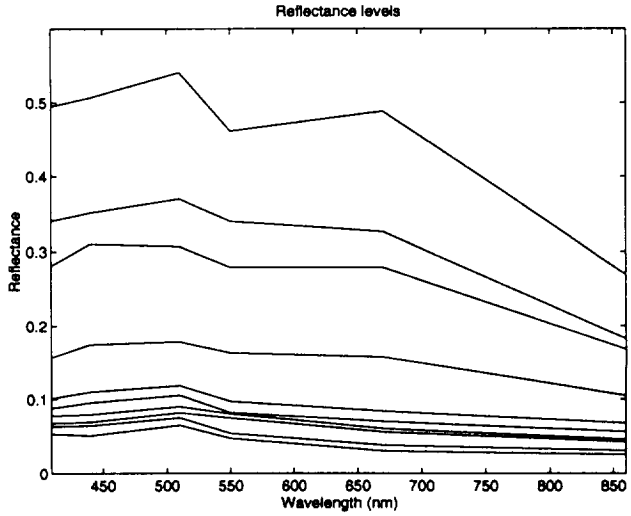

Figure 2–2. Spectral variation of the reflectance curves in Figure 2–1, sorted according to the magnitude of the spectrally averaged reflectance as described in the text.

whitecap of smaller magnitude (sample point 76) and continues to decay out to about sample point 96.

Figure 2–2 provides the spectral reflectance from these whitecaps for different levels of reflectance or foam types. The spectral shape of each level here is the mean of all reflectance values (averaged over wavelength) that fall within a reflectance interval. For this data, the lowest level corresponds to a reflectance between 0.04-0.05, followed by 0.05-0.06, 0.06-0.07, 0.07-0.08, 0.08-0.09, 0.09-0.1, 0.1-0.2, 0.2-0.3, 0.3-0.4 and highest level 0.4-0.5. The lower reflectance levels correspond to the non-whitewater reflectance. Of these, some are higher due to sky reflectance, others are lower due to shadowing by adjacent waves.

The variation in shape in each level is partly due to the small number of samples used in this graph. However, a common feature is the lower 670 and even lower 860 reflectance values due the strong absorption by water at the longer wavelengths. A slight lower reflectance at the 410 channel is also observed.

Now, we examine a larger data set, acquired over 30 minutes, to provide a statistically better breakdown of the spectral reflectance of different foam types. In addition, we estimate the effective augmented reflectance contribution due to whitewater under the given wind and sea state condi-

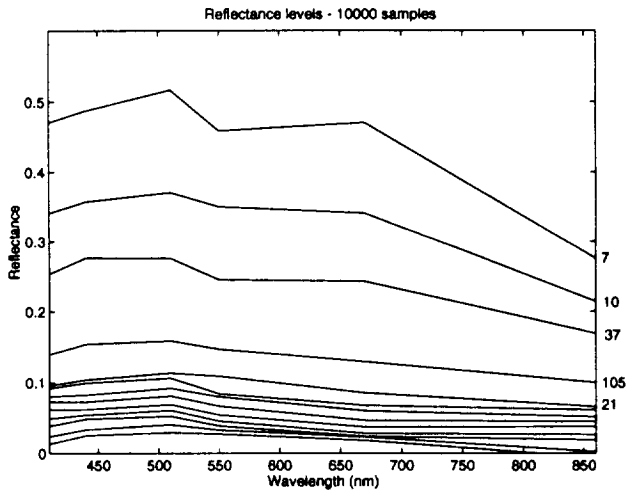

Figure 2–3. Same as Figure 2–2, but for a larger data set.

tions. In Figure 2–3, 10,000 samples are used. The number of occurences of the top 5 reflectance levels is listed along the right-hand margin of the figure. This data set was acquired under overcast

condition, 11 AM, with wind speed ~ 12-13 m/s, air temperature 16.2°C and water temperature 17°C. The results are similar to those in Figure 2–2.

To estimate the augmented reflectance contribution from each reflectance level due to whitewater, the frequency of occurrence of each reflectance level is multiplied by its spectral reflectance value and the background non whitewater reflectance subtracted. Determining the background non-whitewater reflectance is not always a simple matter. The background water reflectance can vary due to specular reflectance, sky reflectance (which in turn can be complicated by the sky condition, i.e., overcast, broken or clear), and by adjacent wave shadowing.

Using the same data set shown in Figure 2–3, examples of the estimated augmented reflectance contribution of whitewater are shown in Figure 2–4 for different estimates of the background water reflectance, (a)-(d). In Panel (a), the augmented reflectance contribution and the fractional coverage is known to contain a large portion of the background water reflectance and yields a high fraction coverage of 15.64%. Panel (b) shows the augmented reflectance with what we believe to be all background water reflectance removed. This yields a fractional coverage of 4.07%. In Panel (c), more background is subtracted, so it is highly unlikely that this contains any background water reflectance; however, it may leave out some whitewater contribution. Its spectral shape is the result of both whitewater and foam. The spectral shape of the augmented reflectance in Panels (b) and (c) are almost identical. In Panel (d), too much background has been subtracted.

We believe that Figure 2–4b is the best estimate of the augmented reflectance, but it should be understood that a small variation in the determination of the background water reflectance could shift this estimate of fractional coverage to a slightly higher or lower value. The augmented reflectance contribution varies from a maximum of 0.0028 to a minimum of 0.0018 at 860 nm and is roughly ~ 35% of the value at 550 nm. This is consistent with the measurements of wave breaking in the surf zone, where *Frouin, Schwindling and Deschamps* [1996] determined the decrease in reflectance at 860 nm to be 40%. The estimate of fractional coverage (4.07%) and augmented reflectance is also consistent with the fractional coverage found in the literature [*Gordon and Wang*, 1994], under fetch-limited conditions for wind speeds of 12-13 m/s.

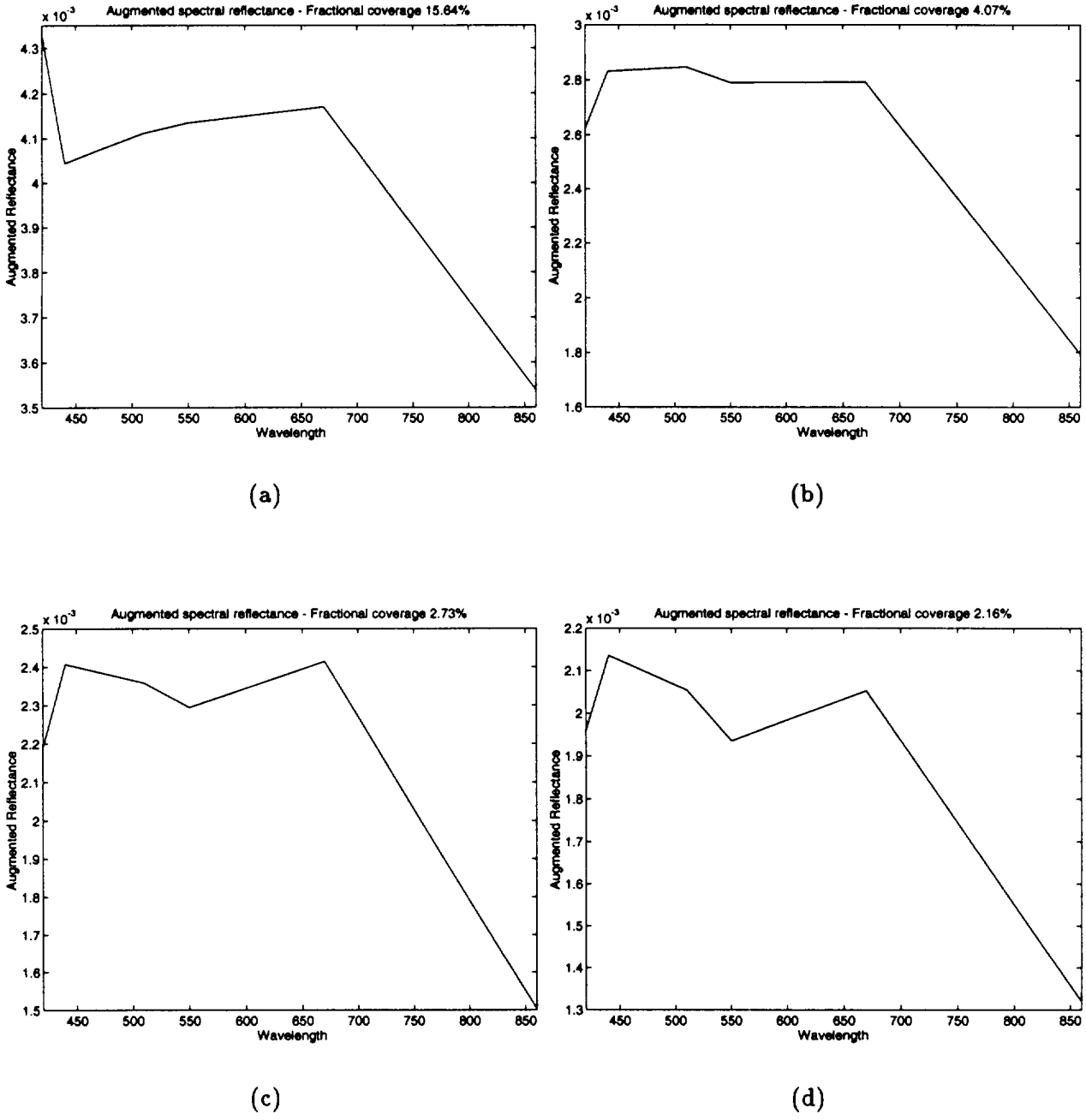

Figure 2–4. Augmented reflectance obtained by subtracting increasing amounts [(a) to (d)] of background water reflectance. Panel (b) is believed to have the correct amount of background subtracted.

d. Anticipated Future Actions:

From preliminary results of the radiometric performance of the radiometer and deck cell under different sky conditions and solar angles, suggests the drop in reflectance at 860 nm may actually be

greater than that shown above. In addition, the drop in reflectance at 410 nm may also be explained and quantified as an artifact of the radiometer/deck cell performance. With this understanding, and with the more rigorous radiometric characterization that is now underway, the whitecap system will be deployed on another cruise. Another interesting aspect of whitecap reflectance that needs to be examined is the the effective change in whitecap reflectance at large solar zenith angles, where the protruding character of the whitecap above the ocean surface can efficiently reflect the red-rich light of the direct solar beam. This may warrant a cruise in high latitude waters where high zenith angles for much of the year are found over these colder waters, and where whitecaps may be of special importance to satellite observations.

e. Problems/Corrective Actions: None

f. Publications:

We are preparing two publications on this work. The first is a description of the whitecap radiometer and the second describes the spectrum of the whitecap reflectance. An abstract "Whitecaps: Spectral reflectance in the open ocean and their contribution to water-leaving radiance," by K.D. Moore, K.J. Voss, and H.R. Gordon, has been accepted for presentation at the SPIE Ocean Optics XIII Meeting.

3. In-water Radiance Distribution (with K.J. Voss).

a. Task Objectives:

The main objective in this task is to obtain upwelling radiance distribution data at sea for a variety of solar zenith angles to understand how the water-leaving radiance varies with viewing angle and sun angle.

b. Work accomplished:

Our efforts with the radiance distribution camera system were focused on the sky measurements during this period (See item 6 below).

c. Data/Analysis/Interpretation: none

d. Anticipated future actions:

We are looking for another opportunity to acquire data at sea. This will probably be on a cruise with Dennis Clark in the fall or winter.

e. Problems/Corrective actions: None.

f. Publications: None.

4. Residual Instrument Polarization.

a. Task Objectives:

The basic question here is: if the MODIS responds to the state of polarization state of the incident radiance, given the polarization-sensitivity characteristics of the sensor, how much will this degrade the performance of the algorithm for atmospheric correction?

b. Work Accomplished:

We have developed a formalism [*Gordon*, 1988] which provides the framework for removal of instrumental polarization-sensitivity effects. The difficulty with removing the polarization sensitivity error is that the polarization properties of the radiance backscattered by the aerosol are unknown. Simulations of this effect for an instrument possessing $\sim$ 3–4 times the polarization sensitivity expected for MODIS have been carried out. Analysis of the results suggest that elimination of the polarization effect is possible at the required level of accuracy by estimating the polarization of the top-of-atmosphere radiance to be that expected for a pure Rayleigh scattering atmosphere.

c. Data/Analysis/Interpretation:

See **b** above.

d. Anticipated Future Actions:

We will prepare a paper on the results of our simulations and correction scheme for publication. The goal will be submission during of CY96

e. Problems/Corrective Actions: None

f. Publications: None.

5. Direct Sun Glint Correction.

a. Task Objectives: None.

6. Pre-launch Atmospheric Correction Validation (with K.J. Voss).

a. Task Objectives:

The long-term objectives of this task are four-fold:

(i) First, we need to study the aerosol phase function and its spectral variation in order to verify the applicability of the aerosol models used in the atmospheric correction algorithm. Effecting this requires obtaining long-term time series of the aerosol optical properties in typical maritime environments. This will be achieved using a CIMEL sun/sky radiometer that can be operated in a remote environment and send data back to the laboratory via a satellite link. These are similar the radiometers used by B. Holben in the AERONET Network. Thus, the objective is to acquire a CIMEL Automatic Sun Tracking Photometer, calibrate it, and deploy it in a suitable location for studying the optical properties of aerosols over the ocean.

(ii) Second, we must be able to measure the aerosol optical properties from a ship during the initialization/calibration/validation cruises. The CIMEL-type instrumentation cannot be used (due to the motion of the ship) for this purpose. The required instrumentation consists of an all-sky camera (which can measure the entire sky radiance, with the exception of the solar aureole region) from a moving ship, an aureole camera (specifically designed for ship use) and a hand-held sun photometer. We have a suitable sky camera and sun photometer and must construct an aureole camera. Our objective for this calendar year is (1) to assemble, characterize and calibrate the solar aureole camera system, (2) to develop data acquisition software, and (3) to test the system.

(iii) The third objective is to determine how accurately the radiance at the top of the atmosphere can be determined based on measurements of sky radiance and aerosol optical thickness at the sea surface. This requires a critical examination of the effect of radiative transfer on "vicarious" calibration exercises.

(iv) The forth objective is to utilize data from other sensors that have achieved orbit (MSX), or are expected to achieve orbit (OCTS, POLDER, SeaWiFS) prior to the launch of MODIS, to validate and fine-tune the correction algorithm.

b. Work Accomplished:

(i) During this last period we have constructed a filter changer assembly for the solar aureole camera system and performed numerous calibration and instrument performance checks. In addition we have improved the data acquisition system, allowing more rapid acquisition once the instrument is pointed at the sun.

The sky camera system has been modified and used to make measurements of the sky light polarization at several locations on several occasions. As we shall see in the discussion under (iii), this new polarization capability of the sky camera will be of considerable value in the initialization/calibration/validation work.

(ii) The CIMEL instrument was installed in the Dry Tortugas during this past quarter. The instrument we had purchased through this contract was found to have a problem and was sent back to CIMEL for repair. In the interim we borrowed an instrument from B. Holben (NASA/GSFC) and installed it at the site. This installation was successful and the instrument performed well in this marine environment. Recently we have replaced this instrument with our own instrument, and we have continued to have good results.

(iii) We have completed the survey phase of the examination of the effect of radiative transfer on "vicarious" calibration exercises and submitted a report to *Applied Optics*. This paper is now in press. Briefly, the radiance at the bottom of the atmosphere (BOA) and the aerosol optical thickness are inserted into a multiple-scattering inversion algorithm to retrieve the aerosol optical properties — the single scattering albedo and scattering phase function. These are then inserted into the radiative transfer equation to predict the radiance at the top of the atmosphere. Most of the simulations were carried out in the near infrared, where a larger fraction of the top of the atmosphere (TOA) radiance is contributed by aerosol scattering compared to molecular scattering, than in the visible, and where the water-leaving radiance can be neglected. The simulations suggest that the TOA radiance can be predicted with an uncertainty typically less than about 1% when the BOA radiances and the optical thickness measurements are error free. The influence of the simplifying

assumptions made in the inversion-prediction process, such as, modeling the atmosphere as a plane-parallel medium, employing a smooth sea surface in the inversion algorithm, using scalar radiative transfer theory, and assuming that the aerosol was confined to a thin layer just above the sea surface, was investigated. In most cases, these assumptions did not increase the error beyond 1%. An exception was the use of scalar radiative transfer theory, for which the error grew to as much as $\sim$ 2.5%. This suggests that using inversion and prediction codes that include polarization may be more appropriate. The uncertainty introduced by unknown aerosol vertical structure was also investigated and found to be negligible. Extension of the analysis to the blue, which requires the additional measurement of the water-leaving radiance, showed significantly better predictions of the TOA radiance because the major portion of it is the result of molecular scattering, which is precisely known. We also simulated the influence of calibration errors in both the sun photometer and BOA radiometer. The results suggest that the relative error in the predicted TOA radiance is similar in magnitude to that in the BOA radiance (actually it is somewhat less). However, the relative error in the TOA radiance induced by error in optical thickness is usually $\ll$ the relative error in optical thickness. Presently, it appears that radiometers can be calibrated with an uncertainty of $\sim$ 2.5%, therefore it is reasonable to conclude that, at present, the most important error source in the prediction of TOA radiance from BOA radiance is likely to be error in the BOA radiance measurement.

(iv) We have been in contact with personnel involved with SeaWiFS, OCTS, and MSX to acquire data formats, and satellite data from these instruments to assess the validity of the atmospheric correction algorithm.

c. Data/Analysis/Interpretation: None.

(i) We do not have real "at sea" data from the aureole camera to work with. We anticipate acquiring such data very early in this next quarter as discussed below.

(ii) The CIMEL instrument has been performing well in the Dry Tortugas. A sample long-term data record is shown in Figure 6–1. This data set will allow us to look at the variability of the optical signature of the marine aerosols, along with issues dealing with vicarious calibration of

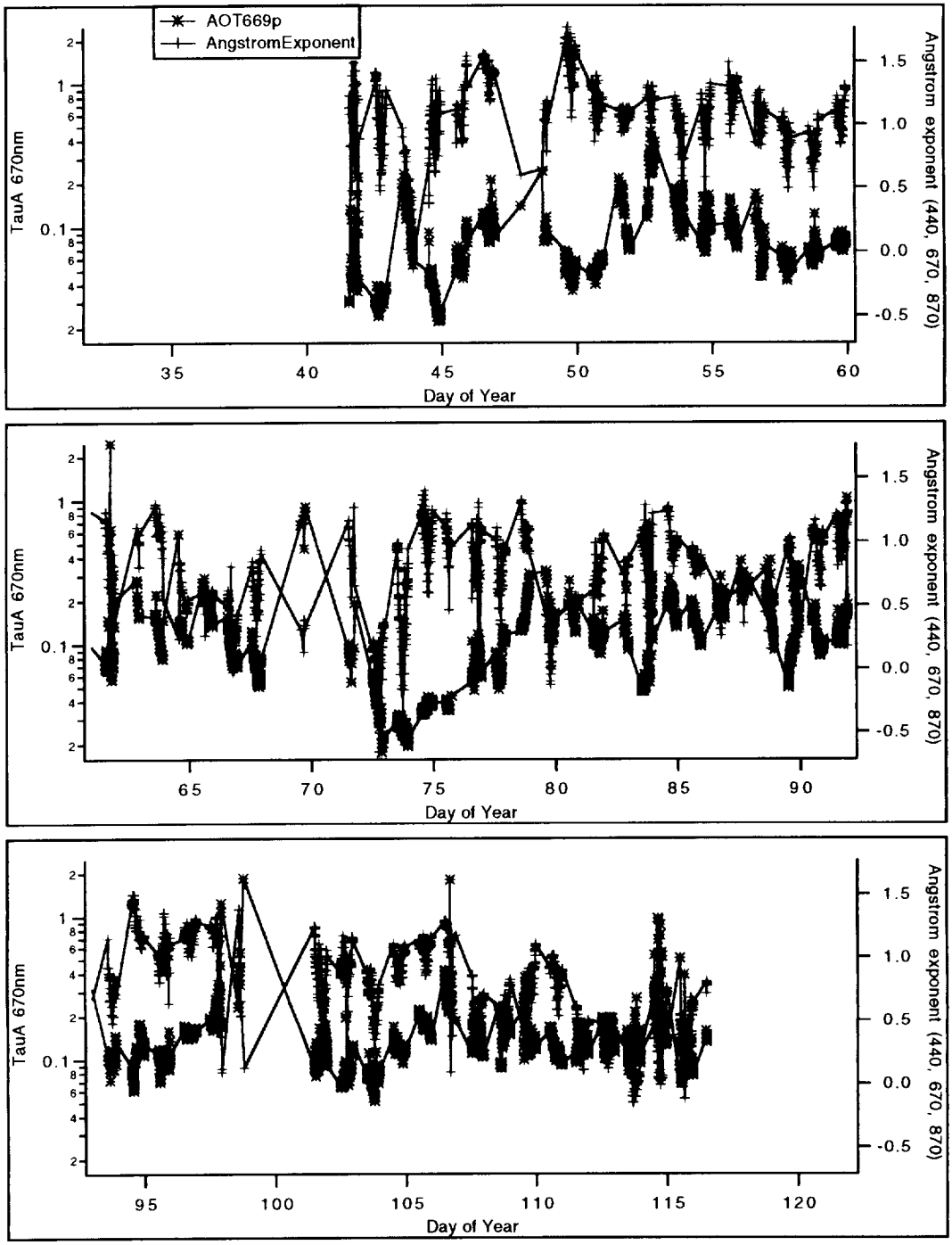

Figure 6-1. Time series of aerosol optical thickness (AOT) at 669 nm and Angstrom exponent at the Dry Tortugas test site.

the sensor. The figure shows the aerosol optical thickness (AOT) at 669 nm as a function of time at the site. Also shown is the Angstrom exponent n that describes the variation of the AOT with

wavelength λ according to $\mathrm{AOT}(\lambda) \propto \lambda^{-n}$. It noteworthy that the AOT is < 0.10 much of the time in winter, but proceeding into the spring it increases to 0.1–0.2 with a simultaneous decrease in n. These continuous measurements confirm the low values of AOT typically observed at sea [*Korotaev et al.*, 1993; *Reddy et al.*, 1990; *Villevalde et al.*, 1994].

Specific periods of time can also be investigated more closely as shown in Figure 6–2, which is an example of a 2-3 day period during which a cold front went through the measurement location. The missing data points are at night (no optical depth information is available at night). The cold front went through during the night of day 43 (43.0-43.5). After the cold front went through the

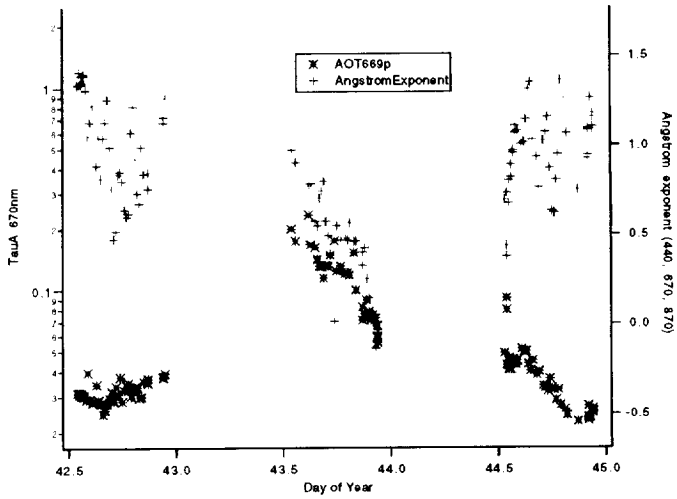

Figure 6–2. Spectral variation of τ_a for the various stratospheric aerosol models. The cirrus cloud model is omitted because $\tau_a(\lambda)$ is constant.

aerosol optical depth and Angstrom exponent decreased quite rapidly. The extreemly low values of the AOT after the passage of a cold front make this an ideal site for vicalrious calibration in winter.

d. Anticipated Future Actions:

(i) We will be participating in the TARFOX experiment during July. TARFOX focuses on measuring atmospheric aerosols emanating from industrial centers in North America and transported over the Atlantic Ocean. Their extent, radiative properties, and transport mechanisms will

be studied from satellite, aircraft, and surface-based sensors. The monitoring effort will concentrate on the corridor extending from Wallops Island, Virginia to Bermuda. In situ aircraft, surface measurements, and satellite observations will simultaneously measure the chemical, physical, and optical properties of the predominant aerosols. This study provides a unique opportunity to validate current satellite remote sensing methods, as well as to provide data needed for developing the atmospheric correction algorithm for regions subjected to absorbing urban aerosols. Brent Holben (NASA/GSFC) has arranged ship logistics to allow us to participate in TARFOX from a ship platform. This is required because the varied land albedo can affect the sky radiance and introduce unnecessary artifacts. The ship platform used is the cruise liner, Meridian. This ship will be making transects continually during the three weeks of TARFOX, between New York and Bermuda (the two of the sites of TARFOX are Wallops and Bermuda). This is an economical way to obtain sky measurements over the ocean, i.e., much cheaper than if a ship had been chartered specifically for this reason. We will be measuring the sky-radiance distribution, solar aureole, and direct solar irradiance during this field trip. Instruments also on board operated by other personnel will be a CIMEL/ASSR, and a possibly a small LIDAR to provide vertical resolution.

In addition to this field trip we will be participating in field exercises with Dennis Clark in September and December in Hawaii. Once again during these trips we will be making field measurements of the sky radiance distribution, solar aureole, and solar irradiance along with some in-water measurements.

Finally, with the demonstration of the importance of the vertical structure in the presence of absorbing aerosols (Section 1 and Appendix 1), it is obvious that knowledge of the vertical structure of such aerosols is critical for developing a climatology to be used for their correction and for validation exercises. Thus, there is a clear need for ship-borne LIDAR to determine the vertical structure of the aerosol over the oceans, particularly in situations in which the aerosol is expected to be strongly absorbing, e.g., in the Saharan dust zone. Thus, during the remainder CY 96, we plan to procure a micropulse lidar (MPL) system for ship-borne use. Our goal is to acquire the system, learn its operation at Miami, and deploy in at sea, in December if possible.

(ii) We will continue to operate the CIMEL instrument in its location in the Dry Tortugas. The instrument is performing well and we do not anticipate problems other than routine maintenance. One issue we are working to resolve is receiving the data in a better format. We are now able to access the data over the network, but at times the speed of the internet line is not adequate. Work will be done in this quarter to address this problem.

(iii) We will develop a sky radiance inversion algorithm that utilized the full vector radiative transfer equation. This should remove the largest radiative transfer error in predicting the TOA radiance from the BOA radiance.

(iv) We will continue to try to obtain ocean color data from other sensors to assess the correction algorithm. We will procure a Unix work station dedicated to image processing that will be suitable for examination of such data and will provide the necessary image processing capability for the post-launch era.

e. Problems/corrective actions: None.

f. Publications:

H.R. Gordon and T. Zhang, How well can radiance reflected from the ocean-atmosphere system be predicted from measurements at the sea surface?, In press in *Applied Optics*.

7. Detached Coccolith Algorithm and Post Launch Studies (W.M. Balch).

We participated in two cruises to the Gulf of Maine, a well known region for mesoscale coccolithophore blooms. We measured coccolithophore abundance, production and optical properties. A thorough understanding of the relationship between calcite abundance and light scatter, in coccolith-rich and coccolith-poor regions, will provide the basis for a generic suspended calcite algorithm.

a. Task Objectives:

The algorithm for retrieval of the detached coccolith concentration from the coccolithophorid, E. huxleyi is described in detail in our ATBD. The key is quantification of the backscattering coefficient of the detached coccoliths. Our earlier studies focussed on laboratory cultures to understand factors affecting the calcite-specific backscattering coefficient. As with algorithms for chlorophyll, and primary productivity, the natural variance between growth related parameters and optical properties needs to be understood before the accuracy of the algorithm can be determined. To this end, the objectives of our coccolith studies have been to define the effect of growth rate on:

(1) the rate that coccoliths detach from cells (this is also a function of turbulence and physical shear),

(2) rates of coccolith production

(3) morphology of coccoliths

(4) volume scattering and backscatter of coccoliths

For perspective on the directions of our work, we provide an overview of our previous activities. During 1995, we focussed on all of the above objectives using chemotstat cultures (in which algal growth rate is precisely controlled). During the latter half of 1995, our work focused on shipboard measurements of suspended calcite and estimates of optical backscattering as validation of the laboratory measurements. We participated on two month-long cruises to the Arabian sea, measuring coccolithophore abundance, production, and optical properties. During the first half of 1996, we

focused again on objectives 2 and 4, during two Gulf of Maine cruises, one in March and one in June.

b. Work Accomplished:

Our work during the last 6 months was mostly directed towards two cruises in the Gulf of Maine, a region known for its dense populations of coccolithophores. We have waited eagerly for an opportunity to take the flow-through instrument into the Gulf of Maine where the coccolithophore, Emiliania huxleyi forms large blooms. (Recall, that our previous cruises were to the Arabian Sea, a region not known for meso-scale coccolithophore blooms, but still containing moderately abundant coccolithophores.) We took our flow-through light scattering photometer, which uses a Wyatt Technologies laser-light scattering photometer equipped with a flow-through cell to measure volume scattering at 18 angles. Integration of this signal in the backward direction allows us to calculate backscattering in real time. During the first 6 months of 1996, we performed considerable programing and instrument interfacing in order to streamline the data flow. The system now monitors chlorophyll fluorescence, pH, temperature, salinity and 18-channel volume scatter. A Global Positioning System was interfaced, as well. The first cruise was in March, a very rough period in this region. We brought our flow-through light scattering detector which functioned flawlessly. In June, we ran 2000 miles of transects in the Gulf of Maine with our flow-through light scattering photometer and may have observed the early stages of coccolithophore bloom development in Wilkinson Basin. During both cruises, we also measured the rate of calcite production (from which we can calculate the turnover of calcite particles in the surface regions of the ocean).

c. Data/Analysis/Interpretation:

As expected, calcite-dependent backscattering was low in the Gulf of Maine during March, but it was still measurable. Typically, calcite scattering accounted for 5-10% of total backscattering. A very different picture was observed in June. Acid-labile scattering increased to 30-40% of total backscattering in Wilkinson Basin, a stratified basin in the middle of the Gulf of Maine. Acid-labile scattering dropped over Georges Bank as the predominant populations were diatoms, and values increased again in the Northeast Channel, similar to previous blooms that we have observed. The

observations are consistent with the calcite being produced in the more stable Wilkinson Basin with subsequent advection around the NE flank of Georges Bank. We are preparing for another Gulf of Maine cruise at the end of October, and again will be taking the flow-through system. Much of these data are still in the process of being worked-up.

Calcification measurements from the March 1996 cruise were remarkably high, given that this was at the beginning of the Spring bloom. We were finding >10% of the carbon being fixed into coccoliths. This also explains the relatively high fraction of calcite-dependent light scattering seen during this time. Calcification rates are still being processed for the June cruise but preliminary results suggest that they were quite high.

d. Anticipated Future Actions:

We are currently performing data analysis for all previous cruise work and this work will continue into the next 6 months. The current state of the data are as follows:

(1) Suspended calcite samples are being run in the graphite furnace atomic absorption spectrometer at the University of Maine. We have completed about 1/5 of our sample backlog and expect the remainder to be done over the summer.

(2) We have hired a full time technician to begin counting our 900 cell and coccolith counts. She is currently working on the Arabian Sea samples from 1995.

(3) All calcification data have been processed to units of gC m^{-3} d^{-1} and integrated over the water column at each station. They still need to be processed into complete sections.

(4) Turnover of the calcite particles needs to be calculated for the Gulf of Maine cruises

(5) The underway data is now processed for temperature, salinity, pH, fluorescence and backscatter (with and without calcite) averaged over each kilometer of all trips. Following final calibration checks have been done for half of the underway data. Hydrographic plots will be made in which light scattering is plotted as a function of temperature and salinity.

(6) Of major interest in this data set will be the relationship between calcite-dependent backscattering (b_b') and the concentration of suspended calcite or concentration of detached coccoliths. This will be of major relevance to our MODIS algorithm efforts. Besides actually checking our algorithm, the net result of these results will be to define the accuracy and precision of the algorithm, exceedingly important for subsequent interpretation.

We are continuing analysis of our previous flow cytometer results.

e. Problems/Corrective Actions: None

f. Publications:

Balch, W. M., K. A. Kilpatrick, P. M. Holligan and C. Trees. 1996. "The 1991 coccolithophore bloom in the central north Atlantic I. Optical properties and factors affecting their distribution." In press. *Limnology and Oceanography.*

Balch, W. M., K. Kilpatrick, P. M. Holligan, D. Harbour, and E. Fernandez. 1996. "The 1991 coccolithophore bloom in the central north Atlantic II. Relating optics to coccolith concentration." In press. *Limnology and Oceanography.*

Balch, W., M. and K. A. Kilpatrick. 1996. "Calcification rates in the equatorial Pacific along 140°W." In press. *Deep Sea Research.*

8. Other Developments.

The PI participated in the MODIS Science Team review of MCST on January 23, 1996 at GSFC.

The PI participated in a conference call with MODIS Science Team members and MCST regarding the SBRS MODIS test schedule on March 8, 1996.

The PI, K.J. Voss, and W. M. Balch participated in the MODIS review meeting in Miami from 30 March to 5 April, 1996.

The PI collaborated with Dennis Clark and Ken Voss in a paper describing a detailed plan for validation of atmospheric correction of MODIS ocean bands. It was presented at the Workshop on Remote Sensing of Aerosols April 15-19 in Washington, D.C. This workshop was organized by Y. Kaufman, D. Tanre, T. Nakajima, and H. Gordon, and was supported by EOS.

The PI attended the MODIS Science Team meeting May, and prepared a memorandum for the MODIS Project Scientist regarding the use of the L1B MODIS data in tracking the MODIS radiometric calibration.

The PI attended the EOS Validation Workshop and chaired the "breakout" group on Validation of Atmospheric Correction of EOS Sensors. With F. Palluconi he prepared a summary report on the activities of the group.

In May we installed an AERONET CIMEL on Barbados at J. Prospero's aerosol monitoring site.

9. Publications, submissions, and abstracts for CY 96.

The following publications, submissions, and abstracts are attached to this report as appendices.

Appendix 1: H.R. Gordon, Atmospheric Correction of Ocean Color Imagery in the Earth Observing System Era, Revised to *Journal of Geophysical Research, Atmospheres.*

Appendix 2: H.R. Gordon, T. Zhang, F. He, and K. Ding, Effects of stratospheric aerosols and thin cirrus clouds on atmospheric correction of ocean color imagery: Simulations, Submitted to *Applied Optics.*

Appendix 3: H.R. Gordon and T. Zhang, How well can radiance reflected from the ocean-atmosphere system be predicted from measurements at the sea surface?, In press in *Applied Optics.*

Appendix 4: Balch, W. M., K. A. Kilpatrick, P. M. Holligan and C. Trees. 1996. "The 1991 coccolithophore bloom in the central north Atlantic I. Optical properties and factors affecting their distribution." In press in *Limnology and Oceanography.*

Appendix 5: Balch, W. M., K. Kilpatrick, P. M. Holligan, D. Harbour, and E. Fernandez. 1996. "The 1991 coccolithophore bloom in the central north Atlantic II. Relating optics to coccolith concentration." In press in *Limnology and Oceanography.*

Appendix 6: Balch, W., M. and K. A. Kilpatrick. 1996. "Calcification rates in the equatorial Pacific along 140°W." In press in *Deep Sea Research.*

Appendix 7: K.D. Moore, K.J. Voss, and H.R. Gordon, Abstract: "Whitecaps: Spectral reflectance in the open ocean and their contribution to water-leaving radiance," Accepted for presentation at the SPIE Ocean Optics XIII Meeting.

10. References.

Frouin, R., M. Schwindling and P. Y. Deschamps, Spectral reflectance of sea foam in the visible and near-infrared: In-situ measurements and implications for remote sensing of ocean color and aerosols, *Jour. Geophys. Res.*, *101C*, 14,361–14,371, 1996.

Gordon, H. R., Ocean Color Remote Sensing Systems: Radiometric Requirements, *Society of Photo-Optical Instrumentation Engineers, Recent Advances in Sensors, Radiometry, and Data Processing for Remote Sensing*, *924*, 151–167, 1988.

Gordon, H. R., O. B. Brown, R. H. Evans, J. W. Brown, R. C. Smith, K. S. Baker and D. K. Clark, A Semi-Analytic Radiance Model of Ocean Color, *Jour. Geophys. Res.*, *93D*, 10909–10924, 1988.

Gordon, H. R. and M. Wang, Influence of Oceanic Whitecaps on Atmospheric Correction of Sea-WiFS, *Applied Optics*, *33*, 7754–7763, 1994.

Korotaev, G. K., S. M. Sakerin, A. M. Ignatov, L. L. Stowe and E. P. McClain, Sun-Photometer Observations of Aerosol Optical Thickness over the North Atlantic from a Soviet Research Vessel for Validation of Satellite Measurements, *Jour. Atmos. Oceanic Technol.*, *10*, 725–735, 1993.

Morel, A. and B. Gentili, Diffuse reflectance of oceanic waters: its dependence on Sun angle as influenced by the molecular scattering contribution, *Applied Optics*, *30*, 4427–4438, 1991.

Morel, A. and B. Gentili, Diffuse reflectance of oceanic waters. II. Bidirectional aspects, *Applied Optics*, *32*, 6864–6879, 1993.

Reddy, P. J., F. W. Kreiner, J. J. Deluisi and Y. Kim, Aerosol Optical Depths Over the Atlantic Derived From Shipboard Sunphotometer Observations During the 1988 Global Change Expedition, *Global Biogeochemical Cycles*, *4*, 225–240, 1990.

Shettle, E. P. and R. W. Fenn, Models for the Aerosols of the Lower Atmosphere and the Effects of Humidity Variations on Their Optical Properties, Air Force Geophysics Laboratory, Hanscomb AFB, MA 01731, AFGL–TR–79-0214, 1979.

Villevalde, Y. V., A. V. Smirnov, N. T. O'Neill, S. P. Smyshlyaev and V. V. Yakovlev, Measurement of Aerosol Optical Depth in the Pacific Ocean and North Atlantic, *Jour. Geophys. Res.*, *99D*, 20983–20988, 1994.

Appendix 1

Atmospheric Correction of Ocean Color Imagery in the Earth Observing System Era

by

Howard R. Gordon

Department of Physics
University of Miami
Coral Gables, FL 33124

Submitted to *Jour. Geophys. Res.*

Abstract

Sensors that can be used for the observation of ocean color in NASA's Earth Observing System era — SeaWiFS, MODIS, and MISR — have been designed with two-four times the radiometric sensitivity of the proof-of-concept ocean color instrument, CZCS. To realize an improvement in the retrieval of biologically important ocean parameters, e.g., the concentration of the photosynthetic pigment chlorophyll a, from this increased sensitivity, significantly better atmospheric correction than was applied to CZCS is required. Atmospheric correction improvement necessitates the inclusion of the effects of multiple scattering, which are strongly dependent on the aerosol size distribution, concentration, and absorption properties. We review the basic concepts of atmospheric correction over the oceans and provide the details of the algorithms currently being developed for SeaWiFS, MODIS, and MISR. An alternate correction algorithm that could be of significant value in the coastal zone, is described for MISR. Related issues such as the influence of aerosol vertical structure in the troposphere, polarization of the light field, sea surface roughness, and oceanic whitecaps on the sea surface are evaluated and plans for their inclusion in the algorithm are described. Unresolved issues, such as the presence of stratospheric aerosol, the appropriateness of the aerosol models used in the assessment of multiple scattering, and the identification of, and difficulties associated with the correction for, the presence of absorbing aerosols, e.g., urban pollution or mineral dust, are identified and suggestions are provided for their resolution.

1. Introduction

Following the work of Clarke, Ewing, and Lorenzen [*Clarke, Ewing and Lorenzen*, 1970] showing that the chlorophyll concentration in the surface waters of the ocean could be deduced from aircraft measurements of the spectrum of upwelling light from the sea — the "ocean color" — NASA launched the Coastal Zone Color Scanner (CZCS) on Nimbus-7 in late 1978 [*Gordon et al.*, 1980; *Hovis et al.*, 1980]. The CZCS was a proof-of-concept mission with the goal of measuring ocean color from space. It was a scanning radiometer that had four bands in the visible at 443, 520, 550, and 670 nm with bandwidths of 20 nm, one band in the near infrared (NIR) at 750 nm with a bandwidth of 100 nm, and a thermal infrared band (10.5 to 12.5 μm) to measure sea surface temperature. The four visible bands possessed high radiometric sensitivity (well over an order of magnitude higher than other visible sensors designed for earth resources at that time, e.g., the MSS sensor on the Landsat series) and were specifically designed for ocean color. The CZCS experience demonstrated the feasibility of the measurement of phytoplankton pigments, and possibly even productivity [*Morel and André*, 1991; *Platt and Sathyendranath*, 1988], on a *global* scale. This feasibility rests squarely on two observations: (1) there exists a more or less universal relationship between the color of the ocean and the phytoplankton pigment concentration for most open ocean waters; and (2) it is possible to develop algorithms to remove the interfering effects of the atmosphere and the sea surface from the imagery. In this paper we will describe the basis of the algorithm for removing the atmospheric and sea surface effects from ocean color sensors to be operating in the Earth Observing System (EOS) [*Asrar and Dozier*, 1994] era to derive the normalized water-leaving radiance in the visible. The process of deriving the normalized water-leaving radiance from imagery of the oceans is usually termed *atmospheric correction*. Three specific sensors will be considered: the sea-viewing wide-field-of-view sensor (SeaWiFS) [*Hooker et al.*, 1992]; the moderate resolution imaging spectroradiometer (MODIS) [*Salomonson et al.*, 1989]; and the multiangle imaging spectroradiometer (MISR) [*Diner et al.*, 1991].

The normalized water-leaving radiance, $[L_w]_N$, was defined by *Gordon and Clark* [1981] through

$$L_w(\lambda) = [L_w(\lambda)]_N \cos\theta_0 \exp\left[-\left(\frac{\tau_r(\lambda)}{2} + \tau_{Oz}(\lambda)\right)\left(\frac{1}{\cos\theta_0}\right)\right], \qquad (1)$$

where $L_w(\lambda)$ is the radiance backscattered *out* of the water toward the zenith at a wavelength λ, $\tau_r(\lambda)$ and $\tau_{Oz}(\lambda)$ are the optical thicknesses of the atmosphere associated with molecular (Rayleigh) scattering and Ozone absorption, respectively. θ_0 is the solar zenith angle. The normalized water-leaving radiance is approximately the radiance that would exit the ocean in the absence of the atmosphere with the sun at the zenith. (This definition was motivated by the desire to remove, as much as possible, the effects of the atmosphere and the solar zenith angle from $L_w(\lambda)$; however, *Morel and Gentili* [1993] have shown that a residual dependence on θ_0 remains in $[L(\lambda)]_N$.) This quantity is used in other algorithms to derive nearly all of the SeaWiFS, MODIS, and MISR ocean products, e.g, the chlorophyll concentration. In what follows, we will abandon the use of radiance in the description of the algorithm in favor of reflectance. The reflectance ρ associated with a radiance L is defined to be $\pi L/F_0 \cos\theta_0$, where F_0 is the extraterrestrial solar irradiance, and θ_0 is the solar zenith angle, i.e., the angle between the line from the point on the sea surface under examination to the sun and the local vertical. Reflectance is favored because it may be possible to more accurately calibrate future sensors in reflectance rather than radiance. The desired normalized water-leaving radiance can easily be converted to normalized water-leaving reflectance $[\rho_w]_N$ through

$$[\rho_w]_N = \frac{\pi}{F_0}[L_w]_N, \tag{2}$$

and Eq. (1) becomes

$$\rho_w(\lambda) = [\rho_w(\lambda)]_N \exp\left[-\left(\frac{\tau_r(\lambda)}{2} + \tau_{Oz}(\lambda)\right)\left(\frac{1}{\cos\theta_0}\right)\right] \equiv [\rho_w(\lambda)]_N t(\theta_0, \lambda), \tag{3}$$

where $t(\theta_0, \lambda)$ is an approximation to the diffuse transmittance of the atmosphere (See Subsection 4.6). Thus, retrieving $[\rho_w]_N$ is equivalent to retrieving $[L_w]_N$. The factor π/F_0 in Eq. (2) is ≈ 0.017 at 443 and 550 nm.

Figures 1a and 1b provide $[\rho_w(\lambda)]_N$ at $\lambda = 443$ and 550 nm as a function of the pigment concentration (C, the sum of the concentrations of chlorophyll a and its degradation product phaeophytin a) for Case 1 waters, i.e., waters for which the optical properties are determined by the water itself along with the phytoplankton and their immediate detrital material. Figure 2 gives the algorithm used to estimate the pigment concentration from $[\rho_w(443)]_N/[\rho_w(550)]_N$. It can be well represented by

$$\log_{10} 3.33C = -1.2\log_{10} R + 0.5(\log_{10} R)^2 - 2.8(\log_{10} R)^3, \tag{4}$$

with $R = 0.5[\rho_w(443)]_N/[\rho_w(550)]_N$. Thus, the pigment concentration C is directly related to the radiance ratios. Analysis [*Gordon*, 1990] suggests that the pigment concentration can be derived from the radiance ratio with an error of $\sim \pm 20\%$. Because of relationships such a these that relate bio-optical parameters to $[\rho_w(\lambda)]_N$, the normalized water-leaving reflectance plays a central

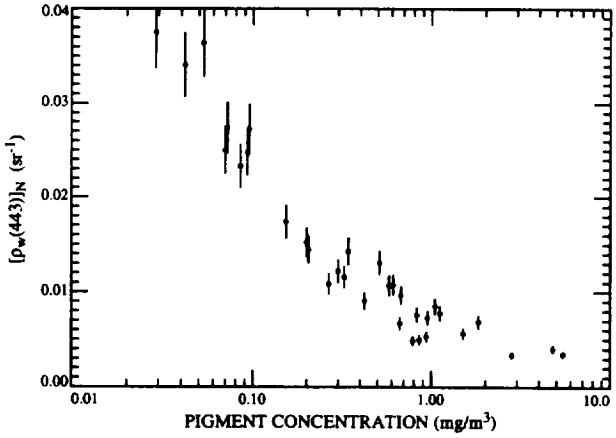

Figure 1a. Normalised water-leaving reflectance at 443 nm as a function of pigment concentration. Redrawn from *Gordon et al.* [1988].

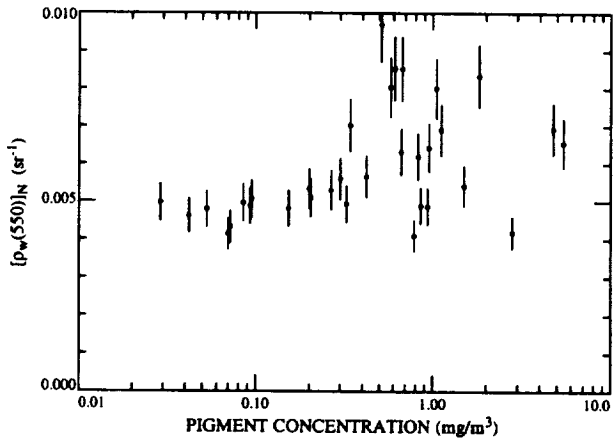

Figure 1b. Normalised water-leaving reflectance at 550 nm as a function of pigment concentration. Redrawn from *Gordon et al.* [1988].

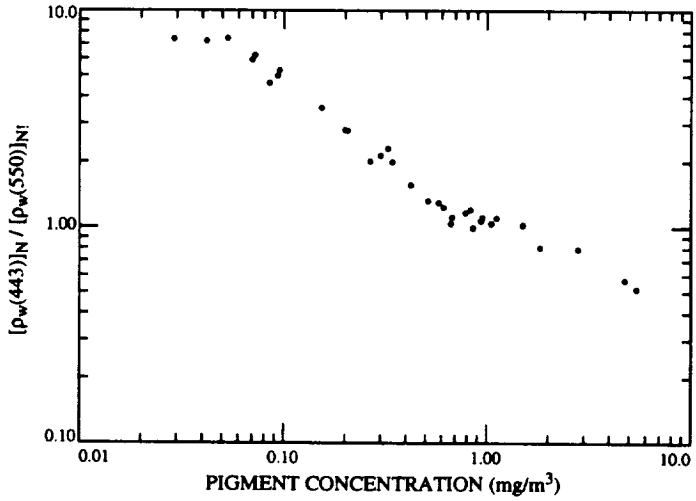

Figure 2. Normalised water-leaving reflectance ratio as a function of pigment concentration. Redrawn from *Gordon et al.* [1988].

role in the application of ocean color imagery to the oceans, and atmospheric correction becomes a critical factor in determining the fidelity with which bio-optical parameters can be retrieved.

We will begin the discussion with a basic overview of atmospheric correction, including the original CZCS algorithm and the advanced algorithm proposed for SeaWiFS (and the prototype for MODIS and MISR). Next we assess the magnitude of errors induced by the simplifying assumptions used to make the SeaWiFS algorithm tractable, and discuss several unresolved issues. Finally, we examine an alternate approach that could be employed with MISR.

Before beginning, however, a few preliminaries are useful. Table 1 provides the radiometric specification for the "ocean" bands on MODIS in terms of reflectance for a solar zenith angle of 60°. In the table, λ is the nominal band center and ρ_{max} is the radiance at which the sensor saturates. For convenience we also provide the "noise equivalent reflectance" (NE$\Delta\rho$) for the Sea-

Table 1: Radiometric performance of MODIS compared with SeaWiFS, MISR, and CZCS for $\theta_0 = 60°$.

Band	λ (nm)	ρ_{max} (Sr^{-1})	ρ_t (Sr^{-1})	$[\rho_w]_N$ (Sr^{-1})	NE$\Delta\rho$ (Sr^{-1})			
					MODIS	SeaWiFS	MISR	CZCS
8	412	0.50	0.34	0.040	0.00018	0.00068	–	–
9	443	0.46	0.29	0.038	0.00016	0.00043	0.00024	0.0011
10	490	0.36	0.23	0.024	0.00014	0.00034	–	–
11	530	0.30	0.19	0.0090	0.00013	0.00031	–	0.00058
12	550	0.25	0.154	0.0050	0.00010	0.00027	0.00020	0.00064
13	670	0.17	0.105	0.0004	0.00004	0.00023	0.00017	0.00051
14	681	0.17	0.105	0.0003	0.00004	–	–	–
15	750	0.15	0.081	–	0.000085	0.00018	–	–
16	865	0.13	0.069	–	0.000076	0.00015	0.00013	–

WiFS, MISR, and CZCS bands closest to the given MODIS band. With the exception of CZCS, the NE$\Delta\rho$ values provided are based on the individual instrument specifications, and may be significantly lower in the completed instruments. The MISR NE$\Delta\rho$ values are for a 1 km $\times$ 1 km pixel size, i.e., approximately the same size as the other sensors. Note that MODIS is typically 2-3 times more sensitive than SeaWiFS, which in turn is approximately twice as sensitive as CZCS. Exceptions are the MODIS bands 13 and 14 which are to be used to measure the chlorophyll *a* fluorescence near 683 nm [*Neville and Gower*, 1977]. These bands are $\sim$ 6 times more sensitive than SeaWiFS and $\sim$ 12 times more sensitive than CZCS. MISR is a little more sensitive than

SeaWiFS. The table also provides the typical top-of-the-atmosphere reflectance ρ_t and the normalized water-leaving reflectance $[\rho_w]_N$ for a very low pigment concentration (Sargasso Sea in summer) [*Gordon and Clark*, 1981]. Note that $[\rho_w]_N$ is only a small fraction of ρ_t. To recover $[\rho_w]_N$ in the blue (443 nm) for these waters with an error $< 5\%$ requires an atmospheric correction of $\sim \pm 0.001$ to ± 0.002 in reflectance, i.e., about five to ten times the NE$\Delta\rho$. This is our goal for MODIS band 9. It is shown later that when this goal is met, the error in $[\rho_w]_N$ at 550 nm will be $\sim$ 3–4 times smaller than that at 443 nm. In this case, Figure 1 shows that the error in the ratio R in Eq. (4) usually will be dominated by error in $[\rho_w]_N$ at 443 nm, the exception being very low values of C.

The critical bands for atmospheric correction are those with nominal band centers $\lambda > 700$ nm, i.e., bands in the near infrared (NIR). Because of the strong absorption by liquid water, virtually no light will exit the ocean in these bands, except in the most turbid coastal waters, so the measured radiance originates from the scattering of solar irradiance by the atmosphere and by the sea surface. These bands can then be used to estimate the atmospheric effects by first assessing the contribution of the atmosphere in the NIR, and then extrapolating it into the visible.

2. Atmospheric Correction

The radiance received by a sensor at the top of the atmosphere (TOA) in a spectral band centered at a wavelength λ_i, $L_t(\lambda_i)$, can be divided into the following components: $L_{path}(\lambda_i)$ the radiance generated along the optical path by scattering in the atmosphere *and* by specular reflection of atmospherically scattered light (skylight) from the sea surface; $L_g(\lambda_i)$ the contribution arising from specular reflection of direct sunlight from the sea surface (sun glitter); $L_{wc}(\lambda_i)$ the contribution arising from sunlight and skylight reflecting from individual whitecaps on the sea surface; and, $L_w(\lambda_i)$ the desired water-leaving radiance; i.e.,

$$L_t(\lambda_i) = L_{path}(\lambda_i) + T(\lambda_i)L_g(\lambda_i) + t(\lambda_i)L_{wc}(\lambda_i) + t(\lambda_i)L_w(\lambda_i). \quad (5)$$

L_{wc} and L_w are area-weighted averages of the radiance leaving whitecap-covered and whitecap-free areas of the surface, respectively. In this equation, T and t are the direct and diffuse, transmittance of the atmosphere, respectively. The diffuse transmittance is appropriate for the water-leaving radiance and the whitecap radiance as they have near-uniform angular distribution. It is

discussed in detail in Subsection 4.6. In contrast, to the diffuse transmittance, the direct transmittance is appropriate when the angular distribution of the radiance is approximately a Dirac delta function. As the sun glitter is highly directional (except at high wind speeds), its transmittance is approximated by the direct transmittance. The direct transmittance is given by

$$T(\theta_v, \lambda) = \exp\left[-\left(\tau_r(\lambda) + \tau_{Oz}(\lambda) + \tau_a(\lambda)\right)\left(\frac{1}{\mu_v}\right)\right],$$

where $\mu_v = \cos\theta_v$, θ_v is the angle the exiting radiance makes with the upward normal at the TOA, and τ_r, τ_a, and τ_{Oz} are, respectively, the Rayleigh, aerosol, and Ozone optical thicknesses. In this equation, we have ignored the possibility of weak continuum (in the atmospheric windows) absorption by water vapor [*Eldridge*, 1967; *Tomasi*, 1979a; *Tomasi*, 1979b] due to the extreme difficulty in separating the direct effect of water vapor absorption from the indirect effect that water vapor will have on the extinction of hygroscopic aerosols [*Fraser*, 1975]. Converting to reflectance Eq. (5) becomes

$$\rho_t(\lambda_i) = \rho_{path}(\lambda_i) + T(\lambda_i)\rho_g(\lambda_i) + t(\lambda_i)\rho_{wc}(\lambda_i) + t(\lambda_i)\rho_w(\lambda_i). \tag{6}$$

Thus, from the measured $\rho_t(\lambda_i)$ we require an algorithm that provides accurate estimates of $\rho_{path}(\lambda_i)$, $T(\lambda_i)\rho_g(\lambda_i)$, $t(\lambda_i)\rho_{wc}(\lambda_i)$, and $t(\lambda_i)$. Near the sun's glitter pattern $T(\lambda_i)\rho_g(\lambda_i)$ is so large that the imagery is virtually useless and must be discarded. A sun glitter mask to remove seriously contaminated pixels is described in Appendix A. Away from the glitter pattern, i.e., where values of $T(\lambda_i)\rho_g(\lambda_i)$ become negligibly small, the largest of the remaining terms, and most difficult to estimate, is $\rho_{path}(\lambda_i)$. This difficulty is principally due to the aerosol by virtue of its highly variable concentration and optical properties. Thus, we concentrate on this term first, then consider $t(\lambda_i)\rho_{wc}(\lambda_i)$ and the ancillary data required to operate the algorithm.

In general, ρ_{path} can be decomposed into several components:

$$\rho_{path} = \rho_r(\lambda) + \rho_a(\lambda) + \rho_{ra}(\lambda) \tag{7}$$

where ρ_r is the reflectance resulting from multiple scattering by air molecules (Rayleigh scattering) in the absence of aerosols, ρ_a is the reflectance resulting from multiple scattering by aerosols in the absence of the air, and ρ_{ra} is the interaction term between molecular and aerosol scattering [*Deschamps, Herman and Tanre*, 1983]. The term ρ_{ra} accounts for the interaction between Rayleigh and aerosol scattering, e.g., photons first scattered by the air then scattered by aerosols,

or photons first scattered by aerosols then air, etc. This term is zero in the single scattering case, in which photons are only scattered once, and it can be ignored as long as the amount of multiple scattering is small, i.e., at small Rayleigh and aerosol optical thicknesses. We note that given the surface atmospheric pressure (to determine the value of τ_r) and the surface wind speed (to define the roughness of the sea surface), ρ_r can be computed accurately, even accounting for polarization effects [*Gordon, Brown and Evans*, 1988; *Gordon and Wang*, 1992b].

In modeling the propagation of radiance in the ocean-atmosphere system, we assume that the atmosphere can be considered to be a vertically stratified, plane parallel medium. The medium is described by providing the extinction coefficient, $c(h)$, as a function of altitude h, the scattering phase function for scattering of radiance from direction $\hat{\xi}'$ to direction $\hat{\xi}$, $P(h;\hat{\xi}' \rightarrow \hat{\xi})$, and the single scattering albedo $\omega_0(h)$. Replacing h by the optical depth τ defined as

$$\tau(h) = \int_h^\infty c(h)\,dh,$$

the propagation of radiance in such a medium in the scalar approximation (the polarization state of the radiance and the change in polarization induced by the scattering process is ignored) is governed by the radiative transfer equation (RTE):

$$\hat{\xi} \bullet \hat{n} \frac{dL(\tau,\hat{\xi})}{d\tau} = -L(\tau,\hat{\xi}) + \frac{\omega_0(\tau)}{4\pi} \int_{\text{all } \hat{\xi}'} P(\tau;\hat{\xi}' \rightarrow \hat{\xi}) L(\tau,\hat{\xi}')\,d\Omega(\hat{\xi}'),$$

where $d\Omega(\hat{\xi}')$ is the differential of solid angle around the direction $\hat{\xi}'$, and $\hat{n}$ is a unit vector in the nadir direction (normal to the sea surface pointed down). Analytical solutions to the RTE are possible only in the simplest case, e.g., $\omega_0 = 0$, so normally one must be satisfied with numerical solutions.

In principal this equation must be solved for the coupled ocean-atmosphere system; however, because of the very low albedo of the ocean (Table 1) it is not necessary to consider the coupling [*Gordon*, 1976], i.e., we can ignore processes such as photons being backscattered out of the water and then scattered back into the water and backscattered out again, etc. The water-leaving radiance simply propagates to the sensor (ρ_{path} is independent of ρ_w in Eq. (6)) and the ocean and atmosphere decouple, hence, we need only understand the solution of the atmospheric part of the problem, i.e., an atmosphere bounded by a Fresnel-reflecting ocean surface.

As the goal of atmospheric correction is to retrieve $\rho_w(443)$ with an uncertainty less than ± 0.002, i.e., $\sim \pm 0.6\%$ of $\rho_t(443)$ (Table 1), for the development and testing of the algorithm we

require solutions of the RTE that yield ρ_t with an uncertainty $\ll 0.6\%$. For the bulk of the work described here, ρ_t was generated using the successive-order-of-scattering method [*van de Hulst*, 1980]. To understand the accuracy of this code, a second code was developed employing Monte Carlo methods. Typically, the values of ρ_t produced by the two codes differ by less than 0.05%. Thus, either code could meet the accuracy required for this work.

We will assume, as justified earlier, that $\rho_w = 0$ in the NIR. The problem we are required to solve can then be stated in a simple manner: given the satellite measurement of the radiance (reflectance) of the ocean-atmosphere system in the NIR, predict the radiance (reflectance) that would be observed in the visible. The difference between the predicted and the measured radiance (reflectance) of the ocean-atmosphere system is the water-leaving radiance (reflectance) transmitted to the top of the atmosphere.

2.1 Single scattering

It is useful to consider $\rho_{path}(\lambda_i)$ in the the limit that the optical thickness of the atmosphere is $\ll 1$. We refer to this as the single-scattering limit. Formulas for the reflectances in this limit are referred to as the single-scattering approximation. The CZCS algorithm was based on the single-scattering approximation. In this approximation the path reflectance reduces to

$$\rho_{path}(\lambda_i) = \rho_r(\lambda_i) + \rho_{as}(\lambda_i), \tag{8}$$

with the aerosol contribution ρ_{as} provided by

$$\rho_{as}(\lambda) = \omega_a(\lambda)\tau_a(\lambda)p_a(\theta_v, \phi_v; \theta_0, \phi_0; \lambda)/4\cos\theta_v \cos\theta_0, \tag{9}$$

$$p_a(\theta_v, \phi_v; \theta_0, \phi_0; \lambda) = P_a(\theta_-, \lambda) + \Big(r(\theta_v) + r(\theta_0)\Big) P_a(\theta_+, \lambda),$$

$$\cos\theta_\pm = \pm\cos\theta_0 \cos\theta_v - \sin\theta_0 \sin\theta_v \cos(\phi_v - \phi_0),$$

where $P_a(\alpha, \lambda)$ is the aerosol scattering phase function for a scattering angle α, ω_a is the aerosol single scattering albedo, and $r(\alpha)$ is the Fresnel reflectance of the interface for an incident angle α. The angles θ_0 and ϕ_0 are, respectively, the zenith and azimuth angles of a vector from the point on the sea surface under examination (pixel) to the sun, and likewise, θ_v and ϕ_v are the zenith and azimuth angles of a vector from the pixel to the sensor. These are measured with respect to the *upward* normal so θ_v and θ_0 are both less than 90° in these equations. In what follows usually we take $\phi_0 = 0$.

We assume we are given the the path reflectance at two bands in the NIR at λ_s and λ_l, where the subscript "s" stands for short and "l" for long, e.g., for MODIS $\lambda_s = 750$ nm and $\lambda_l = 865$ nm, for SeaWiFS $\lambda_s = 765$ and $\lambda_l = 865$, for MISR $\lambda_s = 670$ nm and $\lambda_l = 865$ nm, while for CZCS there were no NIR bands. This would be accomplished in the following manner. We ignore sun glitter, i.e., assume θ_v is outside the glitter pattern, and assume that $t(\lambda_i)\rho_{wc}(\lambda_i)$ has been provided, then, since we can take $\rho_w = 0$ at both λ_s and λ_l, ρ_{path} can be estimated from the measured ρ_t at both λ_s and λ_l. As $\rho_r(\lambda)$ can be computed accurately, $\rho_{as}(\lambda_s)$ and $\rho_{as}(\lambda_l)$ are determined from the associated values of ρ_{path} at λ_s and λ_l. This allows estimation of the parameter $\varepsilon(\lambda_s, \lambda_l)$:

$$\varepsilon(\lambda_s, \lambda_l) \equiv \frac{\rho_{as}(\lambda_s)}{\rho_{as}(\lambda_l)} = \frac{\omega_a(\lambda_s)\tau_a(\lambda_s)p_a(\theta_v, \phi_v; \theta_0, \phi_0; \lambda_s)}{\omega_a(\lambda_l)\tau_a(\lambda_l)p_a(\theta_v, \phi_v; \theta_0, \phi_0; \lambda_l)}. \tag{10}$$

If we can compute the value of $\varepsilon(\lambda_i, \lambda_l)$ for the band at λ_i from the value of $\varepsilon(\lambda_s, \lambda_l)$, this will yield $\rho_{as}(\lambda_i)$, which, when combined with $\rho_r(\lambda_i)$, provides the desired $\rho_{path}(\lambda_i)$:

$$\rho_{path}(\lambda_i) = \rho_r(\lambda_i) + \varepsilon(\lambda_i, \lambda_l)\rho_{as}(\lambda_l). \tag{11}$$

Clearly, the key to utilizing this procedure is the estimation of $\varepsilon(\lambda_i, \lambda_l)$ from $\varepsilon(\lambda_s, \lambda_l)$.

2.1.1 The CZCS algorithm

The atmospheric correction algorithm for CZCS was described in detail in *Evans and Gordon* [1994]. Briefly, the basic CZCS algorithm [*Gordon*, 1978; *Gordon and Clark*, 1980] was based on single scattering; however, $\rho_r(\lambda_i)$ was computed accurately, including the effects of multiple scattering and polarization [*Gordon, Brown and Evans*, 1988]. As there were no NIR bands, the algorithm could not be operated as described in Section 2.1. However, Table 1 shows that $\rho_w(670)$ can generally be taken to be zero (at least if the pigment concentration is low enough). Thus, the single scattering algorithm was typically operated with $\lambda_l = 670$ nm and $\rho_w(\lambda_l) = 0$. Unfortunately, there was no shorter wavelength (λ_s) for which $\rho_w = 0$, so in the processing of the CZCS global data set [*Feldman et al.*, 1989] $\varepsilon(\lambda_i, \lambda_s)$ was set equal to unity. This is characteristic of a maritime aerosol at high relative humidity (Subsection 2.1.2).

For sufficiently low C values, Figure 1b suggests that $[L_w(550)]_N$, and hence $[\rho_w(550)]_N$ is approximately constant. This fact can be used to estimate $\varepsilon(550, 670)$ for such "clear water" regions [*Gordon and Clark*, 1981] in a scene, allowing a basis for extrapolation to 520 and 443 nm.

If the resulting $\varepsilon(\lambda_i, \lambda_l)$ is then assumed to be valid for the entire image, retrieval of $[\rho_w(\lambda_i)]_N$ and C can be effected for the image. This is the procedure used by *Gordon et al.* [1983] in the Middle Atlantic Bight. Unfortunately, there are serious difficulties applying this procedure routinely. For example, the image of interest may contain no "clear water," the ε's may vary over the image because of variations in aerosol type [*André and Morel*, 1991; *Bricaud and Morel*, 1987], and the pigment concentration may not be small enough to take $\rho_w = 0$ at 670 nm. Morel and his co-workers have developed a promising approach for dealing these problems in Case 1 waters [*André and Morel*, 1991; *Bricaud and Morel*, 1987] based on the ideas of *Smith and Wilson* [1981]. This involves utilizing a modeled relationship between C and $[\rho_w(\lambda_i)]_N$. Fortunately, for the sensors of concern in this paper (SeaWiFS, MODIS, and MISR), these problems are circumvented by virtue of the additional spectral band(s) with $\lambda > 700$ nm.

2.1.2 Application to EOS era sensors

As the key extrapolation to $\varepsilon(\lambda_i, \lambda_l)$ from $\varepsilon(\lambda_s, \lambda_l)$ for application of the single scattering algorithm to the EOS era sensors involves more than a factor of two in wavelength, it is important to try to gain some insight into the possible spectral behavior of $\varepsilon(\lambda_i, \lambda_l)$. This has been attempted by *Gordon and Wang* [1994a] by computing $\varepsilon(\lambda_i, \lambda_l)$ for several aerosol models. Briefly, they used aerosol models that were developed by *Shettle and Fenn* [1979] for LOWTRAN-6 [*Kenizys et al.*, 1983]. These models consist of particles distributed in size according to combinations of log-normal distributions. The size frequency distribution $n(D)$ is given by

$$n(D) = \sum_{i=1}^{2} n_i(D),$$

with

$$n_i(D) = \frac{dN_i(D)}{dD} = \frac{N_i}{\log_e(10)\sqrt{2\pi}\sigma_i D} \exp\left[-\frac{1}{2}\left(\frac{\log_{10}(D/D_i)}{\sigma_i}\right)^2\right],$$

where, $dN_i(D)$ is the number of particles per unit volume between D and $D + dD$, D_i and σ_i are the median diameter and the standard deviation, respectively, and N_i is the total number density of the i^{th} component. Since hygroscopic particles swell with increasing relative humidity (RH), D_i and σ_i are functions of RH. The smaller size fraction is a mixture of 70% water soluble and 30% dust-like particles called the Tropospheric aerosol. It has been used to represent the aerosols within the free troposphere above the boundary-layer [*Shettle and Fenn*, 1979]. The refractive index m for this component at 550 nm ranges from $1.53 - 0.0066i$ at RH = 0, to

$1.369 - 0.0012i$ at RH = 98%. Thus as the particles absorb more water, the real part of their refractive index approaches that of water and the imaginary part (proportional to the absorption coefficient) decreases. Because of the moderate imaginary part of the refractive index, these particles have weak absorption and ω_a ranges from 0.959 to 0.989 for $0 \leq$ RH $\leq$ 98%. The modal diameter of this component is always < 0.1 μm. The larger fraction is a sea salt-based component, the "Oceanic" aerosol. Its modal diameter varies from about 0.3 to 1.2 μm as RH varies from 0 to 98%. Its index of refraction is essentially real (imaginary part $\sim 10^{-8}$), so $\omega_a = 1$. Like the tropospheric aerosol its real part ranges from 1.5 at RH = 0 to 1.35 at RH = 98%.

From these components, three basic models were constructed: the Tropospheric model with no Oceanic contribution; the Maritime model for which 99% of the particles have the Tropospheric characteristics and 1% the Oceanic; and the Coastal model for which 99.5% of the particles have the Tropospheric characteristics and 0.5% the Oceanic. *Gordon and Wang* [1994a]

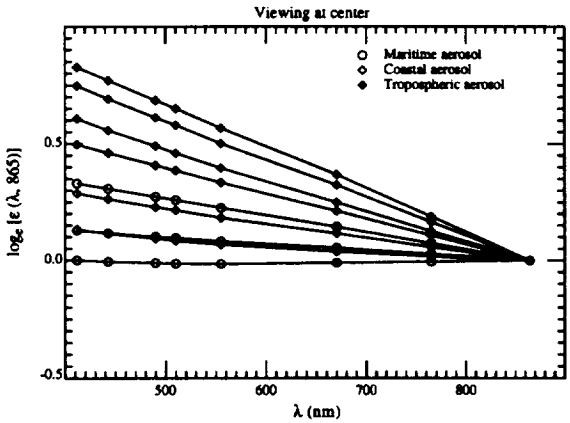

Figure 3a. $\varepsilon(\lambda, 865)$ for nadir viewing with $\theta_0 = 60°$ for the Maritime, Coastal, and Tropospheric aerosol models. For each model, the RH values are 50, 80, and 98% from the upper to the lower curves.

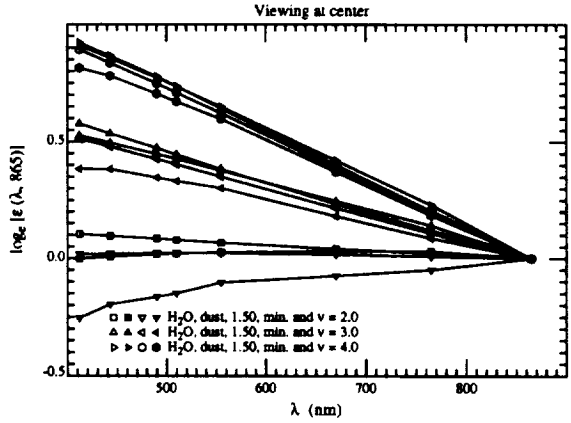

Figure 3b. $\varepsilon(\lambda, 865)$ for nadir viewing with $\theta_0 = 60°$ for the Hase C models. Note that the open symbols are for models with little or no absorption, while the filled symbols are for absorbing models.

introduced the Coastal aerosol model to represent the aerosol over the oceans nearer the coast (less Oceanic contribution). The properties of all three aerosol models depend on the wavelength and relative humidity. With the values of D_i, σ_i, and $m_i(\lambda)$ taken from *Shettle and Fenn* [1979], Mie theory was used to calculate the optical properties for all three models for the SeaWiFS–MODIS–MISR spectral bands at different relative humidities.

Sample results for $\varepsilon(\lambda_i, \lambda_l)$, where λ_l is taken to be 865 nm (SeaWiFS), are presented in Figure 3a. These computations suggest that there should be a strong variation of ε with aerosol model and RH. The increase in particle size (due to swelling) with increasing RH clearly reduces the spectral variation of ε. The spectral variation of ε is due in large part to the spectral variation of the aerosol optical thickness, τ_a; however, additional variation is produced by the aerosol phase function. Note that Figure 3a is plotted in a format that would yield a straight line under the hypothesis that $\varepsilon(\lambda_i, \lambda_l) = \exp\left[c(\lambda_l - \lambda_i)\right]$, where c is a constant. This shows that over the range 412–865 nm $\varepsilon(\lambda_i, \lambda_l)$ can be considered to be an exponential function of $\lambda_l - \lambda_i$, for the *Shettle and Fenn* [1979] models. *Wang and Gordon* [1994b] have used this fact to extend the CZCS algorithm for use with SeaWiFS and MODIS.

We now examine the accuracy of this CZCS-type single-scattering algorithm based on an assumed exponential spectral variation of $\varepsilon(\lambda_i, \lambda_l)$. For this purpose, we simulated atmospheres using an array of aerosol models. First, the aerosol optical properties were taken from the Tropospheric, Coastal, and Maritime models at RH = 80%, denoted, respectively, as T80, C80, and M80. Then, we simulated the aerosol using the *Shettle and Fenn* [1979] Urban model at RH = 80% (U80). This model shows strong absorption. In addition to the water soluble and dust-like particles of the Tropospheric model, the Urban model contains soot-like particles (combustion products). Also, the Urban model has a second, larger particle, mode in addition to that of the Tropospheric model. At 865 nm the Mie theory computations yielded, $\omega_a = 0.9934$, 0.9884, and 0.9528, respectively, for the Maritime, Coastal, and Tropospheric models (RH = 80%), while in contrast, $\omega_a = 0.7481$ for the Urban model. Here, the Urban model is intended to represent aerosols that might be present over the oceans near areas with considerable urban pollution, e.g., the Middle Atlantic Bight off the U.S. East Coast in summer. Finally, we examined aerosols with a different analytical form for the size distribution [*Junge*, 1958]:

$$
\begin{aligned}
n(D) = \frac{dN(D)}{dD} &= K, && D_0 < D < D_1, \\
&= K\left(\frac{D_1}{D}\right)^{\nu+1}, && D_1 < D < D_2, \\
&= 0, && D > D_2,
\end{aligned}
$$

with $D_0 = 0.06$ μm, $D_1 = 0.20$ μm, and $D_2 = 20$ μm. Following *Deirmendjian* [1969] we call these Haze C models. Twelve separate models were considered: $\nu = 2$, 3, and 4, with the refractive index of the particles taken to be that of liquid water (from *Hale and Querry* [1973]), close to that of the dust component in the Tropospheric model ($1.53 - 0.008i$), nonabsorbing crystals

$(1.50 - 0i)$, and absorbing minerals that might be expected from desert aerosols transported over the oceans [*d'Almeida, Koepke and Shettle*, 1991]. The spectral behavior of $\varepsilon(\lambda, 865)$ for these models is presented in Figure 3b. We see that the absorption-free (open symbols) Haze C models display a behavior similar to the Shettle and Fenn models; however, for models with strong absorption (solid symbols) departures are seen, especially for the mineral models for which the imaginary part of the refractive index increases with decreasing λ.

Using these aerosol models we generated hypothetical atmospheres with a two-layer structure: the aerosols occupying the lower layer, and all molecular scattering confined to the upper layer. This distribution of aerosols is similar to that typically found over the oceans when the aerosol is locally generated, i.e., most of the aerosol is confined to the marine boundary layer [*Sasano and Browell*, 1989]. The atmosphere was bounded by a flat (smooth) Fresnel-reflecting sea surface, and all photons that penetrate the interface are assumed to be absorbed in the ocean. The RTE in the scalar approximation was solved for this hypothetical atmosphere using the successive-

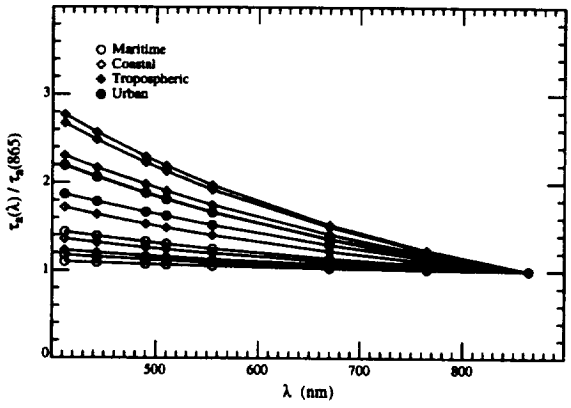

Figure 4a. Spectral variation of τ_a for the Maritime, Coastal, and Tropospheric aerosol models. For each model, the RH values are 50, 80, and 98% from the upper to the lower curves.

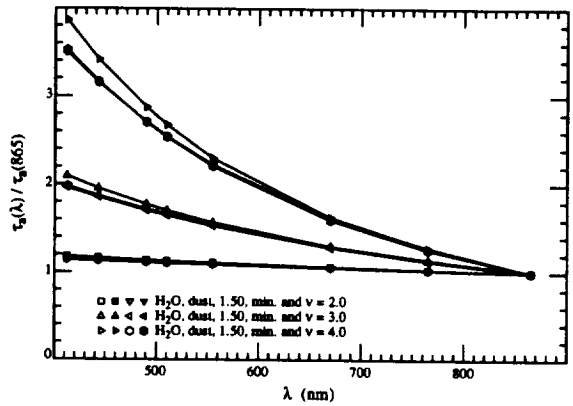

Figure 4b. Spectral variation of τ_a for the Haze C models. Note that the open symbols are for models with little or no absorption, while the filled symbols are for absorbing models.

order-of-scattering method [*van de Hulst*, 1980] to provide pseudo TOA reflectance (ρ_t) data. All significant orders of multiple scattering were included. As the surface was assumed to be smooth (no wind), the sun glitter and whitecap terms in Eq. (6) are absent. The simulations of ρ_t were carried out for the following geometries: $\theta_0 = 20°$, $40°$, and $60°$, with $\theta_v \approx 1°$ and $\phi_v - \phi_0 = 90°$, i.e., viewing near the MODIS scan center: and $\theta_0 = 0°$, $20°$, $40°$, and $60°$, with $\theta_v \approx 45°$ and

$\phi_v - \phi_0 = 90°$, i.e., viewing near the scan edge. In this manner a wide range of sun-viewing geometries were included. Four wavelengths were considered: λ_i = 443, 555, 765, and 865 nm. The values used for the aerosol optical thickness at 865 nm, $\tau_a(865)$, were 0.1, 0.2, 0.3, and 0.4. The values of $\tau_a(\lambda_i)$ at the other wavelengths were determined from the spectral variation of the extinction coefficient for each particular model. These are provided in Figure 4. The Haze C models clearly show that the spectral variation of τ_a is principally determined by the size distribution, with the index of refraction playing only a minor role. Equation (10) suggests that there should be a relationship between $\tau_a(\lambda)/\tau_a(865)$ and $\varepsilon(\lambda, 865)$. Figure 5 provides an example of this for $\theta_0 = 60°$ and nadir viewing, i.e., the same geometry as in Figure 3, with $\varepsilon(765, 865)$ used rather than $\varepsilon(443, 865)$. Thus, for a given $\tau_a(865)$, $\tau_a(443)$ will generally increase with increasing $\varepsilon(765, 865)$. This will be useful in interpreting the results described below.

As the true $\rho_w(\lambda_i)$ is taken to be zero in the pseudo data (all photons entering the water are absorbed), the error in atmospheric correction, i.e., the error in the retrieved water-leaving

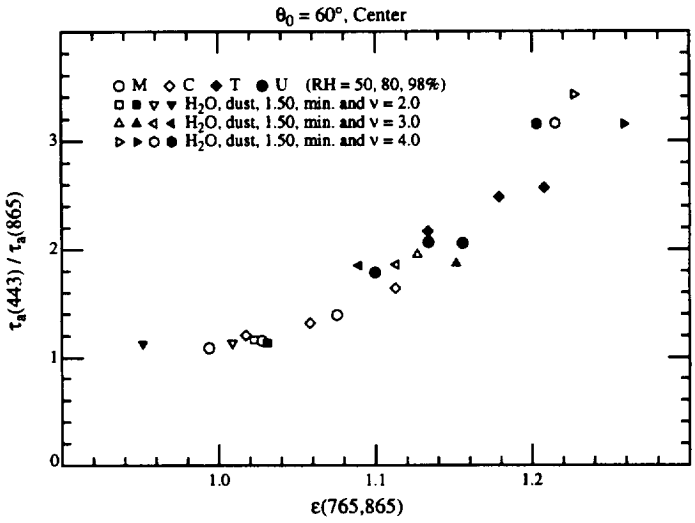

Figure 5. Relationship between $\varepsilon(765, 865)$ and $\tau_a(443)/\tau_a(865)$ for the various aerosol models with $\theta_0 = 60°$ and nadir viewing.

reflectance, $\Delta(t\rho_w)$, is just the error in the predicted path radiance. This is

$$\Delta\left(t\rho_w(\lambda_i)\right) = \rho_t(\lambda_i) - \rho_{path}(\lambda_i) = \rho_t(\lambda_i) - \rho_r(\lambda_i) - \varepsilon^{(e)}(\lambda_i, \lambda_l)\rho_{as}(\lambda_l), \tag{12}$$

where $\varepsilon^{(e)}(\lambda_i, \lambda_l)$ is the estimated value of $\varepsilon(\lambda_i, \lambda_l)$ assuming an exponential variation with λ_i:

$$\varepsilon^{(e)}(\lambda_i, \lambda_l) \equiv \exp[c(\lambda_l - \lambda_i)] = \exp\left[\left(\frac{\lambda_l - \lambda_i}{\lambda_l - \lambda_s}\right) \log_e \left(\frac{\rho_{as}(\lambda_s)}{\rho_{as}(\lambda_l)}\right)\right].$$

$\rho_r(\lambda_i)$ was computed using the same radiative transfer code, i.e., it includes all effects of multiple scattering, but not polarization. In an actual application, $\rho_r(\lambda_i)$ would be computed using a code that included polarization as well [*Gordon, Brown and Evans*, 1988]. Figure 6 provides the error in the retrieved normalized water-leaving reflectance, $\Delta[\rho_w(443)]_N$, for the seven sun-viewing geometries and for $\tau_a(865) = 0.1$ and 0.2. To derive $\Delta[\rho_w]_N$ from $\Delta t\rho_w$, the approximation for t in Eq. (3) was utilized (see Subsection 4.6). The x-axis in Figure 6, $\varepsilon^{(e)}(765, 865)$, is the *estimated* value for the indicated model and geometry.

In the absence of aerosol absorption (open symbols), the performance of this simple algorithm is truly remarkable, as Figures 4b and 5 show that for $\nu = 4$, $\tau_a(443) \approx 0.35$ and 0.70 for Figures 6a and 6b, respectively. The large negative errors for $\nu = 4$ occur at the scan edge with $\theta_0 = 60°$, i.e., the geometry with the most multiple scattering. For $\nu = 3$ ($\tau_a(443) \sim 0.2$ and 0.4 (Figures 4b and 5 for Figures 6a and 6b, respectively), the retrieved value of $[\rho_w(443)]_N$ is usually within the acceptable limits.

In the case of absorbing aerosols, the errors are seen to be mostly negative, and to grow rapidly with $\tau_a(443)$. Negative errors are particularly troublesome as they can lead to negative

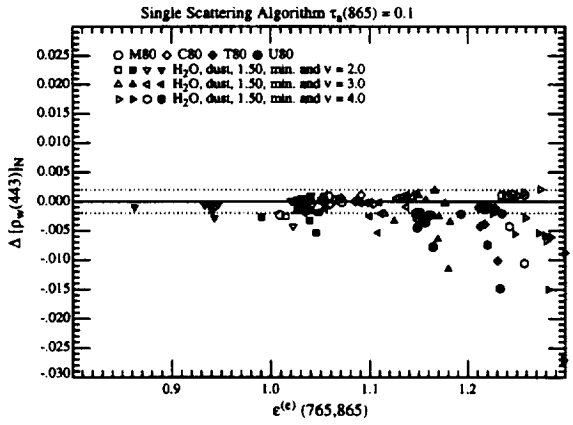

Figure 6a. $\Delta[\rho_w(443)]_N$ as a function of $\varepsilon^{(e)}(765, 865)$ for $\tau_a(865) = 0.1$ and all of the aerosol models and viewing geometries examined in the study.

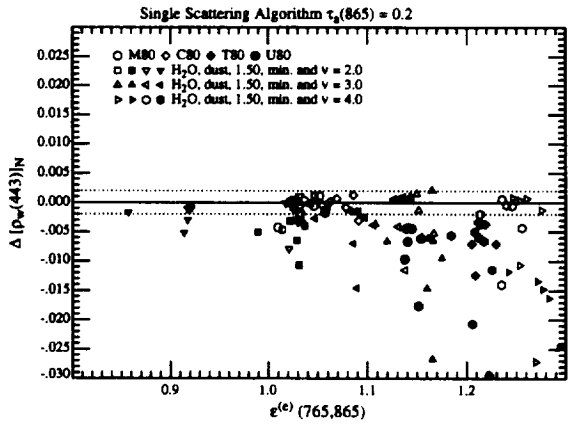

Figure 6b. $\Delta[\rho_w(443)]_N$ as a function of $\varepsilon^{(e)}(765, 865)$ for $\tau_a(865) = 0.2$ and all of the aerosol models and viewing geometries examined in the study.

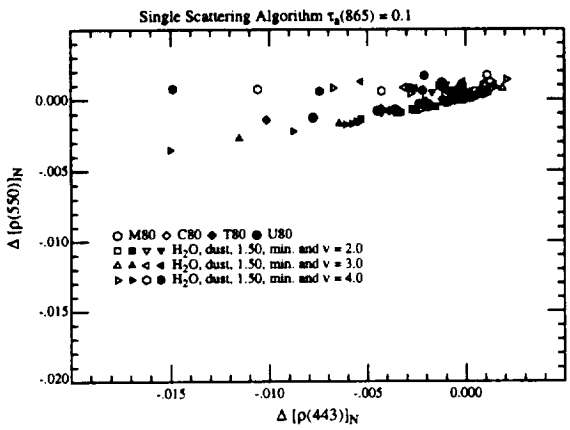

Figure 6c. $\Delta[\rho_w(550)]_N$ as a function of $\Delta[\rho_w(443)]_N$ for the results in Figure 6a.

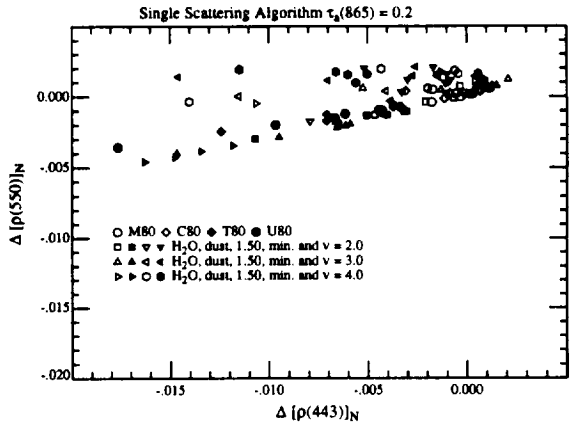

Figure 6d. $\Delta[\rho_w(550)]_N$ as a function of $\Delta[\rho_w(443)]_N$ for the results in Figure 6b.

values in the retrieved $[\rho_w(443)]_N$ when the pigment concentration $\gtrsim 0.5 - 1.0$ mg/m^3. The source of the error for absorbing aerosols is twofold. For the Haze C aerosol, it can be seen from Figure 3b that, in contrast to the nonabsorbing aerosols, an exponential extrapolation of $\varepsilon(765, 865)$ to $\varepsilon(443, 865)$ would lead to an erroneous overestimation of $\varepsilon(443, 865)$, the single exception being the mineral aerosol with $\nu = 2$. This will cause an overestimation of the aerosol contribution at 443 nm, which in turn will result in a negative error in $[\rho_w(443)]_N$. In contrast, the extrapolation does work well for T80 (Figure 3a) and, as we shall see later, in this case the error is principally due to multiple scattering, which is strongly influenced by even weak absorption.

The error in $[\rho_w(550)]_N$ as related to the associated error in $[\rho_w(443)]_N$ is provided in Figures 6c and 6d. The observed improvement in atmospheric correction at 550 compared to 443 nm can be traced to the facts that (1) the ε determination requires a smaller extrapolation at 550 nm, and (2) there is less multiple scattering at 550 nm as both τ_a (Figure 4) and τ_r are smaller. Notably, the error at 550 nm is usually much less than that at 443 nm, there being a tendency for $\Delta[\rho_w(550)]_N \sim (1/4)\Delta[\rho_w(443)]_N$, although occasionally $|\Delta[\rho_w(550)]_N| \gtrsim |\Delta[\rho_w(443)]_N|$. Thus, in a pigment ratio algorithm such as Eq. (4), the error at 443 nm will usually be the more significant error in R.

It is useful at this point to review the sparse direct observations of the aerosol optical thickness over the oceans. In the open ocean, far from sources of pollution and/or sources of desert aerosols, the atmosphere is very clear. In the Pacific $\tau_a(550)$ is found in the range 0.04 to 0.24

with a mean of 0.13 and Angstrom exponent of 0.56 [*Villevalde et al.*, 1994], suggesting a mean $\tau_a(865)$ of $\sim$ 0.1 and a maximum of $\sim$ 0.19. Similar results are obtained for the North Atlantic [*Korotaev et al.*, 1993; *Reddy et al.*, 1990]. In such a region, *Lechner et al.* [1989] found that there were low concentrations of aerosol in the free troposphere possessing a Haze C-like distribution with an average ν of $\sim$ 3.5, while in the marine boundary layer the concentration was much higher (an highly variable) with an average ν of $\sim$ 1.8, and sometimes even a bimodal size distribution (the large mode presumably resulting from local generation of aerosols by breaking waves). In contrast, in the region of the Atlantic off West Africa subject to Saharan dust, *Reddy et al.* [1990] found a mean $\tau_a(550)$ of 0.4 with $\tau_a(865) \approx 0.3$, in agreement with the observations of *Korotaev et al.* [1993], $\tau_a(550) \sim 0.3$ to 0.5. In areas subject to urban pollution, even higher optical thicknesses are observed, e.g., *Reddy et al.* [1990] found a mean $\tau_a(550) \approx 0.5$ and $\tau_a(865) \approx 0.3$ in the Western North Atlantic in summer when trajectory analysis suggested the origin of the air mass was the North American continent.

Thus, direct observation suggests that over the open ocean most of the aerosol is in the marine boundary layer and, for mean conditions $\tau_a(865) \approx 0.1$. Furthermore, the size distribution is either similar to Haze C with $\nu \approx 2.5$ or bimodal like M80 or C80. Such aerosols would have $\varepsilon(765, 865) < 1.1$ (Figure 5). Figure 6a (open symbols) with $\varepsilon(765, 865) < 1.1$ is appropriate to these mean conditions and shows that the single scattering CZCS-type algorithm should be capable of retrieving $[\rho_w(443)]_N$ with the desired accuracy. For the maximum $\tau_a(865)$ ($\sim$ 0.19), Figure 6b is appropriate and under the same conditions for maximum end of the observed $\tau_a(865)$ range, and for most of the geometries good retrievals are obtained, although in some cases, the error is outside the acceptable range.

For situations with a strong continental influence, e.g., Saharan dust or urban pollution carried over the oceans by the wind, the aerosol is likely to be at least moderately absorbing. Also, $\tau_a(\lambda)$ will be sufficiently large that aerosol single scattering will no longer be an adequate approximation. Thus, we are forced to consider a full multiple scattering approach.

2.2 Multiple scattering

Multiple scattering effects have already been shown [*Deschamps, Herman and Tanre*, 1983; *Gordon, Brown and Evans*, 1988; *Gordon and Castaño*, 1987] to be significant at the level of ac-

curacy required for SeaWiFS and MODIS, i.e., $\Delta[\rho_w(443)]_N \approx 0.001 - 0.002$. Although the single scattering approach is seen to work well only for sufficiently small optical depth (Figure 6) and nonabsorbing aerosols, typically the case over the open ocean, we desire an algorithm that can cope with even extreme situations. To begin the study of the effects of multiple scattering, we examine the properties of the solutions to the RTE used in providing the pseudo data for Figure 6. Since we are ignoring sun glitter and whitecaps for the moment, we can assess the multiple scattering effects by noting that

$$\rho_t - \rho_r - t\rho_w = \rho_a + \rho_{ra} \overset{\text{Single Scattering}}{\longrightarrow} \rho_{as}.$$

Thus, comparison of $\rho_t - \rho_r - t\rho_w$ and ρ_{as} provides a direct assessment of multiple scattering. Figures 7a and 7b provide such a comparison for the Tropospheric model with RH = 50%

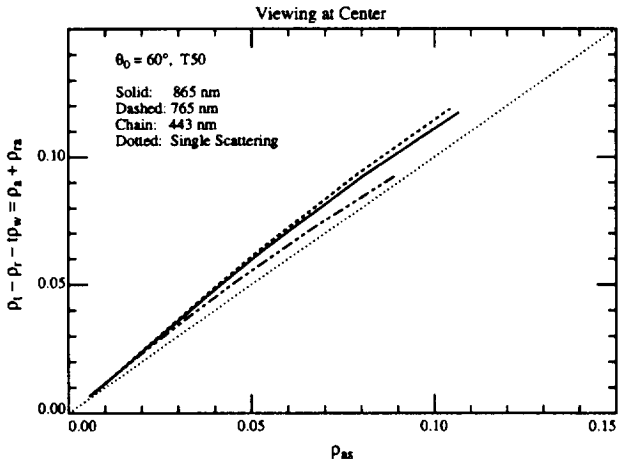

Figure 7a. $\rho_a(\lambda) + \rho_{ra}(\lambda)$ as a function of $\rho_{as}(\lambda)$ for aerosol model T50 at $\theta_0 = 60°$ and nadir viewing.

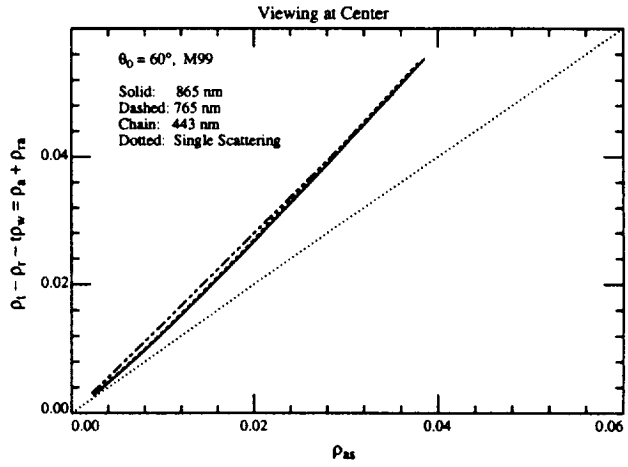

Figure 7b. $\rho_a(\lambda) + \rho_{ra}(\lambda)$ as a function of $\rho_{as}(\lambda)$ for aerosol model M99 at $\theta_0 = 60°$ and nadir viewing.

(T50) and the Maritime model with RH = 99% (M99). Note that for the Maritime aerosol for $\rho_{as} \gtrsim 0.01$, the value of $\rho_a + \rho_{ra}$ is about 40% greater that ρ_{as}, i.e., multiple scattering significantly increases the reflectance due to the aerosol. In contrast, for the Tropospheric model at RH = 50% the aerosol reflectance is only increased by $\sim$ 10%. Thus, we see that the influence of multiple scattering depends significantly on the aerosol model. In contrast to the algorithm in Subsection 2.1.2, for which multiple scattering was ignored, and for which no knowledge of the aerosol properties was required to effect the atmospheric correction, the model-dependent multiple scattering will make it necessary to utilize aerosol models in the ρ_w retrieval algorithm. As the only *direct* link to the aerosol models is through $\varepsilon(\lambda, \lambda_l)$, or in particular through $\varepsilon(\lambda_s, \lambda_l)$, it

seems reasonable to retain the formalism of the single scattering algorithm, but modify it to include multiple scattering. Writing

$$\rho_a(\lambda) + \rho_{ra}(\lambda) = K[\lambda, \rho_{as}(\lambda)]\rho_{as}(\lambda),$$

where the dependence of K on $\rho_{as}(\lambda)$ represents the departure of the $\rho_a(\lambda)+\rho_{ra}(\lambda)$ versus $\rho_{as}(\lambda)$ relationship from linearity, we see that K is nearly the same for the two NIR bands, but can be significantly different at 443 nm (Figure 7a). It is irrelevant whether the dependence of K on λ is explicit ($K = K[\lambda]$) or implicit ($K = K[\rho_{as}(\lambda)]$) or both, the effect is the same: Eq. (12) becomes

$$\Delta\big(t\rho_w(\lambda_i)\big) = \rho_t(\lambda_i) - \rho_r(\lambda_i) - \frac{K[\lambda_i, \rho_{as}(\lambda_i)]}{K[\lambda_l, \rho_{as}(\lambda_l)]}\varepsilon(\lambda_i, \lambda_l)\big[\rho_a(\lambda_l) + \rho_{ra}(\lambda_l)\big],$$

and the $\rho_a(\lambda) + \rho_{ra}(\lambda)$ versus $\rho_{as}(\lambda)$ relationship must be known at each wavelength.

The approach taken by *Gordon and Wang* [1994a] was to solve the RTE for a set of N candidate aerosol models to provide what is essentially a set of lookup tables for $K[\lambda, \rho_{as}(\lambda)]$. As in the single scattering algorithm, the NIR bands are used to provide the aerosol model through

$$\varepsilon(\lambda_s, \lambda_l) = \frac{K[\lambda_l, \rho_{as}(\lambda_l)]}{K[\lambda_s, \rho_{as}(\lambda_s)]}\left[\frac{\rho_a(\lambda_s) + \rho_{ra}(\lambda_s)}{\rho_a(\lambda_l) + \rho_{ra}(\lambda_l)}\right];$$

however, since the aerosol model is not known at this point, the K ratio is unknown. Figure 7 suggests that this K ratio should not deviate significantly from unity, so *Gordon and Wang* [1994a] proposed computing $\varepsilon(\lambda_s, \lambda_l)$ though

$$\varepsilon(\lambda_s, \lambda_l) = \frac{1}{N}\sum_{j=1}^{N} \varepsilon_j(\lambda_s, \lambda_l),$$

where $\varepsilon_j(\lambda_s, \lambda_l)$ is the value of $\varepsilon(\lambda_s, \lambda_l)$ derived from $\rho_a(\lambda_l) + \rho_{ra}(\lambda_l)$ and $\rho_a(\lambda_s) + \rho_{ra}(\lambda_s)$ by assuming that the K ratio for the j^{th} aerosol model is correct. This procedure works reasonably well because the values of ε_j derived using the individual models are all close to the correct value. The procedure has been further modified by recomputing a new average formed by dropping the two models with the largest values of $\varepsilon(\lambda_s, \lambda_l) - \varepsilon_j(\lambda_s, \lambda_l)$ and the two models with the most negative values. This procedure is carried out several times until the final value is computed using four models: two with $\varepsilon - \varepsilon_j < 0$ and two models with $\varepsilon - \varepsilon_j > 0$.

Having derived a value for $\varepsilon(\lambda_s, \lambda_l)$, the next task is to estimate $\varepsilon(\lambda_i, \lambda_l)$. In general, the derived value of $\varepsilon(\lambda_s, \lambda_l)$ will be bracketed by two of the N candidate aerosol models. We then assume that $\varepsilon(\lambda_i, \lambda_l)$ falls between the same two aerosol models proportionately in the same manner as $\varepsilon(\lambda_s, \lambda_l)$. Finally, we also assume that $K[\lambda_i, \rho_{as}(\lambda_i)]$ falls between the two values for these models in the same proportion as $\varepsilon(\lambda_s, \lambda_l)$. These assumptions are required to proceed, and as we shall see, they are not always true. However, to the extent that the actual aerosols are similar in their optical properties to the candidate models, the assumptions appear to be reasonably valid.

In this paper twelve candidate aerosol models are used: the Maritime, Coastal, and Tropospheric models with RH = 50, 70, 90, and 99%. Tables of the $\rho_a(\lambda) + \rho_{ra}(\lambda)$ versus $\rho_{as}(\lambda)$ relationship were constructed by solving the RTE for each model for $\theta_0 = 0$ to 80° in increments of 2.5°, and at 33 values of θ_v. The azimuthal dependence of the reflectance was determined through Fourier analysis. Computations were carried out for eight values of $\tau_a(\lambda_i)$ from 0.05 to 0.8. The total number of separate solutions to the RTE used in the preparation of the tables exceeded 33,000 (including the Urban models described in the next section). To reduce storage, for a given set (θ_0, θ_v) the simulations were fit to

$$\log[\rho_t(\lambda) - \rho_r(\lambda) - t\rho_w(\lambda)] = \log[a(\lambda)] + b(\lambda)\log[\rho_{as}(\lambda)] + c(\lambda)\log^2[\rho_{as}(\lambda)] \qquad (13)$$

by least-squares. In the case of the azimuth angle ϕ_v, we expanded $a(\lambda)$, $b(\lambda)$ and $c(\lambda)$ in a Fourier series in ϕ_v and stored only the Fourier coefficients. As the reflectances are even functions of the relative azimuth angle ϕ_v, $a(\lambda)$, $b(\lambda)$, and $c(\lambda)$ will be even functions of ϕ_v. Thus, we can write

$$a(\theta_v, \theta_0, \phi_v, \lambda) = a^{(0)}(\theta_v, \theta_0, \lambda) + 2\sum_{m=1}^{M} a^{(m)}(\theta_v, \theta_0, \lambda)\cos m\phi_v,$$

with

$$a^{(m)}(\theta_v, \theta_0, \lambda) = \frac{1}{\pi}\int_0^{\pi} a(\theta_v, \theta_0, \lambda, \phi_v)\cos m\phi_v \, d\phi_v,$$

etc. Using Fourier analysis with $M = 14$ produced about the same accuracy in the results as interpolating with a division in ϕ_v of 5° or 10°.

2.2.1 Test of the multiple-scattering algorithm

We have tested this multiple-scattering algorithm by applying it to pseudo data created using the *Shettle and Fenn* [1979] Tropospheric, Coastal, Maritime, and Urban models at RH = 80%, denoted by T80, C80, M80, and U80, respectively. Note that these are *not* part of the candidate aerosol set, although the size and refractive index distributions of T80, C80, and M80 are similar to members of the set. In contrast to the others, and unlike any members of the candidate set, U80 has strong aerosol absorption.

Comparison between the single-scattering and multiple-scattering algorithms for pseudo data

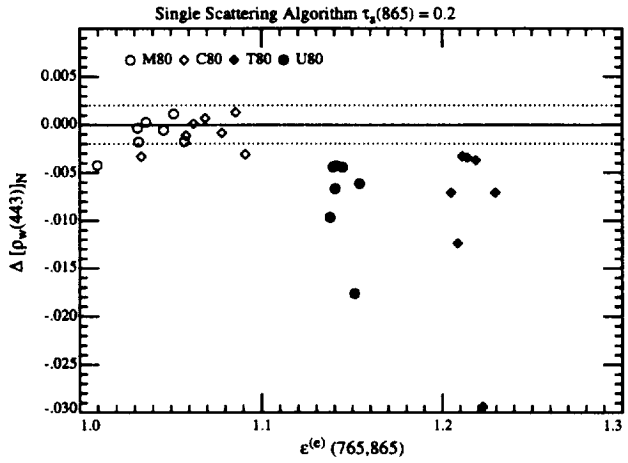

Figure 8a. $\Delta[\rho_w(443)]_N$ as a function of $\varepsilon^{(\epsilon)}(765, 865)$ for $\tau_a(865) = 0.2$ and all of the viewing geometries examined in the study, using the single-scattering algorithm.

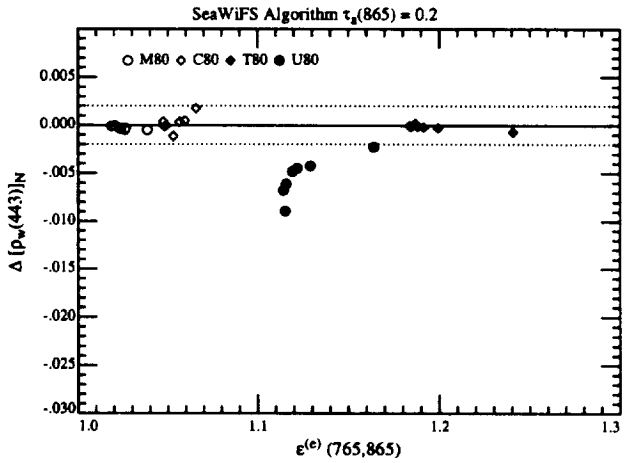

Figure 8b. $\Delta[\rho_w(443)]_N$ as a function of $\varepsilon^{(\epsilon)}(765, 865)$ for $\tau_a(865) = 0.2$ and all of the viewing geometries examined in the study, using the multiple-scattering algorithm.

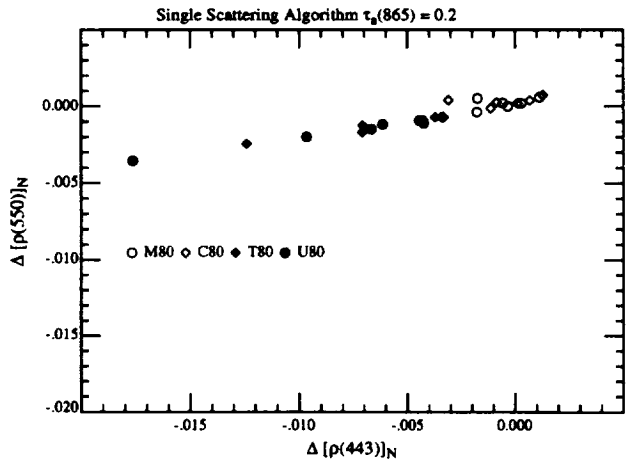

Figure 8c. $\Delta[\rho_w(550)]_N$ as a function of $\Delta[\rho_w(443)]_N$ for the results in Figure 8a.

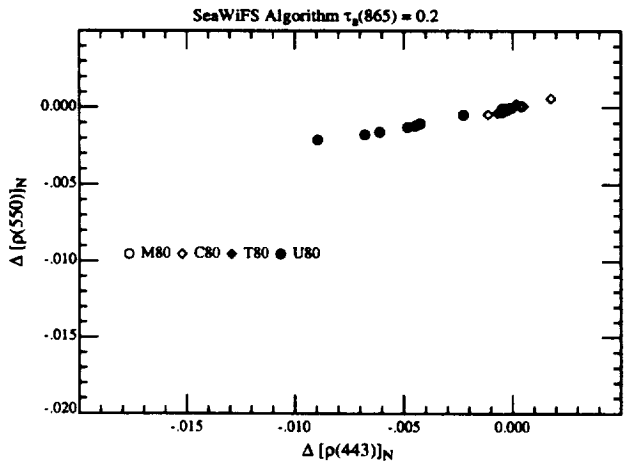

Figure 8d. $\Delta[\rho_w(550)]_N$ as a function of $\Delta[\rho_w(443)]_N$ for the results in Figure 8b.

created with these models at the seven sun-viewing geometries described earlier is provided in Figure 8 for $\tau_a(865) = 0.2$. Clearly, including multiple scattering in the algorithm significantly improves the retrieval of $[\rho_w(443)]_N$ for the T80, C80, and M80 cases, for which $\tau_a(443) \approx 0.50$, 0.32, and 0.24, respectively (Figures 4a and 5). In contrast, the U80 retrievals, although somewhat improved over single scattering, are still very poor. Thus, even though the size distribution of the U80 model is similar to the candidates (both in modal diameter and standard deviation), the fact that the particles are strongly absorbing causes as large an error in the retrieval of $[\rho_w(443)]_N$ as neglecting multiple scattering completely. Clearly, particle absorption must have a profound impact on multiple scattering.

As in Figures 6c and 6d, Figures 8c and 8d provide the relationship between $[\rho_w(550)]_N$ and $[\rho_w(443)]_N$ for the single-scattering and the multiple-scattering (SeaWiFS) algorithms. For the multiple-scattering algorithm, $\Delta[\rho_w(550)]_N \approx (1/4)\Delta[\rho_w(443)]_N$, and with the exception of very low pigment concentrations, the error in atmospheric correction at 443 nm will contribute more significantly to the error in R [Eq. (4)] than that at 550 nm. Fortuitously, the errors at 443 and 550 nm typically have the same sign and, therefore, tend to cancel in R.

Table 2: Mean value of C obtained for seven viewing geometries and three aerosol models (M80, C80, and T80). The number in parenthesis is the standard deviation divided by the mean (in %).

$\tau_a(865)$	$C_{\text{True}} = 0.10$ mg/m^3	$C_{\text{True}} = 0.47$ mg/m^3	$C_{\text{True}} = 0.91$ mg/m^3
0.1	0.101	0.466	0.912
	(1.6)	(3.4)	(9.1)
0.2	0.100	0.470	0.940
	(3.1)	(4.7)	(12.8)
0.3	0.098	0.493	0.936
	(5.5)	(15.3)	(25.3)

The error in the pigment concentration induced by $\Delta[\rho_w(550)]_N$ and $\Delta[\rho_w(443)]_N$ in the multiple-scattering algorithm is provided in Table 2. To prepare this table, the errors were added to values of $[\rho_w(550)]_N$ and $[\rho_w(443)]_N$ that are characteristic of three pigment concentrations

(0.10, 0.47, and 0.91 mg/m^3) in order to produce retrieved reflectances that include the atmospheric correction error. These were then inserted into Eq. (4) and the resulting pigment concentration was derived for each sun-viewing geometry for the M80, C80, and T80 aerosol models. For each true pigment concentration, the twenty-one retrieved values of C (seven geometries times three aerosol models) were averaged and the standard deviation was computed. The computations were carried out for $\tau_a(865) = 0.1$, 0.2, and 0.3.

As expected, the quality of the retrievals is best for the smallest value of $\tau_a(865)$. Excellent retrievals of C (as indicated by excellent mean values and small relative standard deviations) were obtained for $\tau_a(865) = 0.1$ and 0.2, and for the two lower concentrations for $\tau_a(865) = 0.3$. As mentioned earlier, $\tau_a(865)$ is typically $\lesssim 0.2$ in regions not subjected to urban pollution or desert dust. For $\tau_a(865) = 0.3$ and a true value of C of 0.91 mg/m^3, one retrieved value of C was ≈ 9 mg/m^3 ($\theta_0 = 60°$, $\theta_v \approx 45°$, T80, for which $\tau_a(443) \approx 0.75$ and $\tau_a(550) \approx 0.6$). This value was not included in the average or the standard deviation computation. These results suggest that the multiple-scattering algorithm will provide excellent results as long as the candidate aerosol models are similar in size and composition to the aerosol actually present.

2.2.2 Effect of absorption on multiple scattering

To try to understand the effect of particle absorption on multiple scattering, a set of multiple scattering computations of $\rho_a + \rho_{ra}$ was carried out in which particle absorption *alone* was varied. Specifically, we used the phase functions for the T50 and M99 aerosol models evaluated at 865 nm (Figure 9). These models have the most weakly (T50) and the most strongly (M99) forward peaked scattering phase function among the candidate models. Simulations of $\rho_a + \rho_{ra}$ as a function of τ_a (or equivalently ρ_{as}) were made for $\theta_0 = 60°$ and $\theta_v \approx 1°$, with $\tau_r = 0.015$ (865 nm) and 0.236 (443 nm), as ω_a assumed the values of 0.6, 0.8, and 1.0. The results are presented in Figure 10. Two facts concerning the $\rho_a + \rho_{ra}$ versus ρ_{as} relationship emerge from these simulations. First, for $\omega_a = 1$, the relationship is nearly linear and, for the sharply peaked M99 phase

function, the Rayleigh-aerosol interaction ($\sim$ the difference between the dashed and solid curves

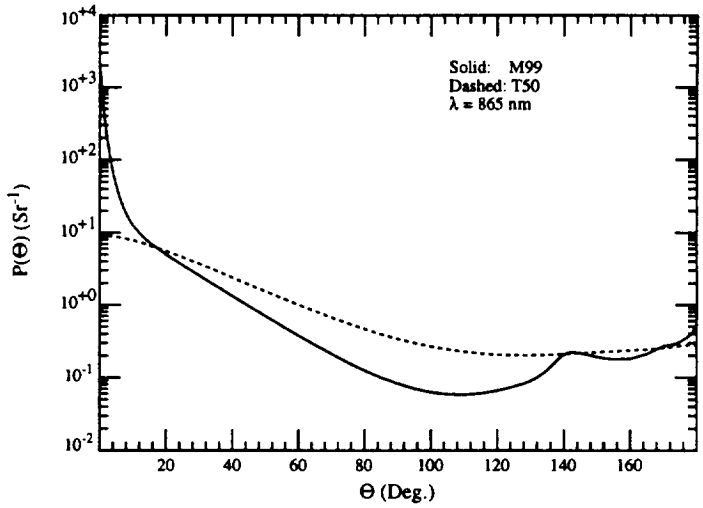

Figure 9. Scattering phase functions for the T50 and M99 aerosol models at 865 nm.

caused by changing τ_r) is small, while for the smoother T50 phase function the Rayleigh-aerosol interaction is significantly larger. This is to be expected, since the mid-angle scattering by T50 is much larger than M99 (Figure 9). Second, as ω_a decreases, there are greater departures from linearity and an increase in the significance of the Rayleigh-aerosol interaction for *both* T50 and

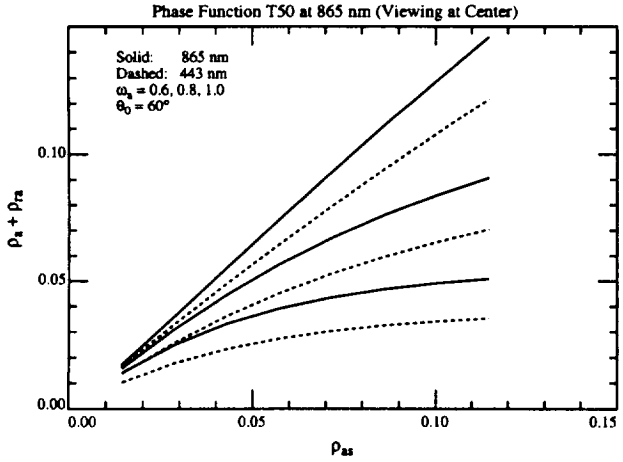

Figure 10a. $\rho_a + \rho_{ra}$ as a function of ρ_{as} and ω_a for 443 nm (dashed) and 865 nm (solid) and the T50 phase function. Curves from bottom to top correspond to ω_a = 0.6, 0.8, and 1.0.

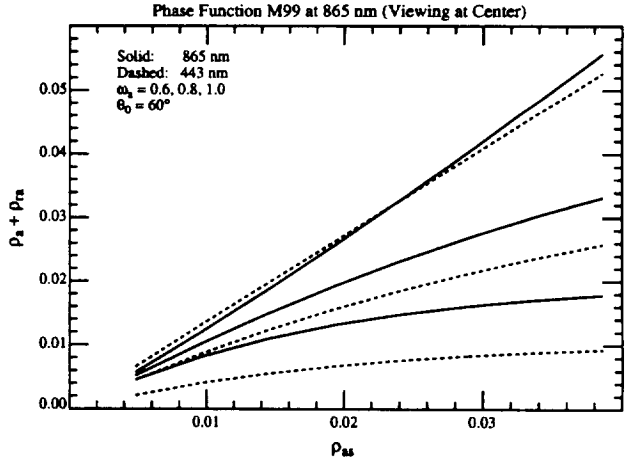

Figure 10b. $\rho_a + \rho_{ra}$ as a function of ρ_{as} and ω_a for 443 nm (dashed) and 865 nm (solid) and the M99 phase function. Curves from bottom to top correspond to ω_a = 0.6, 0.8, and 1.0.

M99. The general shape of the curves is explained by the fact that $\rho_a + \rho_{ra}$ must approach an

asymptotic value as $\tau_a \rightarrow \infty$. Also, increasing τ_r causes more diffuse light to enter the aerosol layer and traverse longer paths through it, with the concomitant greater chance of absorption. This explains the strong influence of ω_a on ρ_{ra}.

The impact of the absorption in Figure 10 is serious. Consider a hypothetical situation in which the M99 phase function is appropriate and $\epsilon(\lambda_i, \lambda_l) = 1$, so $\rho_{as}(\lambda_i) = \rho_{as}(\lambda_l)$. Also, assume that $\epsilon(\lambda_i, \lambda_l)$ is correctly determined by the algorithm and that $\rho_a + \rho_{ra} \approx 0.02$ at 865 nm. Then, if $\omega_a = 1$ were used for estimating $\rho_a + \rho_{ra}$ at 443 nm, but the true value of ω_a was actually 0.8, Figure 10b shows that the error in $\rho_a + \rho_{ra}$ at 443 nm would be ~ -0.004. In contrast, if the $\omega_a = 1$ assumption was correct the error would be $\sim +0.001$. Clearly, the effect of absorption is to produce large negative errors in $t\rho_w$, i.e., to over estimate the effect of the atmosphere. Figure 3a suggests that when $\epsilon(\lambda_i, \lambda_l)$ is estimated from $\epsilon(\lambda_s, \lambda_l)$ using weakly- or nonabsorbing aerosol models, it will be overestimated, i.e., $\epsilon(\lambda_i, \lambda_l)$ will be too large, if the aerosol strongly absorbs. This effect will cause a further over estimation of the atmospheric effect.

As the twelve candidate models in Subsection 2.2.1 are combinations of two components with physical properties dependent on RH, they represent a fixed set of values of ω_a at each wavelength, i.e., there are only twelve different values of ω_a. At 865 nm, these range from 0.99857 (M99) to 0.92951 (T50). Furthermore, each model possesses a unique value of $\varepsilon(\lambda_s, \lambda_l)$ and a more or less unique value of $\varepsilon(\lambda_i, \lambda_l)$ for a given sun-viewing geometry (Figure 3a). Thus, the choice of the twelve candidates forces a definite relationship between ω_a and $\varepsilon(\lambda_i, \lambda_l)$. In the case of the twelve models chosen here, there is a steady decrease in ω_a with increasing $\varepsilon(\lambda_i, \lambda_l)$. If this relationship is more or less correct, an excellent correction is effected (Figure 8b, T80); however, with its low value of ω_a (0.74806 for U80 at 865 nm) the Urban model falls considerably outside this relationship and the resulting atmospheric correction is very poor (U80 in Figure 8b). This is further shown in Figure 11 in which the multiple-scattering algorithm is applied to the Haze C models. In this Figure we have limited the models to those that fall within the range of variation of the values of $\varepsilon(\lambda_s, \lambda_l)$ of the candidate models, and also models for which $\tau_a(443) \lesssim 0.8$, the upper limit of τ_a used in the preparation of the $\rho_a + \rho_{ra}$ versus ρ_{as} look up tables. Haze C models with a real index of refraction ($\omega_a = 1$) and $\nu \geq 3$ do not follow the $\omega_a - \varepsilon(\lambda_s, \lambda_l)$ relationship implied by the candidate models, and the values of $\Delta[\rho_w(443)]_N$ are positive. In contrast, the dust and mineral models both display ω_a-values less than T50, and for these the $\Delta[\rho_w(443)]_N$ are large and negative. Thus, it should be clear that it is imperative to use candidate aerosol models

that possess an approximately correct relationship between ω_a and $\varepsilon(\lambda_s, \lambda_l)$, or physically, an approximately correct relationship between particle size and absorption. Such a relationship must be based on climatology, e.g., when the aerosol optical thickness over the North Atlantic Saharan

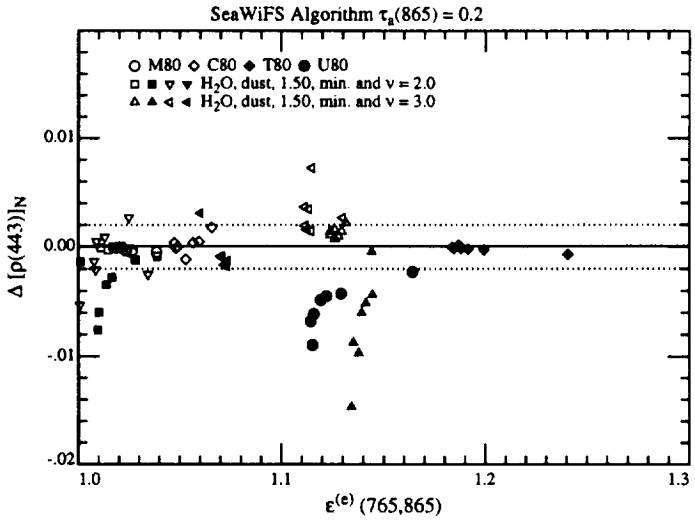

Figure 11. $\Delta[\rho_w(443)]_N$ as a function of $\varepsilon^{(\epsilon)}(765, 865)$ for the Haze C models with $\tau_a(865) = 0.2$ and all of the viewing geometries examined in the study, using the multiple-scattering algorithm.

dust zone is high, one should use candidate models consisting of a linear combination of a Maritime model and Saharan dust model, either uniformly mixed in the marine boundary layer or having a two-layer structure. Given such climatology-based models, preparation of the appropriate lookup tables for incorporation into the algorithm is a simple process.

As an example, we modified the algorithm to utilize only four candidate models, the *Shettle and Fenn* [1979] Urban models at RH = 50%, 70%, 90%, and 99%, and tested it using pseudo data created with the U80 model. In this manner, the ω_a and $\varepsilon(\lambda_s, \lambda_l)$ relationship was approximately correct. The results are provided in Figure 12, which shows the error in $[\rho_w(443)]_N$ as a function of the aerosol optical thickness of U80 at 865 nm. Recall, from Figure 4a, that $\tau_a(443) \approx 1.75\tau_a(865)$. Comparison with Figure 11, for which $\tau_a(865) = 0.2$, shows that the maximum error (which occurs at the scan edge with $\theta_0 = 60°$), when the Urban models are used as candidates, is only twice the minimum error when the original twelve candidate aerosol models were used. This

underscores the necessity of having realistic climatologically-based aerosol models in situations in

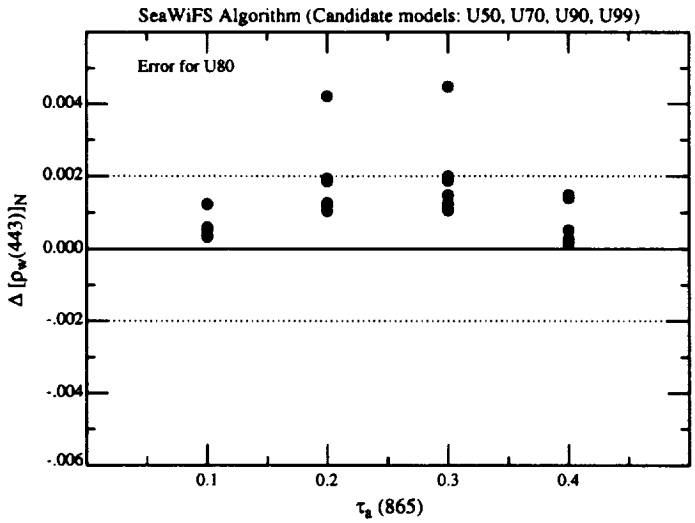

Figure 12. $\Delta[\rho_w(443)]_N$ as a function of $\tau_a(865)$ for the U80 model, when the candidate aerosol models in the multiple-scattering algorithm are restricted to U50, U70, U90, and U99.

which the aerosol concentration is sufficiently large to require consideration of multiple scattering. We shall discuss experimental efforts to obtain such a climatology in a later section.

3. Examination of the approximations

In this Section we assume that the appropriate set of candidate aerosol models can be selected in a given situation and examine the effects of the approximations made in Section 2. These include the influence of whitecaps on the sea surface, the influence of the vertical distribution of the aerosol, the approximation of the atmosphere as a plane-parallel medium, i.e., ignoring the curvature of the earth, the use of scalar radiative transfer theory (ignoring polarization) in preparation of the multiple-scattering lookup tables, and the effect of ignoring sea-surface roughness in the preparation of the lookup tables.

3.1 Whitecaps

As mentioned earlier, the term $t(\lambda_i)\rho_{wc}(\lambda_i)$ in Eq. (6) has been ignored in the development of the algorithm. If we indicate the reflectance measured at the top of the atmosphere as $\rho_t^{(m)}$,

this reflectance consists of two parts; that which would be measured in the absence of whitecaps, and the reflectance added by the whitecaps $t\rho_{wc}$, i.e.,

$$\rho_t^{(m)} = \rho_t + t\rho_{wc}. \tag{14}$$

Since the retrieval algorithms developed in Section 2 must be operated with ρ_t rather than $\rho_t^{(m)}$, $t\rho_{wc}$ must be removed from the imagery *before* the algorithm can be applied.

As in the case of the normalized water-leaving radiance, we define the normalized whitecap reflectance (or the albedo) $[\rho_{wc}]_N$ to be the area-weighted reflectance (over several pixels) of oceanic whitecaps *at* the sea surface in the absence of the atmosphere. Then the whitecap component of the radiance leaving the surface is

$$L_{wc}(\lambda) = [\rho_{wc}(\lambda)]_N \frac{F_0 \cos\theta_0}{\pi} t(\theta_0, \lambda),$$

where the whitecaps are assumed to be lambertian. Converting to reflectance we have

$$\rho_{wc}(\lambda) = [\rho_{wc}(\lambda)]_N \, t(\theta_0, \lambda).$$

At the top of the atmosphere, the whitecaps contribute

$$t\rho_{wc}(\lambda) = [\rho_{wc}(\lambda)]_N \, t(\theta_0, \lambda) t(\theta_v, \lambda).$$

The problem faced in removing $t\rho_{wc}(\lambda)$ from $\rho_t(\lambda)$ in Eq. (6) is the estimation of $[\rho_{wc}(\lambda)]_N$.

Based on previous research on the relationship between whitecaps and environmental parameters, the algorithm adopted for estimating $[\rho_{wc}]_N$ is that of *Koepke* [1984] [*Gordon and Wang*, 1994b]:

$$[\rho_{wc}]_N = 6.49 \times 10^{-7} W^{3.52}, \tag{15}$$

where W is the wind speed in m/s measured 10 m above the sea surface. *Gordon and Wang* [1994b] show that, for a given wavelength, this predicts $[\rho_{wc}]_N$ with a standard deviation approximately equal to $[\rho_{wc}]_N$ itself.

The effect of the any error in the estimation of $[\rho_{wc}]_N$ on the retrieved water-leaving reflectance is strongly dependent on the spectral variation of $[\rho_{wc}(\lambda)]_N$. In *Gordon and Wang* [1994b] it was assumed, based on measurements carried out by *Whitlock, Bartlett and Gurganus* [1982], that $[\rho_{wc}(\lambda)]_N$ was independent of λ; however, *Schwindling* [1995] and *Frouin, Schwindling and*

Deschamps [1995] have reported measurements on breaking waves in the surf zone suggesting that whitecaps may reflect considerably less in the NIR than in the visible, presumably because a significant component of the whitecap reflectivity is due to scattering from submerged bubbles. To understand the effect of spectral variation in $[\rho_{wc}]_N$ on the accuracy of atmospheric correction, the multiple scattering algorithm has been operated in the presence of whitecaps displaying both nonspectral reflectance and the spectral reflectance suggested by *Frouin, Schwindling and Deschamps* [1995]. Figure 13 compares the error in $[\rho_w(443)]_N$ as a function of θ_0 for viewing at the edge of the MODIS scan with the M80 aerosol model ($\tau_a(865) = 0.2$) for these two cases when the error in the *estimate* of $[\rho_{wc}]_N$ at 443 nm is ± 0.002. This error in $[\rho_{wc}(443)]_N$ corresponds to a wind speed of $\sim 8 - 9$ m/s. Figure 13 shows that for wavelength-independent whitecap reflectivity, the resulting error in $[\rho_w(\lambda)]_N$ can be significantly less than ($\sim 1/4$) the error in the estimate of $[\rho_{wc}(443)]_N$. In contrast, if whitecaps reflect in a manner consistent with the

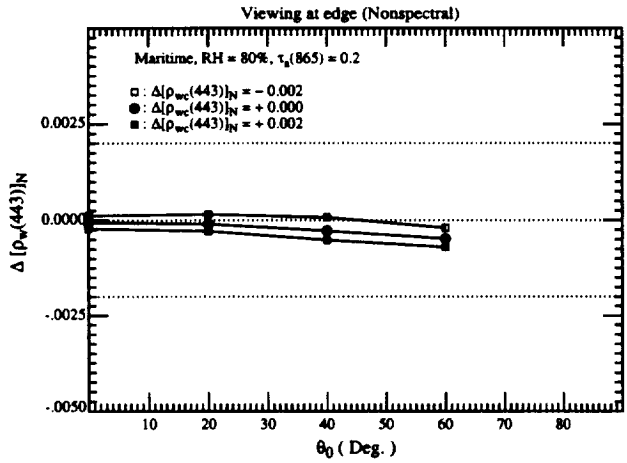

Figure 13a. $\Delta[\rho_w(443)]_N$ **as a function of the error in the whitecap reflectance at 443 nm and** θ_0 **at the edge of the scan for the M80 aerosol model with** $\tau_a(865) = 0.2$**. Whitecap reflectance spectrum is that proposed by** ***Whitlock, Bartlett and Gurganus*** **[1982].**

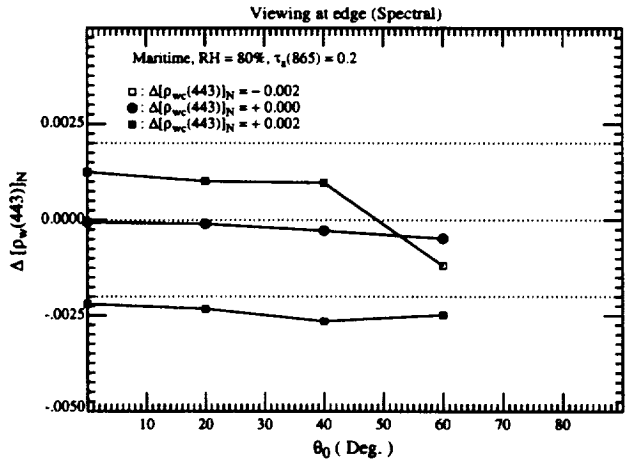

Figure 13b. $\Delta[\rho_w(443)]_N$ **as a function of the error in the whitecap reflectance at 443 nm and** θ_0 **at the edge of the scan for the M80 aerosol model with** $\tau_a(865) = 0.2$**. Whitecap reflectance spectrum is that proposed by** ***Frouin, Schwindling and Deschamps*** **[1995].**

Frouin, Schwindling and Deschamps [1995] observations, the error in $[\rho_w(443)]_N$ can be expected to be of the same order-of-magnitude as the error in $[\rho_{wc}(443)]_N$. Similar simulations using the T80 aerosol model, for which $\varepsilon(\lambda, 865)$ displays strong variation with λ, show similar effects for the case of whitecaps with the *Frouin, Schwindling and Deschamps* [1995] reflectance; however, the error for the *Whitlock, Bartlett and Gurganus* [1982] reflectance model can also be the same order of magnitude as $\Delta[\rho_{wc}(443)]_N$ [*Gordon and Wang*, 1994b]. Figure 13 shows that an overestimation of $[\rho_{wc}(443)]_N$ leads to a negative error in $[\rho_w(443)]_N$. The same is true at 550 nm.

When the errors in $[\rho_w(\lambda)]_N$ are negative, algorithms such as Eq. (4), that use radiance ratios, can lead to very large errors in the derived products. Because of this, it is better to underestimate the $[\rho_{wc}(443)]_N$ in the whitecap correction algorithm rather than overestimating it.

As whitecaps have the potential of producing errors of a magnitude similar to the magnitude of the acceptable error in $[\rho_w(\lambda)]_N$, it is important to obtain radiometric data of actual oceanic whitecaps, and validate its dependence on wind speed.

3.2 Aerosol vertical structure

The reflectance of the atmosphere in the single-scattering approximation is independent of the manner in which the aerosol is distributed with altitude. However, this independence does

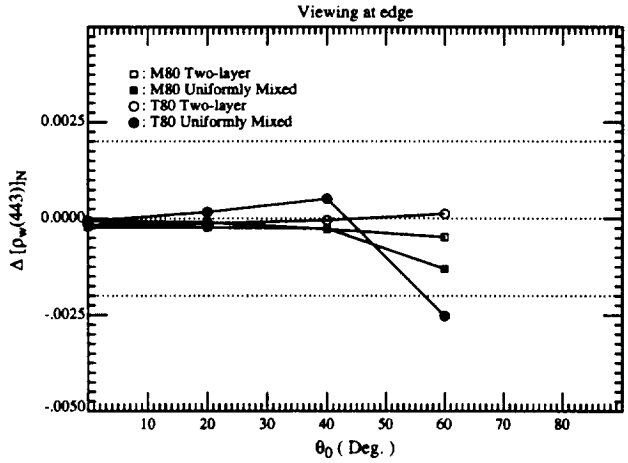

Figure 14a. Effect of the vertical distribution of aerosol on $\Delta[\rho_w(443)]_N$ as a function of θ_0 at the edge of the scan for the T80 and M80 aerosol models with $\tau_a(865) = 0.2$. Note that the correction algorithm assumes that the "Two-layer" stratification is correct.

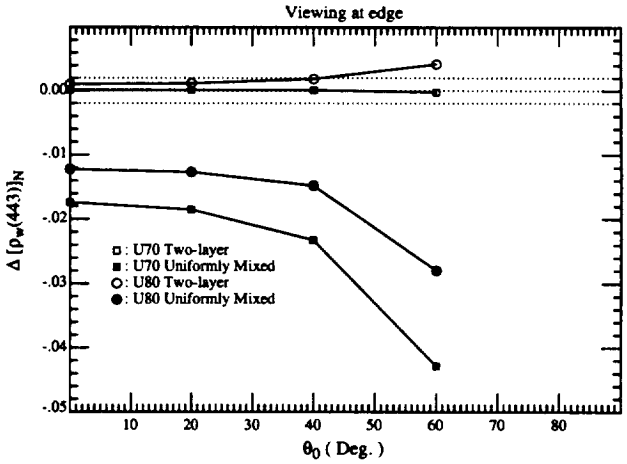

Figure 14b. Effect of the vertical distribution of aerosol on $\Delta[\rho_w(443)]_N$ as a function of θ_0 at the edge of the scan for the U80 and U70 aerosol models with $\tau_a(865) = 0.2$. Note that the correction algorithm assumes that the "Two-layer" stratification is correct.

not extend to a multiple-scattering atmosphere. As the multiple-scattering algorithm assumes that the aerosol is all located in the bottom layer of a two-layer atmosphere, it is important to understand the effect of aerosol vertical structure on the correction algorithm. This has been studied by comparing the error in the algorithm when the pseudo data are simulated using the "correct" two-layer model with the error when the pseudo data are simulated using a model in which the aerosol and Rayleigh scattering have an altitude-independent mixing ratio, i.e., a uniformly mixed model. Figure 14a provides such a comparison for the M80 and T80 aerosol models

with $\tau_a(865) = 0.2$. It is seen that the effect of an incorrect assumption regarding the vertical structure will not lead to serious errors in this case. However, in the case of strongly absorbing aerosols, e.g., the Urban models, the assumed vertical structure is very important. Figure 14b provides the two-layer versus uniformly mixed cases for the Urban models with $\tau_a(865) = 0.2$. In this case the candidate aerosol models were restricted to U50, U70, U90, and U99, as in the results for Figure 12. For the U80 case, the error becomes excessive, increasing by over an order of magnitude compared to the two-layer case. More disturbing is the performance of the U70 aerosol model. U70 is actually one of the candidate aerosol models in this case. When the vertical structure is the same as assumed by the algorithm, the error is negligible. In contrast, when the incorrect structure is assumed, the error becomes very large.

As we have examined only an extreme deviation from that assumed by the correction algorithm, it is of interest to quantify how the correction algorithm performs as the aerosol layer thickens from being confined just near the surface to being mixed higher in the atmosphere. Thus, the top-of-atmosphere reflectance was simulated using a two layer model with aerosol *plus* Rayleigh scattering in the lower layer and *only* Rayleigh scattering in the upper layer. The fraction of the Rayleigh scattering optical thickness assigned to the lower layer was consistent with aerosol-layer thickness of 0, 1 km, 2 km, 4 km, 6 km, and ∞. The aerosol model used in the simulations was U80, and $\tau_a(865)$ was kept constant at 0.2. The multiple-scattering algorithm was then operated with this pseudo data using U50, U70, U90, and U99 as candidate models. The results of this exercise are provided in Figure 15. Clearly, progressive thickening of the layer in which the aerosol resides leads to a progressive increase in the error in the retrieved water-leaving reflectance.

This influence of vertical structure on the algorithm when the aerosol is strongly absorbing is easy to understand. The algorithm assumes all of the aerosol resides in a thin layer beneath the molecular scattering layer. As the aerosol layer thickens and encompasses more and more of the molecular scattering layer, the amount of Rayleigh scattering within the aerosol layer will increase causing an increase in the average path length of photons through the layer, and a concomitant increase in absorption. Thus, for a given τ_a, ρ_t will decrease as the thickness of the aerosol layer increases. Since $\rho_r \sim \lambda^{-4}$, this decrease will be relatively more in the visible than in the NIR, so the algorithm will predict values of $\rho_a + \rho_{ra}$ in the visible that are too large, yielding an over correction, $\Delta[\rho_w(443)]_N < 0$.

Ding and Gordon [1995] (Figures 9 and 10) have provided some examples of the error in the multiple-scattering algorithm for vertical structures in which the aerosol model as well as concentration varies with altitude. For the weakly-absorbing aerosol of the models that they inves-

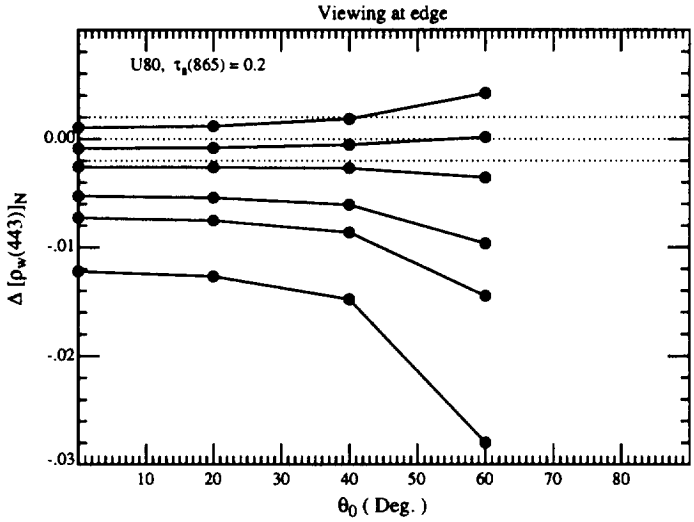

Figure 15. Effect of the vertical distribution of aerosol on $\Delta[\rho_w(443)]_N$ as a function of θ_0 at the edge of the scan for the U80 aerosol models with $\tau_a(865) = 0.2$. Curves from top to bottom refer to situations in which the aerosol is confined to a layer just above the surface, between the surface and 1, 2, 4, and 6 km, and uniformly mixed throughout the atmosphere.

tigated ($\omega_a \gtrsim 0.93$), the conclusions are similar to those here: as long as the aerosol is weakly absorbing, the error is negligible, but as ω_a decreases, the error becomes progressively larger. Clearly, more study is required for a quantitative assessment of the impact of vertical structure in a strongly absorbing atmosphere; however, the computations provided here demonstrate that a large error in the vertical structure of the aerosol layer assumed for the lookup tables will result in a very poor atmospheric correction, even if the candidate aerosol models are appropriate. Figure 15 suggests that at a minimum, the lookup tables for the Urban candidates need to be recalculated under the assumption of an aerosol layer of finite physical thickness, i.e., some Rayleigh scattering in the aerosol layer. It also suggests that, for the case studied, if the lookup tables were computed for an aerosol layer of physical thickness 2 km, they would provide reasonable retrievals for layers with thicknessess from 1 to 3 km, i.e., the algorithm could tolerate a ± 1 km error in the layer thickness for this case.

3.3 Earth curvature

All atmospheric corrections algorithms developed thus far ignore the curvature of the earth, i.e., the plane-parallel atmosphere approximation has been used in the radiative transfer simulations. However, at the level of accuracy required to utilize the full sensitivity of MODIS, it may be necessary to take the curvature of the earth into account, especially at high latitudes with their associated large θ_0 values. *Ding and Gordon* [1994] have examined this problem in detail using a model based on a spherical shell atmosphere solved with Monte Carlo techniques. It was found that as long as ρ_r was computed using a spherical shell atmosphere model, the multiple-scattering algorithm performed as well at high latitudes as at low latitudes. They provided a method for the rapid computation of ρ_r for the spherical shell atmosphere; however, it has yet to be implemented for image processing.

3.4 Polarization

All of the radiative transfer simulations described in Section 2 were carried out using scalar radiative transfer theory, i.e., polarization was ignored. In the case of single scattering, except for the terms involving the Fresnel reflectance, scalar (ignores polarization) and vector (includes polarization) radiative transfer theory lead to the same radiances. Thus, the single scattering algorithm is little influenced by polarization. It is well known, however, that, when multiple scattering is present, the use of scalar theory leads to small errors ($\sim$ few %) in the radiance compared to that computed using exact vector theory [*Gordon, Brown and Evans*, 1988; *Kattawar, Plass and Hitzfelder*, 1976]. As with CZCS, in the actual application of the algorithm, ρ_r will be computed using vector theory; however, the lookup tables relating $\rho_a + \rho_{ra}$ to ρ_{a*} have been computed using scalar theory. To understand the influence of neglecting polarization in the computation of the lookup tables, simulations of the top-of-the-atmosphere reflectance ρ_t were carried out using both scalar and vector radiative transfer theory. In the case of the scalar simulations, $[\rho_w(443)]_N$ was retrieved as described in Section 2.1.2. An identical retrieval procedure was used for the vector simulations with a single exception: as in the case of CZCS, ρ_r was computed using vector theory. The results are presented in Figure 16a and 16b for the M80 and T80 aerosol models respectively. These figures provide $\Delta\rho \equiv t\Delta\rho_w(443)$ (rather than $\Delta[\rho_w(443)]_N$ in the previous figures) produced by the multiple-scattering correction algorithm as a function

of θ_0 for $\tau_a(865) = 0.2$. The notation "S–S" and "V–V" means that *both* ρ_t and ρ_r were computed using scalar (S–S) and vector (V–V) radiative transfer theory, respectively. Note that the difference between computations is the error induced by ignoring polarization in the preparation of the $\rho_a + \rho_{ra}$ versus ρ_{as} lookup tables. At present, only a small number of simulations of the type shown in Figure 16 have been carried out; however, for these the difference between S–S and V–V was typically $\lesssim 0.001$ but reached as much as 0.002 in isolated cases. Thus, compared to

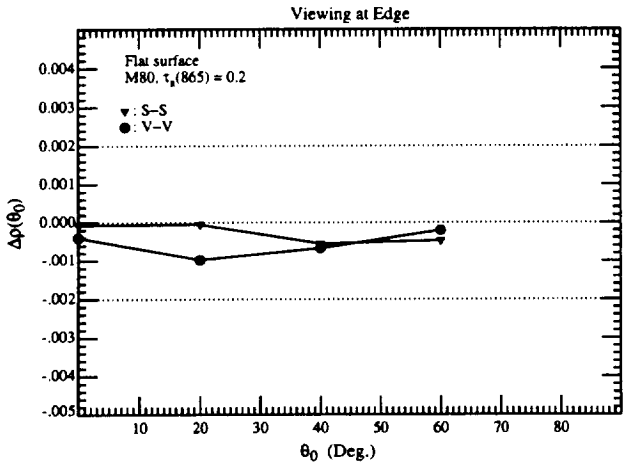

Figure 16a. Effect of neglecting polarisation in the multiple-scattering lookup tables. S–S and V–V are for ρ_t and ρ_r computed using scalar and vector radiative transfer theory, respectively. $\Delta\rho \equiv t\Delta\rho_w$, the aerosol model is M80, and $\tau_a(865) = 0.2$.

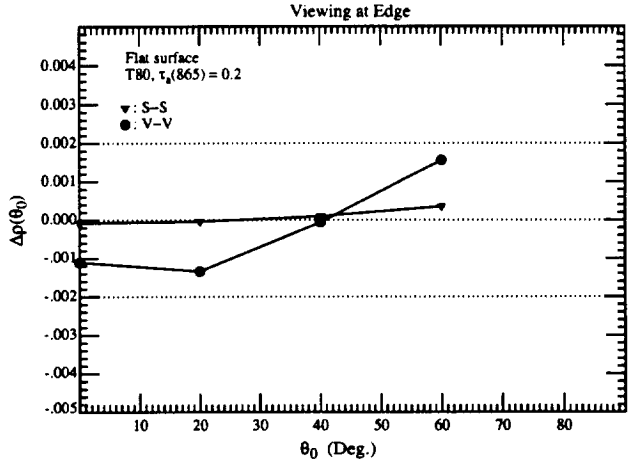

Figure 16b. Effect of neglecting polarisation in the multiple-scattering lookup tables. S–S and V–V are for ρ_t and ρ_r computed using scalar and vector radiative transfer theory, respectively. $\Delta\rho \equiv t\Delta\rho_w$, the aerosol model is T80, and $\tau_a(865) = 0.2$.

the errors possible when strongly absorbing aerosols or whitecaps are present, this error appears negligible. It could be removed by recomputing the lookup tables using vector radiative transfer theory, but at considerable computational cost.

3.5 Sea surface roughness

The roughness of the sea surface caused by the wind can play a large role on the reflectance measured at the top of the atmosphere. The principal effect of the rough surface is to redirect the direct solar beam reflected from the sea surface into a range of angles. This leads to a very large reflectance close to the specular image of the sun, know as sun glitter or the sun's glitter pattern. As this can be many times the radiance exiting the atmosphere in the smooth-surface case, the data in the region of the sun glitter must be discarded. This is accomplished by a mask as described in Appendix A. The remainder of the rough-surface effect is due to a redistribution

of light scattered from the reflected solar beam (because it is redirected) and a redistribution of sky light reflected from the surface (the Fresnel reflection terms in Eq. (9)). This redistribution of radiance contaminates the imagery over all viewing angles. As the lookup tables relating

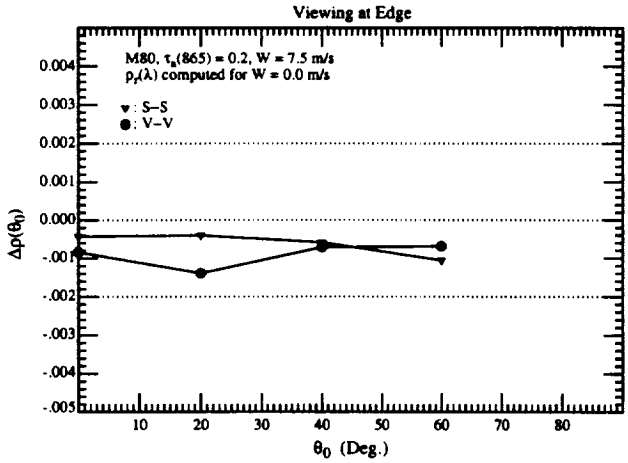

Figure 17a. Effect of neglecting sea surface roughness in the multiple-scattering lookup tables. S–S and V–V are for ρ_t and ρ_r computed using scalar and vector radiative transfer theory, respectively. $\Delta\rho \equiv t\Delta\rho_w$, the aerosol model is M80, and $\tau_a(865) = 0.2$. ρ_r has been computed assuming that $W = 0.0$ m/s.

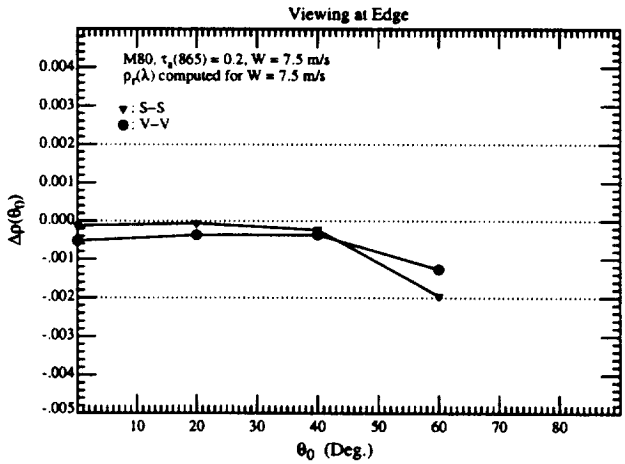

Figure 17b. Effect of neglecting sea surface roughness in the multiple-scattering lookup tables. S–S and V–V are for ρ_t and ρ_r computed using scalar and vector radiative transfer theory, respectively. $\Delta\rho \equiv t\Delta\rho_w$, the aerosol model is M80, and $\tau_a(865) = 0.2$. ρ_r has been computed assuming that $W = 7.5$ m/s.

$\rho_a + \rho_{ra}$ to ρ_{as} were computed under the assumption that the surface was flat, it is necessary to examine the error in the water-leaving reflectance induced when viewing a rough ocean. This was effected by computing ρ_t for an ocean roughened by the wind and inserting the result into the multiple-scattering correction algorithm. In this simulation, the sea surface roughness was based on the *Cox and Munk* [1954] surface slope distribution function (Appendix A). For computational simplicity, an omnidirectional wind was assumed [*Cox and Munk*, 1954]. The wind speed was taken to be $\sim$ 7.5 m/s. Since *Gordon and Wang* [1992b] and *Gordon and Wang* [1992a] showed that at the radiometric sensitivity of SeaWIFS and MODIS, correct computation of the influence of surface roughness on ρ_r required use of vector radiative transfer theory, the computations were carried out using *both* scalar and vector theory. Sample results from one set of the small number of simulations that have been carried out to assess the effect of surface roughness are provided in Figure 17. These are in the same format as Figure 16. The differences between the two panels is that, in Figure 17a ρ_r has been computed assuming a smooth sea surface (a wind speed of zero), while in Figure 17b it has been computed using the correct (7.5 m/s) wind speed. For reference, Figure 16a provides similar results for a smooth sea surface. Comparing Figures 16a

and 17a shows that the residual effect of the rough surface external to the sun's glitter pattern is small ($\Delta\rho \sim 0.0005$), and comparing Figures 16a and 17b shows that the residual effect can be removed by using the correct wind speed in the computation of ρ_r, i.e., ignoring the surface roughness in computation of the lookup tables relating $\rho_a + \rho_{ra}$ to ρ_{as} does not appear to lead to significant error.

4. Remaining issues

We now examine remaining issues in developing and operating the multiple-scattering algorithm. These include the appropriateness of the candidate aerosol models, absorbing aerosols, the effects of stratospheric aerosols, the influence of any sensitivity the sensor might have to the polarization of the top-of-atmosphere reflectance, the angular distribution of the water-leaving reflectance and its influence on the diffuse transmittance, and the effect of sensor calibration errors.

4.1 Appropriateness of aerosol models

Operation of the multiple-scattering algorithm requires a set of candidate aerosol models. Thus far, models from, or derived from, the work of *Shettle and Fenn* [1979] have been used as candidates. These models were basically developed from the analysis of aerosol physical-chemical properties and are believed to provide realistic approximations to the extinction and absorption cross section of real aerosols. However, they have never been validated for the role they are being used for here, i.e., for their ability to provide realistic aerosol phase functions and their spectral variation. As it is important to utilize as candidates, aerosol models that closely approximate the optical properties of actual aerosols over the ocean, work is being carried out or planned to study the optical properties of aerosols over the ocean.

Measurements over and above aerosol optical thickness and its spectral variation are required to understand the adequacy of candidate aerosol models. *Schwindling* [1995] compared estimates of the aerosol scattering phase function obtained from a pier at Scripps Institution of Oceanography at La Jolla, CA, with the properties of the *Shettle and Fenn* [1979] models and concluded that within the accuracy of their measurements the models fit both the phase function and the spectral variation of the aerosol optical thickness. It was also confirmed that $\tau_a(\lambda)$

becomes very low off the coast of CA. Such measurements need to be carried out in different regions and at different times. The aerosol monitoring network based on CIMEL sun/sky radiometers operated by B. Holben [*Holben et al.*, 1996] of NASA/GSFC is presently being expanded to include stations at the coast and on small islands. The plan is to use the methods developed by *Wang and Gordon* [1993] to invert the sky radiance and optical thickness data to obtain the aerosol scattering phase function and the single scattering albedo.

4.2 Absorbing aerosols

In Subsection 2.2.2 it was shown that in the presence of strongly absorbing aerosols, the candidate aerosol models must be restricted to those with values of ω_a similar to the true aerosol. This was effected there by limiting the candidate models to U50, U70, U90, and U99 when the test aerosol was U80 (Figure 12), since when the initial twelve candidate models were used, the error was excessive (Figure 11). Without a method of determining the absorption characteristics of the aerosols from satellite measurements, an aerosol climatology is required to be able to provide realistic candidate models. Furthermore, in Subsection 3.2 it was shown that, for strongly absorbing aerosols, even given the appropriate set of candidate models, knowledge of the vertical distribution of the aerosol was required for an adequate correction (Figure 15). Thus the aerosol climatology needs to contain information concerning the aerosol-layer thickness for regions with strongly absorbing aerosols.

The effort toward building a climatology for absorbing aerosols involves measurements of the type discussed in Subsection 4.1, i.e., measurements of sky radiance and aerosol optical thickness from ships or small islands in the appropriate regions. The *Wang and Gordon* [1993] retrieval algorithm should perform as well for strongly-absorbing as for nonabsorbing aerosols. A climatology for the aerosol vertical distribution can most effectively be built using LIDAR measurements [*Sasano and Browell*, 1989]. An excellent start toward a vertical distribution climatology can be made utilizing data from the Lidar In-Space Technology Experiment (LITE) [*McCormick*, 1995]. On the basis of LITE-based and aircraft-based measurements *Grant et al.* [1995] observed that the Saharan dust layer over the Eastern Caribbean extended in altitude from 1-4 km. This is in contrast to the dust-free atmosphere in which the thickness of the marine boundary layer is typically 1-2 km. Examining a LITE pass from Wallops Island, Virginia to Bermuda, *Ismail et al.* [1995] found that the plume of pollution from the U.S. East Coast was in a 1-2 km thick layer

above the 0.5-1.0 km thick maritime boundary layer. These observations suggest that the principal absorbing aerosols expected in the Atlantic are mixed higher in the atmosphere than assumed in the existing candidate aerosol model lookup tables.

It would be extremely useful to be able to detect the presence of absorbing aerosols from measurements made by the ocean color sensor alone, e.g., to be able to distinguish between absorbing and nonabsorbing aerosols. At present there is no way to effect this; however, computations using Mie scattering suggest that MODIS observations of $\rho_t(\lambda)$ for $\lambda > 865$ nm, may be useful in this regard. Figure 18 compares the $\varepsilon(\lambda, 865)$ for Haze C distributions of nonabsorbing

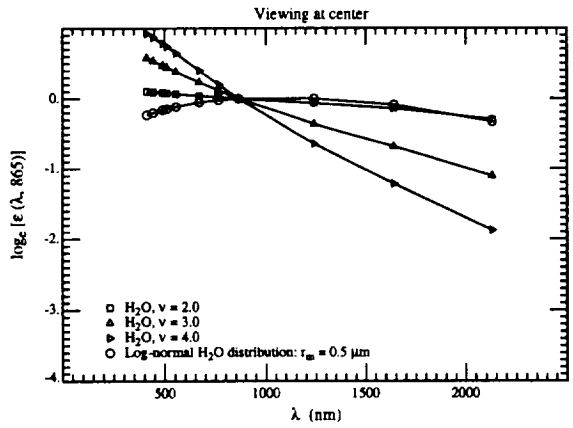

Figure 18a. $\varepsilon(\lambda, 865)$ for nadir viewing with $\theta_0 = 60°$ for the Haze C models composed of liquid water.

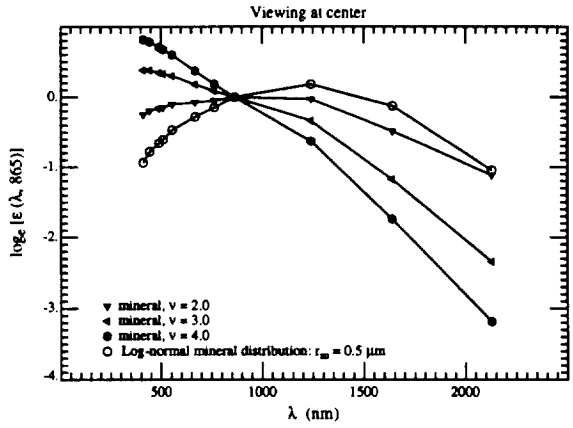

Figure 18b. $\varepsilon(\lambda, 865)$ for nadir viewing with $\theta_0 = 60°$ for the Haze C models composed of absorbing minerals.

(liquid water) and absorbing (minerals transported over the oceans with the index of refraction taken from *d'Almeida, Koepke and Shettle* [1991]) aerosol particles. Also included on Figure 18 are computations for a log-normal distribution suggested in *d'Almeida, Koepke and Shettle* [1991] for minerals transported over large distances to the marine environment. In contrast to nonabsorbing aerosols, the mineral aerosol shows a significant decrease in $\varepsilon(\lambda, 865)$ for $\lambda > 1.26$ μm over that extrapolated from the observed $\varepsilon(765, 865)$ and $\varepsilon(1260, 865)$. This behavior of $\varepsilon(\lambda, 865)$ is apparently due to the rapid decrease in the real part of the mineral refractive index beyond 1260 nm. Notwithstanding the perils of using Mie theory to predict the large-angle scattering for irregularly shaped particles [*Mishchenko and Travis*, 1994; *Mugnai and Wiscombe*, 1989] these computations suggest that it may be reasonable to try to use the short-wave infrared (SWIR) bands on MODIS to differentiate between some types of absorbing and nonabsorbing aerosols. Characteristics of these MODIS bands are provided in Appendix B, where it is shown that these

bands on MODIS have sufficient sensitivity (if pixel averaging is employed) to attempt such a differentiation.

4.3 Stratospheric aerosols

In some situations, e.g., following volcanic eruptions or when there are thin cirrus clouds present, there can be significant quantities of aerosol in the stratosphere. *Gordon and Castaño* [1988] showed that the presence of the El Chichón aerosol [*King, Harshvardhan and Arking*, 1984] had little effect on CZCS atmospheric correction; however, at the higher correction accuracy required for MODIS the *Gordon and Wang* [1994a] algorithm may be degraded by the presence of stratospheric aerosol. Although not listed in Table 1, MODIS is equipped with a spectral band at 1380 nm that can be used to assess the contamination of the imagery by stratospheric aerosol (Appendix B). This spectral band is centered on a strong water vapor absorption band and photons penetrating through the stratosphere will usually be absorbed by water vapor in the free troposphere [*Gao, Goetz and Wiscombe*, 1993]. Thus, any radiance measured at 1.38 μm can, in the first approximation, be assumed to be scattered by the stratospheric aerosol alone, providing a mechanism for estimating the stratospheric contribution.

The author and coworkers are engaged in assessing the effect of stratospheric aerosols on atmospheric correction and studying ways in which to correct the contamination, assuming that all radiance detected at 1380 nm results from scattering by the stratospheric aerosol *alone*. Briefly, the stratospheric aerosol contributes to the reflectance at all wavelengths. Thus, in its presence the total reflectance will be changed by an amount $\delta\rho_t^{(s)}$, i.e.,

$$\rho_t^{(s)}(\lambda) = \rho_t(\lambda) + \delta\rho_t^{(s)}(\lambda),$$

where $\rho_t^{(s)}$ is the reflectance of the entire ocean-atmosphere system in the presence of stratospheric aerosol, and ρ_t the reflectance in its absence. To assess the impact of the stratospheric aerosol, the multiple-scattering algorithm was operated using simulated values of $\rho_t^{(s)}(\lambda)$ in the place of $\rho_t(\lambda)$, for four stratospheric aerosol types. The preliminary results suggest that stratospheric aerosol/cirrus cloud contamination does not seriously degrade the *Gordon and Wang* [1994a] algorithm except for large ($\sim 60°$) solar zenith angles and large ($\sim 45°$) viewing angles, for which multiple scattering effects can be expected to be particularly severe.

The performance of a hierarchy of algorithms for using the 1380 nm MODIS band to correct for stratospheric aerosol/cirrus clouds, are also being examined. The approach is to use $\rho_t^{(s)}(1380)$ to estimate $\delta\rho_t^{(s)}(\lambda)$ in the visible and NIR. The procedures being investigated range from from simply subtracting the reflectance at 1380 nm from that in the visible bands, i.e., $\delta\rho_t^{(s)}(\lambda) = \rho_t^{(s)}(1380)$, to assuming all of the optical properties of the stratospheric aerosol are known (measurement at 1380 nm providing the concentration) and carrying out multiple scattering computations to estimate $\delta\rho_t^{(s)}(\lambda)$. It is not surprising that the most complex procedures yield the best results; however, it is surprising that the complex procedures appear to only reduce the error in the retrieved water-leaving radiance by $\lesssim$ a factor of two compared to the simplest procedures.

4.4 Residual instrument polarization

All scanning radiometers display some sensitivity to the polarization of the radiance they are intended to measure. For MODIS, it was specified that this polarization sensitivity should be less than 2%, and that it be mapped as part of the sensor characterization procedure. Depending on how well the MODIS meets this specification, a correction may be required to remove the residual polarization effects from ρ_t. We have developed a formalism [*Gordon*, 1988] which provides the framework for removal of instrumental polarization-sensitivity effects. The difficulty with removing the polarization sensitivity error is that the polarization properties of the radiance backscattered by the aerosol are unknown. Although the details of the correction process have yet to determined, simulations of this effect for an instrument possessing $\sim$ 3–4 times the polarization sensitivity expected for MODIS are presently being carried out. Preliminary results suggest that elimination of the polarization effect is possible at the required level of accuracy by estimating the polarization of the top-of-atmosphere radiance to be that expected for a pure Rayleigh scattering atmosphere. This is understandable in the blue, where Rayleigh scattering is the principal contributor to ρ_t.

4.5 In-water radiance distribution

Algorithms for retrieving total pigments, chlorophyll, etc., from ocean color imagery are developed by relating the nadir-viewing water-leaving radiance to the quantity in question. In the analysis of ocean color imagery it has always been assumed that $[\rho_w]_N$ is independent of the

viewing angle. This assumption was based on a small number of observations, e.g., see *Smith* [1974] and references therein, which suggests that $L_u(z,\theta,\phi)$, the upwelling radiance at depth z beneath the surface and traveling in a direction specified by the angles (θ,ϕ), is only weakly dependent on θ and ϕ. However, in a series of papers Morel and Gentili [*Morel and Gentili*, 1991; *Morel and Gentili*, 1993; *Morel and Gentili*, 1996] studied theoretically the bidirectional effects as a function of the sun-viewing geometry and the pigment concentration. Their simulations suggest that, although the bidirectional effects nearly cancel in the estimation of the pigment concentration using radiance ratios (Eq. (4)), $L_u(z,\theta,\phi)$ can depend significantly on θ, ϕ and θ_0. This means that the value of $[\rho_w]_N$ retrieved in atmospheric correction is actually appropriate only to the viewing direction in which the measurement of ρ_t is made. Since most in-water algorithms have been developed based on nadir-viewing measurements, the derived $[\rho_w]_N$ values should be corrected to nadir-viewing geometry. This requires understanding the bidirectional effects. This is effected by direct determination of the upwelling radiance distribution for a variety of waters and solar zenith angles using an electro-optics radiance camera system developed by *Voss* [1989], e.g., see *Morel, Voss and Gentili* [1995]. These measurements will provide direct determination of the effect, and will yield an algorithm for extrapolation to the nadir viewing direction as required for derived product algorithms.

4.6 Diffuse transmittance

The diffuse transmittance was mentioned in Section 2. It is defined as the water-leaving radiance in a particular viewing direction (θ_v,ϕ_v) "transmitted" to the top of the atmosphere, i.e.,

$$t(\theta_v,\phi_v) = \frac{\rho_w(\theta_v,\phi_v)_{\text{Top}}}{\rho_w(\theta_v,\phi_v)}.$$

Thus, if the atmosphere were only illuminated from below with radiance $\rho_w(\theta,\phi)$, the radiance measured at the top of the atmosphere in the direction (θ_v,ϕ_v) would be $t(\theta_v,\phi_v)\rho_w(\theta_v,\phi_v)$. The diffuse transmittance accounts for the direct loss from $\rho_w(\theta_v,\phi_v)$ due to absorption and scattering within the atmosphere, as well as for the gain in radiance in the direction (θ_v,ϕ_v) due to scattering of $\rho_w(\theta,\phi)$, i.e., from all other upward directions, into (θ_v,ϕ_v). In the case of the CZCS, it was assumed that $\rho_w(\theta,\phi)$ is independent of (θ,ϕ). Then, $t(\theta_v,\phi_v,\lambda)$ was approximated by [*Gordon et al.*, 1983]

$$t(\theta_v,\phi_v,\lambda) = \exp\left[-\left(\frac{\tau_r(\lambda)}{2}+\tau_{Oz}(\lambda)\right)\left(\frac{1}{\mu_v}\right)\right]t_a(\theta_v,\lambda), \tag{16}$$

where

$$t_a(\theta_v, \lambda) = \exp\Big[-\frac{[1 - \omega_a(\lambda)F_a(\mu_v, \lambda)]\tau_a(\lambda)}{\mu_v}\Big], \tag{17}$$

and $\mu_v = \cos\theta_v$. $F_a(\mu_v, \lambda)$ is related to the scattering phase function of the aerosol and is given by

$$F_a(\mu_v, \lambda) = \frac{1}{4\pi}\int_0^1 P_a(\alpha, \lambda)\, d\mu\, d\phi,$$

where $P_a(\alpha, \lambda)$ is the aerosol phase function at λ (normalized to 4π) for a scattering angle α, and

$$\cos\alpha = \mu\mu_v + \sqrt{(1 - \mu^2)(1 - \mu_v^2)}\cos\phi.$$

If θ_v is $\lesssim 60°$ the factor $[1 - \omega_a(\lambda)F_a(\mu_v, \lambda)]$ is usually $\ll 1$, so t_a depends only weakly on the aerosol optical thickness and was taken to be unity for CZCS.

As retrieval of ρ_w from ρ_t requires t, and relative error in t will yield an equivalent relative error in ρ_w, it is important to compute this quantity as accurately as possible. Because the correction algorithm provides models of the aerosol, it is possible to incorporate all of the multiple scattering and aerosol effects into t in the form of look up tables, and considerably improve its accuracy. Unfortunately, any precomputed t must be based on an assumed form for the water-leaving radiance distribution. The natural distribution to assume is uniform (independent of direction); however, as described in Subsection 4.5, $L_u(\theta, \phi)$ just beneath the surface is not uniform, so this assumption cannot be correct. In fact, the appropriate transmittance to use to propagate the water-leaving reflectance to the top of the atmosphere depends on the actual variation of $L_u(\theta, \phi)$ with θ and ϕ. The extent of the effect of $L_u(\theta, \phi)$ on the transmittance is being studied [*Yang and Gordon*, in preparation], and preliminary results indicate that the difference between a uniform (subsurface) upwelling distribution and a more-realistic $L_u(\theta, \phi)$ is usually $< 5\%$ of t. This suggests that derivation of $\rho_w(443)$ within $\pm 5\%$ may require knowing, or estimating, the shape of the subsurface radiance distribution. *Morel and Gentili* [1996] have devised an iterative scheme for estimating the shape of the subsurface radiance distribution from an estimate of the pigment concentration. Such a scheme may be required to provide a more realistic value for t.

4.7 Sensor calibration

Since the desired water-leaving reflectance is only a small part of ρ_t, at most $\sim 10 - 15\%$ (Table 1), accurate calibration of the sensor is critical [*Gordon*, 1987]. In this section we describe simulations to estimate the magnitude of the effect of the radiometric calibration error, and discuss how accurate on-orbit calibration can be effected.

To assess the effect of calibration errors, we add a small error to each of the measured reflectances, i.e.,

$$\rho_t'(\lambda) = \rho_t(\lambda)[1 + \alpha(\lambda)], \tag{18}$$

where $\alpha(\lambda)$ is the fractional error in $\rho_t(\lambda)$ and $\rho_t'(\lambda)$ is the value of $\rho_t(\lambda)$ that the incorrect sensor calibration would indicate. The atmospheric correction algorithm is then operated by inserting $\rho_t'(\lambda)$ as the measured value rather than the true value $\rho_t(\lambda)$ and $t\Delta\rho_w \equiv \Delta\rho$ is computed as before.

Assuming the single-scattering algorithm, Eq. (12), is exact, and $\varepsilon(\lambda_i, \lambda_l) = \exp[c(\lambda_l - \lambda_i)]$, it is easy to show that to first order in $\alpha(\lambda)$, the error in the retrieved ρ_w is

$$\begin{aligned} t(\lambda_i)\Delta\rho_w(\lambda_i) = {} & \alpha(\lambda_i)\rho_t(\lambda_i) - \varepsilon(\lambda_i, \lambda_l)\alpha(\lambda_l)\rho_t(\lambda_l) \\ & - \left(\frac{\lambda_l - \lambda_i}{\lambda_l - \lambda_s}\right)\left[\frac{\varepsilon(\lambda_i, \lambda_l)}{\varepsilon(\lambda_s, \lambda_l)}\alpha(\lambda_s)\rho_t(\lambda_s) - \varepsilon(\lambda_i, \lambda_l)\alpha(\lambda_l)\rho_t(\lambda_l)\right] \end{aligned} \tag{19}$$

The first term represents the direct effect of calibration error at λ_i on $\rho_w(\lambda_i)$, while the remaining terms represent the indirect effect from calibration error in the atmospheric correction bands at λ_s and λ_l. The second term obviously increases in importance as λ_i decreases. Note that if all of the spectral bands have calibration error with the same sign, i.e., all $\alpha(\lambda)$ have the same sign, significant cancelation of the atmospheric correction contribution can occur; however, if $\alpha(\lambda_s)$ and $\alpha(\lambda_l)$ have different signs, the error is magnified as the last two terms in Eq. (19) will add.

To see if this holds for the multiple-scattering algorithm as well, it was also operated by inserting $\rho_t'(\lambda)$ as the measured value rather than the true value $\rho_t(\lambda)$. The results of this exercise are presented in Figures 19a–19d for the M80 aerosol model at the center of the scan. In Figures 19a and 19b, $\alpha(765) = \alpha(865)$ with $\alpha(443) = 0$ (Figure 19a) or with $\alpha(443) = \alpha(765) = \alpha(865)$ (Figure 19b). Figures 19a and 19b show the effect of a calibration bias that is the same at 765 and 865 nm. Figures 19c and 19d show the effect of having calibration errors that are of opposite

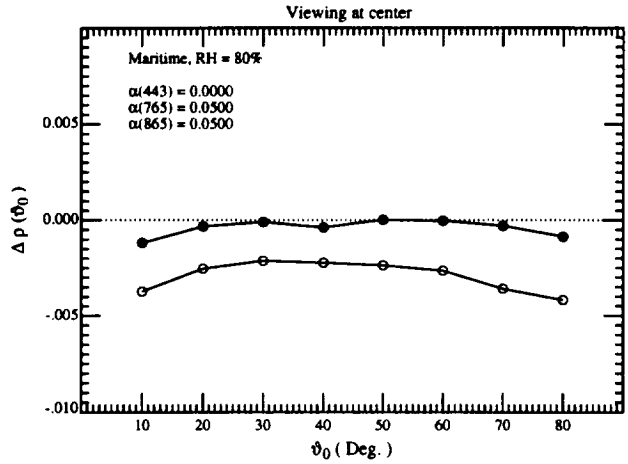

Figure 19a. Error in the retrieved $t(443)\rho_w(443)$ for viewing at the center of the scan with a Maritime aerosol at RH = 80% as a function of the solar zenith angle with $\tau_a(865) = 0.2$ and calibration errors $\alpha(443)$, $\alpha(765)$, and $\alpha(865)$ in Eq. (18) (open circles). Solid circles are for $\alpha(\lambda_i) = 0$ for all λ_i.

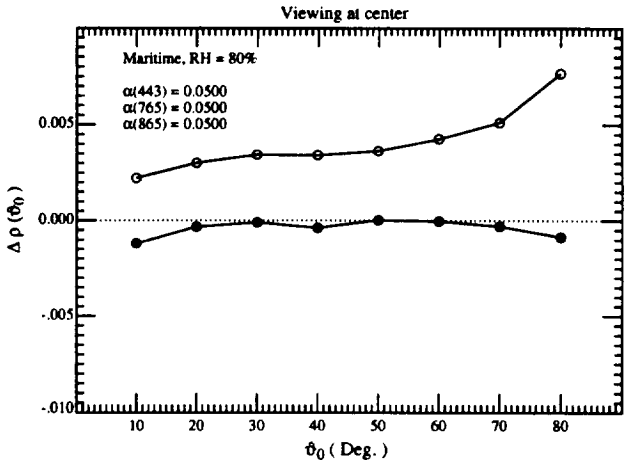

Figure 19b. Error in the retrieved $t(443)\rho_w(443)$ for viewing at the center of the scan with a Maritime aerosol at RH = 80% as a function of the solar zenith angle with $\tau_a(865) = 0.2$ and calibration errors $\alpha(443)$, $\alpha(765)$, and $\alpha(865)$ in Eq. (18) (open circles). Solid circles are for $\alpha(\lambda_i) = 0$ for all λ_i.

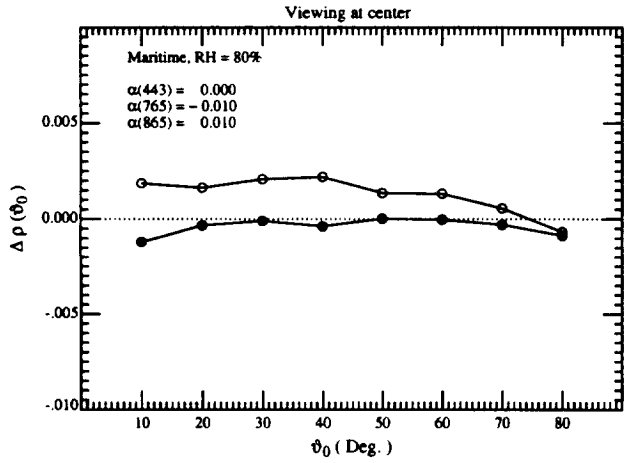

Figure 19c. Error in the retrieved $t(443)\rho_w(443)$ for viewing at the center of the scan with a Maritime aerosol at RH = 80% as a function of the solar zenith angle with $\tau_a(865) = 0.2$ and calibration errors $\alpha(443)$, $\alpha(765)$, and $\alpha(865)$ in Eq. (18) (open circles). Solid circles are for $\alpha(\lambda_i) = 0$ for all λ_i.

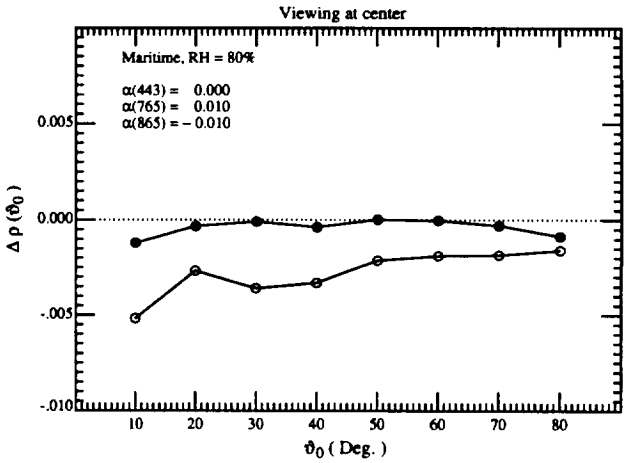

Figure 19d. Error in the retrieved $t(443)\rho_w(443)$ for viewing at the center of the scan with a Maritime aerosol at RH = 80% as a function of the solar zenith angle with $\tau_a(865) = 0.2$ and calibration errors $\alpha(443)$, $\alpha(765)$, and $\alpha(865)$ in Eq. (18) (open circles). Solid circles are for $\alpha(\lambda_i) = 0$ for all λ_i.

sign at 765 and 865 nm. Note that in this case even a small calibration error (1%) can make as significant an error in $\rho_w(443)$ as a large calibration error (5%) when the signs are all the same. As discussed above, the reason the error is so much larger when it is of opposite sign at 765 and 865 nm is that it will cause a large error in the estimated value of $\varepsilon(765, 865)$, and this will propagate through the algorithm causing a large error in the retrieved water-leaving reflectance at 443 nm. In the cases examined in Figure 19, the magnitude of the errors is in quantitative agreement with that predicted by Eq. (19).

As the goal for the calibration of the relevant ocean color bands on MODIS is that L_t have an uncertainty of $< \pm 5\%$, and Figures 19c and 19d show that such an error (even if it were the same in each band) would cause the error in the retrieved $\rho_w(443)$ to be outside the acceptable range. Thus some on-orbit calibration may be required. This is usually termed vicarious calibration [*Evans and Gordon*, 1994; *Fraser and Kaufman*, 1986; *Gordon*, 1987; *Koepke*, 1982; *Slater et al.*, 1987]. It involves making surface measurements of sky radiance, τ_a, ρ_w, etc. to predict ρ_t within a given uncertainty. It is a very attractive method of calibration as the sensor is calibrated in the precise configuration in which it is used. Using the algorithm developed by *Wang and Gordon* [1993] for inverting measurements of sky radiance and τ_a, *Gordon and Zhang* [1996] have shown that with a perfectly calibrated radiometer (to measure the sky radiance) it should be possible to estimate ρ_t with an uncertainty $\sim$ 1–2% in the NIR. This uncertainty combined with an uncertainty of the order of 2–3% in radiometer calibration would mean that $\rho_t(865)$ could be estimated with an uncertainty of $\lesssim 3.5\%$. Thus, in the NIR it should be possible to improve on the 5% uncertainty of MODIS using such surface measurements.

Having achieved this accuracy in the NIR, it is a relatively simple matter to extend this calibration with even higher accuracy to the visible, because there, proportionately more of ρ_t is due to Rayleigh scattering, which is known. Although a complete analysis will be published elsewhere, the basic idea can be seen from the single-scattering approximation. For example, assume that it is desired to estimate ρ_t at 443 nm. First, measurements of $\tau_a(443)/\tau_a(865)$ are made at the surface calibration site. Then Figure 20 provides examples showing the existence of a rough relationship between $\tau_a(443)/\tau_a(865)$ and $\varepsilon(443, 865)$ for all of the aerosol models used in the present work. Such models provide a prediction of $\varepsilon(443, 865)$. Finally, surface measurements of $\rho_w(443)$ are combined with $\rho_r(443)$ to estimate $\rho_{as}(443)$, and thus, the MODIS-derived $\varepsilon(443, 865)$. These two estimates are brought into agreement by adjusting the sensor calibration

at 443 nm. As $\varepsilon(\lambda_i, \lambda_l)$ must be a smooth function of λ_i (Figure 3), it is easy to see that with this procedure, the residual error in all of the spectral bands considered will have the same sign.

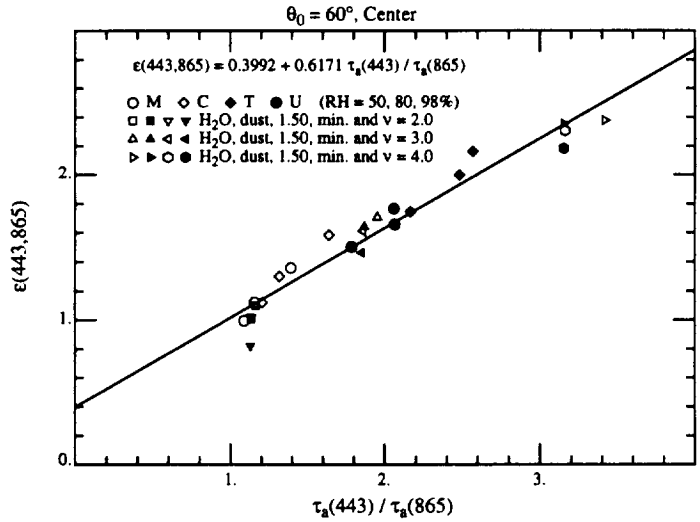

Figure 20. Relationship between $\tau_a(443)/\tau_a(865)$ and $\varepsilon(443, 865)$ at the scan center with $\theta_0 = 60°$ for all of the test aerosol models used in this study.

5. An alternate approach for MISR

The Multiangle Imaging Spectroradiometer [*Diner et al.*, 1989; *Diner et al.*, 1991] (MISR) is scheduled to be flown on the first platform of EOS. MISR consists of a set of nine cameras that view the Earth at nine angles (0, ±26.1°, ±45.6°, ±60.0°, and ±70.5°) to the Earth's surface normal, where positive and negative angles refer to directions ahead of and behind the spacecraft, respectively, and in four spectral bands (Table 1). Thus, MISR will measure the radiance exiting the top of the atmosphere in nine directions at four wavelengths. MISR has a spatial resolution of approximately 250 m at nadir, and if the spatial resolution is degraded by a factor of four to 1 km, it will have sufficient sensitivity to be useful for ocean color observations.

It is easy to adapt the MODIS/SeaWiFS algorithm for use with MISR. In the open ocean, the water-leaving reflectance at 670 nm is very small (Table 1) and can be assumed to be zero

unless the pigment concentration is too large ($\gtrsim 0.5 - 1$ mg/m^3). Thus, one can effect an atmospheric correction using the 670 and 865 nm bands of MISR instead of the 750 (765) and 865 nm bands of MODIS (SeaWiFS).

Alternatively, *Wang and Gordon* [1994c] and *Wang and Gordon* [1994a] describe algorithms for deducing the aerosol optical properties and concentration over the oceans from MISR data. Their algorithms involve comparing the angular distribution of radiance leaving the top of the atmosphere at 865 nm with the predictions of aerosol models. The model that best matches the angular distribution is used to estimate the aerosol properties. The MISR-NIR band is chosen for the retrievals because the water-leaving reflectance can be assumed to be zero there except in the most turbid waters. As the *Wang and Gordon* [1994c] algorithm provides an aerosol model from a set of candidates, it seems reasonable to try to use the chosen candidate model to provide an atmospheric correction in the visible. This method is more attractive than the two-band MODIS/SeaWiFS method, as only a single spectral band (865 nm) is required, i.e., it is not necessary to assume a pigment concentration $\lesssim 0.5 - 1$ mg/m^3.

These two methods of atmospheric correction of the MISR blue band (443 nm) are compared in Table 3. As in *Wang and Gordon* [1994c] we examined two geometries: June 21 with MISR positioned at 30° latitude ($\theta_0 = 20°$, $\phi_v - \phi_0 = 83°, 97°$) called "summer," and Dec. 21 with MISR positioned at 34° latitude ($\theta_0 = 60°$, $\phi_v - \phi_0 = 23°$ and 157°) referred to as "winter." The aerosol model used in generating the pseudo data used to prepare Table 3 was the C80 model with $\tau_a(865) = 0.2$. For MISR, the atmospheric correction was applied to the nadir-viewing camera, and for MODIS the correction was at the scan center (also nadir-viewing). Note that in the Summer geometry, there is little difference between the two atmospheric correction methods, while in the Winter geometry, the MODIS correction is significantly better than the MISR single-band correction; however, even in this case, the MISR correction technique still yields acceptable results.

The test provided in Table 3 suggests that it is possible to atmospherically correct MISR imagery using a single spectral band. This could be of significant value for imagery obtained in coastal zones and large inland lakes. Near the coast, the water is often turbid due to sediments introduced runoff from the land or resuspended from the bottom. The reflectance of such waters generally decreases as the wavelength increases from the green to red to the NIR due to the in-

Table 3: Comparison between performance of the MISR and MODIS (SeaWiFS) atmospheric correction techniques applied to MISR data. The tabulated quantity is $\Delta\rho \equiv t\Delta\rho_w(443)$.

(a) Summer Geometry

Instrument	443 nm	555 nm
MODIS	$+ 3.02 \times 10^{-4}$	$+ 1.03 \times 10^{-4}$
MISR	$- 2.02 \times 10^{-4}$	$- 0.63 \times 10^{-4}$

(b) Winter Geometry

Instrument	443 nm	555 nm
MODIS	$+ 3.42 \times 10^{-4}$	$+ 0.65 \times 10^{-4}$
MISR	-10.01×10^{-4}	$- 9.53 \times 10^{-4}$

creasing absorption with increasing wavelength by the water itself; however, for such waters, it is often not possible to assume $\rho_w \approx 0$ at 670 nm or even 750 nm; however, as long as $\rho_w \approx 0$ at 865 nm, a single-band MISR correction could be made. As the reflectance of coastal waters is generally larger than the open ocean, the accuracy of the atmospheric correction need not be as great as in the open ocean to obtain $\rho_w(443)$ within $\pm 5\%$. In such turbid coastal waters it also appears possible to atmospherically correct MODIS using MISR in the following manner: (1) the MISR aerosol algorithm is used to provide the candidate aerosol model for MODIS; and (2) the MODIS 865 nm band is used along with the candidate aerosol model to correct the other MODIS bands. Finally, combining the wide spectral coverage of MODIS (412 to 2130 nm) and the wide range of viewing angles of MISR may be of considerable value in identifying the presence of absorbing aerosols. Such synergism between MODIS and MISR is only possible because they share the same platform.

6. Concluding remarks

In this paper we have described the atmospheric correction algorithms proposed for SeaWiFS, MODIS, and MISR, and simulated their performance for a variety of aerosol types and concentrations. In addition we have examined the effects of the simplifying assumptions used in the

original development of the algorithm, and examined several remaining issues. One goal of the paper was to try to provide a better understanding of the nature of the weaknesses of the basic algorithm, in order to develop plans for resolving inadequacies. Several conclusions can be made on the basis of the work presented in this paper.

First, considering the fact that the maritime atmosphere, far from the influence land and/or anthropogenic aerosol sources, is very clear, the single-scattering algorithm should be sufficient over most of the open ocean. Since the multiple-scattering algorithm reduces to the single-scattering algorithm in the limit of small $\tau_a(865)$, one expects that this algorithm should also provide an adequate correction in such cases. However, this will only obtain as long as the candidate aerosol models encompass the range of variability of the actual maritime aerosol.

Second, the multiple-scattering algorithm is capable of providing an adequate correction for higher aerosol optical thicknesses, but again, this requires a realistic set of candidate aerosol models. If the aerosols absorb significantly, e.g., the aerosol over the Middle Atlantic Bight during summer air pollution incidents or the dust transported by the winds from Africa over the Tropical North Atlantic, it is absolutely necessary to restrict the candidate aerosol set to include only members that have the proper absorption characteristics. Since proper sets may be appropriate only for a restricted regions, an accurate aerosol climatology will be necessary to correct imagery in regions other than the open ocean. Such a climatology does not exist at present; however, efforts by several research groups are underway to build one.

Third, absorbing aerosols present an additional difficulty. In the case of nonabsorbing aerosols, given a realistic set of candidate aerosol models, the multiple-scattering algorithm is shown through simulations to be insensitive to the vertical structure of the aerosol. Thus, multiple-scattering lookup tables prepared by solving the radiative transfer equations for a two-layer atmosphere, with the aerosols in the lower layer, are adequate for weakly- or nonabsorbing aerosols. In contrast when the aerosol shows significant absorption, the multiple-scattering algorithm was shown to be very sensitive to the physical thickness of the aerosol layer, even if an appropriate set of candidate aerosol models are employed. This implies that expected layer thickness must be included in the aerosol climatology discussed above.

Fourth, the effects of the simplifying assumptions used in the development of the algorithm, such as approximating the atmosphere by a plane-parallel medium, ignoring polarization of the

light field in the simulation of ρ_t, and assuming that the sea surface was smooth, were shown to have been justified to the extent that they introduce little error in the resulting atmospheric correction.

Fifth, the influence of whitecaps was shown to be dependent on the spectral properties of their reflectance, i.e., on whether whitecap reflectance is similar to that measured in the surf zone and significantly smaller in the NIR than in the visible. Thus, effort must be made to understand the spectral reflectance of whitecaps and its relationship to wind speed.

Sixth, other issues such as the appropriateness of candidate aerosol models, stratospheric aerosols, the effect of residual instrument polarization sensitivity, the variability of the in-water radiance distribution and its influence on the diffuse transmittance of the atmosphere, and the assessment of, and correction for, error in the sensor calibration are all under study.

A new atmospheric correction technique, which requires the water-leaving reflectance to be negligible in only a *single* spectral band rather than *two* spectral bands, was developed and applied to simulated MISR data. It was shown that for certain geometries this single-band algorithm produced ρ_w retrievals that were as good as the MODIS-type algorithm based on assuming $\rho_w = 0$ at both 670 and 865 nm. This raises the possibility of synergistically using MISR imagery to provide the proper candidate aerosol model for correcting MODIS imagery in the coastal zone, and to help in identifying absorbing aerosols. Application of such a technique to these EOS sensors would probably require the availability of Level 1 data (calibrated and geometrically-located radiances) at a single processing center.

Finally, based on the simulations presented here, atmospheric correction appears to be limited principally by our ability to correctly predict the reflectivity enhancement of whitecaps, and by the representativeness of the aerosol climatology (particularly in regions with strongly-absorbing aerosols) that must be developed and used in the multiple-scattering algorithm. However, it should be recognized that much of the difficulty associated with the algorithm (absorbing aerosols) applies to a relatively small (although important) portion of the ocean. Except for the whitecap limitation, there will be little difficulty atmospherically correcting most of the imagery from EOS ocean color sensors. Given their improved radiometric sensitivity, wider spectral range, and radiometric calibration stability compared to CZCS, a concomitant increase in the accuracy and stability of the derived products will be realized.

7. Appendices

Appendix A. The sun glitter masking algorithm

In this appendix we provide the equations required to prepare a mask to flag pixels that are seriously contaminated by sun glitter. The intention is that the sun glitter mask be applied to the imagery prior to the application of the normalized water-leaving radiance retrieval algorithm described in the text.

The contribution to the measured radiance at the top of the atmosphere from sun glitter — the specular reflection of sunlight from the sea surface and propagation to the sensor — is based on the formulation of *Cox and Munk* [1954]. In this development the sea surface is modeled as

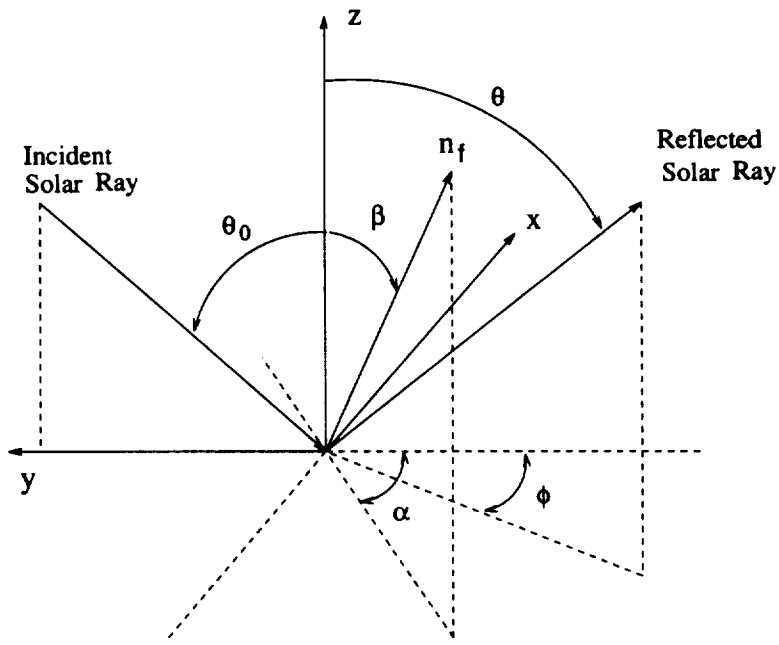

Figure 21. Geometry of reflection from a rough sea surface. n_f is the unit normal to the facet that is oriented properly to reflect the sunlight as shown.

a collection of facets with individual slope components z_x and z_y. In a coordinate system with the $+y$ axis pointing toward the sun (projection of the sun's rays on the sea surface is along the $-y$ axis), given the solar zenith angle and the angles θ and ϕ specifying the reflected ray, the orientation (β, α) of the facet normal n_f (Figure 21) required for a facet to reflect sunlight in the

direction of (θ, ϕ) is found from the following equations

$$\cos(2\omega) = \cos\theta\cos\theta_0 - \sin\theta\sin\theta_0\cos\phi$$

$$\cos\beta = (\cos\theta + \cos\theta_0)/2\cos\omega$$

$$\cos\alpha = (\cos\phi\cos\theta - \sin\theta)/2\cos\omega\sin\beta$$

$$\sin\alpha = (\sin\phi\cos\theta)/2\cos\omega\sin\beta$$

$$z_x = \sin\alpha\tan\beta$$

$$z_y = \cos\alpha\tan\beta.$$

Note that for a flat (smooth) surface, $\phi = 0$. Let χ be the the angle between the projection of the sun's rays on the sea surface and the direction of the wind vector $\vec{W}$, i.e., if $\chi = 0$ the wind vector points in the direction of $-y$ in Figure 1. χ is measured positive in a clockwise direction (looking toward the surface), i.e., if $0 < \chi < 90°$, the wind vector is in the quadrant formed by the $-x$ and $-y$ axes. Then, ρ_g is given by

$$\rho_g(\theta, \phi; \theta_0, \phi_0) = \frac{\pi r(\omega)}{4\cos\theta_0\cos\theta\cos^4\beta} p(z'_x, z'_y)$$

where $p(z'_x, z'_y)$ is the probability density of surface slopes given by

$$p(z'_x, z'_y) = (2\pi\sigma_u\sigma_c)^{-1}\exp[-(\xi^2+\eta^2)/2]\left[1 + \sum_{i=1}^{\infty}\sum_{j=1}^{\infty} c_{ij}H_i(\xi)H_j(\eta)\right],$$

with

$$\xi = z'_x/\sigma_c = \sin\alpha'\tan\beta/\sigma_c$$

$$\eta = z'_y/\sigma_u = \cos\alpha'\tan\beta/\sigma_u$$

$$\alpha' = \alpha - \chi.$$

$r(\omega)$ is the Fresnel reflectance for unpolarized light incident at an angle ω, and H_i is the Hermite polynomial of order i. The constants σ_u, σ_c, and c_{ij} were determined by *Cox and Munk* [1954] by fitting the radiance from glitter patterns photographed from aircraft to these equations. For $\vec{W}$ in m/s, they are

$$\sigma_c^2 = 0.003 + 1.92\times10^{-3}W \quad \pm 0.002$$

$$\sigma_u^2 = 0.000 + 3.16\times10^{-3}W \quad \pm 0.004$$

$$c_{21} = 0.01 - 8.6\times10^{-3}W \quad \pm 0.03$$

$$c_{03} = 0.04 - 33\times10^{-3}W \quad \pm .012$$

$$c_{40} = 0.40 \quad \pm 0.23$$

$$c_{22} = 0.12 \quad \pm 0.06$$

$$c_{04} = 0.23 \quad \pm 0.41$$

The contribution of ρ_g to the reflectance measured at the top of the atmosphere, $T\rho_g$, where T is the direct transmittance of the atmosphere (Section 2), is just

$$\rho_g \exp\left[-\tau\left(\frac{1}{\cos\theta} + \frac{1}{\cos\theta_0}\right)\right],$$

where τ is the total optical thickness of the atmosphere.

The sun glitter mask uses the wind vector $\vec{W}$ to estimate $T\rho_g$ for each pixel, and if the estimate is larger than a threshold value (to be determined) the pixel is flagged and the normalized water-leaving radiance algorithm is not applied. As the aerosol optical thickness is unknown, the conservative approach is taken to maximize the area masked by choosing $\tau_a = 0$.

Appendix B. The MODIS short-wave infrared bands

In Subsection 4.2 it was suggested that the MODIS SWIR bands may be useful in separating situations dominated by absorbing mineral aerosols from those dominated by nonabsorbing aerosols. In this appendix it is shown that MODIS has sufficient radiometric sensitivity in the SWIR to justify attempting such a separation. The specifications of the MODIS SWIR bands are provided in Table 4 in terms of reflectance for a solar zenith angle of 60°. In the table, $\Delta\rho_{\mathrm{Dig}}$

Table 4: Radiometric performance of MODIS in the SWIR

Band	λ (nm)	ρ_{max} (Sr^{-1})	NE$\Delta\rho$ (Sr^{-1})	$\Delta\rho_{\mathrm{Dig}}$ (Sr^{-1})
5	1240	0.94	6.2×10^{-4}	2.2×10^{-4}
6	1640	1.88	7.2×10^{-4}	4.6×10^{-4}
7	2130	1.50	6.2×10^{-4}	3.6×10^{-4}
26	1380	1.64	7.2×10^{-4}	4.0×10^{-4}

represents the quantization interval of the 12-bit digitized reflectance. Bands 5, 6, and 7 have a spatial resolution of 500 m compared to 1000 m for Bands 8-16 and 26. Comparing NE$\Delta\rho$ and $\Delta\rho_{\mathrm{Dig}}$ suggests that averaging four 500 m pixels to form one 1000 m pixel could reduce the effective NE$\Delta\rho$ by $\sim$ a factor of 2, particularly for Band 5. Averaging larger numbers of 500 m pixels should lead to still lower NE$\Delta\rho$'s.

To estimate the aerosol component of the expected reflectance in these bands, we take a conservative approach. We assume a mineral aerosol (strongly absorbing) with $\tau_a(865) = 0.2$ and use the single scattering approximation with the surface reflection terms omitted. Then for nadir viewing and $\theta_0 = 60°$,

$$\rho_{as}(\lambda) = \frac{\omega_a(\lambda) P_a(120°, \lambda) \tau_a(\lambda)}{2}.$$

For the size distribution we use the Haze C model with $\nu = 2$ (the smallest $P_a(120°)$) as well as the log-normal model described in Subsection 4.2. The resulting values of ρ_{as} are presented in Table 5.

These computations suggest that Bands 5 and 6 would be able to detect aerosols with a signal-to-noise ratio of $\sim$ 20, with pixel averaging. In contrast, it appears that Band 7 would be

useful only at higher $\tau_a(865)$, or by averaging a larger number of pixels. One must note, however, that these estimates for ρ_{as} are conservative.

Table 5: Expected aerosol reflectance in the SWIR.
Values for ρ_{as} and NE$\Delta\rho$ have been multiplied by 10^{+4}.

Band	λ (nm)	ρ_{as} (Sr^{-1})		NE$\Delta\rho$ (Sr^{-1})
		Haze C	Log-normal	
16	865	110	103	0.8
5	1240	106	128	6.2
6	1640	68	94	7.2
7	2130	39	37	6.2

Appendix C. Required ancillary data

There are several sets of ancillary data that are required to operate the $[L_w]_N$ retrieval algorithm. These are listed in Table 6. They may be needed on at most a $1° \times 1°$ latitude-longitude grid, but probably a coarser grid, e.g., $3° \times 3°$ will be sufficient considering the expected quality of some of the data. We will now discuss each ancillary data set required.

Table 6: Required ancillary data.

Quantity	Ancillary Data
$\rho_t(\lambda_i)$	$F_0(\lambda_i)$
$\rho_r(\lambda_i)$	$\tau_{Oz}(\lambda_i)$, W, P_0
$\rho_{wc}(\lambda_i)$	W
$\rho_g(\lambda_i)$	$\vec{W}$
$t(\lambda_i)$	$\tau_{Oz}(\lambda_i)$, P_0
$T(\lambda_i)$	$\tau_{Oz}(\lambda_i)$, P_0, $\tau_a(\lambda_i)$
$\epsilon(\lambda_i, \lambda_j)$	RH

The extraterrestrial solar irradiance is required to convert from L_t to ρ_t. It is planned that this be taken from *Neckel and Labs* [1984] unless newer, more accurate, determinations become available in the future. In the event that MODIS is calibrated in reflectance units directly, this quantity is only needed to convert $[\rho_w]_N$ to the desired $[L_w]_N$.

In the radiative transfer model the atmosphere is assumed to be composed of three layers. The top is the Ozone layer and is nonscattering, the second is a molecular scattering layer and the third is the aerosol layer. The Ozone optical thickness $\tau_{Oz}(\lambda)$ is needed to compute the two way transmittance of ρ_r, ρ_w, ρ_{wc} and ρ_g through the Ozone layer. Since the Ozone absorption is small ($\tau_{Oz} \lesssim 0.035$) high accuracy is not needed. It is estimated that an error in the Ozone concentration of $\sim 20 - 40$ mAtm–cm (Dobson Units) could be tolerated. The source will either be MODIS itself (most convenient) or a sensor on the NOAA system.

The atmospheric pressure is needed to compute the Rayleigh optical thickness required for the computation of ρ_r. This is also used in the transmittances t and T. An error $< \pm 5$ hPa should be sufficient.

The wind speed, if known, is used in the computation of ρ_r, otherwise ρ_r is computed with $W = 0$. It is also required for the estimation of $[\rho_{wc}]_N$. The wind vector is required for the construction of a glint mask, i.e., a mask to remove areas contaminated by sun glint from the imagery before processing (Appendix A). The importance of creating a realistic mask is that good data may be masked if the mask is made in too conservative a manner. An error of $< 1 - 2$ m/s in the speed and $< 30°$ on the direction should be sufficient.

The surface relative humidity (RH) is not really needed by the algorithm; however, it could be useful as a constraint on the candidate aerosol models chosen by the correction algorithm. The error in the value of RH should be $< \pm 5 - 10\%$ to be useful. The source of the data for P_0, $\vec{W}$, and RH will be the output of numerical weather models, probably from NMC.

Acknowledgment

The author wishes to acknowledge the students and postdocs who have contributed to this work: Menghua Wang, Kuiyuan Ding, Tianming Zhang, Fan He, Haoyu Yang, and Tao Du. He is also grateful to Drs. R. Fraser and R. Frouin for providing careful reviews resulting in several improvements of the manuscript. This work received support from the National Aeronautics and Space Administration under Grant NAGW-273 and Contracts NAS5-31363 and NAS5-31743, and the Jet Propulsion Laboratory under Contract 959033.

References

d'Almeida, G. A., P. Koepke and E. P. Shettle, *Atmospheric Aerosols — Global Climatology and Radiative Characteristics*, A. Deepak Publishing, Hampton, VA, 1991.

André, J. -M. and A. Morel, Atmospheric Corrections and Interpretation of Marine Radiances in CZCS Imagery, Revisited, *Oceanologica Acta*, *14*, 3–22, 1991.

Asrar, G. and J. Dozier, *EOS: Science Strategy for the Earth Observing System*, AIP Press, Woodbury, N.Y., 1994, 119 pp.

Bricaud, A. and A. Morel, Atmospheric Corrections and Interpretation of Marine Radiances in CZCS Imagery: Use of a Reflectance Model, *Oceanologica Acta*, *7*, 33–50, 1987.

Clarke, G. L., G. C. Ewing and C. J. Lorenzen, Spectra of Backscattered Light from the Sea Obtained From Aircraft as a Measurement of Chlorophyll Concentration, *Science*, *167*, 1119–1121, 1970.

Cox, C. and W. Munk, Measurements of the Roughness of the Sea Surface from Photographs of the Sun's Glitter, *Jour. Opt. Soc. of Am.*, *44*, 838–850, 1954.

Deirmendjian, D., *Electromagnetic Scattering on Spherical Polydispersions*, Elsevier, New York, NY, 1969, 290 pp.

Deschamps, P. Y., M. Herman and D. Tanre, Modeling of the atmospheric effects and its application to the remote sensing of ocean color, *Applied Optics*, *22*, 3751–3758, 1983.

Diner, D. J., C. J. Bruegge, J. V. Martonchik, T. P. Ackerman, R. Davies, S. A. W. Gerstl, H. R. Gordon, P. J. Sellers, J. Clark, J. A. Daniels, E. D. Danielson, V. G. Duval, K. P. Klaasen, G. W. L. A. D. I. Nakamoto, R. Pagano and T. H. Reilly, MISR: A Multi-angle Imaging SpectroRadiometer for Geophysical and Climatological Research from EOS, *IEEE Transactions on Geoscience and Remote Sensing*, *27*, 200–214, 1989.

Diner, D. J., C. J. Bruegge, J. V. Martonchik, G. W. Bothwell, E. D. Danielson, E. L. Floyd, V. G. Ford, L. E. Hovland, K. L. Jones and M. L. White, A Multi-angle Imaging SpectroRadiometer for Terrestrial Remote Sensing from the Earth Observing System, *International Journal of Imaging Systems and Technology*, *3*, 92–107, 1991.

Ding, K. and H. R. Gordon, Atmospheric correction of ocean color sensors: Effects of earth curvature, *Applied Optics*, *33*, 7096–7016, 1994.

Ding, K. and H. R. Gordon, Analysis of the influence of O_2 *A*-band absorption on atmospheric correction of ocean color imagery, *Applied Optics*, *34*, 2068–2080, 1995.

Eldridge, R. G., Water Vapor Absorption of Visible and Near Infrared Radiation, *Applied Optics*, *4*, 709–713, 1967.

Evans, R. H. and H. R. Gordon, CZCS 'System Calibration:' A retrospective examination, *Jour. Geophys. Res.*, *99C*, 7293–7307, 1994.

Feldman, G. C., N. Kuring, C. Ng, W. Esaias, C. R. McClain, J. Elrod, N. Maynard, D. Endres, R. Evans, J. Brown, S. Walsh, M. Carle and G. Podesta, Ocean Color: Availability of the Global Data Set, *EOS Trans. Amer. Geophys. Union*, *70*, 634–641, 1989.

Fraser, R. S., Degree of Interdependence among Atmospheric Optical Thickness in Spectral Bands between 0.36 and 2.4 μm, *Applied Optics*, *14*, 1187–1196, 1975.

Fraser, R. S. and Y. J. Kaufman, Calibration of satellite sensors after launch, *Applied Optics*, *25*, 1177–1185, 1986.

Frouin, R., M. Schwindling and P. Y. Deschamps, 1995, Spectral reflectance of sea foam in the visible and near-infrared: In-situ measurements and implications for remote sensing of ocean color and aerosols, *Jour. Geophys. Res.*, (In press).

Gao, B. -C., A. F. H. Goetz and W. J. Wiscombe, Cirrus cloud detection from airborne imaging spectrometer data using the 1.38 micron water vapor band, *Geophysical Research Letters*, *20*, 301–304, 1993.

Gordon, H. R., Radiative Transfer: A Technique for Simulating the Ocean in Satellite Remote Sensing Calculations, *Applied Optics*, *15*, 1974–1979, 1976.

Gordon, H. R., Removal of Atmospheric Effects from Satellite Imagery of the Oceans, *Applied Optics*, *17*, 1631–1636, 1978.

Gordon, H. R., Calibration Requirements and Methodology for Remote Sensors Viewing the Oceans in the Visible, *Remote Sensing of Environment*, *22*, 103–126, 1987.

Gordon, H. R., Ocean Color Remote Sensing Systems: Radiometric Requirements, *Society of Photo-Optical Instrumentation Engineers, Recent Advances in Sensors, Radiometry, and Data Processing for Remote Sensing*, *924*, 151–167, 1988.

Gordon, H. R., Radiometric Considerations for Ocean Color Remote Sensors, *Applied Optics*, *29*, 3228–3236, 1990.

Gordon, H. R., J. W. Brown and R. H. Evans, Exact Rayleigh Scattering Calculations for use with the Nimbus-7 Coastal Zone Color Scanner, *Applied Optics*, *27*, 862–871, 1988.

Gordon, H. R., O. B. Brown, R. H. Evans, J. W. Brown, R. C. Smith, K. S. Baker and D. K. Clark, A Semi-Analytic Radiance Model of Ocean Color, *Jour. Geophys. Res.*, *93D*, 10909–10924, 1988.

Gordon, H. R. and D. J. Castaño, The Coastal Zone Color Scanner Atmospheric Correction Algorithm: Multiple Scattering Effects, *Applied Optics*, *26*, 2111–2122, 1987.

Gordon, H. R. and D. J. Castaño, The Coastal Zone Color Scanner Atmospheric Correction Algorithm: Influence of El Chichón, *Applied Optics*, *27*, 3319–3321, 1988.

Gordon, H. R. and D. K. Clark, Atmospheric effects in the remote sensing of phytoplankton pigments, *Boundary-Layer Meteorology*, *18*, 299–313, 1980.

Gordon, H. R. and D. K. Clark, Clear water radiances for atmospheric correction of coastal zone color scanner imagery, *Applied Optics*, *20*, 4175–4180, 1981.

Gordon, H. R., D. K. Clark, J. W. Brown, O. B. Brown, R. H. Evans and W. W. Broenkow, Phytoplankton pigment concentrations in the Middle Atlantic Bight: comparison between ship determinations and Coastal Zone Color Scanner estimates, *Applied Optics*, *22*, 20–36, 1983.

Gordon, H. R., D. K. Clark, J. L. Mueller and W. A. Hovis, Phytoplankton pigments derived from the Nimbus–7 CZCS: initial comparisons with surface measurements, *Science*, *210*, 63–66, 1980.

Gordon, H. R. and M. Wang, Surface Roughness Considerations for Atmospheric Correction of Ocean Color Sensors. 2: Error in the Retrieved Water-leaving Radiance, *Applied Optics*, *31*, 4261–4267, 1992a.

Gordon, H. R. and M. Wang, Surface Roughness Considerations for Atmospheric Correction of Ocean Color Sensors. 1: The Rayleigh Scattering Component, *Applied Optics*, *31*, 4247–4260, 1992b.

Gordon, H. R. and M. Wang, Retrieval of water-leaving radiance and aerosol optical thickness over the oceans with SeaWiFS: A preliminary algorithm, *Applied Optics*, *33*, 443–452, 1994a.

Gordon, H. R. and M. Wang, Influence of Oceanic Whitecaps on Atmospheric Correction of SeaWiFS, *Applied Optics*, *33*, 7754–7763, 1994b.

Gordon, H. R. and T. Zhang, 1996, How well can radiance reflected from the ocean-atmosphere system be predicted from measurements at the sea surface?, *Applied Optics* (In press).

Grant, W. B., E. V. Browell, C. F. Butler, M. A. Fenn and G. D. Nowicki, Comparisons of Electra-Lidar and LITE Atmospheric Measurements Near the East Coast of the U.S. and the Caribbean, *EOS, Transactions, American Geophysical Union*, *76*, S70, 1995.

Hale, G. M. and M. R. Querry, Optical Constants of Water in the 200-nm to 200-μm Wavelength Region, *Applied Optics*, *12*, 555–563, 1973.

Holben, B.N., T.F. Eck, I. Slutsker, D. Tanre, J.P. Buis, A. Setzer, E. Vermote, J. Reagan, Y. Kaufman, T. Nakajima, F. Lavenu and I. Jankowiak, 1996, Automatic Sun and Sky Scanning Raiometer System for Network Aerosol Monitoring, *Remote Sensing of Environment* (In press) .

Hooker, S.B., W.E. Esaias, G.C. Feldman, W.W. Gregg and C.R. McClain, *SeaWiFS Technical Report Series: Volume 1, An Overview of SeaWiFS and Ocean Color*, NASA, Greenbelt, MD, Technical Memorandum 104566, July 1992.

Hovis, W.A., D.K. Clark, F. Anderson, R.W. Austin, W.H. Wilson, E.T. Baker, D. Ball, H.R. Gordon, J.L. Mueller, S.Y.E. Sayed, B. Strum, R.C. Wrigley and C.S. Yentsch, Nimbus 7 coastal zone color scanner: system description and initial imagery, *Science*, *210*, 60–63, 1980.

van de Hulst, H.C., *Multiple Light Scattering*, Academic Press, New York, 1980, 739 pp.

Ismail, S., E.V. Browell, S.A. Kooi and G.D. Nowicki, Simultaneous LASE and LITE Aerosol Profile Measurements over the Atlantic, *EOS, Transactions, American Geophysical Union*, *76*, S71, 1995.

Junge, C., Atmospheric Chemistry, *Advances in Geophysics*, *4*, 1–108, 1958.

Kattawar, G.W., G.N. Plass and S.J. Hitzfelder, Multiple scattered radiation emerging from Rayleigh and continental haze layers. 1: Radiance, polarization, and neutral points, *Applied Optics*, *15*, 632–647, 1976.

Kenizys, F.X., E.P. Shettle, W.O. Gallery, J.H.Chetwynd, L.W. Abreu, J.E.A. Selby, S.A. Clough and R.W. Fenn, Atmospheric Transmittance/Radiance: The LOWTRAN 6 Model, Air Force Geophysics Laboratory, Hanscomb AFB, MA 01731, AFGL–TR–83–0187, 1983, NTIS AD A137796.

King, M.D., Harshvardhan and A. Arking, A Model of the Radiative Properties of the El Chichón Stratospheric Aerosol Layer, *Journal of Climate and Applied Meteorology*, *23*, 1121–1137, 1984.

Koepke, P., Vicarious Satellite Calibration in the Solar Spectral Range by Means of Calculated Radiances and its Application to Meteosat, *Applied Optics*, *21*, 2845–2854, 1982.

Koepke, P., Effective Reflectance of Oceanic Whitecaps, *Applied Optics*, *23*, 1816–1824, 1984.

Korotaev, G. K., S. M. Sakerin, A. M. Ignatov, L. L. Stowe and E. P. McClain, Sun-Photometer Observations of Aerosol Optical Thickness over the North Atlantic from a Soviet Research Vessel for Validation of Satellite Measurements, *Jour. Atmos. Oceanic Technol.*, *10*, 725–735, 1993.

Lechner, I. S., G. W. Fisher, H. R. Larsen, M. J. Harvey and R. A. Knobben, Aerosol Size Distributions in the Southwest Pacific, *Jour. Geophys. Res.*, *94D*, 14893–14903, 1989.

McCormick, M. P., LITE – An Overview, *EOS, Transactions, American Geophysical Union*, *76*, S66, 1995.

Mishchenko, M. I. and L. D. Travis, Light scattering by polydispersions of randomly oriented spheriods with sizes comparable to wavelengths of observation, *Applied Optics*, *33*, 7206–7225, 1994.

Morel, A. and J. -M. André, Pigment Distribution and Primary Production in the Western Mediterranean as Derived and Modeled From Coastal Zone Color Scanner Observations, *Jour. Geophys. Res.*, *96C*, 12,685–12,698, 1991.

Morel, A. and B. Gentili, Diffuse reflectance of oceanic waters: its dependence on Sun angle as influenced by the molecular scattering contribution, *Applied Optics*, *30*, 4427–4438, 1991.

Morel, A. and B. Gentili, Diffuse reflectance of oceanic waters. II. Bidirectional aspects, *Applied Optics*, *32*, 6864–6879, 1993.

Morel, A. and B. Gentili, 1996, Diffuse reflectance of oceanic waters. III. Implication of bidirectionality for the remote sensing problem, *Applied Optics* (In press).

Morel, A., K. J. Voss and B. Gentili, Bidirectional reflectance of oceanic waters: A comparison of modeled and measured upward radiance fields, *Jour. Geophys. Res.*, *100C*, 13,143–13,150, 1995.

Mugnai, A. and W. J. Wiscombe, Scattering from nonspherical Chebyshev particles. 3: Variability in angular scattering patterns, *Applied Optics*, *28*, 3061–3073, 1989.

Neckel, H. and D. Labs, The Solar Radiation Between 3300 and 12500 Å, *Solar Physics* , *90*, 205–258, 1984.

Neville, R. A. and J. F. R. Gower, Passive Remote Sensing of Phytoplankton via Chlorophyll α Fluorescence, *Jour. Geophys. Res.*, *82C*, 3487–3493, 1977.

Platt, T. and S. Sathyendranath, Oceanic Primary Production: Estimation by Remote Sensing at Local and Regional Scales, *Science*, *241*, 1613–1620, 1988.

Reddy, P. J., F. W. Kreiner, J. J. Deluisi and Y. Kim, Aerosol Optical Depths Over the Atlantic Derived From Shipboard Sunphotometer Observations During the 1988 Global Change Expedition, *Global Biogeochemical Cycles*, *4*, 225–240, 1990.

Salomonson, V. V., W. L. Barnes, P. W. Maymon, H. E. Montgomery and H. Ostrow, MODIS: Advanced Facility Instrument for Studies of the Earth as a System, *IEEE Geosci. Rem. Sens.*, *27*, 145–152, 1989.

Sasano, Y. and E. V. Browell, Light scattering characteristics of various aerosol types derived from multiple wavelength lidar observations, *Applied Optics*, *28*, 1670–1679, 1989.

Schwindling, M., Modeles et measures pour l'observation spatiale de la couleur de l'ocean: Diffusion atmospherique par les aerosols et reflexion de surface par l'ecume, 1995, Docteur de L'Universite these, Univ. des Sci. et Tech. de Lille. 245 pp.

Shettle, E. P. and R. W. Fenn, Models for the Aerosols of the Lower Atmosphere and the Effects of Humidity Variations on Their Optical Properties, Air Force Geophysics Laboratory, Hanscomb AFB, MA 01731, AFGL–TR–79-0214, 1979.

Slater, P. N., S. F. Biggar, R. G. Holm, R. D. Jackson, Y. Mao, M. S. Moran, J. M. Palmer and B. Yuan, Reflectance- and Radiance-Based Methods for the In-Flight Absolute Calibration of Multispectral Sensors, *Remote Sensing of Environment*, *22*, 11–37, 1987.

Smith, R. C., Structure of Solar Radiation in the Upper Layers of the Sea, in *Optical Aspects of Oceanography*, edited by N. G. Jerlov and E. S. Nielsen, pp. 95–119, Academic Press, New York, NY, 1974.

Smith, R. C. and W. H. Wilson, Ship and satellite bio-optical research in the California Bight, in *Oceanography from Space*, edited by J. F. R. Gower, pp. 281–294, Plenum, New York, NY, 1981.

Tomasi, C., Weak Absorption by Atmospheric Water Vapour in the Visible and Near-Infrared Spectral Region, *Nuovo Cimento*, *2C*, 511–526, 1979a.

Tomasi, C., Non-selective absorption by atmospheric water vapour at visible and near infrared wavelengths, *Quart. J. R. Met. Soc.*, *105*, 1027–1040, 1979b.

Villevalde, Y. V., A. V. Smirnov, N. T. O'Neill, S. P. Smyshlyaev and V. V. Yakovlev, Measurement of Aerosol Optical Depth in the Pacific Ocean and North Atlantic, *Jour. Geophys. Res.*, *99D*, 20983–20988, 1994.

Voss, K. J., Electro-optic Camera System for Measurement of the Underwater Radiance Distribution, *Optical Engineering*, *28*, 241–247, 1989.

Wang, M. and H. R. Gordon, Retrieval of the Columnar Aerosol Phase Function and Single Scattering Albedo from Sky Radiance over the Ocean: Simulations, *Applied Optics*, *32*, 4598–4609, 1993.

Wang, M. and H. R. Gordon, Radiance reflected from the ocean-atmosphere system: Synthesis from individual components of the aerosol size distribution, *Applied Optics*, *33*, 7088–7095, 1994a.

Wang, M. and H. R. Gordon, A Simple, Moderately Accurate, Atmospheric Correction Algorithm for SeaWiFS, *Remote Sensing of Environment*, *50*, 231–239, 1994b.

Wang, M. and H. R. Gordon, Estimating aerosol optical properties over the oceans with the multiangle imaging spectroradiometer: Some preliminary studies, *Applied Optics*, *33*, 4042–4057, 1994c.

Whitlock, C. H., D. S. Bartlett and E. A. Gurganus, Sea Foam Reflectance and Influence on Optimum Wavelength for Remote Sensing of Ocean Aerosols, *Geophys. Res. Lett.*, *7*, 719–722, 1982.

Appendix 2

Effects of stratospheric aerosols and thin cirrus clouds on atmospheric correction of ocean color imagery: Simulations

Howard R. Gordon, Tianming Zhang, Fan He, and Kuiyuan Ding
University of Miami
Department of Physics
Coral Gables, FL 33124

(Submitted for publication in *Applied Optics*)

Abstract

Using simulations, we determine the influence of stratospheric aerosol and thin cirrus clouds on the performance of the proposed atmospheric correction algorithm for the MODerate resolution Imaging Spectroradiometer (MODIS) data over the oceans. Further, we investigate the possibility of using the radiance exiting the top of the atmosphere in the 1.38 μm water vapor absorption band to remove their effects prior to application of the algorithm. The computations suggest that for moderate optical thicknesses in the stratosphere, i.e., $\tau_s \lesssim 0.15$, the stratospheric aerosol/cirrus cloud contamination does not seriously degrade the MODIS except for the combination of large ($\sim 60°$) solar zenith angles and large ($\sim 45°$) viewing angles, for which multiple scattering effects can be expected to be particularly severe. The performance of a hierarchy of stratospheric aerosol/cirrus cloud removal procedures for employing the 1.38 μm water vapor absorption band to correct for stratospheric aerosol/cirrus clouds, ranging from simply subtracting the reflectance at 1.38 μm from that in the visible bands, to assuming that their optical properties are known and carrying out multiple scattering computations of their effect using the 1.38 μm reflectance-derived concentration, are studied for stratospheric aerosol optical thicknesses at 865 nm as large as 0.15 and cirrus cloud optical thicknesses at 865 nm as large as 1.0. Typically, those procedures requiring the most knowledge concerning the aerosol optical properties (and also the most complex) performed the best; however, for $\tau_s \lesssim 0.15$ their performance is usually not significantly better than applying the simplest correction procedure. A semi-empirical algorithm is presented that enables accurate correction for thin cirrus clouds with τ_s as large as unity. Application of this correction requires an estimate of the stratospheric aerosol optical properties, and given these, implementation of the algorithm using a set of lookup tables appears to be straightforward.

1. Introduction

The radiance exiting the ocean-atmosphere system contains information on the concentration of marine phytoplankton — the first link in the marine food chain — through the variations they produce in the color of the water.[1] The flight of the Coastal Zone Color Scanner (CZCS)[2,3] was a proof-of-concept mission to demonstrate the feasibility of quantitatively estimating the concentration of chlorophyll a, a photosynthetic pigment contained in phytoplankton and used as a surrogate for their concentration. Based on the success of the CZCS, a number of instruments for ocean color measurements will be launched in the 1990's, e.g., the Sea-viewing Wide Field-of-view Sensor (SeaWiFS)[4] and the MODerate resolution Imaging Spectroradiometer (MODIS).[5]

The contribution from beneath the sea surface to the radiance exiting the ocean-atmosphere system in the visible is very small, i.e., at most 10-20% of the total in the blue and less at longer wavelengths. The remainder of the radiance is due to scattering from the atmosphere and reflection from the sea surface. Thus, it is of the utmost importance to remove these interfering effects in order to isolate the water-leaving radiance that contains the information regarding phytoplankton. This process is termed atmospheric correction. The CZCS atmospheric correction algorithm,[6] which was based on the single scattering approximation, was not sufficiently accurate to be applied to SeaWiFS and MODIS because they have far better radiometric sensitivity. Gordon and Wang[7] developed a multiple-scattering correction algorithm suitable for use with these sensors. The algorithm assumes that all of the aerosol in the atmosphere is in the marine boundary layer (MBL) and uses aerosol models to deal with the multiple scattering. The requirement for aerosol models stems from the fact that the magnitude of the multiple-scattering effects is model dependent.

In some situations, e.g., following volcanic eruptions or when there are thin cirrus clouds present, there can be significant quantities of aerosol in the stratosphere. Although Gordon and Castaño[8] showed that the presence of the El Chichón aerosol[9] had little effect on CZCS atmospheric correction, at the higher correction accuracy required for SeaWiFS and MODIS the Gordon and Wang[7] algorithm may be degraded by the presence of stratospheric aerosol. In the case of SeaWiFS, influence of the stratospheric aerosol on the absorption by the O_2 A-band at 762 nm introduces an additional complication. This has been discussed in detail by Ding and Gordon[10] and, as there is no direct way of assessing the presence of stratospheric aerosol with SeaWiFS, we shall not discuss that sensor further here. In contrast, MODIS, which avoids the O_2 A-band, is equipped with a spectral band at 1.38 μm that can be used to assess the contamination by stratospheric aerosol.

This spectral band is centered on a strong water vapor absorption band and photons penetrating through the stratosphere will usually be absorbed by water vapor in the free troposphere.[11] Thus, any radiance measured at 1.38 μm can, in the first approximation, be assumed to be scattered by the stratospheric aerosol alone. This provides a mechanism for estimating the stratospheric contribution. In this paper we assess the degradation in atmospheric correction of MODIS resulting from the presence of stratospheric aerosols. We assume that the radiance measured at 1.38 μm is totally due to the stratosphere and examine several possibilities for using this information in the proposed atmospheric correction algorithm[7] to correct ocean color imagery.

2. The proposed SeaWiFS-MODIS atmospheric correction algorithm

The Gordon and Wang[7] atmospheric correction algorithm uses the reflectance ρ rather than the radiance L. They are related by $\rho = \pi L / F_0 \cos\theta_0$, where F_0 is the extraterrestrial solar irradiance, and θ_0 is the solar zenith angle. In the absence of stratospheric aerosol, the total reflectance of the ocean-atmosphere system, $\rho_t(\lambda)$, measured at a wavelength λ, can be decomposed as follows:

$$\rho_t(\lambda) = \rho_r(\lambda) + \rho_a(\lambda) + \rho_{ra}(\lambda) + t(\theta_v, \lambda)\rho_w(\lambda),$$

where $\rho_r(\lambda)$ is the radiance resulting from multiple scattering by air molecules (Rayleigh scattering) in the absence of aerosols, $\rho_a(\lambda)$ is the radiance resulting from multiple scattering by aerosols in the absence of the air, and $\rho_{ra}(\lambda)$ is the interaction term between molecular and aerosol scattering.[12] In this equation, t is the diffuse transmittance of the atmosphere along the viewing direction specified by θ_v, the angle between the normal to the sea surface and the sensor.[13] Radiance arising from specular reflection of direct sunlight from the sea surface (sun glitter) has been ignored. This means that the correction cannot be valid near the glitter pattern. The influence of whitecaps has also been ignored under the assumption that their contribution can be removed, prior to application of the correction algorithm, using an estimate of the surface wind speed.[14]

The goal of the atmospheric correction is the retrieval of ρ_w from ρ_t. This is effected by measuring ρ_t in the near infrared (NIR) near 765 and 865 nm for SeaWiFS and 750 and 865 nm for MODIS. In this spectral region, the ρ_w can be taken to be zero because of the strong absorption by the water itself. ρ_r can be computed given an estimate of the atmospheric pressure, so $\rho_a + \rho_{ra}$ can be determined directly in the NIR. From a set of candidate aerosol models, the spectral variation of $\rho_a + \rho_{ra}$ in the NIR is used to select a pair of aerosol models for accounting for

multiple scattering and for determining the spectral dependence of $\rho_a + \rho_{ra}$ for extrapolation into the visible, thus providing ρ_w there.[7] In the absence of stratospheric aerosol, simulations suggest that this algorithm will meet the goal of retrieval of ρ_w at 443 nm with an error $\lesssim$ 0.001–0.002, i.e., an error of $\lesssim$ 5% in ρ_w in the blue in very clear ocean water.

Incorporation of multiple scattering is effected through the use of lookup tables based on a large number (~33,000) radiative transfer simulations using various aerosol models[15] thought to be representative of aerosols occurring over the oceans. In the simulations it was assumed that all of the aerosol is resident in the MBL, i.e., the simulations were carried out using an accurate (error $\lesssim$ 0.1%) two-layer radiative transfer code with aerosols occupying the lower layer and molecular (Rayleigh) scattering occupying the upper layer. This vertical structure is similar to that normally found over the oceans, i.e., typically most of the aerosol is in the MBL.[16]

3. Simulation of the effects of stratospheric aerosol

In situations where there is significant stratospheric aerosol present, the aerosol vertical profile described in Section 2 is very unrealistic. A more realistic profile would be a three-layer atmosphere with aerosol in both the lower and upper layers and molecular scattering in the central layer. This is the profile that we adopt for simulating ρ_t in the presence of stratospheric aerosol.

We examine three different stratospheric aerosol models. The first is the background stratospheric aerosol[17] consisting of a 75% solution of H_2SO_4 with a size distribution given by

$$\frac{dn}{dD} = 81 D \exp(-9\,D),$$

where dn is the number of particles per unit volume with diameters (D) in μm between D and $D + dD$. The second is the El Chichon aerosol,[9] also a 75% solution of H_2SO_4, with a size distribution:

$$\frac{dn}{dD} = 1.79386 \times 10^8\, D^{12.65} \exp(-19.65\,D).$$

The third represents aged volcanic ash. It consists of an absorbing mineral distributed in size according to

$$\frac{dn}{dD} = 1365.33\, D \exp(-11.3137\sqrt{D})$$

with a wavelength-independent index of refraction $m = 1.50 - 0.008i$. For the background and the El Chichon aerosol, the index of refraction is taken from Palmer and Williams.[18] The final aerosol

model is that for thin cirrus clouds taken from Takano and Liou.[19] In this case we assume that the scattering properties of the thin cirrus are independent of wavelength. The scattering phase functions for these four models are presented in Figures 1a through 1d, and the spectral variation in their extinction (or stratospheric optical thickness, τ_a) is presented in Figure 2. The first three were calculated from the size distributions and the refractive indices using Mie theory. The fourth was taken from the tabulated values of Ref. 19. Note the significant spectral variation of the shape of some of the aerosol phase functions.

As suggested above, we simulated the reflectance in the presence of stratospheric aerosol using a three-layer radiative transfer code. The lower layer contained the Shettle and Fenn[15] Maritime aerosol at 80% relative humidity (M80). This was used as the MBL aerosol because, in the absence of stratospheric aerosol, the performance of the atmospheric correction algorithm is excellent (error in ρ_w found by Gordon and Wang[7] was less than about 0.0005 for this aerosol) and, thus, provides an ideal choice for examination of the interfering effects of the stratospheric aerosol. The upper layer contains the stratospheric aerosol and the middle layer exhibits only molecular scattering. A Fresnel-reflecting flat sea surface constitutes the lower boundary. There is no radiance exiting the ocean, i.e., all photons penetrating the sea surface are absorbed. In the case of MODIS, to simulate the reflectance at 1380 nm, a one-layer model with a totally absorbing lower boundary (no Fresnel reflection) was employed. The rational for this is the assumption that all radiation penetrating through the stratosphere at this wavelength is absorbed by water vapor in the troposphere, so no radiance is reflected to the top of the atmosphere from below the stratospheric layer. Note that for the purpose of utilizing the 1380 nm MODIS band to correct for the stratospheric aerosol, this is the ideal setting, i.e., all of the reflected radiance at 1380 nm is due to the stratosphere, there is no contamination from Rayleigh scattering in the free troposphere (middle layer), aerosol scattering in the MBL (lower layer), or reflection from the sea surface.

4. Impact of stratospheric aerosol on atmospheric correction

As described earlier, we simulated $\rho_t^{(a)}$ at 443, 765, 865, and 1380 nm using a three-layer model of the atmosphere. The upper layer used the four stratospheric aerosol models with stratospheric optical thickness $\tau_a = 0.05$ and 0.15 at 865 nm. A Maritime aerosol (M80) with MBL optical thickness $\tau_b = 0.15$ and 0.30 was placed in the lowest layer. There was no aerosol (only Rayleigh scattering) in the middle layer. Seven geometries were simulated: near-nadir viewing ($\theta_v \approx 0$) and viewing near the scan edge ($\theta_v \approx 45°$) in the perpendicular plane, both for solar zenith angles

of 0, 20°, 40°, and 60°. $\theta_0 = 0$ and $\theta_v \approx 0$ was not examined as it would be at the center of the sun's glitter pattern. For the Background, Aged Volcanic Ash, and El Chichón aerosols, the computations were performed using a successive-order-of-scattering radiative transfer code.[20] In the case of the cirrus cloud model, a Monte Carlo code was used because the presence of considerable angular structure in the scattering phase function (Figure 1) would have required computation of too many Fourier coefficients in the azimuthal decomposition of the radiance in the successive-order-of-scattering code to provide a reliable simulation.

The simulated values of $\rho_t^{(s)}$ at 443, 765, and 865 were then inserted into the Gordon and Wang[7] atmospheric correction algorithm to retrieve $t\rho_w(\lambda)$, the water-leaving radiance transmitted to the top of the atmosphere. The reflectance at 1380 nm was not used and the presence of the stratospheric aerosol was simply ignored. The results of these simulations are presented in Figure 3 for the various combinations of τ_s, τ_a, and stratospheric aerosol model. In the figure we present histograms of the error for each stratospheric model. The taller bars in Figure 3 represent the maximum value of $|\Delta[t\rho_w(\lambda)]|$ for $\lambda = 443$ nm for the seven combinations of angles. Typically, this occurs at the scan edge with $\theta_0 = 60°$, i.e., at the position where multiple scattering is expected to be most severe. The shorter bars in the histogram represent the average of $|\Delta[t\rho_w(\lambda)]|$ for $\lambda = 443$ nm over the remaining six combinations of angles. The horizontal dashed line is the upper limit of the acceptable error, i.e., 0.002. Figure 3 clearly shows that, even at small values of τ_s, stratospheric aerosols can degrade the performance of the atmospheric correction algorithm, particularly in geometries where multiple scattering is expected to be large.

These results are based on simulations assuming τ_s at 865 to be either 0.05 or 0.15 for all of the stratospheric aerosol models. Is this a realistic range? For background conditions in the stratosphere the optical thickness at 1000 nm from the Stratospheric Aerosol and Gas Experiment (SAGE) solar occultation data is typically $\lesssim 0.01$, while following a major volcanic eruption and subsequent global dispersal of the aerosol, e.g., El Chichón or Pinatubo, $\tau_s \sim 0.10$ at ~ 1000 nm (L. Thomason, NASA/LaRC, personal communication). Thus, in the case of the Background aerosol model, τ_s at 865 nm is too high by at least a factor of 5, and one would expect the error shown in Figure 3 to be much too large. Because of its low τ_s, the error due to the Background stratospheric aerosol will be negligible, and we shall not consider it further. In contrast, the values of τ_s used for the El Chichón and Aged Volcanic Ash models are in the appropriate range, and Figure 3 should be representative of the performance of the algorithm[7] in the presence of aerosols with these properties. Clearly the

Aged Volcanic Ash causes the greater degradation in atmospheric correction, presumably due to its higher absorption. Also, it should be noted that optical thickness (τ_b) in the MBL at 865 nm rarely exceeds 0.2 in the absence of aerosol transported from deserts and/or anthropogenic aerosol sources.[21] Therefore, of the situations presented here, the most likely are those with $\tau_b(865) = 0.15$, i.e., panels *a* and *b* in Figure 3. With these observations in mind, we conclude that typically the error in atmospheric correction due to volcanically-produced sulfate stratospheric aerosol should be ~ 0.002 except near the scan edge at high solar zenith angles, while for Aged Volcanic Ash the error is expected to be significantly larger at the same τ_s. Thus, if no correction were made for the presence of stratospheric aerosol, in the case of Aged Volcanic Ash one would have to wait for some of the ash to be removed from the atmosphere before an adequate atmospheric correction could be made. The observation, that simply ignoring the stratospheric aerosol provides a reasonable correction for small τ_s, agrees with the conclusion of Gordon and Castaño[8] that the presence of the El Chichón aerosol had little effect on CZCS atmospheric correction, taking into consideration that CZCS did not require as accurate a correction.

In the case of cirrus clouds, we do not know the appropriate range of τ_s. Thus, we carried out additional simulations for $\tau_s = 0.5$ and 1.0. The results for all of the cirrus cloud simulations are presented in Figure 4. They show a consistent pattern of increasing error as τ_s increases, with the average error in atmospheric correction exceeding the goal (± 0.002) for τ_s between 0.15 and 0.50.

5. Requirements for precise correction for stratospheric aerosols

Before discussing our efforts to remove the effects of stratospheric aerosols using the 1380 nm band, it is useful to determine what would be required for a precise correction for stratospheric aerosols.

The most direct way of understanding the effects of adding stratospheric aerosol is to consider the adding or matrix operator method of solution of the radiative transfer equation (RTE). We first Fourier analyze the radiance field in the azimuthal direction, i.e.,

$$L(\tau, \theta_v, \phi_v) = L^{(0)}(\tau, \theta_v) + 2 \sum_{m=1}^{\infty} L^{(m)}(\tau, \theta_v) \cos m\phi_v,$$

where ϕ_v is the azimuth of propagation relative to the solar azimuth, and θ_v is the angle between the propagation direction and the vertical. Then, we assume that the radiance has been discretized into n upward and n downward streams, e.g., at the gaussian quadrature values of the angle θ_v.

Finally, following Plass Kattawar and Catchings,[22] we write a particular Fourier component of the downward radiance as a column vector

$$L^+(\tau) = \begin{pmatrix} L^+(\tau,\theta_1) \\ L^+(\tau,\theta_2) \\ \vdots \\ L^+(\tau,\theta_n) \end{pmatrix},$$

where θ_i are the polar angles for radiance in the downward direction, and τ is the optical depth. Similarly, a column vector $L^-(\tau)$ is composed of radiance propagating in the upward direction. Note that all of the equations that follow in this section refer to a single Fourier component $L^{(m)}(\tau)$ and all of the quantities in the equations should carry the superscript (m); however, to simplify the notation this superscript is suppressed.

Consider a layer from τ_0 to τ_1, and let $S^{\pm}(\tau_1,\tau_0)$ represent the exiting boundary radiances at τ_0 $(-)$ and τ_1 $(+)$ due to sources between τ_0 and τ_1, e.g., the unscattered solar beam. Then the boundary radiances exiting the layer, $L^+(\tau_1)$ and $L^-(\tau_0)$ can be written in terms of the entering boundary radiances $L^+(\tau_0)$ and $L^-(\tau_1)$ according to

$$L_1^+ = t_{01}L_0^+ + r_{10}L_1^- + S_{01}^+$$
$$L_0^- = r_{01}L_0^+ + t_{10}L_1^- + S_{01}^-,$$

where $L_1^+ \equiv L^+(\tau_1)$, etc. The $n \times n$ matrices r_{10}, r_{01}, t_{10}, and t_{01} describe the transmittance and reflectance of any radiance that is incident on the layer. If the layer is homogeneous, $r_{10} = r_{01}$ and $t_{10} = t_{01}$. If we write similar equations for a layer from τ_1 to τ_2, and for the combined layer from τ_0 to τ_2, it is found that the r's, t's, and S's for the combined layers can be determined from those of the individual layers.

In the problem of interest here, we take τ_0 to τ_1 to represent the stratospheric layer, and τ_1 to τ_2 to represent everything else, i.e., the troposphere, sea surface, and the body of the ocean. Consider the stratosphere alone. If the only source is the solar beam, which produces S_{01}^-, then the radiance exiting the TOA is just $L_0^- = S_{01}^-$. Now consider the second layer alone. Again, if the solar beam is the only source, $L_1^- = S_{12}^-$. In order to operate the Gordon and Wang[7] algorithm, we require S_{12}^-, the radiance that the atmosphere-ocean system would have reflected were the stratosphere absent.

Combining the two layers and using the adding algorithm,[22] we find

$$S_{02}^- = S_{01}^- + t_{10}(E - r_{12}r_{10})^{-1}(S_{12}^- + r_{12}S_{01}^+),$$

where E is the identity matrix. This can be solved for S_{12}^- yielding

$$S_{12}^- = (E - r_{12}r_{10})\, t_{10}^{-1}\, (S_{02}^- - S_{01}^-) - r_{12}S_{01}^+.$$

However, because the stratospheric layer is in place, the solar beam illuminating the second layer must be reduced by a factor $\exp[-(\tau_1 - \tau_0)/\mu_0]$, where $\mu_0 = \cos\theta_0$, so S_{12}^- in these equations must be replaced by $S_{12}^- \exp[-(\tau_1 - \tau_0)/\mu_0]$. Thus, the desired radiance is

$$S_{12}^- = \exp[+\tau_s/\mu_0]\left[(E - r_{12}r_{10})\, t_{10}^{-1}\, (S_{02}^- - S_{01}^-) - r_{12}S_{01}^+\right], \tag{1}$$

where τ_s is the stratospheric optical thickness. Note that all of the quantities in this equation are functions of wavelength λ, and all quantities except τ_s refer to the m^{th} Fourier component. The desired reflectance in the viewing direction, specified by (θ_v, ϕ_v), is just $\rho_t = \pi S_{12}^-(\tau_1, \theta_v, \phi_v)/\mu_0 F_0$, where

$$S_{12}^-(\tau_1, \theta_v, \phi_v) = S_{12}^{-(0)}(\tau_1, \theta_v) + 2\sum_{m=1}^{\infty} S_{12}^{-(m)}(\tau_1, \theta_v)\cos m\phi_v,$$

and $\tau_1 = \tau_s$. Note that this requires only a single row of the matrices $(E - r_{12}r_{10})\, t_{10}^{-1}$ and r_{12}.

This equation delineates the quantities needed in order to retrieve $\rho_t(\lambda)$ from the TOA reflectance in the presence of stratospheric aerosol. Can we have enough information to retrieve ρ_t? Measurement of the TOA radiance in the visible and NIR provides the quantity S_{02}^- at any wavelength λ, but only in the viewing direction. As it is assumed that the TOA radiance at 1380 nm is due entirely to the stratosphere, this will provide S_{01}^- at 1380 nm, but again, only the component in the viewing direction. If we had a model of the stratospheric aerosol, S_{01}^- at 1380 nm in the viewing direction could be used to estimate τ_s at 1380 nm. Then τ_s at 1380 nm and the aerosol model could be used to determine the full matrices S_{01}^-, S_{01}^+, r_{10}, and t_{10} at any wavelength.

Unfortunately, even with full knowledge of the optics of the stratosphere, neither the operator r_{12}, the radiance reflectance matrix for the troposphere, sea surface, and ocean, nor the full column vector S_{02}^-, can be determined with precision as they depend on the (unknown) tropospheric aerosol properties and the (unknown) concentration, as well as the properties of the ocean. One could use standard models to estimate r_{12} to within a multiplicative constant; however, this constant would depend on the tropospheric aerosol concentration. Thus, it appears impossible to estimate r_{12}. If this is set to zero, single and multiple reflection interactions between the stratosphere and troposphere are neglected.

6. Simplified procedures for correcting for stratospheric aerosol

As it is clear that a precise value of ρ_t cannot be derived based on the available information, we now examine several simplified procedures for correction for the presence of stratospheric aerosol. In the limit that $\tau_s \rightarrow 0$, we expect

$$T\rho_t = \rho_t^{(s)} - \delta\rho_t^{(s)}, \tag{2}$$

where $\rho_t^{(s)}$ is the reflectance of the entire ocean-atmosphere system in the presence of stratospheric aerosol, T is a "transmittance" factor that indicates the reduction in ρ_t due to the presence of the layer, and $\delta\rho_t^{(s)}$ is the reflectance added by the layer. As we expect the stratospheric perturbation to be small,[8] our strategy for MODIS is to try to estimate $\delta\rho_t^{(s)}$ and remove it from $\rho_t^{(s)}$ for an estimate of $T\rho_t$. T would then be estimated, and the existing atmospheric correction algorithm[7] operated with the resulting ρ_t as the ocean-atmosphere reflectance. In this manner the existing algorithm will be used in the setting for which it was developed: a two-layer atmosphere (the effects of the third layer having been removed) with all of the aerosol in the lower layer. Thus, the goal is to be able to remove as much of $\delta\rho_t^{(s)}$ from $\rho_t^{(s)}$ as possible.

Using the $\rho_t^{(s)}(\lambda)$ pseudo data described in Section 4, we examined atmospheric correction for MODIS. We considered six possibilities for utilizing the 1380 nm band for correction for stratospheric aerosols. As described in Section 3, we assumed that the reflectance at 1380 nm was totally due to the stratospheric aerosol. The six correction schemes for removal of the stratospheric aerosol component follow.

1. The "measured" reflectances at 443, 765 and 865 nm was used in the Gordon and Wang algorithm as usual, i.e., no attention was paid to the fact that a stratospheric aerosol may be present [$\rho_t^{(s)}(\lambda)$ was assumed to be $\rho_t(\lambda)$], and the error in the atmospheric correction at 443 nm was determined. This is identical to the procedure used to generate the results provided in Figures 3 and 4.

2. The presence of stratospheric aerosol was incorporated into the algorithm by simply subtracting the reflectance at 1380 nm from those at 443, 765, and 865, i.e., $T(\lambda)\rho_t(\lambda) = \rho_t^{(s)}(\lambda) - \rho_t^{(s)}(1380)$. The values of $\rho_t(\lambda)$ were then inserted into the correction algorithm and the error in the correction at 443 nm was determined.

3. It was assumed that the spectral variation of the optical thickness of the stratospheric aerosol is known, e.g., from measurements from the surface. The reflectance at 1380 nm (due entirely to the stratospheric aerosol) was scaled by the ratio of the stratospheric optical depth at the given λ, $\tau_s(\lambda)$, to that at (or in the case of surface measurements, near) 1380 nm, and subtracted from the measured reflectances at the other wavelengths, i.e.,

$$T(\lambda)\rho_t(\lambda) = \rho_t^{(s)}(\lambda) - \frac{\tau_s(\lambda)}{\tau_s(1380)}\rho_t^{(s)}(1380)$$

The values of $\rho_t(\lambda)$ were then inserted into the correction algorithm and the error in the correction at 443 nm determined.

4. It was assumed that accurate measurements or predictions of the other optical properties of the stratospheric aerosol, the spectral scattering phase function and single scattering albedo, along with the spectral variation of the optical depth are available for the stratospheric aerosol, e.g., from inversions of $\tau_s(\lambda)$ measurements made at the surface to obtain the size distribution from which the other optical properties are computed.[9] Only the stratospheric aerosol concentration was assumed to be unknown. It is estimated based on the measurement of $\rho_t^{(s)}(1380)$. The reflectance at 1380 nm was then scaled, by the ratio of the single-scattered stratospheric aerosol reflectances at λ to that at 1380 nm, and subtracted from the reflectances in the visible and NIR, i.e.,

$$T(\lambda)\rho_t(\lambda) = \rho_t^{(s)}(\lambda) - \frac{\omega_s(\lambda)\tau_s(\lambda)p_s(\theta_v,\phi_v;\theta_0,\phi_0;\lambda)}{\omega_s(1380)\tau_s(1380)p_s(\theta_v,\phi_v;\theta_0,\phi_0;1380)}\rho_t^{(s)}(1380),$$

where

$$p_s(\theta_v,\phi_v;\theta_0,\phi_0;\lambda) = P_s(\theta_-,\lambda) + \Big(r(\theta_v) + r(\theta_0)\Big)P_s(\theta_+,\lambda),$$

$$\cos\theta_\pm = \pm\cos\theta_0\cos\theta_v - \sin\theta_0\sin\theta_v\cos(\phi_v - \phi_0),$$

and $r(\alpha)$ is the Fresnel reflectance of the interface for an incident angle α. The parameters $\tau_s(\lambda)$, $\omega_s(\lambda)$, and $P_s(\alpha,\lambda)$ are, respectively, the stratospheric aerosol optical thickness, single scattering albedo, and scattering phase function for a scattering angle α. The angles θ_0 and ϕ_0 are, respectively, the zenith and azimuth angles of a vector from the point on the sea surface under examination (pixel) to the sun, and likewise, θ_v and ϕ_v are the zenith and azimuth angles of a vector from

the pixel to the sensor. These are measured with respect to the *upward* normal so θ_v and θ_0 are both less than 90°. At 1380 nm, $r(\alpha)$ was set to zero since the radiation at this wavelength cannot interact with the surface. The resulting values of $\rho_t(\lambda)$ were then inserted into the correction algorithm and the error at 443 nm was determined. This procedure is based on the assumption that the stratospheric aerosol enhancement of ρ_t is all due to single scattering.

5. As in (4) it was assumed that all of the optical properties of the aerosol are known except the concentration. A one-layer multiple scattering code (with a totally absorbing lower surface to represent the troposphere) was used to determine $\tau_s(1380)$ from $\rho_t^{(s)}(1380)$. This determines all of the optical properties of the stratospheric aerosol. These properties were inserted into a one-layer multiple scattering code (with a Fresnel-reflecting sea surface as the lower boundary) to compute $\delta\rho_t^{(s)}(\lambda)$, which was subtracted from the measured reflectances $\rho_t^{(s)}(\lambda)$ to provide $T(\lambda)\rho_t(\lambda)$. The resulting values of $\rho_t(\lambda)$ were then inserted into the correction algorithm and the error at 443 nm was determined. This procedure is similar to that in procedure 4; however, the single-scattering approximation was replaced by a full multiple-scattering computation. It is based on the assumption that there is *no radiative interaction* between the stratospheric aerosol layer and the other two layers in the visible.

6. Except for the step in which $\delta\rho_t^{(s)}(\lambda)$ is removed from $\rho_t(\lambda)$, this is identical to procedure 5. Once all of the optical properties of the stratospheric aerosol are known, they were inserted into a *two-layer* multiple scattering code (as opposed to a *one-layer* code in procedure 5 above) with a Fresnel-reflecting sea surface as the lower boundary. The top layer consisted of the stratospheric aerosol and the lower layer had only Rayleigh scattering. This incorporated the Rayleigh-stratospheric aerosol interaction explicitly (albeit approximately because of the absence of the tropospheric aerosol), leaving only the Rayleigh-tropospheric aerosol and stratospheric-tropospheric aerosol interactions not addressed. After subtracting the result of this computation from $\rho_t^{(s)}(\lambda)$, the result was inserted into the standard correction algorithm in which allowance was made for the fact that $\rho_r(\lambda)$ has already been removed along with the stratospheric component. This approach is

possible because the optical properties of the Rayleigh scattering layer as well as the stratospheric aerosol layer are completely known.

These approaches clearly require increasing amounts of knowledge concerning the optical properties of the stratospheric aerosol and increasing computational complexity. Although knowledge of the stratospheric aerosol optical properties may be good in certain instances, e.g., the El Chichon aerosol,[9] in general such will not be available.

7. Results for the simplified procedures

The procedures listed in Section 6 were all designed to utilize $\rho_t^{(s)}$ at 1380 nm to remove the stratospheric contribution to ρ_t. With the exception of the first, they all require an estimate of the transmittance factor T. Unfortunately, because of the nature of the approximations in passing from Eq. (1) to Eq. (2), there is no *a priori* way to determine the appropriate T in a multiple scattering regime. Initially, we assumed $T = 1$, which would be appropriate in the single scattering regime.

Examination of results the individual cases revealed the following for most of the correction procedures: (1) for a given stratospheric aerosol model, the largest values of $\Delta[t\rho_w(443)]$, the resulting error in $t\rho_w$ at 443 nm, occur at the scan edge with $\theta_0 = 60°$ where one would expect the largest effect of multiple scattering; (2) for a given θ_0, the error for viewing at the scan center is usually less than the error at the scan edge; (3) the correction errors are usually negative (too much radiance has been assigned to the atmosphere) with the Aged Volcanic Ash aerosol more negative than the others, presumably due to its moderate absorption; and (4) the general patterns of the correction error as a function of θ_0 at the scan center and edge for a given model remain the same as τ_b and τ_s are varied, but patterns for different stratospheric models are not similar. As might be expected, the most complex methods of dealing with the stratospheric aerosol (procedures 5 and 6 in Section 6) usually yielded the best overall correction, however, as long as $\tau_s \leq 0.05$, most of the procedures produced acceptable results (except at the scan edge with $\theta_0 = 60°$). In the case of large optical thicknesses for cirrus clouds, the error became excessive with none of the procedures producing satisfactory results.

To try to improve the retrieval of $t\rho_w$, we decided to attempt to model T. In the first model we assumed that most of the radiance being scattered by the stratospheric layer is scattered through small angles (Figure 1 shows that this is certainly true for cirrus clouds). This being the case, the

contribution of the downward path through the stratosphere to T is just the *irradiance* (or flux) transmittance, which is identical to the diffuse transmittance $t(\theta_0)$. We then argued that the upward radiance distribution can be approximated as diffuse (albeit poorly), hence its traverse through the stratosphere is also described by the diffuse transmittance. Thus, $T(\theta_0, \theta_v) \approx t(\theta_0)t(\theta_v)$. This assumption for T led to large positive errors in the water-leaving reflectance, which suggested that T was reduced too far from unity. However, the pattern of the error did suggest that a better result would be obtained with $T(\theta_0, \theta_v) \approx t(\theta_0)$. This in fact worked fairly well, and a sample of the results using this approximation for T are provided in Figures 5 and 6 for $\tau_b = 0.15$. As with Figures 3 and 4, in these figures we present histograms of the error as a function of the stratospheric aerosol removal procedure (procedures 1–6). Along the horizontal axes "No C." refers to procedure 1, "Cons." to procedure 2, "τ_a" to procedure 3, "Sing." to procedure 4, "3L–R–S" to procedure 5, "3L–(R+S)" to procedure 6, and "2L–R" to the correction algorithm in the absence of stratospheric aerosol. The taller bars in these figures represent the maximum value of $|\Delta[t\rho_w(\lambda)]|$ for $\lambda = 443$ nm for the seven combinations of angles. Typically, this occurs at the scan edge with $\theta_0 = 60°$. The shorter bars in the histogram represent the average of $|\Delta[t\rho_w(\lambda)]|$ for $\lambda = 443$ nm over the remaining six combinations of angles. The horizontal dashed line is the upper limit of the acceptable error, i.e., 0.002. The results show that, with the exception of the scan edge at $\theta_0 = 60°$, at least one of the procedures will usually produce a mean absolute error < 0.002.

8. A semi-empirical approach for correcting for stratospheric aerosols

To derive the results provided in Figure 5 and 6 (except for procedure 1) it was necessary to have a model of the aerosol for the computation of the diffuse transmittance T. Detailed stratospheric aerosol models are also required to provide $\delta\rho^{(a)}(\lambda)$ for the operation of procedures 4, 5, and 6. Thus, it is reasonable to use these models to estimate the *exact* value of T to use with each geometry and model. If the exact value of T does not depend too strongly on τ_b or on the aerosol properties in the troposphere, then tables of T could be used to effect a better correction for stratospheric aerosols. As the required value of T depends on the procedure used to correct for the stratosphere, one procedure must be selected. For this purpose, procedure 5 appears to be the best for three reasons. First, for cirrus clouds, which are expected to contaminate more of the imagery than volcanically-produced stratospheric aerosol, procedure 5 reduces to the very simple procedure 2 since the optical properties are assumed to be independent of wavelength. Next, in contrast to procedure 6, procedure 5 requires no modification to the Gordon and Wang[7] algorithm. Finally,

procedure 2 assumes that the optical properties of the aerosol at λ are the same as at 1380 nm, which is only reasonable for cirrus clouds. Thus, we use procedure 5 (which includes all significant orders of multiple scattering in the stratospheric layer) for the computation of T; however, to make it reduce to procedure 2 for wavelength-independent aerosol, we modified the computation of the $\delta\rho^{(s)}$ so that there was no contribution from the sea surface at any wavelength, i.e., as a single layer above a totally absorbing surface. Figure 7 provides the resulting value of T as a function of the value of the reflectance at 1380 nm.

At 443 nm (Figure 7a) it is seen that, for cirrus clouds, $T < 1$ and is remarkably insensitive to τ_b. In contrast, for 765 and 865 nm (Figures 7b and 7c) $T > 1$ and is strongly dependent on τ_b. This indicates that in the NIR, multiple reflections between the stratosphere and the troposphere are very important. Multiple reflections must also be important in the visible, although their effects are apparently negated, possibly due to the strong limb brightening associated with multiple Rayleigh scattering compared to that of aerosols. Also, the insensitivity of T to variation in τ_b in the blue reflects the fact that most of S_{12}^- there is the result of Rayleigh scattering not MBL aerosol. Similar effects are seen for the El Chichón and Aged Volcanic Ash aerosols models; however, the required values of T are strongly dependent on the stratospheric aerosol model.

The systematic variation of T with $\rho_t^{(s)}(1380)$ seen in Figure 7 suggests that the measured value of $\rho_t^{(s)}(1380)$ could be used to estimate the proper value of T given the appropriate stratospheric aerosol model. We have tried to utilize this to make a better correction for stratospheric aerosols. As mentioned above, cirrus clouds are expected to contaminate more of the imagery than volcanically-produced stratospheric aerosol, thus, it is natural to employ the cirrus cloud model to estimate the value of T given $\rho_t^{(s)}(1380)$. To effect the correction, we used the cirrus cloud model to compute the required values of T, producing figures similar to Figure 7 for each of the seven combinations of θ_0 and θ_v. For each geometry, T was then fit by least squares to a parabola in $\rho_t^{(s)}(1380)$ by pooling the results for $\tau_b = 0.15$ and 0.30. If T were to fit $\rho_t^{(s)}(1380)$ exactly, then when the stratospheric aerosol actually is cirrus clouds and they are removed using T determined from $\rho_t^{(s)}(1380)$, and the atmospheric correction algorithm is operated using the retrieved ρ_t as the input reflectance, the resulting error in $t\rho_w$ would be that shown in Figure 4 in the absence of stratospheric aerosol (MBL). However, it is clear from Figure 7 that the fit cannot be exact, so there will be some residual error in $t\rho_w$. In Figure 8 we show the residual error in $t\rho_w$ when this procedure is applied to the cirrus cloud pseudo data as before. Clearly, the residual error is significantly smaller than that shown in

Figure 6 for the 6 simple procedures in Section 6, and corrections appear possible even for large τ_s. Figure 9 shows the residual error when this procedure is applied to pseudo data created with the El Chichón and Aged Volcanic Ash aerosol in the stratosphere. Clearly, the results are poorer than for cirrus clouds, and are also poorer than those in Figure 5 for the simplified procedures. Thus, it appears that if this method is to be used to correct for stratospheric aerosols, separate T versus $\rho_t^{(s)}(1380)$ relationships would need to be used for volcanically-derived stratospheric aerosols and for cirrus clouds.

In all of the simulations thus far, we have used the M80 aerosol model to represent the aerosol in the MBL. As the T versus $\rho_t^{(s)}(1380)$ relationship depends on τ_b (in the NIR), we expect that it might also depend on the aerosol type in the MBL. To study this dependence, we carried out a series of simulations with the Shettle and Fenn[15] Tropospheric model at 80% relative humidity (T80) in the troposphere and cirrus clouds in the stratosphere. The scattering phase function for T80 shows much more scattering than M80 in the range of scattering angels from 40° to 140°, about the same for angles > 140° and significantly less at small scattering angles (see Ref. 23, Figure 4). Also, τ_b for T80 is a much stronger function of wavelength, with $\tau_b(443)/\tau_b(865) \approx 2.48$ compared to ≈ 1.16 for M80. This in itself makes atmospheric correction, even in the absence of stratospheric aerosols, more difficult for the T80 aerosol, given the same value of $\tau_b(865)$. The resulting T versus $\rho_t^{(s)}(1380)$ relationships are similar to those shown in Figure 7; however, for a given value of $\rho_t^{(s)}(1380)$, the required value of T in the NIR is often considerably different from that for M80, although the general pattern is the same. Interestingly, at 443 nm there is very little difference in the required value of T between T80 and M80, in agreement with Figure 7a which shows that T is nearly independent of τ_b in the blue. Clearly, if the T versus $\rho_t^{(s)}(1380)$ relationship generated for M80 is used when the actual aerosol in the MBL is T80, there will be significant error in stratospheric aerosol correction in the NIR, and after application of the Gordon and Wang algorithm, error in the retrieved $t\rho_w$. This is confirmed in Figure 10, which provides results similar to those in Figure 8, but for T80 in the MBL. Clearly, the results are not satisfactory, and they suggest that it is necessary to have some knowledge regarding the aerosol type in the MBL in order to improve on the correction.

We have examined the possibility of estimating the aerosol type in the MBL for the purpose of improving the correction, and it appears to be straightforward. Briefly, in the SeaWiFS atmospheric correction algorithm,[7] in the absence of stratospheric aerosol, the spectral variation of $\rho_t - \rho_r$

between 765 and 865 nm is used to estimate a parameter called ϵ. This quantity is then compared with the value for individual members of a set of candidate aerosol models to determine a pair of

Table 1. Value of the parameter ϵ for the 12 candidate MBL models used in the Gordon and Wang[7] correction algorithm. The ϵ values are at the scan edge for $\theta_0 = 60°$.

Model	RH (%)	ϵ
Maritime	50	1.079
Maritime	70	1.066
Maritime	90	1.020
Maritime	99	0.983
Coastal	50	1.115
Coastal	70	1.101
Coastal	90	1.049
Coastal	99	1.008
Tropospheric	50	1.207
Tropospheric	70	1.198
Tropospheric	90	1.153
Tropospheric	99	1.112

models that best fit the variation. These models are then used to assess the multiple scattering and to extrapolate the aerosol contribution into the visible. We have found that when the T versus $\rho_t^{(s)}(1380)$ relationship derived from the M80 model is used to correct for stratospheric aerosols with either T80 or M80 located in the MBL, and the resulting values of ρ_t are inserted into the Gordon and Wang algorithm, the derived values of ϵ are very near the correct values, i.e., based on the retrieved ϵ one would make a correct conclusion regarding which model (M80 or T80) is appropriate for the MBL. For example, in the geometry with the most multiple scattering, $\theta_0 = 60°$ at the scan edge, with T80 in the MBL and $\tau_b = 0.15$, the combination cirrus cloud/MBL algorithms produced ϵ values of 1.185, 1.183, 1.180, 1.165, and 1.158 for $\tau_s = 0$, 0.05, 0.15, 0.50, and 1.00, respectively. These values should be compared with the true values of ϵ in the same geometry for the twelve candidate aerosol models in the Gordon and Wang algorithm. These are provided in Table 1. It is seen that for each value of τ_s, the combined algorithm chooses a candidate aerosol model between the Tropospheric models at 70% and 90% relative humidity (RH) — exactly the position of T80 — even though the T versus $\rho_t^{(s)}(1380)$ relationship was based on M80 in the MBL! This implies that

it is feasible to estimate the aerosol type in the MBL even though an incorrect T versus $\rho_t^{(s)}(1380)$ relationship is used. Thus, we envisage a correction for thin cirrus clouds as follows. First, the T versus $\rho_t^{(s)}(1380)$ relationship for M80 is used to estimate ρ_t. Next ρ_t is used in the Gordon and Wang algorithm to estimate ϵ. Finally, this value of ϵ is used to provide a more appropriate model for estimating the T versus $\rho_t^{(s)}(1380)$ relationship to be used to derive a final set of values for ρ_t. Thus, there would be two passes through both the stratospheric correction algorithm and the Gordon and Wang algorithm, unless after the first pass it was decided that a second pass was not necessary, i.e., the retrieved ϵ was close to that for M80. If the aerosol model for the MBL is chosen judiciously, then much of the time only one pass through the combined algorithm would be necessary.

Based on our observations of the accuracy that ϵ could be estimated for T80 in the MBL using the M80 T versus $\rho_t^{(s)}(1380)$ relationship, we prepared Figure 11 which shows the overall error in atmospheric correction when the *correct* T80 T versus $\rho_t^{(s)}(1380)$ relationship (derived by pooling the $\tau_b = 0.15$ and 0.30 simulations) is used with T80 in the MBL. Clearly, accurate corrections in the presence of cirrus clouds would be possible with such an algorithm. It should be noted that further improvement on this procedure is possible, as the first pass through the algorithm could be used to estimate τ_b as well as the aerosol type. Thus, a T versus $\rho_t^{(s)}(1380)$ relationship tailored to the MBL aerosol type and concentration could be utilized. This would provide significantly better results than those shown in Figures 8 and 11.

9. Discussion and concluding remarks

In this paper we have investigated the effect of the presence of stratospheric aerosol on the atmospheric correction of ocean color sensors. The goal of the study was two-fold: (1) estimation the severity of the degradation of atmospheric correction using the Gordon and Wang[7] algorithm; and (2) examination of several methods of removal of the stratospheric component using the MODIS 1380 nm spectral band prior to application of the Gordon and Wang algorithm. This latter goal is of particular interest because, if it were possible to remove the stratospheric component, little or no modification of the present atmospheric correction algorithm would be required to accommodate correction for the stratospheric aerosol. After showing that a precise correction is not possible due to the lack of knowledge of the aerosol in the MBL, six simple procedures were examined for addressing the effect of the stratospheric aerosol ranging from simply ignoring its presence (procedure 1) to requiring full knowledge of its spectral optical properties (procedures 4–6).

As might be expected, the stratospheric aerosol correction procedure requiring full knowledge of the spectral optical properties, except the concentration which would be determined by the reflectance at 1380 nm, and employing multiple and interactive scattering between stratospheric aerosol and tropospheric molecular scattering in the visible (procedure 6) usually yielded the best overall correction at large values of τ_a when combined with the Gordon and Wang algorithm. However, at small values of τ_a this was often not significantly better than the simplest procedure (2), and sometimes worse. The fact that procedure 1, simply ignoring the stratospheric aerosol, provides a reasonable correction for small τ_a agrees with the conclusion of Gordon and Castaño[8] that the presence of the El Chichón aerosol had little effect on CZCS atmospheric correction, taking into consideration that CZCS did not require as accurate a correction as MODIS.

Subsequently, we examined a semi-empirical stratospheric aerosol correction scheme in which a generalized transmittance T was determined in such a manner as to provide the exact value of ρ_t for each geometry and combination of MBL and stratospheric aerosols. It was found that this approach appears viable for atmospheric correction and an overall stratospheric/MBL correction algorithm was proposed. In the case of thin cirrus clouds, this algorithm should typically yield $t\rho_w$ with an error that is within the acceptable range for τ_a as large as 1.00. This is rather remarkable considering that the perturbation caused by the presence of the cirrus cloud is not small. For example, in the absence of the cirrus cloud for $\theta_0 = 60°$ at the scan edge with $\tau_b = 0.15$, $\rho_t(\lambda) \approx 0.18$, 0.036, and 0.028 at 443, 765, and 865 nm, respectively, while $\rho_t^{(a)}(1380) \approx 0.0078$, 0.024, 0.085, and 0.17 for $\tau_a = 0.05$, 0.15, 0.5, and 1.0, respectively. Thus, even at $\tau_a = 0.15$, the cirrus contribution alone is comparable with the value of the total reflectance at 865 nm in its absence.

Several simplifying assumptions were used in our simulations: (1) all of the tropospheric aerosol is assumed to be in the MBL; (2) all of the radiance exiting the top of the atmosphere at 1380 nm is assumed to be due to scattering from the stratospheric aerosol alone; (3) there is assumed to be no water vapor above the stratospheric aerosol, and (4) there is assumed to be no horizontal variability in the stratospheric aerosol optical thickness. Thus, our simulations are an idealization, as in reality, some radiance at 1380 nm can originate from below the stratospheric aerosol either from molecular scattering in the free troposphere or possibly even from the MBL under conditions of very low relative humidity.[24] Also, there may be water vapor above thin cirrus clouds in which case their reflectance would be underestimated at 1380 nm, and cirrus typically display considerable horizontal structure.

Other than the errors introduced through these simplifying assumptions, we see two remaining difficulties in applying this algorithm in practice: first, at low τ_b it is necessary to be able to determine whether the principal contributor to $\rho_t^{(s)}(1380)$ is thin cirrus or volcanically-produced aerosol; and second, in order to utilize the algorithm, the full optical properties of the cirrus/aerosol are required with $\rho_t^{(s)}(1380)$ providing the concentration and T. It may be possible to distinguish thin cirrus from volcanically-produced aerosol by examination of the pixel-to-pixel variation in $\rho_t^{(s)}(1380)$, as the horizontal variability of cirrus should be much greater. Alternatively, it may be possible to distinguish them using MODIS bands in the thermal IR. Also, in the case of cirrus, we need to assess accuracy with which the scattering phase function must be known to provide an adequate correction.

Based on the computations presented here, we recommend that the semi-empirical procedure be developed as an operational method of correcting for cirrus clouds, and to the extent that they can be separated from volcanically-produced aerosol, for these as well. In addition to the large set of lookup tables required for operation of the Gordon and Wang[7] algorithm, implementation of this algorithm would require a second set of lookup tables of the T versus $\rho_t^{(s)}(1380)$ for each, or at least some, MBL models for each stratospheric aerosol model.

References

[1] H. R. Gordon and A. Y. Morel, *Remote Assessment of Ocean Color for Interpretation of Satellite Visible Imagery: A Review* (Springer-Verlag, New York, 1983), 114 pp.

[2] W. A. Hovis, D. K. Clark, F. Anderson, R. W. Austin, W. H. Wilson, E. T. Baker, D. Ball, H. R. Gordon, J. L. Mueller, S. Y. E. Sayed, B. Strum, R. C. Wrigley and C. S. Yentsch, "Nimbus 7 coastal zone color scanner: system description and initial imagery," Science **210**, 60–63 (1980).

[3] H. R. Gordon, D. K. Clark, J. L. Mueller and W. A. Hovis, "Phytoplankton pigments derived from the Nimbus–7 CZCS: initial comparisons with surface measurements," Science **210**, 63–66 (1980).

[4] S. B. Hooker, W. E. Esaias, G. C. Feldman, W. W. Gregg and C. R. McClain, *SeaWiFS Technical Report Series: Volume 1, An Overview of SeaWiFS and Ocean Color* (NASA, Greenbelt, MD, Technical Memorandum 104566, July 1992).

[5] V. V. Salomonson, W. L. Barnes, P. W. Maymon, H. E. Montgomery and H. Ostrow, "MODIS: Advanced Facility Instrument for Studies of the Earth as a System," IEEE Geosci. Rem. Sens. **27**, 145–152 (1989).

[6] H. R. Gordon and D. K. Clark, "Atmospheric effects in the remote sensing of phytoplankton pigments," Boundary-Layer Meteorology **18**, 299–313 (1980).

[7] H. R. Gordon and M. Wang, "Retrieval of water-leaving radiance and aerosol optical thickness over the oceans with SeaWiFS: A preliminary algorithm," Applied Optics **33**, 443–452 (1994).

[8] H. R. Gordon and D. J. Castaño, "The Coastal Zone Color Scanner Atmospheric Correction Algorithm: Influence of El Chichón," Applied Optics **27**, 3319–3321 (1988).

[9] M. D. King, Harshvardhan and A. Arking, "A Model of the Radiative Properties of the El Chichón Stratospheric Aerosol Layer," Journal of Climate and Applied Meteorology **23**, 1121–1137 (1984).

[10] K. Ding and H. R. Gordon, "Analysis of the influence of O_2 A-band absorption on atmospheric correction of ocean color imagery," Applied Optics **34**, 2068–2080 (1995).

[11] B. -C. Gao, A. F. H. Goetz and W. J. Wiscombe, "Cirrus cloud detection from airborne imaging spectrometer data using the 1.38 micron water vapor band," Geophysical Research Letters **20**, 301–304 (1993).

[12] P. Y. Deschamps, M. Herman and D. Tanre, "Modeling of the atmospheric effects and its application to the remote sensing of ocean color," Applied Optics **22**, 3751–3758 (1983).

[13] H. R. Gordon, D. K. Clark, J. W. Brown, O. B. Brown, R. H. Evans and W. W. Broenkow, "Phytoplankton pigment concentrations in the Middle Atlantic Bight: comparison between ship determinations and Coastal Zone Color Scanner estimates," Applied Optics **22**, 20–36 (1983).

[14] H. R. Gordon and M. Wang, "Influence of Oceanic Whitecaps on Atmospheric Correction of SeaWiFS," Applied Optics **33**, 7754–7763 (1994).

[15] E. P. Shettle and R. W. Fenn, *Models for the Aerosols of the Lower Atmosphere and the Effects of Humidity Variations on Their Optical Properties* (Air Force Geophysics Laboratory, Hanscomb AFB, MA 01731, AFGL–TR–79-0214, 1979).

[16] Y. Sasano and E. V. Browell, "Light scattering characteristics of various aerosol types derived from multiple wavelength lidar observations," Applied Optics **28**, 1670–1679 (1989).

[17] WCP–112, *A preliminary cloudless standard atmosphere for radiation computation* (World Meteorological Organization, WMO/TD–No. 24, Geneva, 1986).

[18] K. F. Palmer and D. Williams, "Optical constants of sulfuric acid; Application to the clouds of Venus?," Applied Oprics **14**, 208–219 (1975).

[19] Y. Takano and K. N. Liou, "Solar Radiative Transfer in Cirrus Clouds. Part I: Single-Scattering and Optical Properties of Hexagonal Ice Crystals," Jour. Atm. Sci. **46**, 224–240 (1989).

[20] H. C. van de Hulst, *Multiple Light Scattering* (Academic Press, New York, 1980), 739 pp.

[21] P. J. Reddy, F. W. Kreiner, J. J. Deluisi and Y. Kim, "Aerosol Optical Depths Over the Atlantic Derived From Shipboard Sunphotometer Observations During the 1988 Global Change Expedition," Global Biogeochemical Cycles **4**, 225–240 (1990).

[22] G. N. Plass, G. W. Kattawar and F. E. Catchings, "Matrix Operator Theory of Radiative Transfer 1: Rayleigh Scattering," Applied Optics **12**, 314–328 (1973).

[23] M. Wang and H. R. Gordon, "Estimating aerosol optical properties over the oceans with the multiangle imaging spectroradiometer: Some preliminary studies," Applied Optics **33**, 4042–4057 (1994).

[24] E. Ben-Dor, "A Precaution Regarding Cirrus Cloud Detection from Airborne Imaging Spectrometer Data Using the 1.38μm Water Vapor Band," Remote Sensing of Environment **50**, 346–350 (1994).

Figure Captions

Figure 1. Phase functions for the various stratospheric aerosol models used in the study: (a) Background; (b) Aged Volcanic Ash; (c) El Chichon; and (d) thin cirrus clouds.

Figure 2. Spectral variation of τ_s for the various stratospheric aerosol models. The cirrus cloud model is omitted because $\tau_s(\lambda)$ is constant.

Figure 3. Histogram of the average $|\Delta t \rho_w(443)|$ (short bars) and the maximum $|\Delta t \rho_w(443)|$ (tall bars) for all of the stratospheric aerosol models examined. The symbols E, B, V, C, and MBL refer to El Chichoń, Background, Aged Volcanic Ash, cirrus clouds, and no stratospheric aerosol, respectively. τ_b and τ_s: (a) $\tau_b(865) = 0.15$, $\tau_s(865) = 0.05$; (b) $\tau_b(865) = 0.15$, $\tau_s(865) = 0.15$; (c) $\tau_b(865) = 0.30$, $\tau_s(865) = 0.05$; and (d) $\tau_b(865) = 0.30$, $\tau_s(865) = 0.15$.

Figure 4. Histogram of the average $|\Delta t \rho_w(443)|$ (short bars) and the maximum $|\Delta t \rho_w(443)|$ (tall bars) for the cirrus clouds for various combinations of τ_b and τ_s: (a) $\tau_b(865) = 0.15$; (b) $\tau_b(865) = 0.30$.

Figure 5. Histogram of the average $|\Delta t \rho_w(443)|$ (short bars) and the maximum $|\Delta t \rho_w(443)|$ (tall bars) for the Aged Volcanic Ash (a) and (b) and the El Chichon (c) and (d) stratospheric aerosols for $\tau_b(865) = 0.15$ and (a) $\tau_s(865) = 0.05$; (b) $\tau_s(865) = 0.15$; (c) $\tau_s(865) = 0.05$; and (d) $\tau_s(865) = 0.15$.

Figure 6. Histogram of the average $|\Delta t \rho_w(443)|$ (short bars) and the maximum $|\Delta t \rho_w(443)|$ (tall bars) for the cirrus clouds with $\tau_b(865) = 0.15$: (a) $\tau_s(865) = 0.05$; (b) $\tau_s(865) = 0.15$; (c) $\tau_s(865) = 0.50$; and (d) $\tau_s(865) = 1.00$.

Figure 7. Exact value of T derived for procedure 5 as a function of $\rho_t^{(s)}(1380)$ for $\theta_0 = 60°$ at the scan edge. Open symbols are for $\tau_b = 0.15$ and closed symbols for $\tau_b = 0.30$. (a) 443 nm, (b) 765 nm, (c) 865 nm.

Figure 8. Same as Figure 4, except the stratospheric aerosol has been removed using the T versus $\rho_t^{(s)}(1380)$ relationship derived for cirrus clouds in the stratosphere and M80 in the MBL as described in the text.

Figure 9. Same as Figure 3 except the stratospheric aerosol has been removed using the T versus $\rho_t^{(s)}(1380)$ relationship derived for cirrus clouds in the stratosphere and M80 in the MBL as described in the text.

Figure 10. Same as Figure 8 except the aerosol described by T80 occupies the marine boundary layer, but the T versus $\rho_t^{(s)}(1380)$ relationship derived for cirrus clouds in the stratosphere and M80 in the MBL was used.

Figure 11. Same as Figure 10 except the T versus $\rho_t^{(s)}(1380)$ relationship derived for cirrus clouds in the stratosphere and T80 in the MBL was used.

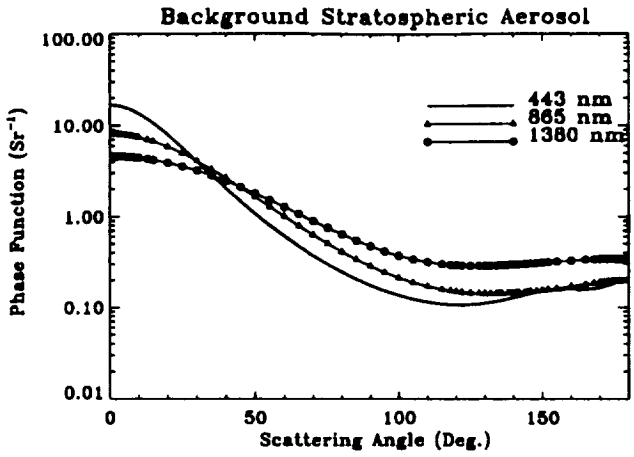

Figure 1a.

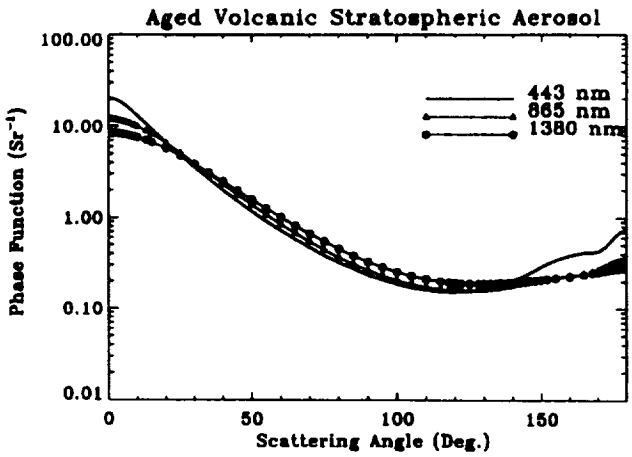

Figure 1b.

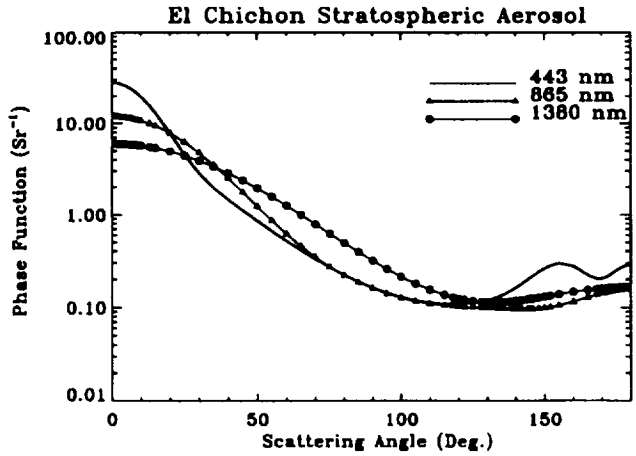

Figure 1c.

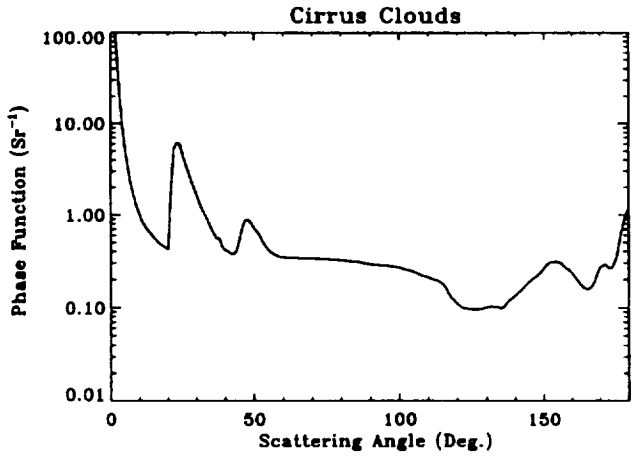

Figure 1d.

Figure 1. Phase functions for the various stratospheric aerosol models used in the study: (a) Background; (b) Aged Volcanic Ash; (c) El Chichon; and (d) thin cirrus clouds.

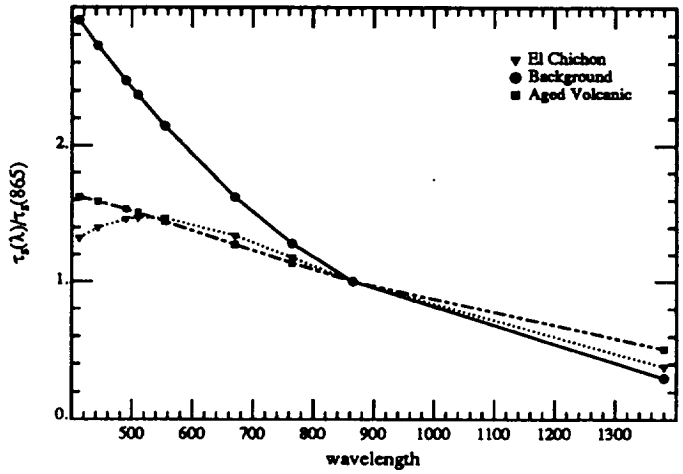

Figure 2. Spectral variation of τ_a for the various stratospheric aerosol models. The cirrus cloud model is omitted because $\tau_a(\lambda)$ is constant.

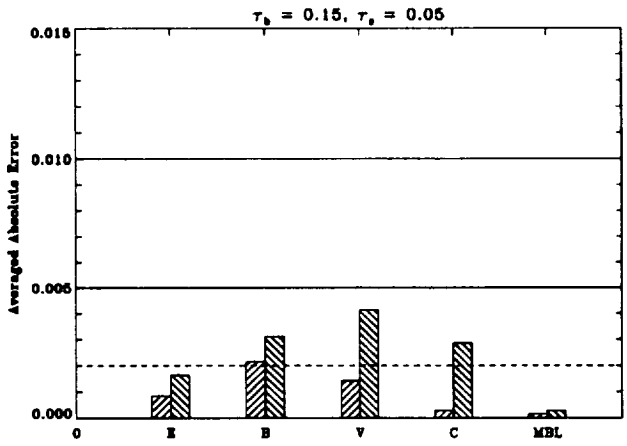

Figure 3a.

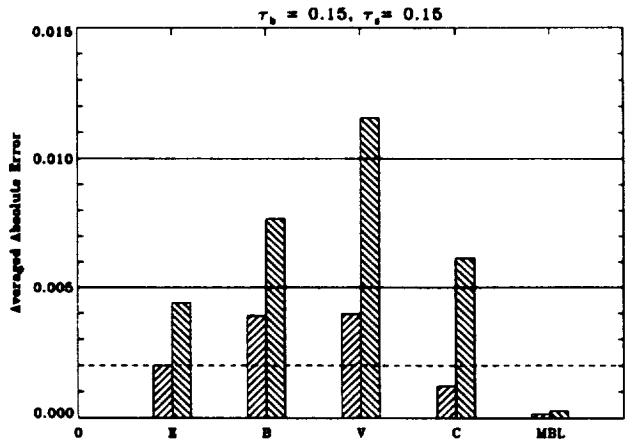

Figure 3b.

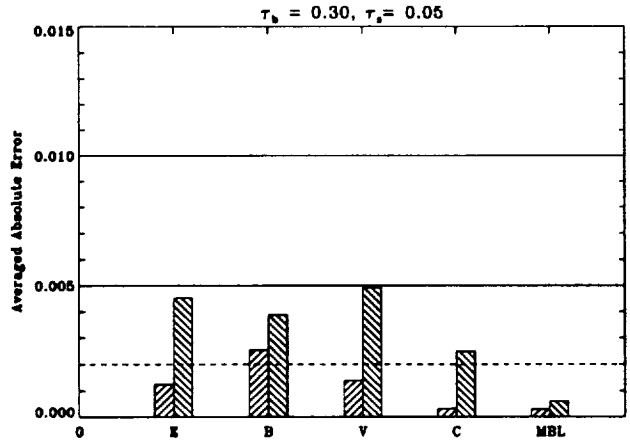

Figure 3c.

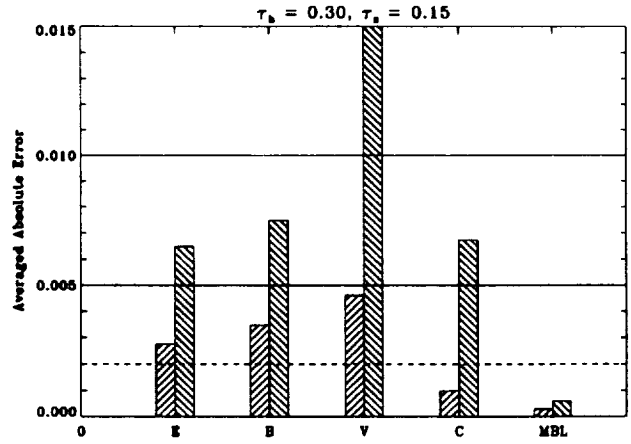

Figure 3d.

Figure 3. Histogram of the average $|\Delta t\rho_w(443)|$ (short bars) and the maximum $|\Delta t\rho_w(443)|$ (tall bars) for all of the stratospheric aerosol models examined. The symbols E, B, V, C, and MBL refer to El Chichoń, Background, Aged Volcanic Ash, cirrus clouds, and no stratospheric aerosol, respectively. τ_b and τ_s: (a) $\tau_b(865) = 0.15$, $\tau_s(865) = 0.05$; (b) $\tau_b(865) = 0.15$, $\tau_s(865) = 0.15$; (c) $\tau_b(865) = 0.30$, $\tau_s(865) = 0.05$; and (d) $\tau_b(865) = 0.30$, $\tau_s(865) = 0.15$.

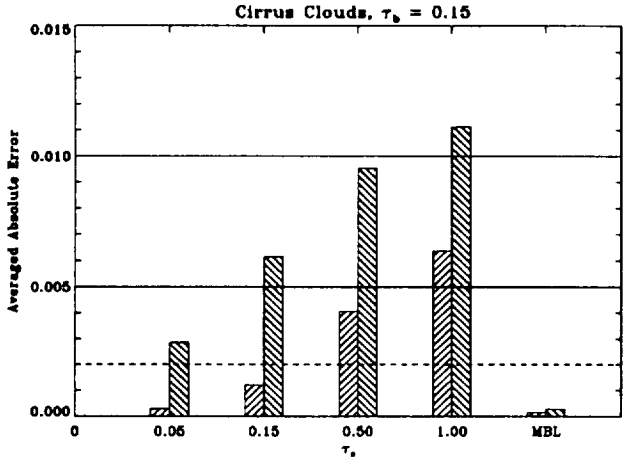

Figure 4a.

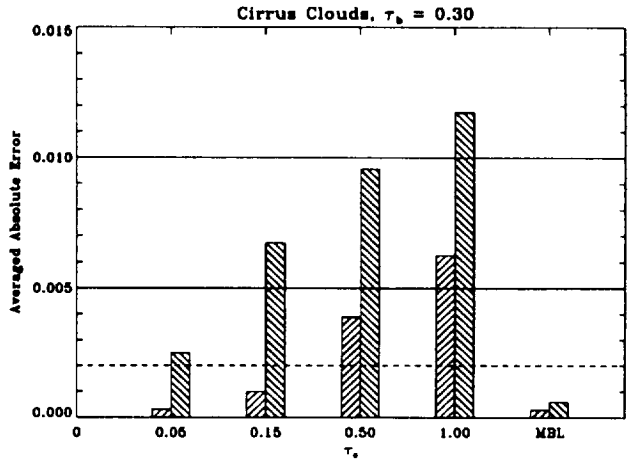

Figure 4b.

Figure 4. Histogram of the average $|\Delta t \rho_w(443)|$ (short bars) and the maximum $|\Delta t \rho_w(443)|$ (tall bars) for the cirrus clouds for various combinations of τ_b and τ_s: (a) $\tau_b(865) = 0.15$; (b) $\tau_b(865) = 0.30$.

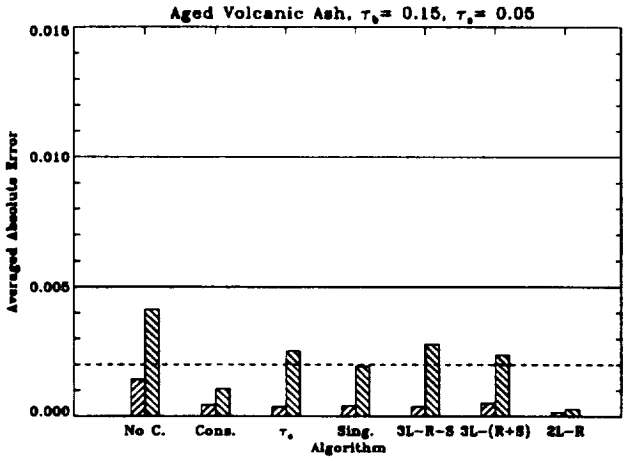

Figure 5a.

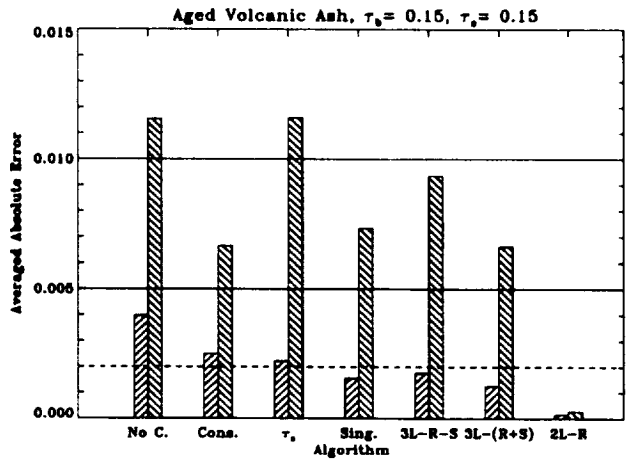

Figure 5b.

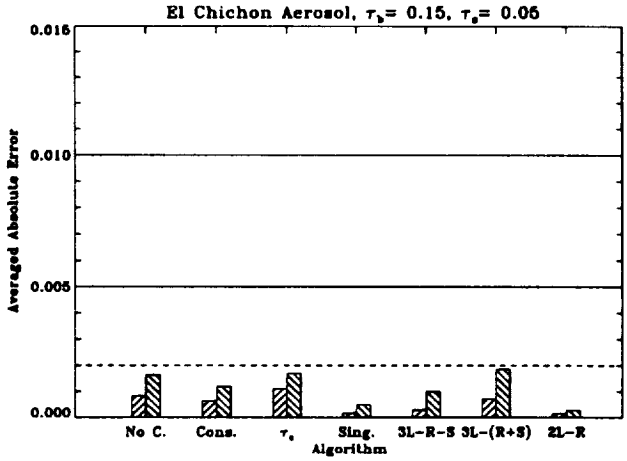

Figure 5c.

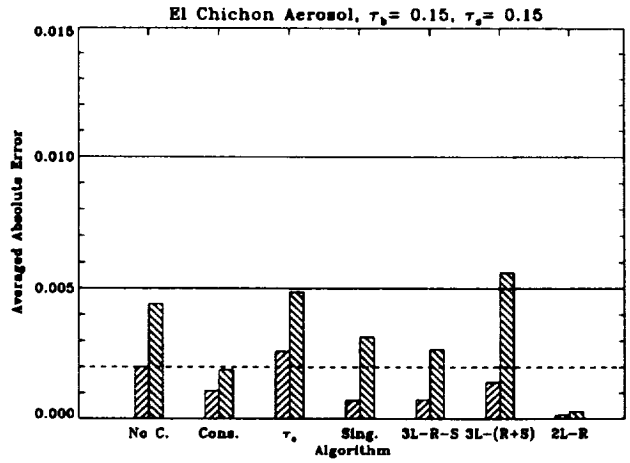

Figure 5d.

Figure 5. Histogram of the average $|\Delta t \rho_w(443)|$ (short bars) and the maximum $|\Delta t \rho_w(443)|$ (tall bars) for the Aged Volcanic Ash (a) and (b) and the El Chichon (c) and (d) stratospheric aerosols for $\tau_b(865) = 0.15$ and (a) $\tau_s(865) = 0.05$; (b) $\tau_s(865) = 0.15$; (c) $\tau_s(865) = 0.05$; and (d) $\tau_s(865) = 0.15$.

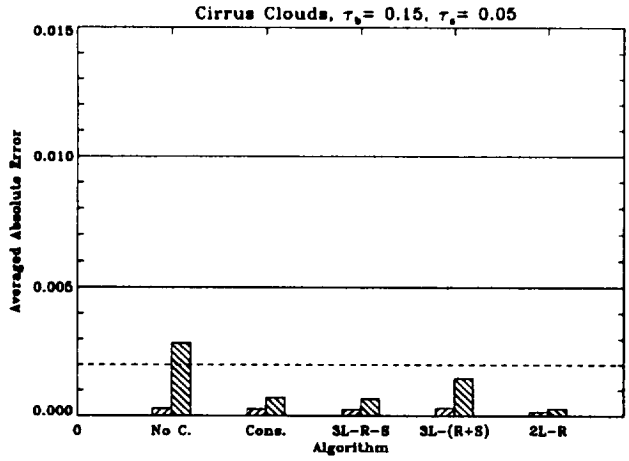

Figure 6a.

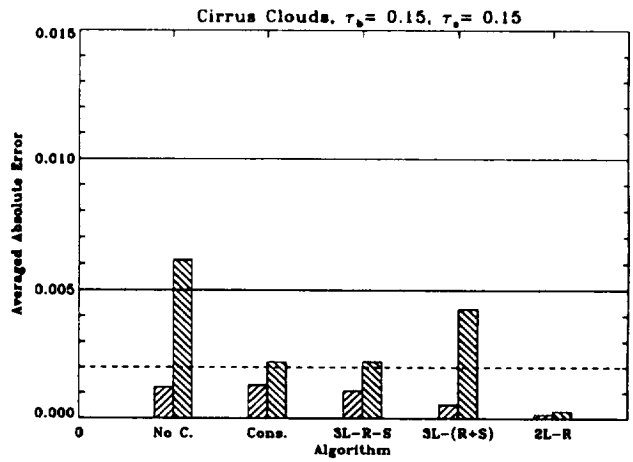

Figure 6b.

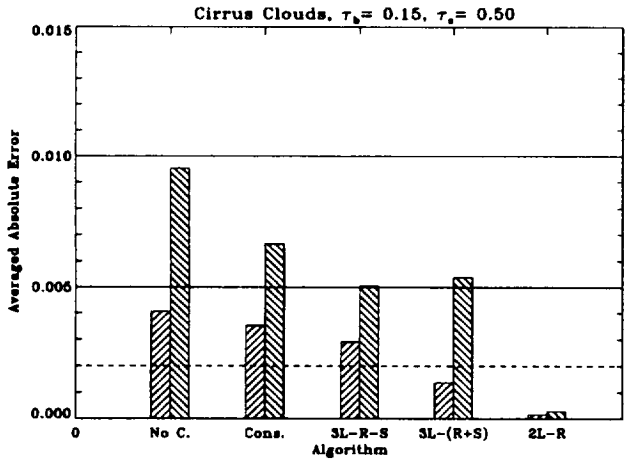

Figure 6c.

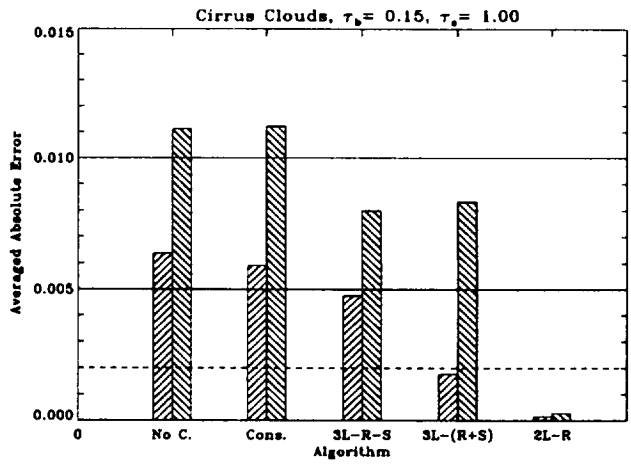

Figure 6d.

Figure 6. Histogram of the average $|\Delta t\rho_w(443)|$ (short bars) and the maximum $|\Delta t\rho_w(443)|$ (tall bars) for the cirrus clouds with $\tau_b(865) = 0.15$: (a) $\tau_s(865) = 0.05$; (b) $\tau_s(865) = 0.15$; (c) $\tau_s(865) = 0.50$; and (d) $\tau_s(865) = 1.00$.

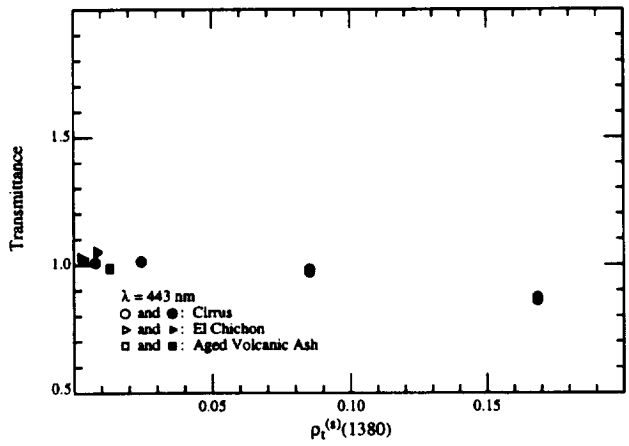

Figure 7a.

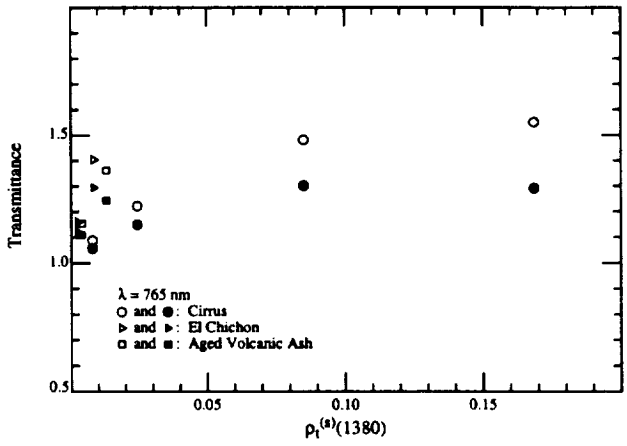

Figure 7b.

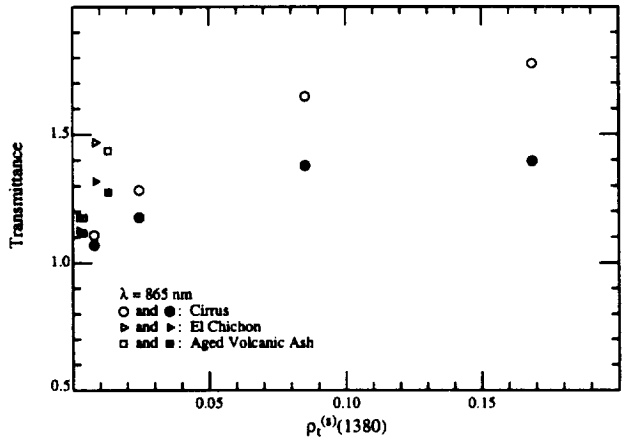

Figure 7c.

Figure 7. Exact value of T derived for procedure 5 as a function of $\rho_t^{(s)}(1380)$ for $\theta_0 = 60°$ at the scan edge. Open symbols are for $\tau_b = 0.15$ and closed symbols for $\tau_b = 0.30$. (a) 443 nm, (b) 765 nm, (c) 865 nm.

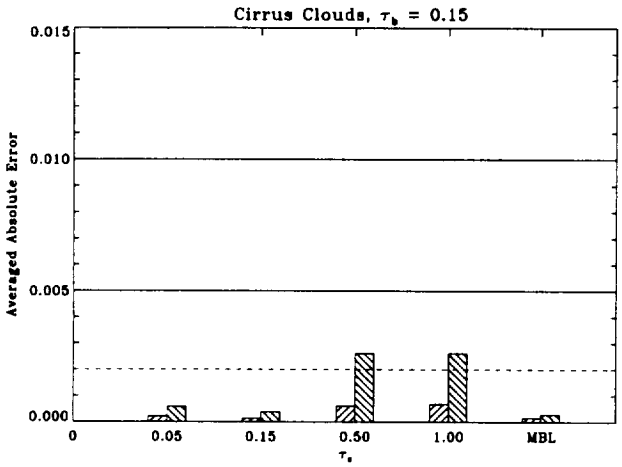

Figure 8a.

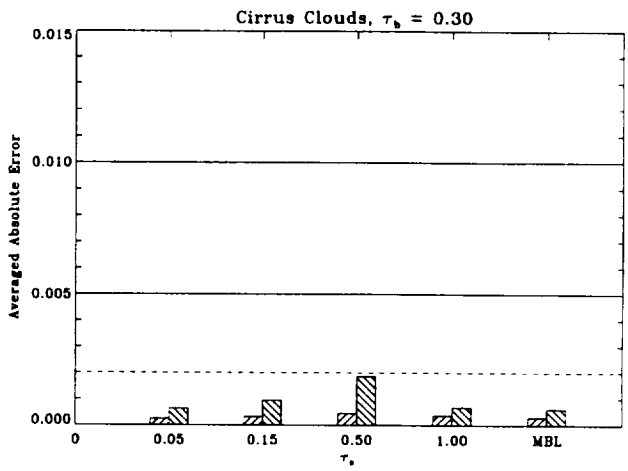

Figure 8b.

Figure 8. Same as Figure 4, except the stratospheric aerosol has been removed using the T versus $\rho_a(1380)$ relationship derived for cirrus clouds in the stratosphere and M80 in the boundary layer as described in the text.

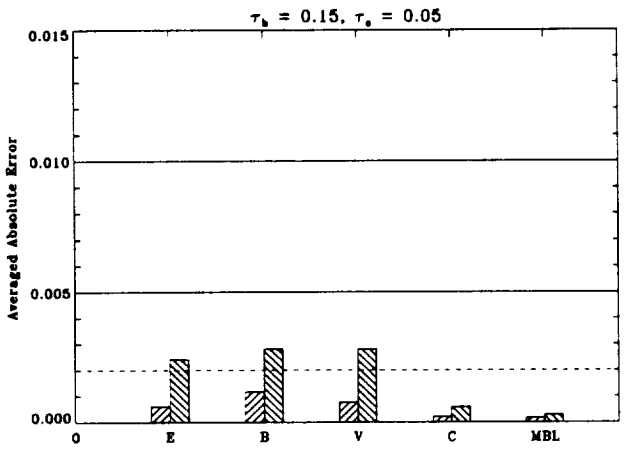

Figure 9a.

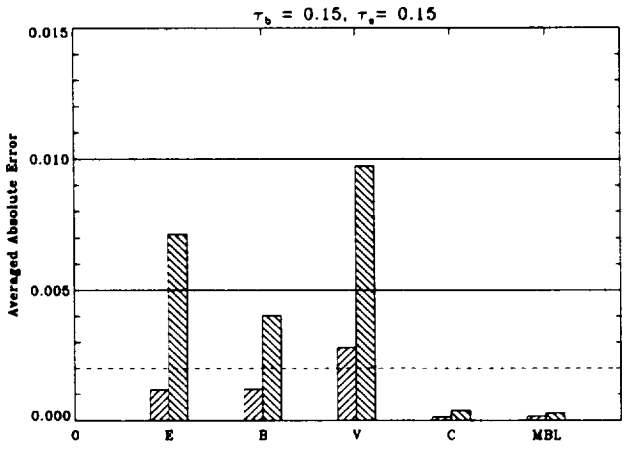

Figure 9b.

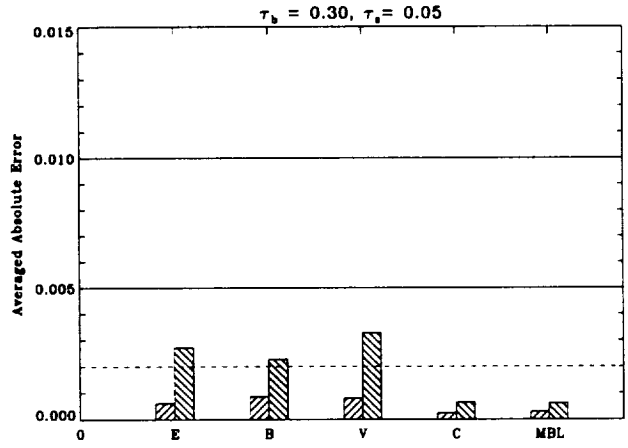

Figure 9c.

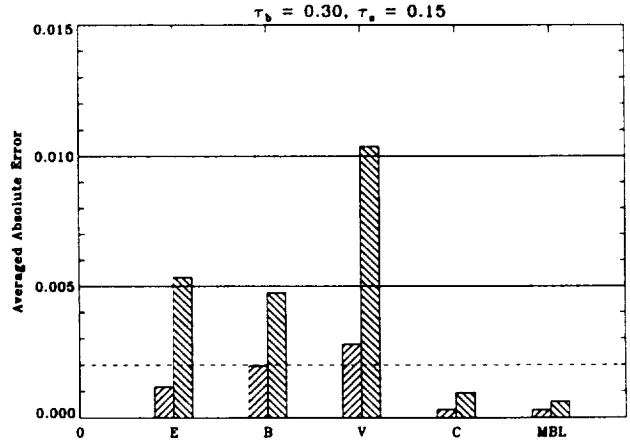

Figure 9d.

Figure 9. Same as Figure 3 except the stratospheric aerosol has been removed using the T versus $\rho_s(1380)$ relationship derived for cirrus clouds in the stratosphere and M80 in the boundary layer as described in the text.

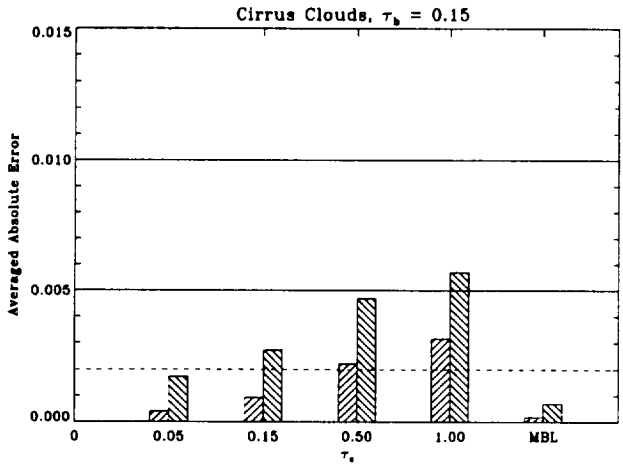

Figure 10a.

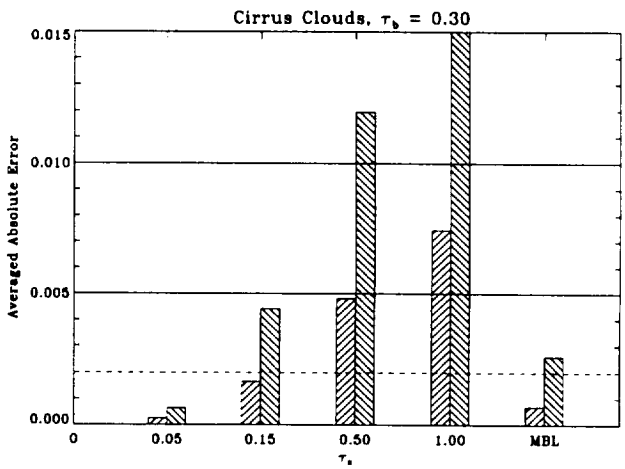

Figure 10b.

Figure 10. Same as Figure 8 except the aerosol described by T80 occupies the marine boundary layer, but the T versus $\rho_a(1380)$ relationship derived for cirrus clouds in the stratosphere and M80 in the boundary layer was used.

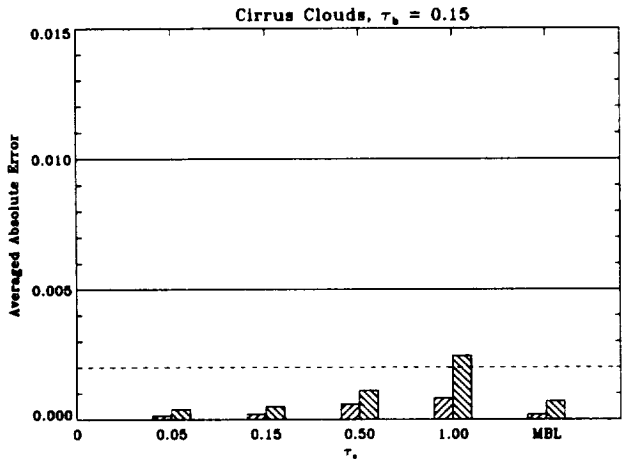

Figure 11a.

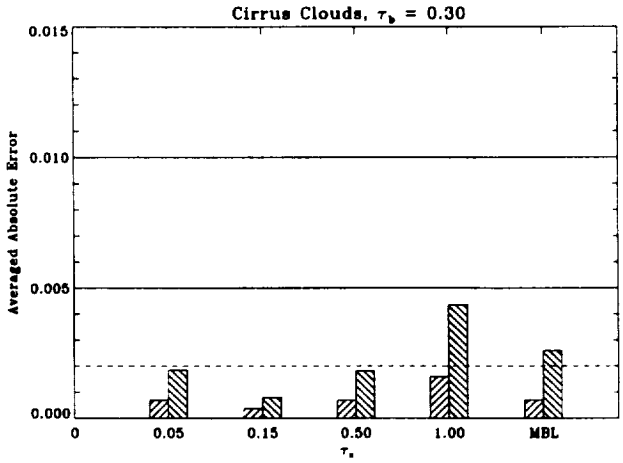

Figure 11b.

Figure 11. Same as Figure 10 except the T versus $\rho_s(1380)$ relationship derived for cirrus clouds in the stratosphere and T80 in the boundary layer was used.

Appendix 3

How well can radiance reflected from the ocean-atmosphere system be predicted from measurements at the sea surface?

by

Howard R. Gordon and Tianming Zhang

Department of Physics
University of Miami
Coral Gables, FL 33124

(Accepted for publication in *Applied Optics*)

Abstract

There is interest in predicting the top-of-atmosphere (TOA) reflectance of the ocean-atmosphere system for in-orbit calibration of ocean color sensors. Here, using simulations, we examine the accuracy one could expect in estimating the reflectance ρ_T of the ocean-atmosphere system based on a measurement suite carried out at the sea surface, i.e., measurement of the normalized sky radiance (ρ_B) and the aerosol optical thickness (τ_a), under ideal conditions — a cloud free, horizontally-homogeneous atmosphere. Briefly, ρ_B and τ_a are inserted into a multiple-scattering inversion algorithm to retrieve the aerosol optical properties — the single scattering albedo and the scattering phase function. These retrieved quantities are then inserted into the radiative transfer equation to predict ρ_T. Most of the simulations were carried out in the near infrared (865 nm), where a larger fraction of ρ_T is contributed by aerosol scattering compared to molecular scattering, than in the visible, and where the water-leaving radiance can be neglected. The simulations suggest that ρ_T can be predicted with an uncertainty typically $\lesssim 1\%$ when the ρ_B and τ_a measurements are error free. The influence of the simplifying assumptions that were made in the inversion-prediction process, such as, modeling the atmosphere as a plane-parallel medium, employing a smooth sea surface in the inversion algorithm, using scalar radiative transfer theory, and assuming that the aerosol was confined to a thin layer just above the sea surface, was investigated. In most cases, these assumptions did not increase the error beyond $\pm 1\%$. An exception was the use of scalar radiative transfer theory, for which the error grew to as much as $\sim 2.5\%$, suggesting that using ρ_B-inversion and ρ_T-prediction codes that include polarization would be more appropriate. However, their use would necessitate measurement of the polarization associated with ρ_B. The uncertainty introduced by unknown aerosol vertical structure was also investigated and found to be negligible if the aerosols were nonabsorbing or weakly absorbing. Extension of the analysis to the blue, which requires measurement of the water-leaving radiance, showed significantly better predictions of ρ_T because the major portion of ρ_T is the result of molecular scattering, which is precisely known. We also simulated the influence of calibration errors in both the sun photometer and ρ_B radiometer. The results suggest that the relative error in the predicted ρ_T is similar in magnitude to that in ρ_B (actually it was somewhat less). However, the relative error in ρ_T induced by error in τ_a is usually $\ll$ the relative error in τ_a. Presently, it appears that radiometers can be calibrated with an

uncertainty of $\sim \pm 2.5\%$, therefore it is reasonable to conclude that, at present, the most important error source in the prediction of ρ_T from ρ_B is likely to be error in the ρ_B measurement.

1. Introduction

Most satellite remote sensing instruments show significant variations in radiometric sensitivity after launch. Because of this, considerable effort has been placed on so-called *vicarious* calibration, i.e., in-orbit calibration utilizing the radiance predicted at the sensor by a variety of methods.[1–12] Some sensors, e.g., the Polarization and Directionality of Earth Radiation[13] (POLDER) to be launched on the Advanced Earth Observation Satellite (ADEOS), have no on-board provision for examination of the radiometric performance, so the entire calibration strategy must be a vicarious effort.

The prediction of the radiance at the sensor can be made by using high-altitude aircraft radiometric measurements extrapolated to the top-of-the-atmosphere (TOA).[7,9] Alternatively, one can make measurements of the surface reflectance and the aerosol optical thickness from the ground, followed by scattering computations to estimate the aerosol scattering phase function and the single scattering albedo, e.g., using Mie theory, and radiative transfer computations to predict the TOA radiance.[9] The focus of this paper is the accuracy with which the TOA radiance can be predicted by the latter method under ideal circumstances — a cloud-free horizontally-homogeneous atmosphere. However, as we wish to remove as many assumptions as possible regarding the aerosol, we derive estimates of the aerosol scattering phase function and single scattering albedo using sky radiance measurements, rather than computing them using Mie theory. In this way, questions regarding the error in the estimate of these radiatively important parameters due to errors in the estimated aerosol complex index of refraction and the size (and shape) distribution are circumvented. Since our interest is mainly in sensors for measuring the color of the ocean, e.g., the Sea-Viewing Wide-field-of-view Sensor[14] (SeaWiFS) and the Moderate Resolution Spectral Radiometer[15] (MODIS), we restrict our analysis to situations when sensors are viewing the oceans as opposed to the land surface. The analysis is still valid for calibrating sensors designed for the land surface when they are over the oceans, but in practice that would only be useful for vicarious calibration of the low end of their radiometric sensitivity.

We assume the following measurements, carried out at the sea surface, are available for the analysis: (1) the aerosol optical thickness at the wavelength of interest measured by a radiometer

with a narrow field of view aimed directly at the sun (sun photometer); and (2) the sky radiance at the wavelength of interest measured in the solar almucantar and in the principal plane. Since a large portion of the TOA radiance over the oceans is due to backscattering from the aerosol, we will assume that the solar zenith angle is sufficiently large that such backscattering can be assessed with the surface measurements, e.g., solar zenith angles $\gtrsim 60°$. Using these measurements (simulated by solving the radiative transfer equation), we apply a variant of the inversion algorithm developed by Wang and Gordon[16] to retrieve the columnar aerosol scattering phase function and the single scattering albedo. These retrieved optical properties are then inserted into the radiative transfer equation to predict the TOA radiance for comparison with that based on the true optical properties of the atmosphere, and to determinate the error in the procedure. Then, we examine the influence of errors in the measurement of the sky radiance and the aerosol optical thickness. Next, we examine the possible reduction of accuracy when measurements of the solar aureole (which is difficult to measure from a ship) are absent. Finally, we examine the effects of the assumptions used in the retrieval-prediction process, e.g., the use of scalar radiative transfer theory for a plane parallel atmosphere over a smooth sea surface.

2. Basis of estimation of TOA radiance

The basic idea for the estimation of the radiance, $L_T(\theta_T)$, at the TOA given the aerosol optical thickness, τ_a, and radiance measurements, $L_B(\theta_B)$, at the bottom of the atmosphere (BOA), is provided schematically in Figure 1. We normalize the radiances, L's, to form normalized radiances (or generalized reflectances and transmittances), ρ's, given by $\rho = \pi L / F_0 \cos\theta_0$, where F_0 is the extraterrestrial solar irradiance and θ_0 is the solar zenith angle. If we ignore the presence of the ocean, i.e, we assume it is totally absorbing, ignore molecular (Rayleigh) scattering, and assume that τ_a is sufficiently small that the single scattering approximation is appropriate, then, for the geometry shown in the figure, the normalized radiances are given by

$$\begin{aligned} \rho_T(\theta_T) &= \frac{\omega_0 P(\Theta)\tau_a}{4\cos\theta_T \cos\theta_0}, \\ \rho_B(\theta_B) &= \frac{\omega_0 P(\Theta)\tau_a}{4\cos\theta_B \cos\theta_0}, \end{aligned} \tag{1}$$

where ω_0 is the single scattering albedo of the aerosol, $P(\Theta)$ is the aerosol scattering phase function, and Θ is the scattering angle common to both viewing directions (Figure 1). Thus, in the geometry shown,

$$\cos\theta_T \rho_T(\theta_T) = \cos\theta_B \rho_B(\theta_B), \tag{2}$$

and the radiance $L_T(\theta_T)$ is completely determined from the radiance $L_B(\theta_B)$. Alternatively, one could use Eq. (1) to estimate the value of $\omega_0 P(\Theta)\tau_a$ for all values of Θ available from the surface, and then evaluate L_T for those directions for which $\omega_0 P(\Theta)\tau_a$ is available. Note that to compute L_T from L_B, independent measurement of the aerosol optical thickness is not required. If Rayleigh scattering is also present, then $\omega_0 P(\Theta)\tau_a$ in Eq. (1) must be replaced by $\omega_0 P(\Theta)\tau_a + P_r(\Theta)\tau_r$, where $P_r(\Theta)$ is the Rayleigh scattering phase function and τ_r is the Rayleigh optical thickness; however, it is still possible to compute L_T from L_B without an independent measurement of the aerosol optical thickness.

In this simple example, we see that in the limit of small optical thickness, the only error in the radiance L_T is the measurement error in L_B. In fact, Eq. (2) shows that the fractional errors in L_T, L_B, ρ_T, and ρ_B are all identical — the radiative transfer process introduces no additional error in L_T or ρ_T. This is an important conclusion that we shall see is approximately true, even in a multiple-scattering atmosphere bounded by a Fresnel-reflecting sea surface, i.e., the error added by the radiative transfer process is small.

3. Estimation of the aerosol optical properties.

In the presence of a Fresnel-reflecting sea surface, the situation is more complex because of reflection from the surface. For example, at the TOA, reflection of the solar beam from the surface followed by scattering, or reflection from the sea surface of radiance scattered from the incident solar beam, can make a significant contribution to ρ_T. Similarly, scattering from the surface-reflected solar beam contributes to ρ_B. This is true even in the single-scattering regime, where it is easy to see that there is no geometry in which a simple analytical expression similar to Eq. (2) exists. In this case it is necessary to employ a two-step procedure to estimate ρ_T from ρ_B. In the first step, one retrieves $\omega_0 P(\Theta)\tau_a$ from the measurement of $\rho_B(\theta)$, and in the second step, this quantity

is used to predict $\rho_T(\theta)$. In this section we discuss the first step, retrieval of the aerosol optical properties.

3.A. Limit of small optical depth

In the absence of Rayleigh scattering and in the presence of a Fresnel-reflecting sea surface, the relationship between $\rho_B(\theta_B)$ and the aerosol properties is

$$\rho_B(\theta_B) = \frac{\omega_0 \tau_a}{4 \cos\theta_B \cos\theta_0} \Big[P(\Theta) + r(\theta_0) P(\Theta_B^r) \Big], \tag{3}$$

where $r(\alpha)$ is the Fresnel reflectance of the flat sea surface for an incident angle α. The first term in the square brackets represents the contribution from photons scattered through an angle Θ by the incident solar beam *before* it reflects from the sea surface, while the second term represents the contribution from photons scattered through an angle Θ_B^r by the incident solar beam *after* it has reflected from the surface. For most aerosol phase functions, the second term will be negligible for values of θ_B for which $\Theta \lesssim 50°$; however, for larger values of Θ, the second term can make a significant contribution ($\sim 30\%$) to $\rho_B(\theta_B)$, and interferes with the estimation of $P(\Theta)$. In fact, there is no set of measurements that can be used to uniquely separate the two terms in Eq. (3), and provide $\omega_0 P(\Theta)\tau_a$. Thus, in contrast to the situation with the sea surface absent, for which $\omega_0 P(\Theta)\tau_a$ could be precisely estimated for $\Theta < \pi/2 + \theta_0$ using Eq. (1), when the sea surface is present this is not possible.

We now examine how one might extract $\omega_0 P(\Theta)\tau_a$ from measurements of ρ_B. We consider two schemes for effecting this: (1) using ρ_B measured in the principal plane (PP), and (2) combining principal plane and solar almucantar measurements (PP+A). The largest scattering angle accessible to direct observation (the first term in Eq. (3)) is $\Theta_{\mathrm{Max}} = \pi/2 + \theta_0$. It is unrealistic to expect to retrieve accurate values of $\omega_0 P(\Theta)\tau_a$ for larger scattering angles, because their contribution to ρ_B always involves $r(\theta_0)$, which in a typical experiment ($\theta_0 \sim 60°$) will be < 0.1. For larger values of θ_0, $r(\theta_0)$ will be even larger which further increases the difficulty. Thus, some assumption regarding $P(\Theta)$ for $\Theta > \pi/2 + \theta_0$ is necessary. The assumption that we use is that $P(\Theta) = P(\Theta_{\mathrm{Max}})$ for $\Theta > \Theta_{\mathrm{Max}}$. [Actually we assume that this is true for Θ a few degrees $< \Theta_{\mathrm{Max}}$ because measurements

cannot be made at the horizon.] With this assumption, $\rho_B(\theta_B)$ measured in the principal plane with $\theta_B \sim 90°$ in a direction opposite to the sun (viewing in a direction with the sun at the observer's back) can be used to provide $\omega_0 P(\Theta)\tau_a$ for $\Theta > \Theta_{\mathbf{Max}}$. Measurements of $\rho_B(\theta_B)$ in the rest of the principal plane can then be used to provide $\omega_0 P(\Theta)\tau_a$ for $\Theta < \Theta_{\mathbf{Max}}$. An alternative scheme which provides more accurate values of $\omega_0 P(\Theta)\tau_a$ near $\Theta = 90°$ is to use values of $\rho_B(\theta_B)$ in the principal plane (opposite to the sun) for only $\theta_0 \leq \theta_B \leq 90°$ to obtain $\omega_0 P(\Theta)\tau_a$ for $\Theta > 2\theta_0$, and then use the almucantar values to obtain it for $\Theta < 2\theta_0$. In the second procedure, the dependence of ρ_B on the estimated part of the phase function ($\Theta > \Theta_{\mathbf{Max}}$) is quadratic in r, rather than linear, for $\Theta <$ some angle Θ'. This reduces the error in $\omega_0 P(\Theta)\tau_a$ for $\Theta < \Theta'$. In the case we concentrate on in detail in this paper, $\theta_0 = 60°$, $\Theta' \approx 110°$.

We tested these ideas by assuming that single scattering was the correct physics and computing ρ_t at 865 nm using the Maritime aerosol model of Shettle and Fenn[17] with a relative humidity of 99%, which we indicate by M99. The scattering phase function for M99 computed from Mie theory is provided in Figure 2. The M99 model is employed because it yields the most sharply peaked phase function with the most structure in the vicinity of the rainbow angle ($\Theta \sim 140°$), of any of the Shettle and Fenn models. These characteristics make accurate retrieval of $\omega_0 P(\Theta)\tau_a$ particularly difficult, and as such, provide a severe test of the technique. Figure 3 provides the error in the retrieved values of $\omega_0 P(\Theta)\tau_a$ obtained for $\theta_0 = 60°$ using these two methods for the M99 aerosol model. The large error for $\Theta > 150°$ is expected, as this is the region for which a guess was made for $\omega_0 P(\Theta)\tau_a$. The large spike near $\Theta = 120°$ results from the large error in the estimated $\omega_0 P(\Theta)\tau_a$ near the backscattering direction. The small spike near $\Theta = 90°$ for the PP+A case is due to the overestimation of $\omega_0 P(\Theta)\tau_a$ near $\Theta = 120°$. In the forward direction, the error is negligible. Clearly, the PP+A method is superior to the PP method. It should be noted that if the aerosol had a phase function with less backscattering (and/or less variation in backscattering with Θ), the error would be significantly reduced. For example, using the Shettle and Fenn Tropospheric model at 50% relative humidity (T50 in Figure 2) under the same conditions, resulted in a maximum error for $\Theta < \Theta_{\mathbf{Max}}$ of ~1.9%.

3.B. The multiple scattering regime

In general, the single-scattering approximation will not be valid, and its application will result in very poor retrievals. We carried out multiple scattering computations using the same aerosol model as in the example above (M99 at 865 nm) with an aerosol optical thickness of 0.2 to simulate ρ_T and ρ_B. After subtraction of the component due to molecular scattering, the single scattering formula Eq. (3) was used to derive $\omega_0 P(\Theta)$. The error in the retrieved $\omega_0 P(\Theta)$ was nearly a factor of two for $\Theta \gtrsim 80°$. Clearly, multiple scattering must be considered in carrying out such inversions.

A procedure similar to that in the single scattering case can be employed in a multiply scattering atmosphere, i.e., we will use the surface measurements to estimate ω_0 and $P(\Theta)$. The estimate of ω_0 and $P(\Theta)$ is effected by using the retrieval algorithm described by Wang and Gordon.[16] Based on measurement of the sky radiance and the aerosol optical thickness at the sea surface, the Wang and Gordon algorithm finds aerosol optical properties that, when inserted into the radiative transfer equation (RTE), yield the measured values of ρ_B. This is accomplished in the following manner. With initial guesses for ω_0 and $P(\Theta)$, the RTE is solved using the measured value of τ_a to find the predicted sky radiance. The differences $\Delta\rho(\hat{\xi}_B)$, where $-\hat{\xi}_B$ denotes the direction in which the radiometer points in the sky, between the predicted and measured sky radiance is then used to estimate a new phase function and value for ω_0. This estimate is accomplished using the single scattering approximation, Eq. (1), i.e., ignoring the Fresnel reflection contribution $r(\theta_0)$, in the following manner. First, the scattering angle Θ_B that would be appropriate to the single scattering of the direct incident solar radiation in the direction $\hat{\xi}_B$ is determined for each point at which the sky radiance is measured, i.e., each $\hat{\xi}_B$. Next, the error in the computed sky radiance is used to estimate the error $\Delta[\omega_0 P(\Theta_B)]$ in the trial value of $\omega_0 P(\Theta_B)$ using the single scattering formula. Finally, the value of $\omega_0 P(\Theta_B)$ is then changed by a fraction (usually 0.5) of $\Delta[\omega_0 P(\Theta_B)]$ yielding a revised value. The revised $\omega_0 P(\Theta_B)$ is then inserted into the RTE and new values of $\rho_t(\hat{\xi}_B)$ are computed. The process is repeated until the measured and computed $\rho_B(\hat{\xi}_B)$ are in agreement within the experimental error. Using pseudo data simulated by solving the RTE for a two-layer atmosphere (aerosols in the lower layer) bounded by a flat Fresnel-reflecting sea surface, Wang and Gordon[16] found that the rms error between the measured and computed $\rho_B(\hat{\xi}_B)$'s could usually be reduced to a fraction of 1% when the correct vertical structure was employed in the correction algorithm.

As in the single scattering case, there are scattering angles Θ that are inaccessible with this procedure, i.e., the maximum value of Θ is $\Theta_{\mathbf{Max}} = \pi/2 + \theta_0$, where θ_0 is the solar zenith angle. Thus, there is no way to derive $P(\Theta)$ for $\Theta > \Theta_{\mathbf{Max}}$. For these angles, a guess is made for P, e.g., $P(\Theta) = P(\Theta_{\mathbf{Max}})$ for $\Theta > \Theta_{\mathbf{Max}}$. The guess enables the completion of the phase function for the next iteration and also for the estimation of ω_0 from $\omega_0 P(\Theta)$ by integration over solid angle.

As an example of this procedure, we carried out multiple scattering computations of ρ_B at a wavelength of 865 nm. We used an aerosol optical thickness of 0.2 and assumed that the aerosol was all located in the marine boundary layer, i.e., a physically thin layer at the bottom of the atmosphere. For reference, this value for τ_a is about two to three times the average for the North Atlantic in a pure maritime atmosphere.[18] The error in the resulting retrieval is provided in Figure 4. The retrieved ω_0 (0.986) compares favorably with the true value of 0.998. The small bump in the retrieval near $\Theta = 120°$ is due to reflection of the solar beam from the sea surface and subsequent scattering through $\sim 180°$. It would not appear were $\omega_0 P(\Theta)$ estimated accurately near $\Theta = 180°$. It could be removed by simply not using the almucantar and principal plane pseudo data for scattering angles near $\Theta = 120°$, or its presence could be used to improve the estimate of $\omega_0 P(\Theta)$ near $\Theta = 180°$. As we have not thoroughly investigated its removal or use, we shall simply ignore its presence here, i.e., when we estimate the TOA radiance, we will know what viewing angles will be influenced by its presence and simply avoid those viewing angles. Clearly, the retrieval in this multiple-scattering atmosphere is nearly as effective as it would be were single scattering the correct physics (Figure 3).

It is important to note that this procedure provides a full multiple scattering inversion of the sky radiance; the single scattering formulas are *only* used to provide a coarse estimate of the amount that $\omega_0 P(\Theta)$ should be changed at each step of the iteration. As mentioned above, had we used the single-scattering algorithm of Section 3.A, the error in the retrieved $\omega_0 P(\Theta)$ for $80° \lesssim \Theta \lesssim 130°$ would have been $\sim$ a factor of two or greater.

4. Estimation of the TOA radiance

In this section we apply the retrieved aerosol properties to estimate the radiance exiting the TOA in the perpendicular plane, near where most ocean color instruments view.

4.A. Limit of small optical depth.

In the limit of small τ_a, the reflectance at the TOA is simply given by

$$\rho_T(\theta_T) = \frac{\omega_0 \tau_a}{4 \cos\theta_T \cos\theta_0} \Big[P(\Theta) + [r(\theta_T) + r(\theta_0)] P(\Theta_T^r) \Big], \tag{4}$$

where Θ_T^r is the appropriate angle for scattering the surface-reflected solar beam toward the sensor. We need only insert the retrieved $\omega_0 P(\Theta)\tau_a$ into this expression to predict ρ_T. Figure 5 provides the error in $\rho_T(\theta_T)$ using the single-scattering estimate of $\omega_0 P(\Theta)\tau_a$ derived in Section 3.C by the two methods. As expected, the PP+A method is superior to the PP method alone. When the PP+A method is used, the relative error in ρ_T (or L_T) is $\lesssim 2.5\%$ for $\theta_T \gtrsim 15°$. Note that we have ignored any molecular scattering component in ρ_T. As this component is precisely known, including it in the analysis will reduce the error in ρ_T in Figure 5 by a factor $(1 + \rho_M/\rho_A)$, where ρ_M and ρ_A are, respectively, the molecular and aerosol contributions to ρ_T.

4.B. The multiple-scattering regime.

Given the values of ω_0 and $P(\Theta)$, estimated from measurements of ρ_B and τ_a, prediction of the radiance at the TOA is straightforward. We simply insert $\omega_0 P(\Theta)$ and τ_a into the RTE with an assumed aerosol vertical profile and solve for the radiance. In this section we examine the accuracy of the TOA-radiance computed in this manner. As in the single scattering case, we examine the error induced by errors in τ_a and in $\rho_B(\theta_B)$.

As described in Section 3.B, we simulated the sky radiance and the associated TOA radiances using the M99 aerosol model with $\tau_a = 0.2$ at 865 nm in the lower layer of a two-layer atmosphere. All molecular scattering (Rayleigh scattering) was placed in the upper layer. The solar zenith angle at the time of the sky radiance measurement was taken to be 60°. The sky radiance was assumed to be measured in the solar almucantar (beginning with an azimuth angle 1° from the sun)

and from the zenith to near the horizon in the principal plane, facing away from the sun (PP+A measurements). Figure 4 provides the error in the retrieved ω_0 and $\omega_0 P(\Theta)$ for this case.

The retrieved $\omega_0 P(\Theta)$ and the measured value of τ_a were then inserted into the RTE and the resulting radiance at the TOA was computed. Figure 6 provides the error in the computed TOA radiance, i.e., the percent difference between the reflectance ρ_T computed using the retrieved aerosol optical properties and that computed using the true aerosol optical properties. At the TOA viewing was assumed to take place in the perpendicular plane, i.e., the azimuth of the viewing angle was taken normal to the plane formed by the sun's rays and the zenith. The TOA computations were carried out for solar zenith angles of 60°, 50°, and 45°, where for the latter two it was assumed that the aerosol is unchanged in concentration or properties as θ_0 varies from 60° to 45°. The reason for considering these other values of θ_0 was to simulate the measurement of the aerosol optical properties when θ_0 is large (so that $\omega_0 P(\Theta)$ can be obtained at large values of Θ), but computation of the TOA radiance when a satellite sensor might view the surface (later in the day, therefore a smaller value of θ_0). The retrieval of $\omega_0 P(\Theta)$ and the subsequent computation of ρ_T, for each solar zenith angle, was carried out for several values of τ_a in order to determine the effect of measurement error in τ_a on the TOA radiance. It is important to note that the same value of τ_a was used in the retrieval algorithm and the TOA-radiance prediction code during this process; however, the value of τ_a used to generate the pseudo data was 0.2. Error in the measurement of τ_a is manifest in error in the retrieved value of ω_0. Table 1 provides the retrieved value of ω_0 corresponding to a given value of τ_a.

The large spike in error in the TOA radiance for $\theta_0 = 50°$ and 45°, Figures 6c and 6d, respectively, is due to the bump in the retrieved phase function near $\Theta = 120°$. Ignoring this, the results presented in the figures clearly show that when the correct value of τ_a is avaliable the error in the predicted TOA radiance is always less than 2% and is usually $\lesssim$ 1% as long as $\theta_T \lesssim 60°$, a condition met by all satellite-borne scanning radiometers of interest. A given percent error in τ_a results in a significantly smaller percent error in the TOA radiance, e.g., a 30% error in τ_a produces at most a $\sim$ 3% error in radiance at $\theta_0 = 60°$, a 5% error at $\theta_0 = 50°$, and $\lesssim$ 9% error at $\theta_0 = 45°$.

This is consistent with the fact that τ_a is not even required in the single scattering regime (Section 2).

Figure 7 provides the error in the predicted TOA radiance for a given error in the measured radiance at the surface. It was assumed that a single radiometer is used to measure L_B, and therefore the calibration error was taken to be the same for all the measurement angles (here $\pm 5\%$). In contrast to the small effect that error in τ_a has on the predicted TOA radiance, error in L_B results in an error of similar magnitude in the predicted L_T. This is also in agreement with the single scattering analysis in Section 2. Thus, the results of the simulations presented in this section suggest that the radiative transfer process in the multiple scattering regime does not add significant error to the prediction of L_T over and above that predicted by the single scattering analysis. As the optical thickness increases, the accuracy of the method will likely decrease, and the sensitivity to error will surely increase; however, the value of τ_a used here is already high for the marine atmosphere,[18–20] so the method should be applicable in most situations.

5. Sensitivity analysis.

In this section we report the sensitivity of the predicted TOA radiances to the various assumptions that were made in the retrieval process. In particular, we examine the effect of omitting measurement of the solar aureole, the effect of an incorrect assumption regarding the vertical structure of the atmosphere, and the effects of ignoring the roughness of the sea surface, the curvature of the atmosphere, and the polarization of the radiation, in the $\omega_0 P(\Theta)$ retrieval algorithm.

5.A. Absence of solar aureole measurements.

In the results presented in Section 4.B for multiple scattering it was assumed that measurements of the sky radiance could be made at angles as small as 0.92° from the sun. In practice, this is very difficult. However, Nakajima et al.,[21] have reported solar aureole measurements to angles as small as 2° from the sun. For measurements carried out at sea, the motion of the ship requires the use of an all-sky camera[22] for measuring the sky radiance and, due to dynamic range limitations,

a portion of the aureole must be blocked in such measurements. This further restricts the amount of the solar aureole that can be obtained. Thus, it is important to understand the effect that the minimum angle that can be observed in the solar aureole has on the prediction of the radiance at the top of the atmosphere, from ρ_B measured at the surface. The difficulty with not measuring a significant portion of the solar aureole is that in the inversion process there will be an inconsistency between the measured value of τ_a and the aerosol phase function at each stage of the iteration process. Because of the lack of small-angle measurements, the phase function will not be correct in the aureole region for aerosols possessing a phase function with a strong forward peak. For such aerosols, a significant portion of the aerosol optical thickness is due to small-angle scattering. Thus if the aureole is not measured, usually a smaller value of τ_a would be appropriate in the inversion process to arrive at the correct values of $\omega_0 P(\Theta)$ outside the aureole region.

To investigate the aureole influence, we repeated the computations carried out in Section 4.B for three simulations in which pseudo data in the almucantar with $\Theta_{\text{Min}} = 2.62°$, 8.68°, and 17.33° were utilized. Figure 8 provides the error in the TOA radiance when $\Theta_{\text{Min}} = 2.62°$, a value that would be possible if the measurements were made from a stable platform such as an island. As before, in addition to the correct value of τ_a, the computations were also carried out for six other values of τ_a near the correct value. It is seen that the error in the TOA radiance is similar to that in Figure 7, where $\Theta_{\text{Min}} = 0.92°$. Figures 9 and 10 provide the error for $\Theta_{\text{Min}} = 8.68°$ and 17.33° respectively. Examination of these shows that when the measurements are made at $\theta_0 = 60°$ and the TOA-radiance is constructed at the same value of θ_0 the error is only slightly greater than that provided in Figure 7; however, when the TOA radiance is predicted at $\theta_0 = 45°$ and 50°, the inconsistency between the measured value of τ_a and the aerosol phase function is apparent. To achieve small errors in the TOA radiance a smaller value of τ_a must be used in both the retrieval and the TOA-radiance prediction codes. Is there any way of knowing what value of τ_a to use? Table 2 provides the values of ω_0 retrieved in our simulations for a given value of Θ_{Min} and τ_a. Comparing Figures 8–10 with Table 2, one sees that when the value of τ_a that produces a value of ω_0 that is closest to the correct value is used in these two codes, the error is essentially the same as the error for $\Theta_{\text{Min}} = 0.92°$. But how can we know the correct value of ω_0? In general there is no way of knowing ω_0; however, in an open-ocean regime in which the aerosol is locally

generated, it is reasonable to expect that ω_0 will be very close to unity. As aureole measurements need only be absent when the sky radiance is measured from a ship at sea, the assumption that $\omega_0 \approx 1$ should be justified when it is needed. An alternate method of dealing with the absence of aureole measurements is discussed in the appendix.

5.B. Incorrect vertical structure assumed in the inversion algorithm.

In all of the simulations studied in Section 4.B, the vertical structure of the atmosphere — two layers with all of the aerosols in the lower layer and all of the molecular scattering confined to the upper layer — assumed in the inversion code, and also the code to predict the TOA radiance from the retrieved optical properties, was the same as the vertical structure used to generate the pseudo data, i.e., the correct vertical structure was used in the retrieval and prediction process. As the aerosol over the oceans is usually mostly confined to the marine boundary layer, we expect this to be similar to the typical situation. However, it is important to understand the error in the TOA radiances when an incorrect vertical structure is assumed. For this purpose, we generated pseudo sky radiance data using the following vertical structure of the atmosphere: a maritime aerosol in the marine boundary layer (M99 in Figure 2) and an aerosol represented by the Shettle and Fenn[17] tropospheric model with a 50% relative humidity (T50 in Figure 2) in the free troposphere. The aerosol optical thickness were taken to be 0.15 and 0.05 in the boundary layer and free troposphere, respectively. The thickness of the boundary layer was assumed to be $\sim$ 2 km, so 22% of the molecular scattering was placed in the lower layer and 78% in the free troposphere. It was assumed that the total aerosol optical thickness was correctly measured, i.e., the measured τ_a was assumed to be error free. The pseudo data were introduced into the $\omega_0 P(\Theta)$ retrieval algorithm used in Section 4.B, which assumed a vertical structure in which all of the aerosol was in the boundary layer and the free troposphere was aerosol free. Thus, an incorrect vertical structure was assumed in the retrieval algorithm. The same incorrect vertical structure was also used in the TOA radiance-prediction code. Figure 11 provides the error in the predicted TOA radiance using this procedure. It is seen that the error is not significantly different from that shown in Figure 6, i.e., $\lesssim$ 1.5%. If the correct vertical structure were known, e.g., from LIDAR observations, and used in the retrieval and TOA-radiance prediction codes the resulting error is provided in Figure 12. In this case it

was assumed in the retrieval process that the aerosol possesses the same $\omega_0 P(\Theta)$ in both layers, but τ_a was correctly divided between the two layers. Comparison of Figures 11 and 12 shows that using the correct vertical structure leads to some improvement; however, it does not appear that significantly better results are obtained by knowing the vertical structure of the aerosol. These simulations suggest that knowledge of the vertical structure of the atmosphere is not critical for estimating the TOA radiance from measurements of ρ_B and τ_a.

The aerosol models used in the preparation of Figures 11 and 12 were only weakly absorbing, i.e., ω_0 was ≈ 0.930 and 0.999 for T50 and M99, respectively. To examine the effect of a strongly-absorbing aerosol, we replaced T50 in the simulations presented in Figures 11 and 12 with the Shettle and Fenn Urban model for a relative humidity of 50% (U50). For U50, $\omega_0 \approx 0.603$ at 865 nm. This situation could represent an example of a layer of polluted urban air transported over the ocean above the marine boundary layer. Observations of such incidents off the U.S. East Coast have been reported.[23] When the incorrect vertical distribution was used, the results were similar to those for weakly-absorbing aerosols in Figure 11, but with the curves moved vertically by $\sim 1.5\%$ (Figure 11a), $\sim 1.7\%$ (Figure 11b), and $\sim 2\%$ (Figure 11c), i.e., the error for $\theta_0 = 45°$ near $\theta_T = 0$ was $\sim 3.7\%$ for the U50 aerosol compared to $\sim 1.7\%$ for T50 (Figure 11c). When the correct vertical structure in τ_a was used, and the aerosol was assumed to have the same $\omega_0 P(\Theta)$ in both layers in the retrieval and prediction codes, the results were significantly improved. In this case, the curves were similar to those in Figure 12, having the values of $\sim 1\%$, $\sim 1.3\%$, and $\sim 2\%$ near $\theta_T = 0$ for $\theta_0 = 60°$, 50°, and 45°, respectively. Clearly, replacing the weakly-absorbing T50 with the strongly-absorbing U50 increases the overall error in ρ_T; however, the error can be reduced significantly by knowing the correct vertical structure.

5.C. Use of a flat sea surface in the inversion algorithm.

In all of the simulations discussed thus far it has been assumed that the sea surface was flat, i.e., there were no surface waves; however, even under light wind conditions the surface will become roughened. To understand the effect of ignoring the surface roughness in the retrieval code, we simulated the surface and TOA radiances for an ocean obeying the Cox and Munk[24] surface slope

distribution with a wind speed of $\sim$ 7.5 m/s. The simulated radiances were then used in the retrieval code, which employs a flat sea surface, to estimate $\omega_0 P(\Theta)$. The correct value of τ_a was used and $\Theta_{\text{Min}} = 0.92°$. The retrieved $\omega_0 P(\Theta)$ was then used in the TOA-radiance prediction code, which included the correct surface roughness, to estimate the TOA radiance. Thus, the assumption of a flat sea surface was used *only* in the retrieval code. The resulting error in the TOA radiance is presented in Figure 13, which shows that the error using this procedure is similar to that when the surface is actually flat (Figure 6) except near $\theta_T \approx 37°$ for $\theta_0 = 50°$ and $\theta_T \approx 45°$ for $\theta_0 = 45°$ (Figures 6c and 6d). The dissimilarity at these values of θ_T is due to the absence of the "spike" in the retrieved $\omega_0 P(\Theta)$ near $\Theta = 120°$ in the rough surface case. Recall, the spike was due to backscattering following reflection of direct solar radiation from the surface. When the surface is rough, the reflected solar beam is diffused over a range of angles, so ρ_B does not contain a maximum opposite the reflected solar beam. Rather, the radiance backscattered from the reflected solar beam is spread over a range of θ_B and the error it induces in the retrieved $\omega_0 P(\Theta)$ is no longer concentrated near $\Theta = 120°$. Note that the correct surface roughness was used in the prediction code for ρ_T. This is acceptable, as surface measurements of the wind speed would be expected to be available at any ρ_B-measurement site, i.e., the correct value of the wind speed could always be used with the flat-surface retrieved $\omega_0 P(\Theta)$ to estimate the TOA radiance.

5.D. Approximation of a plane-parallel atmosphere in the inversion algorithm.

Thus far, we have been assuming that radiative transfer in the atmosphere could be adequately approximated by treating the atmosphere as a plane-parallel medium (PPM), i.e., we have ignored the curvature of the atmosphere. To understand the error in our procedure induced by this assumption, we used a two-layer Monte Carlo radiative transfer code in spherical geometry[25] to simulate the normalized radiance that would be measured at the top and bottom of an atmosphere, ρ_T and ρ_B, modeled as a spherical shell medium (SSM). In the code it was assumed that the aerosol layer was 2 km thick and the molecular-scattering layer was 18 km thick (the total thickness of the atmosphere was 20 km). The aerosol optical properties were provided by the M99 model (Figure 2). The values of ρ_B in the solar almucantar and principal plane from this code were then inserted in the retrieval program (that assumes the atmosphere is plane parallel) and $\omega_0 P(\Theta)$ was retrieved.

The retrieved $\omega_0 P(\Theta)$ was then used in the plane-parallel prediction code to compute the radiance at the top of the atmosphere for comparison with ρ_T. Figure 14 provides the comparison between the predicted and true values of ρ_T using this procedure. This figure should be compared with Figure 6, which used the identical procedure except that the "true" values of ρ_T and ρ_B were also generated for a plane-parallel atmosphere. Other than the ragged nature of the curves in Figure 14 (caused by Monte Carlo fluctuations in both the ρ_B pseudo data used in the retrieval algorithm and in ρ_T used to test the efficacy of the procedure), there is no significant difference between the two simulations. This suggests that the approximation of a plane-parallel atmosphere does not significantly degrade the prediction ρ_T, for $\theta_0 \sim 60°$.

5.E. Ignoring polarization in the inversion algorithm.

In our simulations, scalar radiative transfer theory (ignores polarization) has been used in all of the inversions. However, it is known that scalar theory leads to error in the computed radiance of a few percent.[26,27] To understand the error that could result from the use of scalar theory, we used vector theory (includes polarization) to create the sky radiance pseudo data ρ_B and the "true" TOA radiance ρ_T. The scattering phase matrix used in the simulation was computed from the aerosol model (M99) size distribution and index of refraction using Mie theory. The resulting values of ρ_B were then inserted into the inversion algorithm (scalar) and the phase function and single scattering albedo were retrieved. These were then used in the scalar radiative transfer equation to compute the TOA radiance. The results are provided in Figure 15 for $\theta_0 = 60°$ with $\Theta_{\min} = 0.92°$ and 2.62°. To see the effect of ignoring polarization, compare Figures 15a and 15b with Figures 6b and 8a, respectively. We note that when polarization is included in the pseudo data, but neglected in the inversion algorithm and the prediction code, there is little difference in the retrieval error near $\theta_T = 0$, however, the difference gradually increases to become about 2% near $\theta_T = 40°$. The error in the predicted TOA radiance ranges from $\sim +1\%$ near $\theta_T = 10°$ to $\sim -2\%$ near $\theta_T = 40°$. This error is primarily derived from two single-scattering processes: Fresnel reflection of the solar beam from the sea surface and subsequent aerosol scattering toward the sensor; and aerosol scattering toward the sea surface and subsequent Fresnel reflection from the sea surface toward the sensor. These processes lead to different values of ρ_T in scalar and vector radiative transfer theory. In

the standard Stokes vector (I,Q,U,V) representation of partially polarized light, e.g., see van de Hulst,[28] correctly accounting for these processes requires an estimate for $\Theta \lesssim 90°$ of the scattering phase matrix element that couples I and Q. This, in turn, requires measurement of the polarization (Stokes vector) associated with ρ_B.

6. Application to shorter wavelengths.

The preceeding analysis has centered on 865 nm, where the water-leaving radiance can be taken to be zero in nearly all oceanic environments, and therefore need not be measured. At shorter wavelengths, e.g., in the blue, the water-leaving reflectance transmitted to the top of the atmosphere can make a significant contribution to ρ_T, so to attempt such analysis in the blue, one must have measurements of the water-leaving reflectance. In the presence of such measurements, can the prediction of ρ_T be carried out at the accuracy suggested in Sections 4 and 5 for 865 nm? Considering the fact that the major contributor to ρ_T is molecular scattering, the properties of which are precisely known, it seems reasonable to expect that ρ_T could be estimated with even higher accuracy in the blue than in the near infrared. However, the presence of radiometric calibration errors will make a more severe impact on the retrieval algorithm in the blue because the reflectance error will be much larger in relation to the magnitude of the aerosol reflectance than it was at 865 nm. Thus, the retrieved aerosol phase function in the blue can be expected to be much poorer in the presence of similar radiometric calibration errors than at 865 nm. In this section we examine the accuracy that one might realistically expect in the blue, given measurements of the water-leaving reflectance.

As in the earlier examples, we assumed the aerosol was that provided by the Shettle and Fenn[17] Maritime model for relative humidity 99%, but at a wavelength of 443 nm. The aerosol optical thickness at 443 nm was taken to be 0.20, which is approximately the value that would be obtained at 443 nm for M99 if τ_a at 865 nm were 0.20 as in the earlier sections. As before, we perform the $\omega_0 P(\Theta)$ retrievals assuming several values of τ_a (0.16, 0.18, 0.20, 0.22, and 0.24) around the correct value to simulate error in the measured value. Figures 16 and 17 provide the error in the predicted TOA radiance for various values of τ_a for $\Theta_{\mathrm{Min}} = 0.92°$ and 2.62°, respectively. We note that

the error in the predicted radiance is negligible for $\Theta_{\text{Min}} = 0.92°$, and $\lesssim 1\%$ for $\Theta_{\text{Min}} = 2.62°$, when the correct value of τ_a is used. Also, as in the case of the near infrared, a given % error in τ_a results in a much smaller % error in the predicted radiance (Figures 6 and 8–10). Figure 18 provides the error in the predicted radiance that is obtained when the correct value of τ_a is used in the retrieval and prediction, but the measurement of ρ_B is assumed to have a $\pm 5\%$ error. As in the near infrared (Figure 7) the error in the predicted radiance is somewhat less than the radiometric error. These simulations suggest that, given measurements of the water-leaving radiance in the blue, the predictability of the TOA radiance from measurements made at the surface is as good at 443 nm as it is at 865 nm.

7. Concluding remarks

In this paper we have examined the accuracy that one could expect in estimating the reflectance ρ_T of the ocean-atmosphere system based on a measurement suite carried out at the sea surface. Simulations were carried out in which the aerosol scattering phase function and single scattering albedo were derived when the solar zenith angle was 60°. Based on these retrievals, ρ_T was estimated for $\theta_0 = 60°$, 50°, and 45°, under the assumption that the aerosol optical properties, as defined by $\omega_0 P(\Theta)$ do not change as θ_0 varies from 60° to 45°.

Initially, the wavelength was taken to be 865 nm, as the water-leaving radiance at this wavelength would be negligible in all but the most turbid coastal waters. Also, it was assumed that there were no errors in the measurements of the sky radiance, ρ_B, and in the aerosol optical thickness τ_a.

For viewing angles $\theta_T \lesssim 20°$ the error in the predicted radiance at the top of the atmosphere was typically $\lesssim 1\%$ when measurements of the solar aureole were made with $\Theta_{\text{Min}} = 0.92°$ (Figure 6). Omitting the solar aureole increases the error because it is then inconsistent to use the correct value of τ_a in the inversion-prediction process. However, if the correct value of ω_0 can be estimated, e.g., in the case of a locally-generated maritime aerosol for which $\omega_0 \approx 1$, excellent results can still be obtained if the value of τ_a that provides the correct value of ω_0 in the inversion algorithm is also used in the prediction algorithm. Alternatively, if a wide-field-of-view sun photometer is used to

estimate τ_a, and the sky radiance measurements exclude the portion of the solar aureole observed by the sun photometer, then using this photometer-measured value of τ_a in the inversion-prediction process will yield an excellent prediction of ρ_T (Appendix A, Figure 19).

We systematically investigated the influence of the simplifying assumptions made in the inversion-prediction process, such as, modeling the atmosphere as a plane-parallel medium, employing a smooth sea surface in the inversion algorithm, using scalar radiative transfer theory, and assuming that the aerosol was confined to a thin layer just above the sea surface. In most cases, these assumptions did not increase the error beyond $\pm 1\%$. The single exception was the use of scalar radiative transfer theory, for which the error grew to as much as $\sim 2\%$ for $\theta_T \gtrsim 30°$, even though it was within $\pm 1\%$ for $\theta_T \lesssim 20°$ (Figure 15). This error could be reduced by measuring the polarization associated with ρ_B, and using an inversion-prediction code that includes polarization.

In simulations in which the aerosol consisted of two types (M99 uniformly mixed in the marine boundary layer and T50 uniformly mixed in the free troposphere), knowledge and use of the vertical distribution of τ_a, as might be inferred from LIDAR measurements, did not appreciably improve the predicted ρ_T over that predicted by assuming all of the aerosol was in the marine boundary layer. This suggests that the vertical distribution of the aerosol is unimportant; however, this derives from the fact that the aerosol models used were only weakly absorbing. When T50 was replaced by the strongly-absorbing U50, sensitivity to the vertical structure was observed. Also, the error was larger than that for the weakly-absorbing aerosols, suggesting that, for the purpose of vicarious calibration of space-borne radiometers, regions that may be influenced by strongly-absorbing aerosols should be avoided.

It is possible to extend this analysis to the blue region of the spectrum, when ρ_w is available there. We found significantly better predictions of ρ_T in the blue (443 nm) than in the NIR because a major portion of ρ_T is the result of molecular scattering, which is precisely known.

It is important to note that our simulations have been carried out using the Shettle and Fenn[17] M99 phase function (Figure 2), which has a very sharp forward peak. As the $\omega_0 P(\Theta)$ retrieval algorithm performs most poorly with such phase functions, we believe that the results

described in this paper represent a near worst-case scenario. In general, the error in the retrieved $\omega_0 P(\Theta)$ and the predicted ρ_T should be significantly less than that provided by M99.

We also simulated the influence of calibration errors in both the sun photometer and the ρ_B radiometer. The results suggest that the relative error in the predicted ρ_T is similar in magnitude to that in the measured ρ_B (actually it is somewhat less). However, the relative error in ρ_T induced by error in τ_a is usually $\ll$ the relative error in τ_a (Figure 6), and in fact, as τ_a becomes small (single scattering) error in τ_a becomes irrelevant (Eq. (4)).

The purpose of undertaking this study was to investigate the accuracy that one might reasonably expect in computing the TOA radiance for the purpose of vicarious calibration of space-borne sensors. We note the results presented here apply only to the idealized case of a cloud-free sky and a horizontally-homogeneous aerosol. However, we do not consider this a blemish. We believe a reasonable strategy for vicarious calibration over the oceans in the NIR ($\rho_w = 0$) is to place unattended sun photometer/sky radiometer units[29] on small remote islands, but to use, for vicarious calibration, only the surface data that was acquired simultaneously with ρ_T under near-ideal conditions. Under such circumstances, the results presented here should be applicable.

It is now possible to calibrate a radiometer relative to a standard lamp to within $\pm 2.5\%$,[12] although it is believed that detector-based calibration could reduce the uncertainty to $\pm 1\%$.[30] Thus, from our simulations, it appears safe to conclude that at present, the most important error source in the prediction of ρ_T from ρ_B is likely to be error in the ρ_B measurement.

Appendix A: Is the solar aureole really needed?

It is interesting to see if there is a method of dealing with the absence of the solar aureole without having to resort to assuming the $\omega_0 = 1$ for the aerosol as described in the text. Here we examine the possibility of using a wide-field-of-view sun photometer to measure the appropriate optical thickness to be used in the retrieval. The idea is simple: if sky radiance measurements can only be made at angles greater than α from the sun, use a sun photometer that has an acceptance half angle of α. In this way, neglecting multiple scattering near the aureole, the photometer will measure an optical thickness $\tau_a^{(m)}$ that is related to the actual optical thickness τ_a through

$$\frac{\tau_a^{(m)}}{\tau_a} = \frac{\int_\alpha^\pi P(\Theta) \sin\Theta \, d\Theta}{\int_0^\pi P(\Theta) \sin\Theta \, d\Theta}.$$

$\tau_a^{(m)}$ is hypothesized to be the appropriate value of aerosol optical thickness to be used in the aureole-free retrievals, with $P(\Theta)$ truncated at $\Theta = \alpha$. Results of tests of this idea are presented in Figure 19, which provides the error in the TOA radiance when the both the inversion algorithm and the TOA-radiance prediction are carried out using $\tau_a^{(m)}$ for the four values of $\Theta_{\text{Min}} = \alpha$ used in this study. For $\Theta < \Theta_{\text{Min}}$, $P(\Theta)$ was taken to be $P(\Theta_{\text{Min}})$ in *both* the inversion and prediction codes. For the range of θ_T of interest here ($\theta_T < 60°$) the difference between $\Theta_{\text{Min}} = 0.92°$ and 17.33° is less than 1% in the error in the predicted TOA radiance and the difference between 0.92° and 8.68° is usually less than 0.4%. These results suggest that if a calibrated solar photometer were available with the proper (wide) field of view, measurement of the solar aureole would not be necessary.

References

[1] H. R. Gordon, "A preliminary assessment of the Nimbus-7 CZCS atmospheric correction algorithm in a horizontally inhomogeneous atmosphere," in *Oceanography from Space*, edited by J. R. F. Gower (Plenum Press, New York, NY, 1981) p. 257–266.

[2] H. R. Gordon, "Reduction of error introduced in the processing of coastal zone color scanner-type imagery resulting from sensor calibration and solar irradiance uncertainty," Applied Optics **20**, 207–210 (1981).

[3] P. Koepke, "Vicarious Satellite Calibration in the Solar Spectral Range by Means of Calculated Radiances and its Application to Meteosat," Applied Optics **21**, 2845–2854 (1982).

[4] M. Viollier, "Radiance calibration of the Coastal Zone Color Scanner: a proposed adjustment," Applied Optics **21**, 1142–1145 (1982).

[5] H. R. Gordon, D. K. Clark, J. W. Brown, O. B. Brown, R. H. Evans and W. W. Broenkow, "Phytoplankton pigment concentrations in the Middle Atlantic Bight: comparison between ship determinations and Coastal Zone Color Scanner estimates," Applied Optics **22**, 20–36 (1983).

[6] H. R. Gordon, J. W. Brown, O. B. Brown, R. H. Evans and D. K. Clark, "Nimbus 7 Coastal Zone Color Scanner: reduction of its radiometric sensitivity with time," Applied Optics **22**, 3929–3931 (1983).

[7] W. A. Hovis, J. S. Knoll and G. R. Smith, "Aircraft Measurements for Calibration of an Orbiting Spacecraft Sensor," Applied Optics **24**, 407–410 (1985).

[8] R. S. Fraser and Y. J. Kaufman, "Calibration of satellite sensors after launch," Applied Optics **25**, 1177–1185 (1986).

[9] P. N. Slater, S. F. Biggar, R. G. Holm, R. D. Jackson, Y. Mao, M. S. Moran, J. M. Palmer and B. Yuan, "Reflectance- and Radiance-Based Methods for the In-Flight Absolute Calibration of Multispectral Sensors," Remote Sensing of Environment **22**, 11–37 (1987).

[10] R. Frouin and C. Gautier, "Calibration of NOAA-7 AVHRR, GOES-5, and GOES-6 VISSR/VAS Solar Channels," Remote Sensing of Environment **22**, 73–101 (1987).

[11] Y. J. Kaufman and B. N. Holben, "Calibration of the AVHRR visible and near-IR bands by atmospheric scattering, ocean glint, and desert reflection," Int. Jour. Rem. Sens. **14**, 21–52 (1993).

[12] S. F. Biggar, P. N. Slater and D. I. Gellman, "Uncertainties in the in-flight calibration of sensors with reference to measured ground sites in the 0.4 to 1.1 μm range," Remote Sensing of Environment **48**, 245–252 (1994).

[13] P. Y. Deschamps, F. M. Bréon, M. Leroy, A. Podaire, A. Bricaud, J. C. Buriez and G. Sèze, "The POLDER Mission: Instrument characteristics and scientific objectives," IEEE Trans. Geoscience and Remote Sensing **32**, 598–615 (1994).

[14] S. B. Hooker, W. E. Esaias, G. C. Feldman, W. W. Gregg and C. R. McClain, *SeaWiFS Technical Report Series: Volume 1, An Overview of SeaWiFS and Ocean Color* (NASA, Greenbelt, MD, Technical Memorandum 104566, July 1992).

[15] V. V. Salomonson, W. L. Barnes, P. W. Maymon, H. E. Montgomery and H. Ostrow, "MODIS: Advanced Facility Instrument for Studies of the Earth as a System," IEEE Geosci. Rem. Sens. **27**, 145–152 (1989).

[16] M. Wang and H. R. Gordon, "Retrieval of the Columnar Aerosol Phase Function and Single Scattering Albedo from Sky Radiance over the Ocean: Simulations," Applied Optics **32**, 4598–4609 (1993).

[17] E. P. Shettle and R. W. Fenn, *Models for the Aerosols of the Lower Atmosphere and the Effects of Humidity Variations on Their Optical Properties* (Air Force Geophysics Laboratory, Hanscomb AFB, MA 01731, AFGL–TR–79-0214, 1979).

[18] P. J. Reddy, F. W. Kreiner, J. J. Deluisi and Y. Kim, "Aerosol Optical Depths Over the Atlantic Derived From Shipboard Sunphotometer Observations During the 1988 Global Change Expedition," Global Biogeochemical Cycles **4**, 225–240 (1990).

[19] G. K. Korotaev, S. M. Sakerin, A. M. Ignatov, L. L. Stowe and E. P. McClain, "Sun-Photometer Observations of Aerosol Optical Thickness over the North Atlantic from a Soviet Research Vessel for Validation of Satellite Measurements," Jour. Atmos. Oceanic Technol. **10**, 725–735 (1993).

[20] Y. V. Villevalde, A. V. Smirnov, N. T. O'Neill, S. P. Smyshlyaev and V. V. Yakovlev, "Measurement of Aerosol Optical Depth in the Pacific Ocean and North Atlantic," Jour. Geophys. Res. **99D**, 20983–20988 (1994).

[21] T. Nakajima, M. Tanaka and T. Yamauchi, "Retrieval of the Optical Properties of Aerosols from Aureole and Extinction Data," Applied Optics **22**, 2951–2959 (1983).

[22] K. J. Voss and G. Zibordi, "Radiometric and Geometric Calibration of a Visible Spectral Electro-Optic "Fisheye" Camera Radiance Distribution System," Jour. Atmos. and Oceanic Technology **6**, 652–662 (1989).

[23] S. Ismail, E. V. Browell, S. A. Kooi and G. D. Nowicki, "Simultaneous LASE and LITE Aerosol Profile Measurements over the Atlantic," EOS, Transactions, American Geophysical Union **76**, S71 (1995).

[24] C. Cox and W. Munk, "Measurements of the Roughness of the Sea Surface from Photographs of the Sun's Glitter," Jour. Opt. Soc. of Am. **44**, 838–850 (1954).

[25] K. Ding and H. R. Gordon, "Atmospheric correction of ocean color sensors: Effects of earth curvature," Applied Optics **33**, 7096–7016 (1994).

[26] G. W. Kattawar, G. N. Plass and S. J. Hitzfelder, "Multiple scattered radiation emerging from Rayleigh and continental haze layers. 1: Radiance, polarization, and neutral points," Applied Optics **15**, 632–647 (1976).

[27] H. R. Gordon, J. W. Brown and R. H. Evans, "Exact Rayleigh Scattering Calculations for use with the Nimbus-7 Coastal Zone Color Scanner," Applied Optics **27**, 862–871 (1988).

[28] H. C. van de Hulst, *Multiple Light Scattering* (Academic Press, New York, 1980), 739 pp.

[29] B. N. Holben, T. F. Eck, I. Slutsker, D. Tanre, J. P. Buis, A. Setzer, E. Vermote, J. Reagan, Y. Kaufman, T. Nakajima, F. Lavenu and I. Jankowiak,, 1996, Automatic Sun and Sky Scanning Raiometer System for Network Aerosol Monitoring, *Remote Sensing of Environment* (Accepted) .

[30] P. N. Slater, S. F. Biggar, K. J. Thome, D. I. Gellman and P. R. Spyak, *Journal of Atmospheric and Oceanic Technology* (1995), (In press).

Figure Captions

Figure 1. The basic idea behind vicarious calibration. BOA and TOA are, respectively, the top and bottom of the atmosphere. L_T and L_B are the radiances measured at the TOA and BOA for a solar zenith angle θ_0. In the geometry shown, the single-scattering angle Θ is common to both L_T and L_B.

Figure 2. Scattering phase functions for the Shettle and Fenn[17] Maritime aerosol models with a relative humidity of 99% (M99) and the Tropospheric model with relative humidity 50% (T50).

Figure 3. Error in the retrieved $\omega_0 P(\Theta)$ for the M99 model if the single-scattering approximation were the correct physics for radiative transfer.

Figure 4. Error in the retrieved $\omega_0 P(\Theta)$ for the M99 model when multiple scattering is included in the radiative transfer.

Figure 5. Error in the estimated ρ_T as a function of θ_T when single scattering was assumed to be the correct radiative transfer physics. The error in $\omega_0 P(\Theta)$ for this case is provided in Figure 3. There was assumed to be no contribution from molecular scattering to ρ_B or ρ_T.

Figure 6. (a): Comparison between the aerosol phase function retrieved (circles) from ρ_B at 865 nm and the true phase function (line) when $\theta_0 = 60°$ for the M99 model with $\tau_a = 0.20$ and $\Theta_{\mathrm{Min}} = 0.92°$. (b): Error in estimation of ρ_T using the retrieved phase function in (a) with $\theta_0 = 60°$. (c): Same as (b) except $\theta_0 = 50°$. (d): Same as (c) except $\theta_0 = 45°$. In panels (b)–(d), the curves from bottom to top correspond to using $\tau_a = 0.14$, 0.16, 0.18, 0.20, 0.22, 0.24, and 0.26, in both the retrieval and prediction codes.

Figure 7. Error in ρ_T induced by a $\pm 5\%$ error in the measurement of ρ_B. The measurement of τ_a is assumed to be error-free. The retrieval of $\omega_0 P(\Theta)$ is carried out when $\theta_0 = 60°$. (a): $\theta_0 = 60°$. (b): $\theta_0 = 50°$. (c): $\theta_0 = 45°$.

Figure 8. Same as Figure 6 except $\Theta_{\mathrm{Min}} = 2.62°$.

Figure 9. Same as Figure 6 except $\Theta_{\mathrm{Min}} = 8.68°$.

Figure 10. Same as Figure 6 except $\Theta_{\mathrm{Min}} = 17.33°$.

Figure 11. Error in ρ_T for a two-layer atmosphere with aerosol in both layers. The retrieval and prediction codes both assume that the aerosol is only in the lower layer and use the correct value of $\tau_a = \tau_T + \tau_B$. "R" stands for Rayleigh and "A" stands for aerosol. (a): $\theta_0 = 60°$. (b): $\theta_0 = 50°$. (c): $\theta_0 = 45°$.

Figure 12. Same as Figure 11 except the retrieval and prediction codes use the correct vertical structure in τ_a.

Figure 13. Same as Figure 6, showing the effect of sea surface roughness. Retrieval code assumes $W = 0$, while the prediction code uses the correct value of W.

Figure 14. Same as Figure 13 showing the effect of the curvature of the Earth's atmosphere. Retrieval and prediction codes assume a plane-parallel atmosphere.

Figure 15. Same as Figure 14 showing the effect of ignoring polarization in the retrieval and prediction codes: (a) $\Theta_{\mathrm{Min}} = 0.92°$; (b) $\Theta_{\mathrm{Min}} = 2.62°$.

Figure 16. Same as Figure 6 except the wavelength is 443 nm.

Figure 17. Same as Figure 16, except Θ_{Min} is increased from 0.92° to 2.62°.

Figure 18. Error in the predicted ρ_T at 443 nm for a $\pm 5\%$ error in ρ_B for $\Theta_{\mathrm{Min}} = 0.92°$ (solid lines) and $\Theta_{\mathrm{Min}} = 2.62°$ (dashed lines). Positive (negative) errors in ρ_T correspond to positive (negative) errors in ρ_B.

Figure 19. Error in the predicted ρ_T when the phase function is truncated at Θ_{Min} and the value of τ_a, measured with a sun photometer of half-angle field-of-view Θ_{Min}, is used in the retrieval

and prediction codes. τ_a = 0.187, 0.162, 0.122, and 0.92 for the curves from top to bottom, corresponding to Θ_{Min} = 0.92°, 2.62°, 8.68°, and 17.33°.

Table 1: Retrieved ω_0 for a given τ_a. True value of τ_a is 0.2 and true value of $\omega_0 = 0.998$.

τ_a:	0.14	0.16	0.18	0.20	0.22	0.24	0.26
ω_0:	1.235	1.131	1.050	0.986	0.934	0.891	0.855

Table 2: Retrieved ω_0 for a given Θ_{Min} and τ_a. The true value of τ_a is 0.20 and true value of $\omega_0 = 0.998$.

Θ_{Min}	τ_a						
	0.14	0.16	0.18	0.20	0.22	0.24	0.26
0.92°	1.235	1.131	1.050	0.986	0.934	0.891	0.855
2.62°	1.207	1.105	1.026	0.964	0.913	0.871	0.837
8.68°	1.067	0.978	0.910	0.856	0.912	0.776	0.747
17.33°	0.978	0.898	0.836	0.778	0.749	0.717	0.619

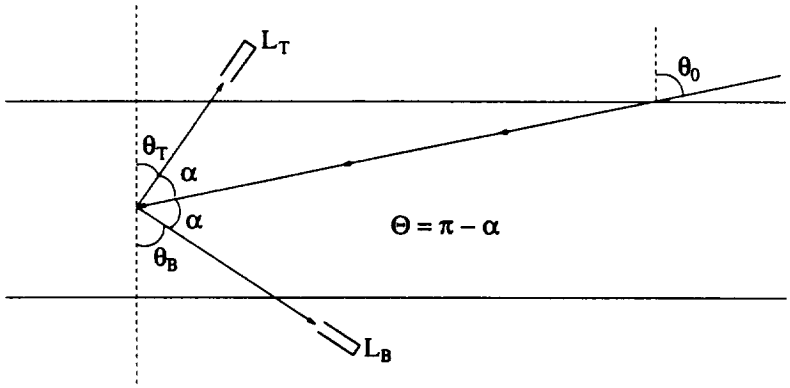

Figure 1. The basic idea behind vicarious calibration. BOA and TOA are, respectively, the top and bottom of the atmosphere. L_T and L_B are the radiances measured at the TOA and BOA for a solar zenith angle θ_0. In the geometry shown, the single-scattering angle Θ is common to both L_T and L_B.

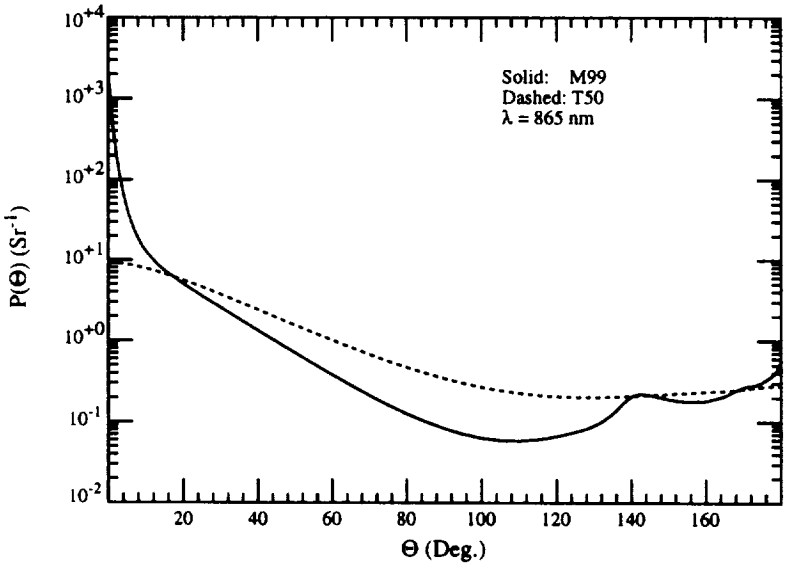

Figure 2. Scattering phase functions for the Shettle and Fenn[17] Maritime aerosol models with a relative humidity of 99% (M99) and the Tropospheric model with relative humidity 50% (T50).

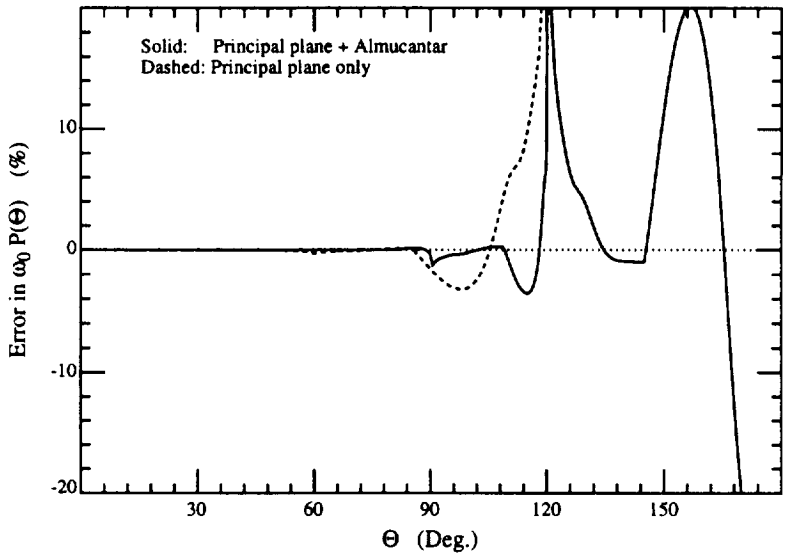

Figure 3. Error in the retrieved $\omega_0 P(\Theta)$ for the M99 model if the single-scattering approximation were the correct physics for radiative transfer.

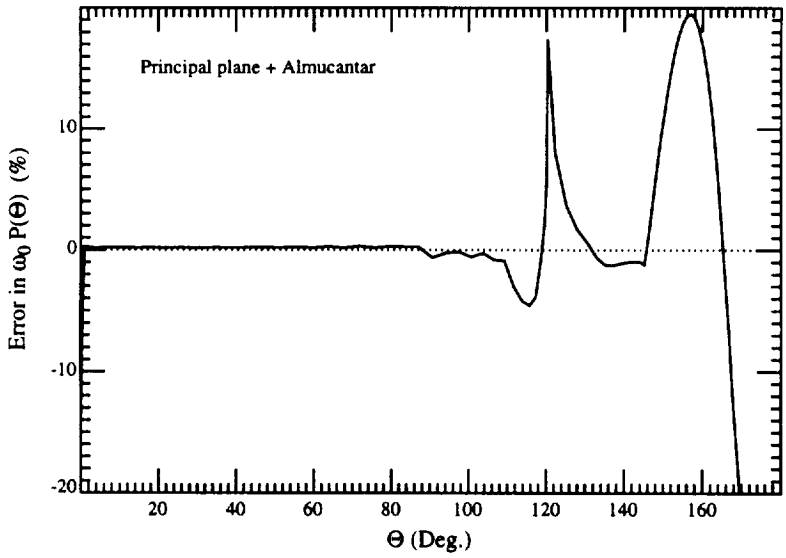

Figure 4. Error in the retrieved $\omega_0 P(\Theta)$ for the M99 model when multiple scattering is included in the radiative transfer.

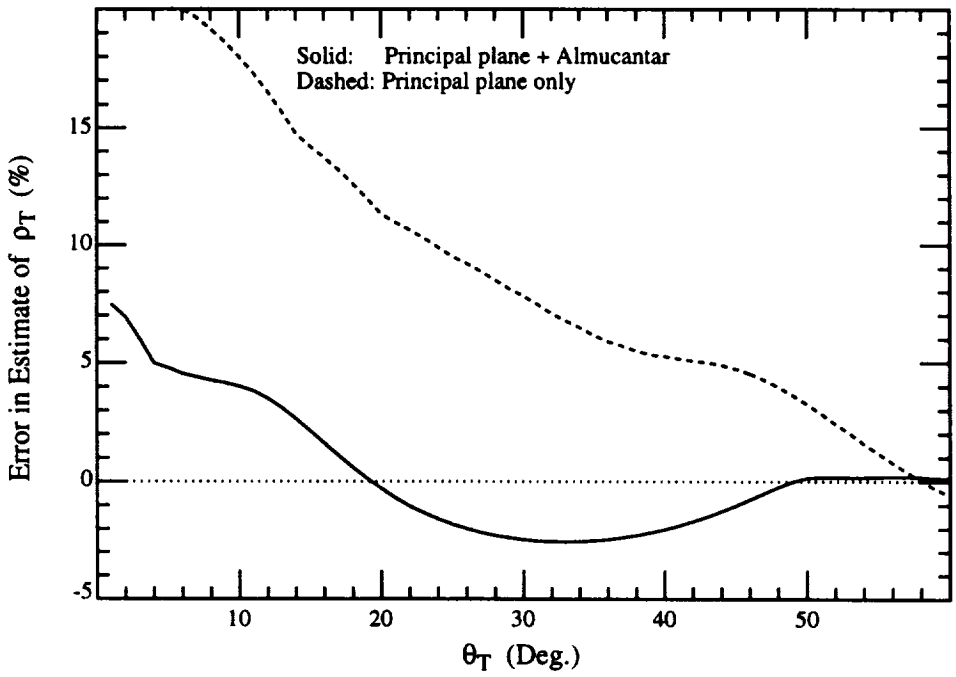

Figure 5. Error in the estimated ρ_T as a function of θ_T when single scattering was assumed to be the correct radiative transfer physics. The error in $\omega_0 P(\Theta)$ for this case is provided in Figure 3. There was assumed to be no contribution from molecular scattering to ρ_B or ρ_T.

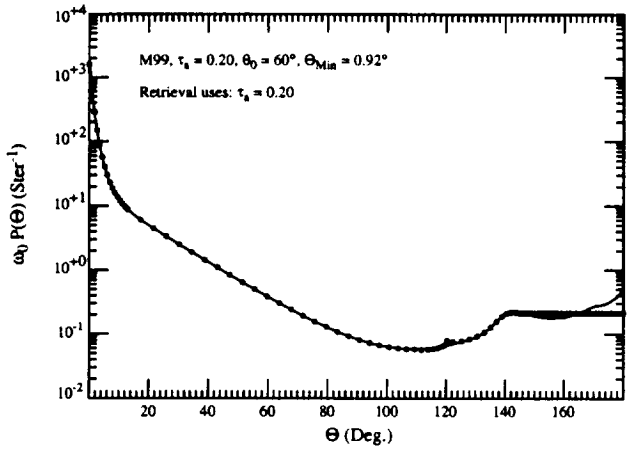

Figure 6a.

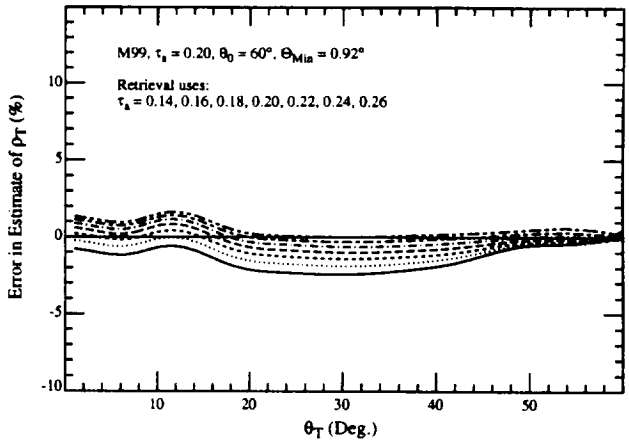

Figure 6b.

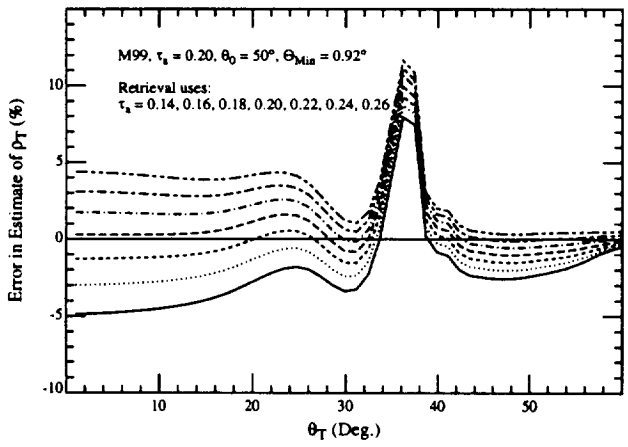

Figure 6c.

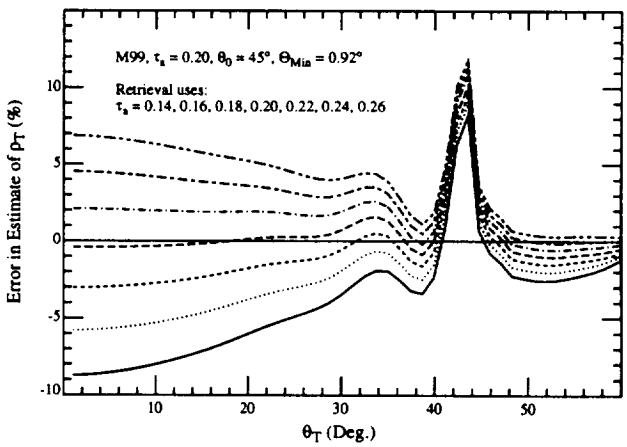

Figure 6d.

Figure 6. (a): Comparison between the aerosol phase function retrieved (circles) from ρ_B at 865 nm and the true phase function (line) when $\theta_0 = 60°$ for the M99 model with $\tau_a = 0.20$ and $\Theta_{\mathrm{Min}} = 0.92°$. (b): Error in estimation of ρ_T using the retrieved phase function in (a) with $\theta_0 = 60°$. (c): Same as (b) except $\theta_0 = 50°$. (d): Same as (c) except $\theta_0 = 45°$. In panels (b)–(d), the curves from bottom to top correspond to using $\tau_a = 0.14$, 0.16, 0.18, 0.20, 0.22, 0.24, and 0.26, in both the retrieval and prediction codes.

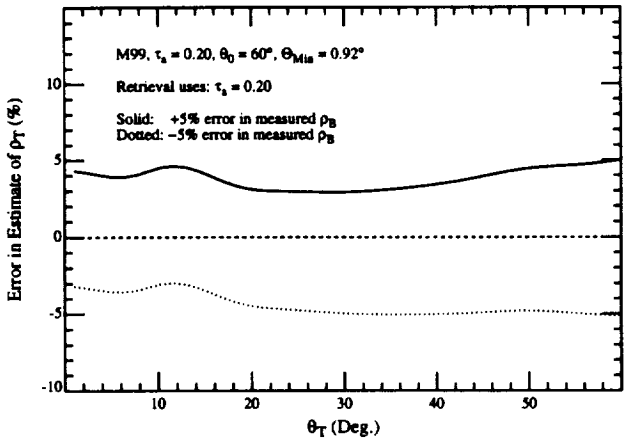

Figure 7a.

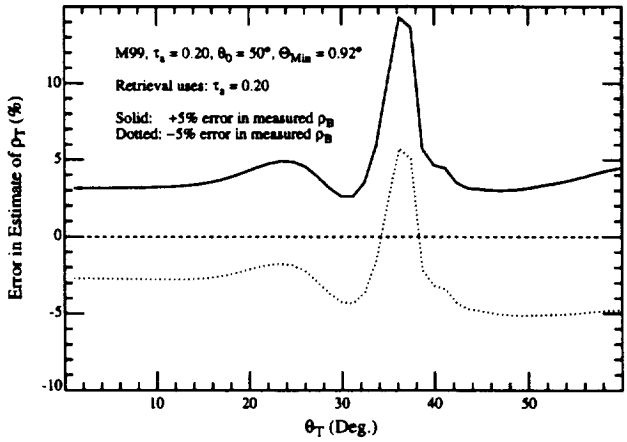

Figure 7b.

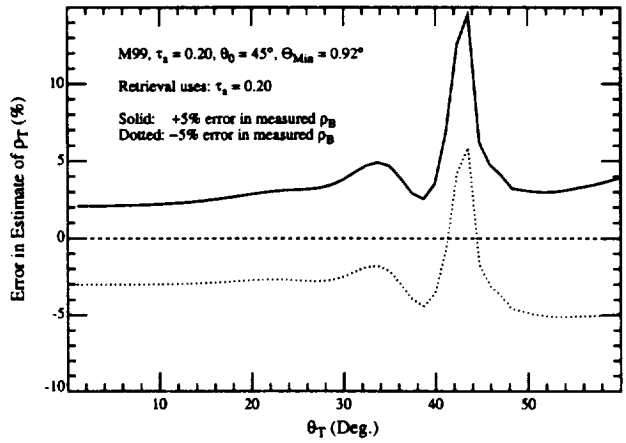

Figure 7c.

Figure 7. Error in ρ_T induced by a $\pm 5\%$ error in the measurement of ρ_B. The measurement of τ_a is assumed to be error-free. The retrieval of $\omega_0 P(\Theta)$ is carried out when $\theta_0 = 60°$. (a): $\theta_0 = 60°$. (b): $\theta_0 = 50°$. (c): $\theta_0 = 45°$.

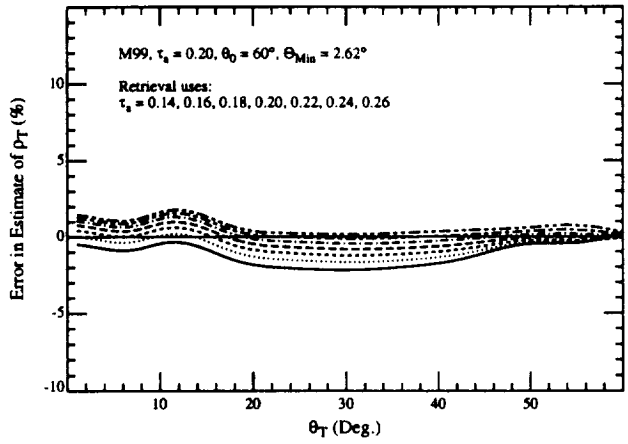

Figure 8a.

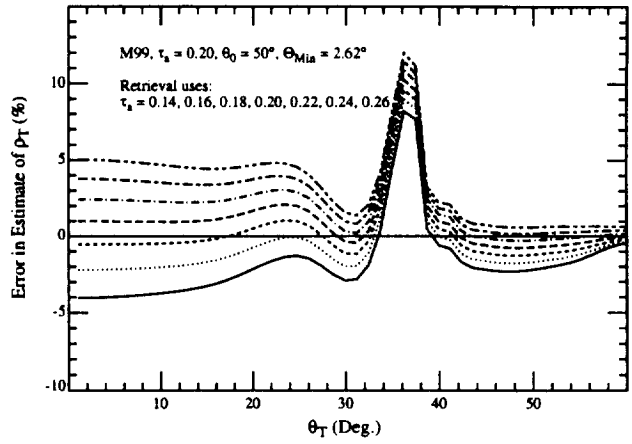

Figure 8b.

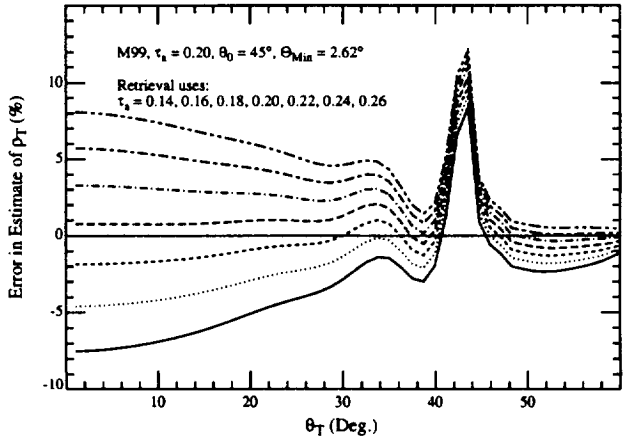

Figure 8c.

Figure 8. Same as Figure 6 except $\Theta_{Min} = 2.62°$.

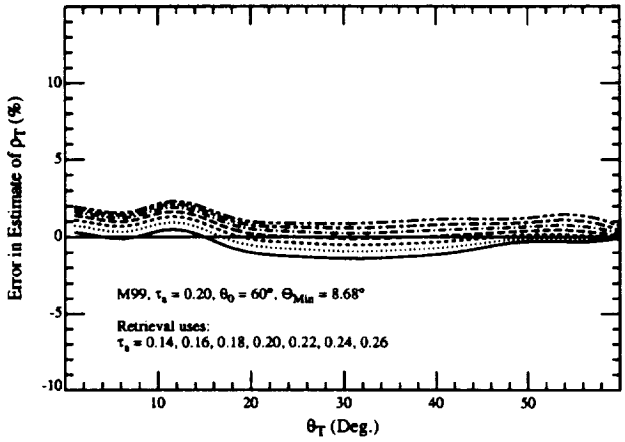

Figure 9a.

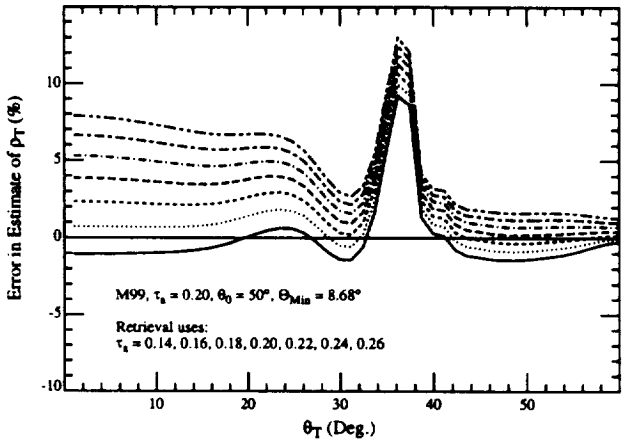

Figure 9b.

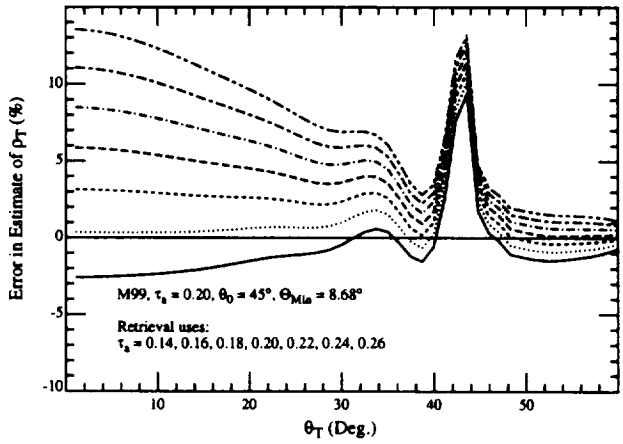

Figure 9c.

Figure 9. Same as Figure 6 except $\Theta_{\mathbf{Min}} = 8.68°$.

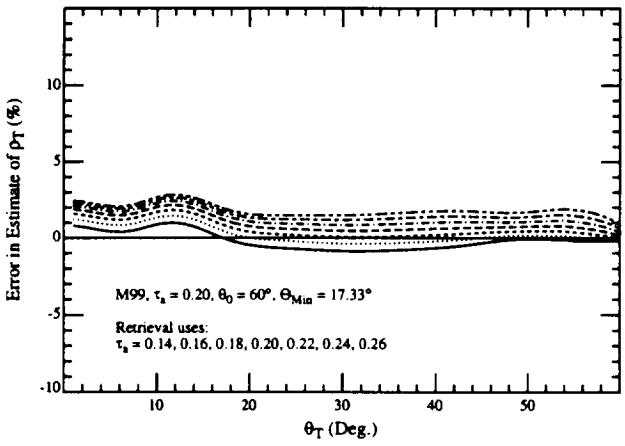

Figure 10a.

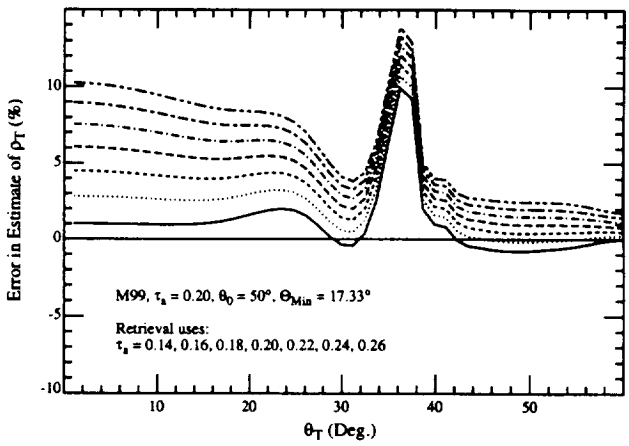

Figure 10b.

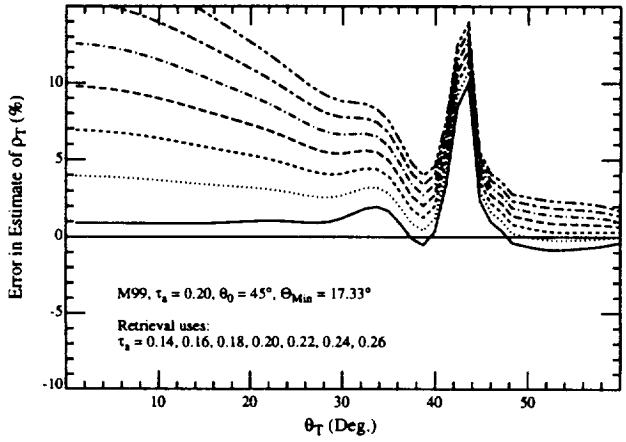

Figure 10c.

Figure 10. Same as Figure 6 except $\Theta_{Min} = 17.33°$.

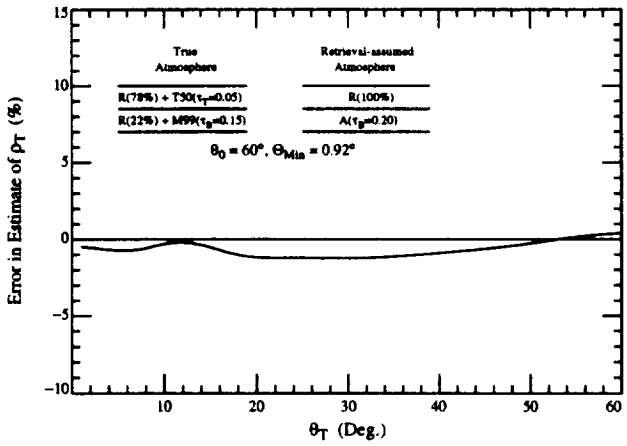

Figure 11a.

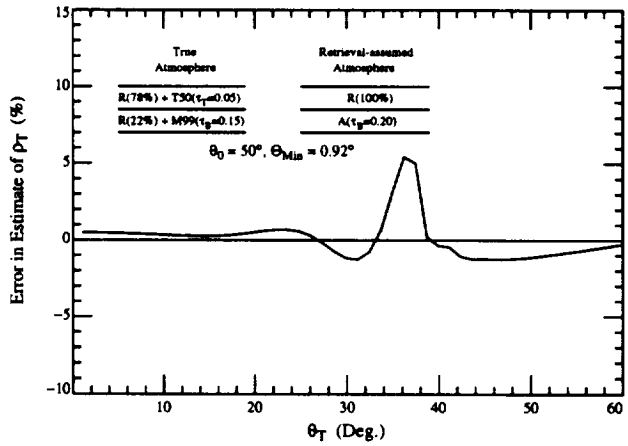

Figure 11b.

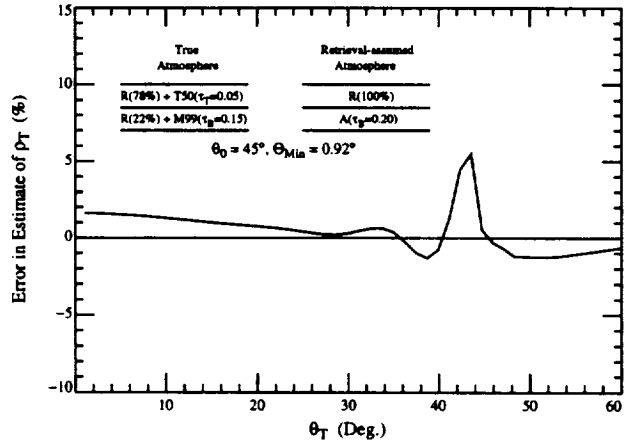

Figure 11c.

Figure 11. Error in ρ_T for a two-layer atmosphere with aerosol in both layers. The retrieval and prediction codes both assume that the aerosol is only in the lower layer and use the correct value of $\tau_a = \tau_T + \tau_B$. "R" stands for Rayleigh and "A" stands for aerosol. (a): $\theta_0 = 60°$. (b): $\theta_0 = 50°$. (c): $\theta_0 = 45°$.

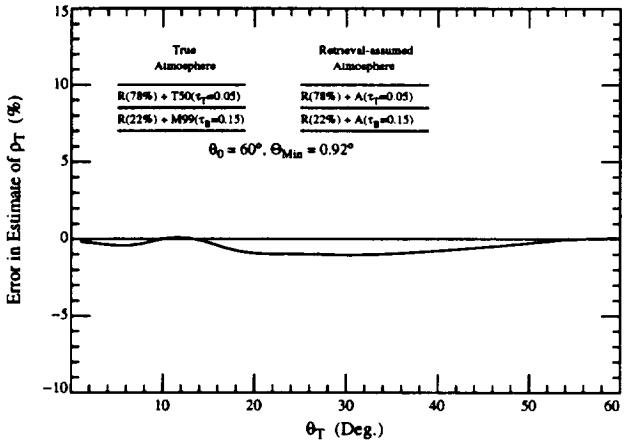

Figure 12a.

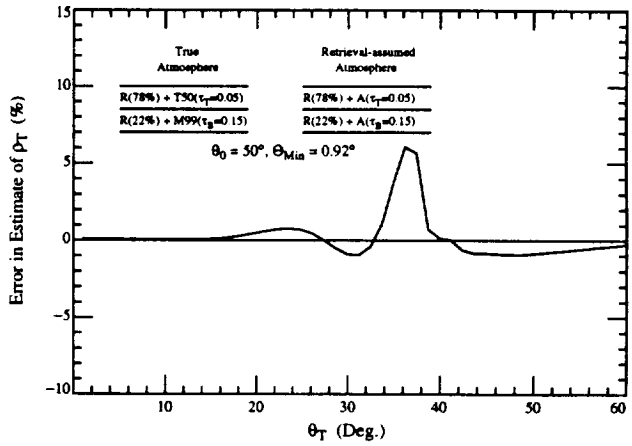

Figure 12b.

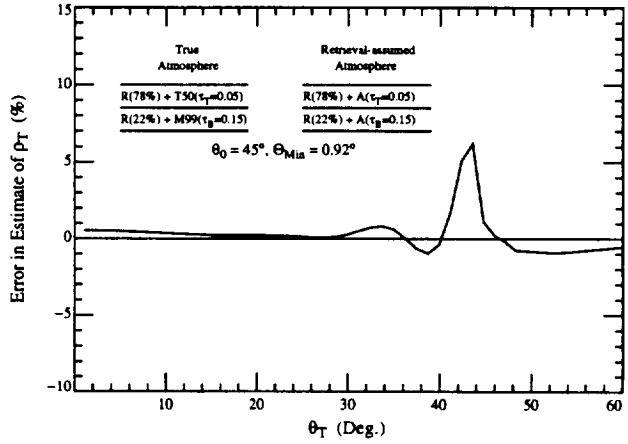

Figure 12c.

Figure 12. Same as Figure 11 except the retrieval and prediction codes use the correct vertical structure in τ_a.

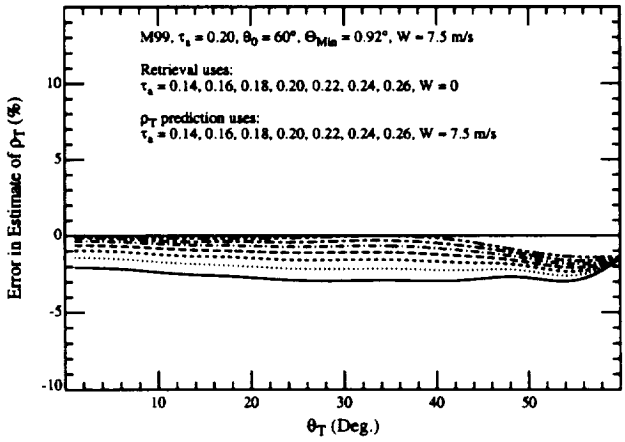

Figure 13a.

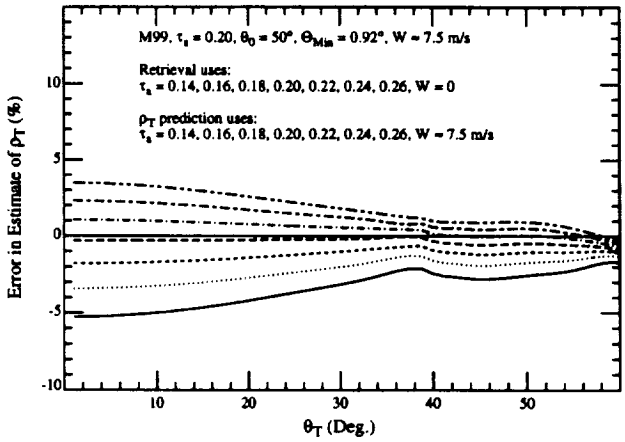

Figure 13b.

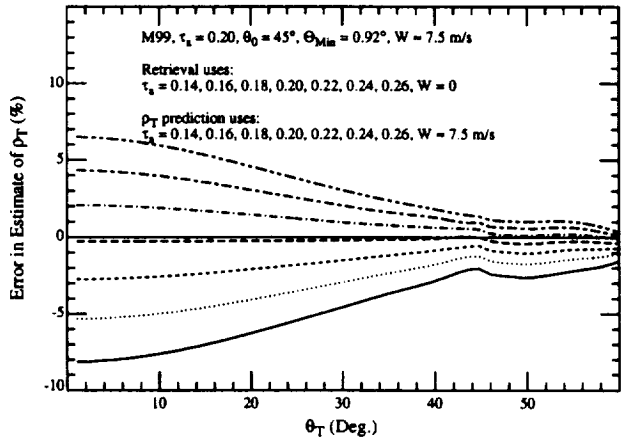

Figure 13c.

Figure 13. Same as Figure 6, showing the effect of sea surface roughness. Retrieval code assumes $W = 0$, while the prediction code uses the correct value of W.

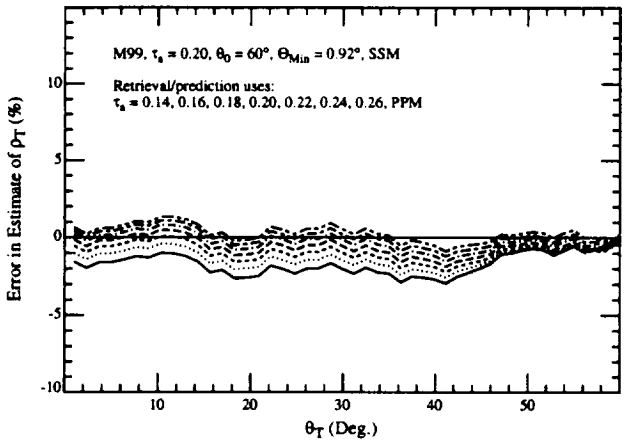

Figure 14a.

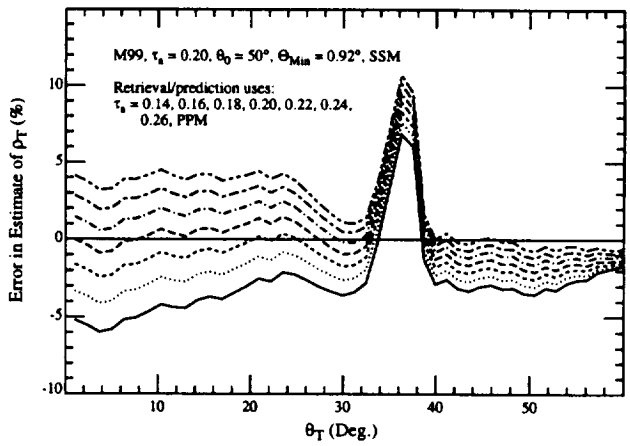

Figure 14b.

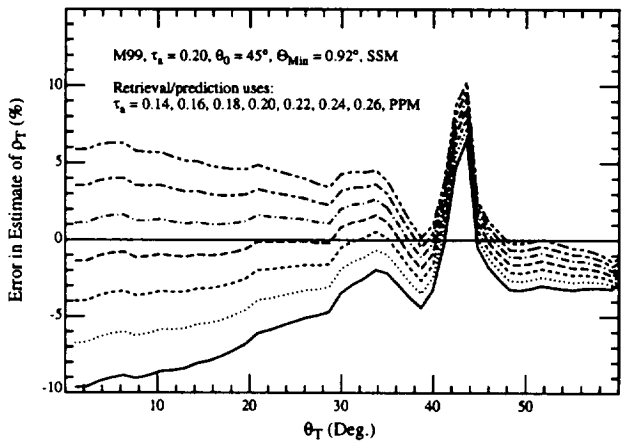

Figure 14c.

Figure 14. Same as Figure 13 showing the effect of the curvature of the Earth's atmosphere. Retrieval and prediction codes assume a plane-parallel atmosphere.

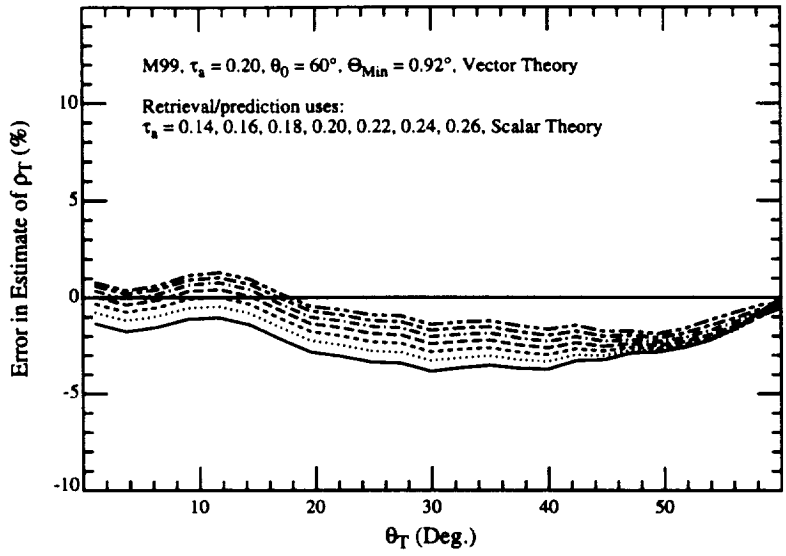

Figure 15a.

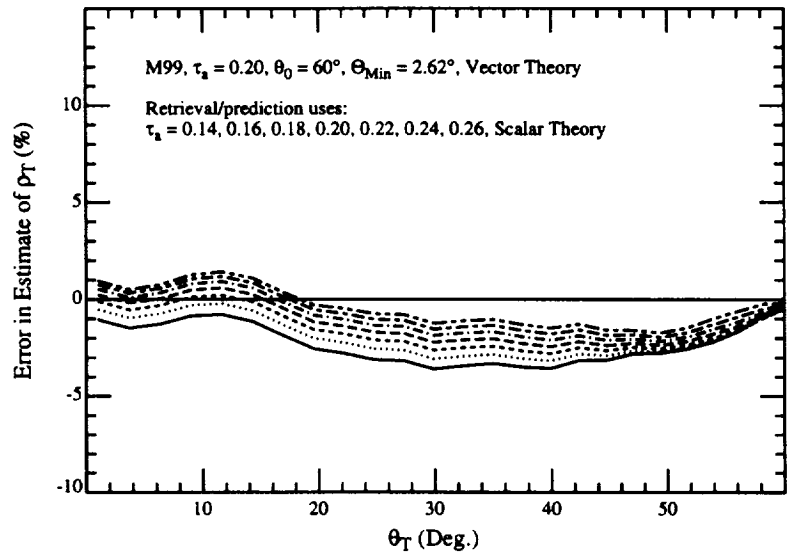

Figure 15b.

Figure 15. Same as Figure 14 showing the effect of ignoring polarization in the retrieval and prediction codes: (a) Θ_{Min} = 0.92°; (b) Θ_{Min} = 2.62°.

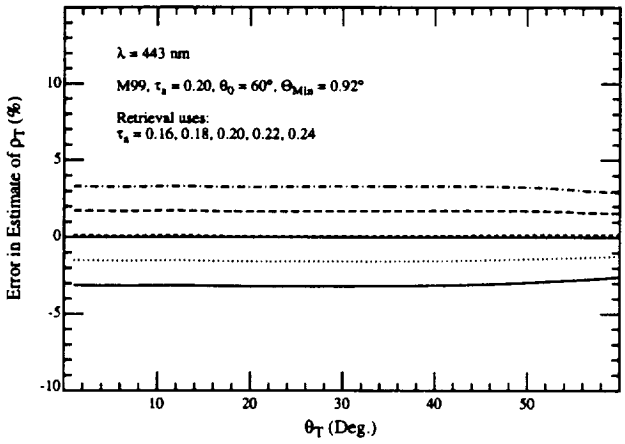

Figure 16a.

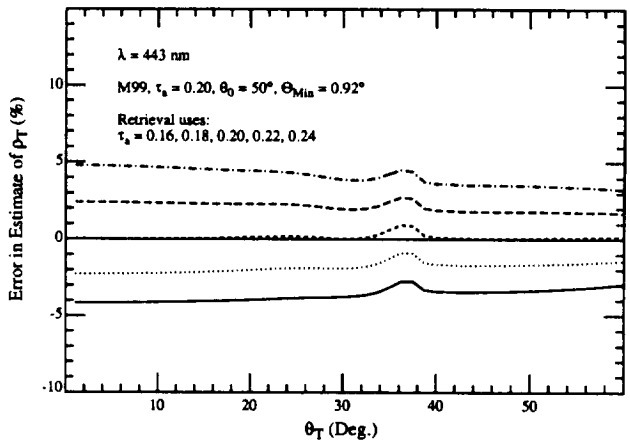

Figure 16b.

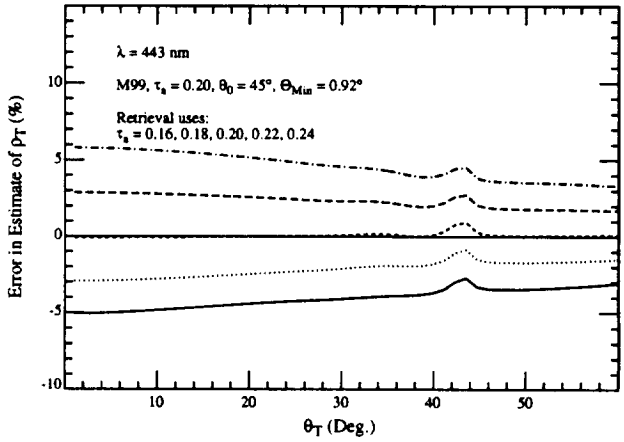

Figure 16c.

Figure 16. Same as Figure 6 except the wavelength is 443 nm.

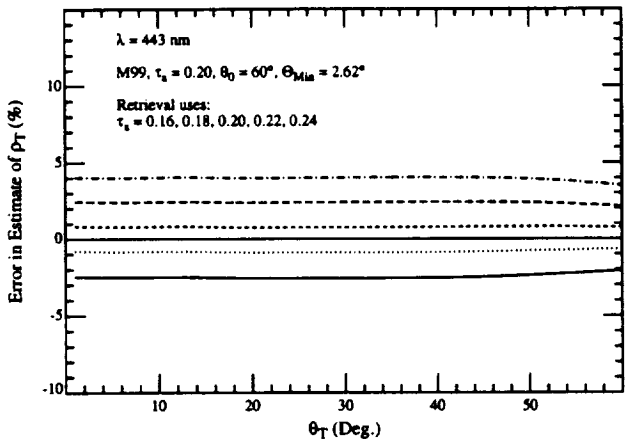

Figure 17a.

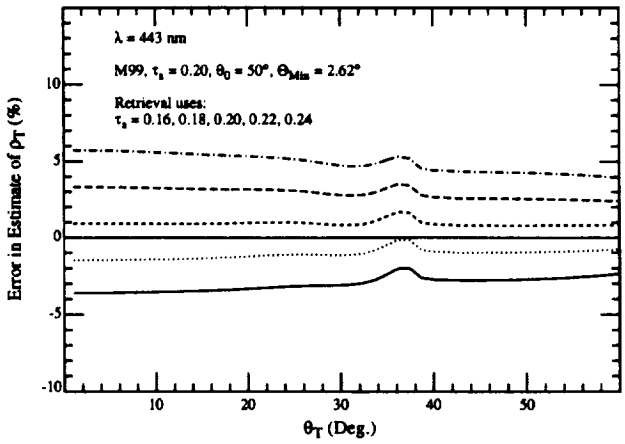

Figure 17b.

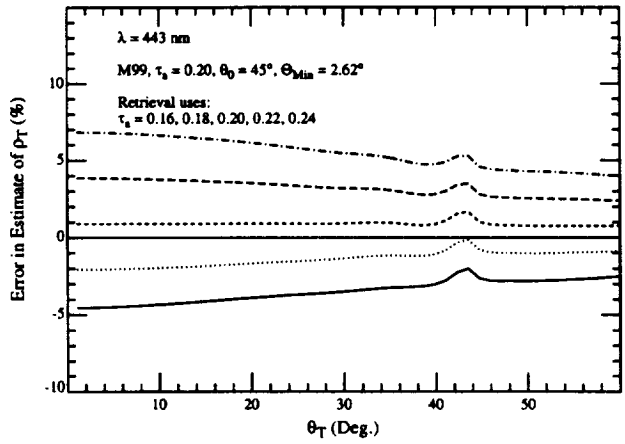

Figure 17c.

Figure 17. Same as Figure 16, except Θ_{Min} is increased from 0.92° to 2.62°.

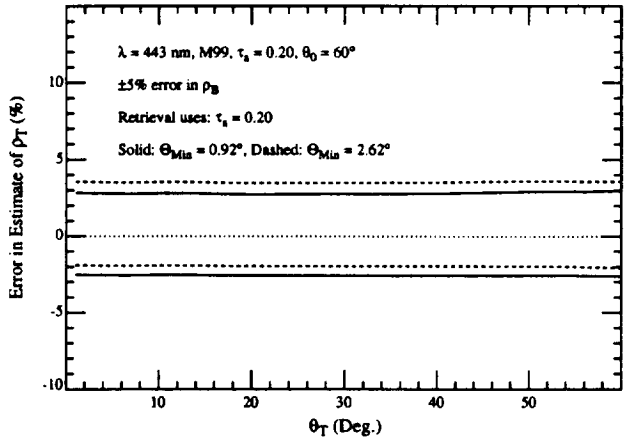

Figure 18a.

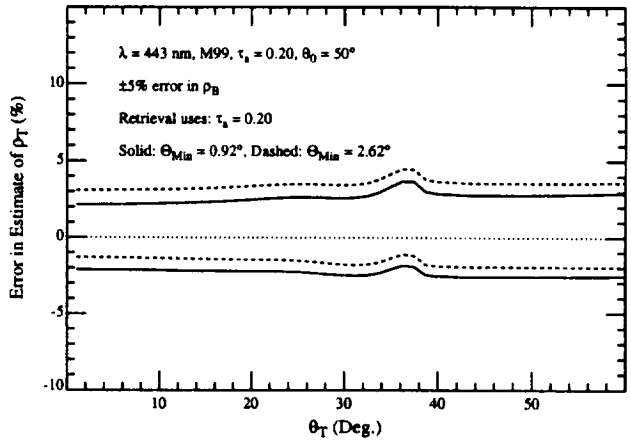

Figure 18b.

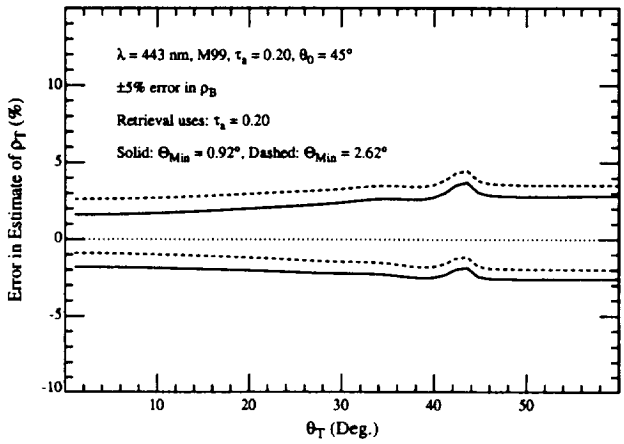

Figure 18c.

Figure 18. Error in the predicted ρ_T at 443 nm for a $\pm 5\%$ error in ρ_B for $\Theta_{\mathrm{Min}} = 0.92°$ (solid lines) and $\Theta_{\mathrm{Min}} = 2.62°$ (dashed lines). Positive (negative) errors in ρ_T correspond to positive (negative) errors in ρ_B.

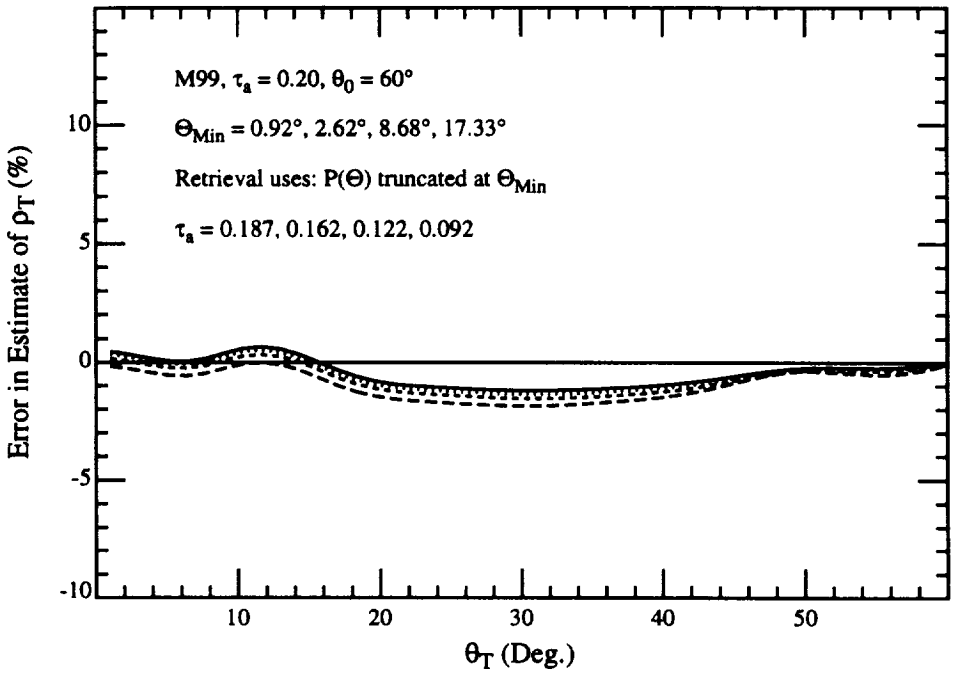

Figure 19. Error in the predicted ρ_T when the phase function is truncated at Θ_{Min} and the value of τ_a, measured with a sun photometer of half-angle field-of-view Θ_{Min}, is used in the retrieval and prediction codes. τ_a = 0.187, 0.162, 0.122, and 0.92 for the curves from top to bottom, corresponding to Θ_{Min} = 0.92°, 2.62°, 8.68°, and 17.33°.

Draft 11 December 1995

In Press
Revised for Limnology and Oceanography

Appendix 4

The 1991 coccolithophore bloom in the central north Atlantic

I. Optical properties and factors affecting their distribution

William M. Balch

Bigelow Laboratory for Ocean Sciences, McKown Point, West Boothbay Harbor, ME 04575

Katherine A. Kilpatrick

Division of Meterology and Physical Oceanography, Rosenstiel School for Marine and Atmospheric Science, University of Miami, 4600 Rickenbacker Causeway, Miami, FL 33149-1098

Charles C. Trees

Center for Hydro-Optics and Remote Sensing, San Diego State University, 6505 Alvarado Rd., Suite 206, San Diego, CA, 92182

Running head- Coccolithophore bio-optics

Acknowledgements

Derek Harbour kindly provided phytoplankton taxonomic information. The officers and crew of the RRS Charles Darwin are acknowledged for their expert ship handling and the staff of the Research Vessel Services, Barry, U.K. are thanked for their support of the ship studies. Don Heuer helped with the figures. Patrick Holligan provided considerable logistical support and helped with data interpretation along with Emilio Fernandez. The AVHRR data were provided by P.E. Baylis at the Satellite Receiving Station, University of Dundee, U.K. Some of the beam attenuation data used to calculate total scatter were kindly provided by Roy Lowry of the British Oceanographic Data Centre, Bidston, U.K. Howard Gordon and Kenneth Voss (Univ. of Miami Physics Dept.) have provided help in data interpretation. Two anonymous reviewers provided valuable comments on an earlier version of this manuscript. This work was generously supported by ONR Ocean Optics Program (N00014-91-J-1048), NASA Global Biogeochemistry (NAGW 2426) and NSF Biological Oceanography Program (OCE-8900189 and OCE-9022227) to WMB. This paper is contribution ### to the U.S. Global Ocean Flux Program.

Abstract

Optical scatter and absorption were measured in the central north Atlantic Ocean during a mesoscale bloom of the coccolithophorid, *Emiliania huxleyi*.. The chlorophyll-specific absorption was similar to previously reported measurements of the same species in laboratory cultures. Suspended coccoliths were responsible for about 80% of the total backscattering in the center of the bloom and the greatest calcite-dependent backscattering was observed just below the base of the mixed layer. Areal maps of calcite-dependent backscattering and reflectance were similar, due to the dominance of backscatter over absorption. Calculated reflectance at 440 and 550 nm reached about 24%, slightly less than what has been observed previously in Gulf of Maine blooms. Total scattering (b) was also calculated as the difference between beam attenuation and absorption. The ratio $\tilde{b}_b$ (backscattering divided by total scatter) was about 0.01-0.02 at 440 nm and 550 nm at the most turbid parts of the coccolithophore bloom (b= 1- 3 m^{-1}). As total scattering decreased below 1 m^{-1}, $\tilde{b}_b$ increased. The behavior of $\tilde{b}_b$ was compared for coccolith-dominated versus chlorophyll-dominated waters. Vertical profiles of calcite-dependent scattering, combined with satellite remote sensing data, were used to assess the factors responsible for vertical transport of calcite. The subsurface peak in calcite-dependent scattering did not result from detached coccoliths sinking but resulted either from plated coccolithophores sinking, then detaching their plates, or from deep coccolithophores producing and detaching their plates *in situ*.

Introduction

Coccolithophores are members of the algal class Prymnesiophyceae (Green et al. 1990). These cells produce calcium carbonate scales called coccoliths which, when released from the cells, increase its turbidity. They are known as an important part of the organic and calcite carbon production in the north Atlantic (Lohmann 1920; Hentschel 1936; Halldal 1953 as cited by Braarud 1963). Their optical properties have been the subject of considerable attention since the discovery that these organisms produce meso-scale blooms, observable by satellite (Holligan et al. 1983; Aiken and Bellan 1990, Balch et al. 1991; Trees et al. 1992; Fukushima and Ishizaka 1993; Brown and Yoder 1993). Satellite data withstanding, observations of turbid coccolithophore blooms have been made before. Birkenes and Braarud (1952) recorded turbid blooms of *Emiliania huxleyi* in Norwegian fjords. Anecdotal evidence of white-water blooms in the three major ocean basins can be found in Brongersma-Saunders (1957) although in some cases, bacteria have also been implicated (Lapota et al. 1988). Nevertheless, references to "milky" blooms caused by coccolithophores are fairly common. Berge (1962) cited a bloom in 1955 in Fǿrdesfjord, Norway with coccolith concentrations of 115,000 mL^{-1} plus other observations dating back to 1911, while Braarud (1945) cited a bloom in August 1935 near other Norwegian fjords with coccolith concentrations of 33,500 mL^{-1}.

Turbidity in coccolithophore blooms is thought to be principally due to the light scattering properties of the algal cells and associated coccoliths (Ackleson et al. 1994) although the exact relationships remain poorly defined. By "scattering" we are referring to particle scattering (as opposed to Rayleigh scattering) where the wavelength of light is less than, or equal to, the particle size. Such light scattering is mainly in the forward direction (Hodkinson and Greenleaves 1963) and is size dependent; smaller particles have a smaller efficiency of scattering than do large particles. Particle scattering in most natural waters is dominated by particles greater than 2μm (Jerlov 1976). Light scattering of homogeneous spheres has been modeled (beginning with Mie 1908) but scattering by intricately shaped

particles like coccoliths, or by particles of varying refractive index, such as organic matter and calcite, is much more complex to solve analytically (Bricaud et al. 1992). The reader is referred to Kirk (1994) or Jerlov (1976) for excellent reviews of light scattering in the sea.

The scattering coefficient in the sea has often been related to chlorophyll concentration (Gordon and Morel 1983; Morel 1987) although it is well known that other types of biogenic particles scatter light (Morel and Ahn 1991). For example, Kitchen and Zaneveld (1990) observed vertical profiles of scatter that were significantly different from chlorophyll profiles. Suspended minerals also are thought to dominate the backscattering signal in certain areas (Brown and Gordon 1974) but the magnitude of the light scattering by minerals has been poorly understood in space and time. Given the ubiquitous distribution of coccolithophores in the world ocean, it is also likely that a significant amount of reflected light detected by satellite remote sensors is from calcite which may cause error in the remote determination of chlorophyll (Balch et al. 1989). Knowledge of the bio-optical properties of coccoliths are important for correction of remotely sensed pigment data.

Interestingly, there have been virtually no published laboratory studies of coccolithophore light scattering (this is currently ongoing in our laboratory) and one laboratory study on absorption by *E. huxleyi* (Morel and Bricaud 1981). The only observations of light scattering by coccolithophores are from a scant few field studies. This paucity of data is striking, given the importance of calcite to carbon sedimentation, burial, as well as its potential impact on water-leaving radiance, and the remote sensing of phytoplankton chlorophyll.

We have studied the optical properties of *E. huxleyi* in nature. There are three important constraints that affect the interpretation of field data. First, measurements must be made in situations dominated by coccolithophores, with minimal representation by other algal groups. Second, the growth dynamics of the populations must be well-documented because bio-optical properties of coccolithophores change as populations age and cells drop

their coccoliths (Balch et al. 1992, 1993). Third, the optical properties of the calcite must be separable from the properties of other organic and inorganic matter.

A meso-scale coccolithophore bloom formed south of Iceland during June-July of 1991 which met all of these requirements. The turbid bloom covered an area of about 0.5 million km^2, *E. huxleyi* was the dominant phytoplankton species. There was excellent satellite coverage from the beginning to the end of the bloom (about 3 weeks), so the growth dynamics were well documented in space and time (Holligan et al. 1993; Fernandez et al. 1993). We were able to separate the optical properties of calcite from organic matter by making measurements before and after calcite dissolution. This paper is the first of a two part series; part I summarizes the absorption, scattering and backscattering properties of this spectacular algal event and part II (Balch et al. submitted) relates these properties to the particle concentrations, as well as their size.

Methods

Observations were made on cruise 60 of the RRS Charles Darwin (CD60) from 13 June to 3 July, 1991. The cruise track is shown in figure 1. Two transects were made along the 20°W and 15°W meridian. Detailed vertical profiles of light scattering and absorption in the top 100-200 meters depth,were performed at 24 hydrographic stations (Table 1). One of the stations was close to an optics mooring at 59° 39' N x 20° 59' W. While steaming, underway surface samples were taken hourly for particle absorption, volume scattering, chlorophyll concentration, and beam attenuation. The concentration of suspended calcite, cell and coccolith counts also were measured but the relevance of these to the optical signal will be discussed in the second paper of this series (Balch et al. submitted). Other measurement details can be found in Holligan et al. (1993).

Pigment Concentration

Pigment measurements were made using the technique of Yentsch and Menzel (1963), modified by Holm-Hansen et al. (1965). A seawater sample of 200mL was

filtered onto Gelman GFF filters, then the pigment extracted overnight at 4°C in 10mL of 90% acetone. Fluorescence was measured with a Turner 111 fluorometer.

Volume Scattering Measurements

Samples for measuring volume scattering were collected from Niskin bottles and stored in polyethylene bottles prior to the measurements (which immediately followed the cast). Volume scattering is defined by Kirk (1994) as "the radiant intensity in a given direction from a volume element, dV, illuminated by a parallel beam of light, per unit of irradiance on the cross-section of the the volume, and per unit volume". Measurements of volume scattering were made with a Brice Phoenix model 2000 light scattering photometer (Brice et al. 1950). The reader is referred to Spilhaus (1965), and Pak (1970) for discussions on the accuracy and precision of the Brice Phoenix light scattering photometer when used with sea water samples. Each 30mL sample was placed in a 6-sided glass cuvette designed for sampling at 45°, 90° and 135°. Occasionally, samples were allowed to warm several degrees before making measurements to eliminate condensation on the cuvette windows. Replicate measurements made over 30 minutes of warming showed no effect on the volume scattering function. Calibration of the instrument was made with an opal glass reference and working standard supplied with the instrument. Calibration constants were checked routinely to determine the instrument's stability. Finally, distilled water blanks were run to verify instrument calibration and to check the absolute accuracy of the instrument. These consisted of 0.2μm-filtered distilled water from a Milli-Q system, and were run 27 times during the cruise . Dark current measurements were performed after every sample. During one experiment, volume scatter of a bottled sample was examined immediately and after 16.5h in a surface-cooled deck incubator to verify any containment effects. The 90° volume scatter decreased about 12% over 16.5h (about 0.7% per hour). Given that our samples were run immediately following a cast, and only 3 angles were measured, any containment effect would have been negligible. This is in

agreement with Spilhaus (1965) who demonstrated that containment effects were negligible provided storage time was <= 1h (he took readings at 5^{o} intervals between 30^{o} and 135^{o} thus sampling time was potentially longer).

Volume scattering of each seawater sample was measured at the three angles stated above and at two wavelengths (436 nm and 546 nm). Then the sample was bubbled for 30s with CO2 (Paasche 1962) which reduced the pH to 5.0 and dissolved the calcium carbonate. Volume scattering measurements were repeated on the de-calcified samples. Cell counts were performed as a control to verify that the cell concentration was unaffected by the CO_2 bubbling and only the calcite dissolved. An Olympus BH2 microscope equipped with polarization optics and epifluorescence was used on board the ship for this purpose.

The technique of Gordon (1976) was used to calculate the backscattering coefficient (b_b, that fraction of light scattered in the backwards direction per unit thickness; See Table 2 for complete list of symbols used in this work). The method uses volume scattering at 45^{o}, 90^{o}, and 135^{o} as input. Essentially, the input volume scattering data are fit to an analytic expression of Beardsley and Zaneveld (1969), and this function is integrated in the backwards direction to calculate the backscattering coefficient. The difference between the raw and the acidified backscattering was considered "calcite-dependent backscattering" (b_b').

Particulate Absorption Measurements

A reflectometer technique was used to measure the particulate absorption coefficient (ap, the fraction of incident quanta that are absorbed per unit thickness of a material). A complete description of the technique, with comparisons to the spectrophotometric method, can be found in Balch and Kilpatrick (1992). One liter samples were filtered through baked Gelman GFF filters for particulate absorption measurements. The filters were stored in plastic petri dishes and frozen at $-20^{o}C$ for up to 3 days. Mitchell and Kiefer (1988) have

indicated that absorption spectra of filter pads with phytoplankton are stable at this temperature. Before analysis, a flat-black circular mask was placed over each filter to cover the clean white rim, free of particles. Spectral reflectance of each filter was measured every 10 nm between 400 and 700 nm using a hand-held Colormet spectral reflectometer (Instrumar Engineering Limited, St John's, Newfoundland, Canada). Absorbance was calculated based on the ratios of reflectance from sample and blank using the Kubelka-Munk function (Kubelka and Munk 1931 as cited in Kortüm 1969). The absorption coefficient is calculated using the clearance area of the filter, the volume filtered, and a path correction. Pigment-specific absorption coefficients are within 5% of those calculated using the spectrophotometric filter pad technique of Mitchell (1990) performed on the same samples, provided the optical densities of the filtered sample >0.3 (see Balch and Kilpatrick 1992; their Fig. 7). *In situ* absorption measurements were not available to compare to the filter pad measurements. No detrital correction was made for the particulate absorption, thus, ap values may have been overestimated, although in the middle Atlantic, the concentration of colored dissolved organic matter is expected to be low. No correction was needed for coccolith absorption; it has been previously demonstrated in other coccolithophore blooms that coccoliths absorb negligible light between 400 and 700 nm (Balch et al. 1991; their Fig. 9).

Beam Attenuation Measurements and Scatter Calculations

Beam attenuation (fraction of a parallel light beam which is absorbed or scattered per unit pathlength) was measured using two beam transmissometers, a Sea Tech 0.25m pathlength transmissometer with a wavelength of 660 nm and the Scripps Vis Lab Spectral Transmissometer (VLST; Petzold and Austin 1968) with a folded 1 m pathlength. The model of Voss (1992) was first used to calculate c_{440} and c_{550} from measured values of c_{660} (Sea Tech) and c_{535} (VLST) respectively. Voss (1992; his Fig. 8) has tested and verified this model in a wide variety of water types, including coccolithophore blooms with

attenuation values >1m^{-1}. Following the correction of the data for wavelength, the differences in optical geometry were corrected according to Voss and Austin (1993). Voss (1992) and Voss and Austin (1993) should be consulted for complete details about the correction procedures.

Total scatter (b; the integrated volume scattering function over all solid angles) was calculated as the difference between beam attenuation (c) and the sum of water absorption (aw) and particulate absorption (ap). Values of aw were taken from Smith and Baker (1981).

Spectroradiometer Measurements

Measurements of radiance (quantum flux per unit solid angle) and irradiance (quantum flux on a surface normalized by area) were made with a Biospherical Instruments MER 1032 spectroradiometer. Data discussed in this work are for downwelling irradiance (410, 441, 488, 532, 550, 589, 633, 656, 671, and 694 nm), upwelling irradiance (410,441, 488, 520, 550, 589, 633, and 671nm), upwelling radiance (410,441, 488, 520, 550, 589, and 710nm), and scalar irradiance (PAR).

Results

The performance of the Brice Phoenix Light Scattering Photometer showed negligible drift in both calibration constants and distilled water checks over the period of this cruise. Distilled water blanks (n=27) were run over the two weeks and values were close to pure water values in absolute terms, and stable. Average volume scattering at 90^{o} (β90) was 2.99x10^{-4} m^{-1} sr^{-1} at 436nm (standard deviation=1.91x10^{-5}; coefficient of variation=6.5%) and 1.41x10^{-4} m^{-1} sr^{-1} at 546nm (standard deviation=1.89x10^{-5}; coefficient of variation=13.4%). Interpolated pure water values published by Jerlov (1976) were 2.527x10^{-4} m^{-1} sr^{-1} at 436 nm and 0.9604x10^{-4} m^{-1} sr^{-1} at 546nm; the reason the ship values were higher than pure water values is probably due to the difficulty in achieving

particle-free water aboard ship. The other measure of the stability of this instrument was the variation of the calibration coefficients. Calibration records are available for this particular instrument for the last 14.5 years, and show that between 1978 and 1993, using the same opal glass standard, the calibration coefficient at 436nm and 546nm decreased by 0.47% per year and 0.12% per year respectively. Thus, over the course of this 3 week cruise, instrument drift would have been negligible.

Volume scattering at 90^{o} reached extremely high values within the north Atlantic coccolithophore bloom: 0.02 m^{-1} sr^{-1} at 440 nm and 550 nm which is about 70X and 165X the value of pure seawater at the respective wavelengths (Gordon et al. 1980). Over the entire North Atlantic study area, 90^{o} volume scattering and backscattering were linearly related at both wavelengths, with the most variability in the relationship seen with the clearest water. The relationships relating backscattering to 90^{o} volume scattering at 440 nm and 550 nm are given in Table 3. The least-squares fits were highly significant (r^2>=0.997; P(Type 1)<0.1%; F statistics exceeding 55,000!).

The difference between raw and acidified backscatter (b_b') was almost always measurable. It should be noted that in samples where coccolithophores were absent, no significant change in scatter was observed upon bubbling with CO2. Some b_b' values of zero were observed in the southern portion of the study area, but negative values were rare, indicating that cell breakage was negligible.

Calcite-dependent backscattering represented over 70% of the total backscatter in vertical profiles and was highest within the top 40m. Below 40m, bb' values were about 10-15% of the total backscattering at 440 nm and 550 nm (Fig. 2A and B). While the phytoplankton population was dominated by *E. huxleyi* in the high reflectance feature, non-calcareous species dominated outside the patch. However, two species of calcareous algae were found at 59^{o} 39' N x 20^{o} 59', outside the dense coccolithophore bloom, *Coccolithus pelagicus* (78 cells mL^{-1}) and *E. huxleyi* (681 cells ml^{-1}) with a very low concentration of detached *E. huxleyi* coccoliths (9 ml^{-1}). *C. pelagicus* did not drop its

plates appreciably. Due to the large size of *C. pelagicus* cells, their calcite dominated the total suspended calcite. Even in this "non-bloom" station, about 25-33% of the total backscattering was due to calcite (bb') down to 50m depth (Fig. 2C and D).

At all of the stations, both total backscattering and calcite-dependent backscattering showed well-defined wavelength dependence. Least squares linear fits for b_b440 versus b_b550 and $b_b'440$ versus $b_b'550$ are given in Table 3. These relationships translated to a wavelength dependence of $\lambda^{-1.212}$ for total backscatter and $\lambda^{-1.196}$ for calcite-dependent backscatter which was highly significant ($P=0.001$; F statistic>7000; $r^2>0.979$).

Chlorophyll (Chl) and particulate absorbance were positively correlated, although there was somewhat more variability than in the above scattering relationships (P(Type 1)<0.001, F statistic= 648 and 273 and $r^2=0.721$ and 0.521 at 440 and 550 nm respectively; Table 3). Using these results, the value of ap^*_{440} varied from 0.18 at the lowest chlorophyll concentrations to 0.078 at the upper chlorophyll concentrations. There was no significant covariation between ap and b_b or ap and b_b'.

Maps of surface ap, b_b and b_b' at 440 nm and 550 nm allowed examination of the large-scale patchiness of these optical properties. Within the bloom, values of ap_{440} and ap_{550} were highest along the 15°W transect and in the far western part of the survey area between 22°W and 23°W. Lowest particulate absorbance values within the bloom were observed along the 20°W transect. Outside the bloom, the highest particulate absorption was observed at the shelf break off of the northwest coast of Ireland (Fig. 3A and B). Patterns of b_b and b_b' were very similar for both wavelengths; this was expected given that calcite backscattering represented at least 70% of the total backscattering in the bloom. Highest backscattering values were observed in the western part of the survey area (Fig. 3C,D,E, and F).

Vertical sections of ap at 440 nm and 550 nm (Fig. 4A and B) showed greater absorbance at the northern part of the transect, with a peak between 58-58.5°N, similar to the chlorophyll pattern (Fernandez et al 1993) but outside of the region of maximum

turbidity. Below about 50 m, phytoplankton absorption generally declined. The vertical section of backscattering (Fig. 4C and D) showed greatest values at 61°N and at 25m depth. This same pattern was observed for the b_b' data (Fig. 4E and F), again suggesting that the backscattering in the surface water column was dominated by calcite-dependent scattering.

The beam attenuation data were first corrected for wavelength differences, then instrument differences. At 8 stations of the cruise, there were simultaneous transmittance measurements using both instruments. Uncorrected VLST transmittance (with water subtracted,$cvlst_{535}$) was correlated to uncorrected ST transmittance (with water subtracted, cst_{660}; Fig 5A; $r^2 = 0.97$) but the least squares fit to the data showed significantly higher beam attenuation of suspended material at 535 nm than 660 nm. After adjusting both to the same wavelength according to Voss (1992; see Fig. 5B for example of c corrected to 550 nm; $r^2 = 0.97$), the VLST still gave significantly larger beam attenuation values after water was subtracted. Following correction of the data for differences in optical geometry, the data fell considerably closer to the 1:1 line, although some deviation still was observed at low attenuation values (Fig. 5C; $r^2 = 0.97$). These results showed that the correction algorithms of Voss (1992) and Voss and Austin (1993) functioned adequately; henceforth, these algorithms were applied to all c measurements to make the data from the two transmissometers intercomparable.

Once beam attenuation results were tabulated, then total light scatter (b) was calculated as the difference between total beam attenuation and total absorption. Values of b reached as high as 3 m^{-1} in the center of the bloom. Due to the time-consuming nature of the measuring absorption and beam attenuation to calculate the scattering coefficient, we derived an empirical algorithm to conveniently estimate $b(\lambda)$ based on the easier measurement of $bb(\lambda)$:

$$b(\lambda)=bmax(\lambda)\left[\frac{bb(\lambda)-bb0(\lambda)}{Kb(\lambda)+(bb(\lambda)-bb0(\lambda))}\right] \quad (7)$$

The parameter bmax(λ) represented the maximum scattering, $bb_0(\lambda)$ represented the lower limit of total backscattering, as b(λ) approached clear water values, and Kb(λ) represented the value of bb(λ) when b(λ) was one half its maximal value. The equation was iteratively solved at varying values of total backscattering and the results are given in Table 4 and Fig. 6. The same data were plotted showing the backscattering probability, bb(λ)/b(λ) ($=\tilde{b}_b$) as a function of b(λ) (Fig. 7). It can be seen that at b(440) and b(550) values of 1 m^{-1}, $\tilde{b}_b$ was 0.01 to 0.02. Below 1 m^{-1}, $\tilde{b}_b$ increased to high values of 0.3 at 440nm and 0.6 at 550 nm in the clearest ocean water but such high values are questionable as will be discussed later.

Discussion

Optical observations

Backscattering and the shape of the volume scattering function (VSF) were similar to previously described VSF's of coccolithophore blooms (Balch et al. 1991) as indicated by the ratio of bb/β90. Pure seawater without particles should have a bb/β90 ratio of about 8 sr at 550nm (Gordon et al 1980). In clear water off the Bahamas, the bb/β90 ratio at 530nm was 6.67 while in the very turbid water of San Diego Harbor, the bb/β90 ratio was 4.16 (Petzold 1972). Clearly, as turbidity increases, the volume scattering function flattens in the backwards direction so that bb/β90 falls. The same was true in the mesoscale coccolithophore bloom studied here. Brice Phoenix measurements showed that β135 values generally were close to the β90 values when coccolith concentrations were highest (approaching a flat VSF in the backwards direction). Moreover, the least square fits to the backscattering versus volume scattering relationships (Table 3) gave bb/β90

ratios of 5 sr (440nm) and 4 sr (550nm) when large numbers of suspended coccoliths were present. This can be compared to previously measured $bb/\beta 90$ ratios of the 1989 coccolithophore bloom in the Gulf of Maine (Balch et al. 1991; their table 1, station 4) which were 4.3 sr (440 nm) and 5.9 sr (550 nm).

The North Atlantic bloom differed from the Gulf of Maine blooms in that the wavelength dependence of backscattering was less than published previously ($\lambda^{-1.19}$ as opposed to $\lambda^{-1.45}$; see Balch et al. 1991) but this should be interpreted cautiously since it is based on only two wavelengths. There also were two similarities between the aforementioned blooms. Water with high backscattering coefficients was confined to the top 20-30 m in the North Atlantic, as in the Gulf of Maine. Finally, in the Gulf of Maine, >75% of the backscatter was from coccoliths, similar to the North Atlantic bloom.

Regional variability of bio-optical properties

The aerial extent of the bloom was probably larger than indicated by the Advanced Very High Resolution Radiometer (AVHRR) imagery. In regions thought to be well outside the bloom, based on the satellite images, 1/3 of the backscattered light was still attributed to suspended calcite (Fig. 2C and D). The extent to which the bloom size was underestimated from the satellite images can be seen in Fig. 8 which shows b_b' overlaid on the AVHRR image of June 19, 1994. When this image was made (19 June, 1991; 1504 GMT) , the ship was at about 60^oN x 20^oW and it can be seen that there was low reflectance in the satellite image yet there was measurable b_b' (Fig.8). Generally, the patterns of the high reflectance measured by the satellite agreed well with the patterns defined by the objective contouring of bb'. More important, though, is that there was measurable b_b' along the 20^oW transect as far south as 55^oN (500 km south of the first visible high reflectance water at 61^oN;). Indeed, Holligan et al. (1993) reported concentrations of coccoliths of 5000-10,000 mL^{-1} at 57 ^oN. While there is no doubt that

the very high reflectance water extended from 61°N to 63°N, it should be kept in mind that *E. huxleyi* significantly impacted the optical properties of the water as far south as 55°N.

We predicted irradiance reflectance, R, of the surface water based on the measured values of ap and bb using equation 2 of Gordon et al. (1988):

$$R = Q * \sum_{i=1}^{2} l_i * \{bb/(a+bb)\}^i \qquad (2)$$

where l_1 and l_2 are empirically-fit coefficients equal to 0.0949 and 0.0794 respectively. Total absorption (a) was set equal to the sum of particulate absorption and water absorption. This model required knowledge of Q, the ratio of upwelling radiance to the upwelling irradiance toward zenith. Q equals π for a totally diffuse radiance distribution and increases with zenith angle. Average values of Q at 440 and 550 nm were 6.00 and 6.12 respectively and these values were used in all subsequent reflectance calculations (Table 5). Patterns of surface reflectance (Fig. 9) were remarkably similar to the patterns of bb' (Fig. 3E and 3F). Reflectance values predicted by equation 2 were as high as 21% at 440 nm and 24% at 550 nm in the northwest sector of the survey area. The predicted reflectance values at 440nm and 550nm were compared with values measured with the MER spectroradiometer. There were seven stations where this comparison was possible (Fig 10). At both wavelengths, the predicted irradiance reflectance accounted for 89% or 93% of the true variance in R440 and R550, respectively. The standard error of the predicted reflectances based on these relationships is +/- 3.4% and 2.3% at 440nm and 550 nm respectively. For the comparison shown in Figure 10, the slopes were not significantly different than 1 nor were the intercepts significantly different from zero (P(Type 1)<0.05). Such reflectance values are a bit lower than those measured with a spectroradiometer in the 1989 Gulf of Maine coccolithophore bloom (26.8% and 32.8%

respectively; Balch et al. 1991, their Table 1). It also should be noted that the ship crossed through a shelf-break coccolithophore bloom while returning to Scotland which can be seen in the southeast portions of the contour maps (Fig. 3).

The particulate absorption data allowed calculation of the chlorophyll-specific absorption coefficient of a coccolithophore population dominated by *E. huxleyi*. There were other species present such as cyanobacteria, naked dinoflagellates, and other miscellaneous eukaryotic microflagellates, thus while coccolithophores dominated the algal assemblage, it was not a pure population. The range of chlorophyll-specific absorption--0.098 to 0.14 m^2 mg chl^{-1} at chlorophyll concentrations of 1.5 and 0.1 $\mu g\ L^{-1}$ respectively-- was similar to the range observed by others and is indicative of a package effect (Morel and Bricaud 1981; see also Yentsch and Phinney 1989; their Fig. 6). While the chlorophyll-specific absorption was high relative to non-coccolithophore species (Mitchell and Kiefer,1988), the average ap^*_{440} in the most turbid part of the coccolithophore bloom was about 0.10 m^2 mg chl^{-1}, in good agreement with Morel and Bricaud (1981) who found ap^*_{440} of *E. huxleyi* cultures to be about 0.093 m^2 mg chl^{-1}. The ap^*_{440} values showed no significant correlation to b_b throughout the study area. Absorption at 440 nm was well correlated to chlorophyll biomass, but it is worthy of note that the high concentrations of coccoliths were not necessarily associated with the maximum chlorophyll biomass. In fact, along the 20°W transect, the largest 440 nm absorption (hence highest biomass; Fernandez et al. 1993) was observed at the edge of the high reflectance feature, not inside it (Fig. 3 and 4). This further supports the view that the term "bloom" is a misnomer with coccolithophores.

Variability in the ratio of backscatter to scatter

Clearly, in the North Atlantic coccolithophore event, scatter dominated absorption in terms of its impact on beam attenuation. Total scatter calculated from the difference between beam attenuation and absorption was as high as 3.3 m^{-1} at 440 nm and 2.9 m^{-1} at 550nm, almost 25-fold greater than the largest 440 nm absorption and 100-fold bigger

than 550 nm absorption observed in the bloom. The relation of total scatter to backscatter was highly nonlinear (Fig. 6), as would be expected since the forward part of the volume scatter function changes shape dramatically with increasing particle load. The volume scattering function of pure water is symmetrical which sets the upper value of $\tilde{b}_b$ at 0.5. The same results in Fig. 6 were replotted (Fig. 7) to show the values of $\tilde{bb}$ as a function of b. It can be seen that in the most turbid parts of the bloom with b>1.0, the value of $\tilde{b}_b$ was about 0.01, regardless of wavelength. The most difficult region to calculate $\tilde{b}_b$ (that is when $\tilde{b}_b$ is changing most rapidly) is when b falls between 0 and 0.5 m^{-1} which also happens to be when absorption becomes a more important part of the total beam attenuation. Note that measured $\tilde{b}_b$ values approached the value of 0.5 in deep water samples, when b was lowest. This must be interpreted cautiously since such clear water in nature is highly unlikely. Most likely, this resulted from significant error in the b calculation (c-a) at these low pigment concentrations.

Values of $\tilde{b}_b$ were compared in this coccolithophore bloom as well as in chlorophyll-dominated waters (using the least squares relationship of Gordon and Morel 1983; their p. 62). Plots of $\tilde{b}_{b\,550}$ vs $\tilde{b}_{b\,440}$ showed the characteristic decrease of $\tilde{b}_{b\,550}$ and $\tilde{b}_{b\,440}$ in turbid water whether chlorophyll or calcite dominated the scattering (Fig. 11). In other words, backward scattering decreased relative to total scatter in the coccolithophore bloom for scattering values up to 3 m^{-1} (Fig. 7) or chlorophyll concentrations up to 10μg L^{-1}. At low chlorophyll concentrations with no suspended calcite, $\tilde{b}_{b\,440} > \tilde{b}_{b\,550}$. When the chlorophyll *a* concentration exceeds 1mg m^{-3}, $\tilde{b}_{b\,550} > \tilde{b}_{b\,440}$; the volume scatter function is changing as a function of both chlorophyll and wavelength. In the coccolithophore bloom, $\tilde{b}_{b\,440}$ always exceeded $\tilde{b}_{b\,550}$ and the ratio $\tilde{b}_{b\,550}/\tilde{b}_{b\,440}$ was essentially constant at high coccolith concentrations (Fig. 11). Thus, backscattering was a constant fraction of total scattering at the two wavelengths. For plots of $\tilde{b}_{b\,550}$ vs $\tilde{b}_{b\,440}$, the data for chlorophyll-dominated vs. calcite-dominated waters intersected at a chlorophyll concentration of about 0.25μg L^{-1} and coccolith

concentration of about 100,000 mL^{-1}, implying similarly shaped volume scattering functions. Moreover, this confounding effect of variable chlorophyll made for a poor relationship between coccolith concentration and $\tilde{b}_b$ in the coccolithophore bloom in the North Atlantic.

In previous coccolithophore blooms, coccolith concentration has been best calculated based on 550nm backscattering or reflectance, not $\tilde{b}_b$, because the former is less affected by chlorophyll a. Unfortunately, coccolith reflectance still contaminates the 440nm absorption band of chlorophyll (Gordon et al. 1988; Balch et al. 1991, Ackleson et al. 1994), which causes R_{440}/R_{550} to increase, and the calculated pigment concentration to be underestimated (Morel and Prieur 1977). The extent of this error still needs to be defined. To do this, one must first define the quantitative relationship between suspended calcite concentrations or coccolith concentrations, absorption, and scatter. This was done in this meso-scale coccolithophore patch in the north Atlantic and is the subject of Balch et al. (submitted).

The vertical distribution of calcite light scatter

Vertical profiles of light scatter in the mesoscale coccolithophore feature may have been influenced by several processes: sinking of plated cells and detached coccoliths, production and detachment of coccoliths at depth, grazing and defication of coccoliths, and vertical mixing. While it is not possible to quantitatively determine the importance of these various processes using this data set, a discussion of the qualitative impact of of these processes is in order, given the space and time constraints of the bloom.

To estimate the importance of sinking to our optical profiles, we needed to know the time scale of bloom formation. On June 10 at 20°W and 60°N, there was no high reflectance apparent in the satellite imagery, however, the bloom was well underway by 15 June (Holligan et al. 1993). Thus, assuming June 10th as the start date of the surface bloom means that bloom ages may be overestimated. Nevertheless, a reasonable time scale

for the development of the optical profiles shown in Figure 2A is about 14 d. The issue becomes whether sinking coccoliths could explain the variability in the shape of the light scatter profiles that we observed.

Sinking rate estimates of detached coccoliths are rare in the literature. Bramlette (1961) cited a sinking rate for detached coccoliths of about 5000m in 10 years (or ~ 1.4 m d^{-1}) but gave no details on the calculation. This seems too fast given the empirical data of Honjo (1976), who measured sinking rates of detached *E. huxleyi* coccoliths at 0.14 m d^{-1}. To assess the applicability of Honjo's sinking rates to other species, classic stokes sinking rates were calculated for comparison. According to Eppley et al. (1967), based on earlier work of McNown and Malaika (1950), the sinking velocity can be described by the equation:

$$vs = (\rho c - \rho w)\ V\ g/(3K\ \eta\ D\ \pi) \qquad (3)$$

where vs is the sinking rate (m s^{-1}), ρc and ρw are the density of the calcite (2700 kg m^{-3}) and water (1025 kg m^{-3}) respectively, V is the coccolith volume (1.227 x 10^{-18} m^3), g is the gravitational constant (9.8m s^{-2}), K is a shape factor (which for flat discs at low Reynolds numbers =1.35; see McNown and Malaika 1950; their fig. 4), η is the dynamic viscosity (1.08 x 10^{-3} $Kg(ms)^{-1}$ at 20°C), and D is the nominal diameter of an oval coccolith (D= 1.156 x 10^{-6}m defined as $2(abc)^{0.333}$ where a, b, and c equal one-half of the thickness (0.25μm), length (2.8μm), and width (2.2μm) respectively). The sinking rate calculated from the above equation was 0.11 m d^{-1} in good agreement with Honjo (1976). Thus the deepest that surface coccoliths could have sunk in 14 d was about 2m, so sinking of detached coccoliths would not have been expected to significantly influence the optical profiles over a fortnight.

The backscattering profile from 24 June 1991 (Figs. 2A and B) showed little calcite-dependent light scattering deeper than 40m depth. The mixed layer at this station

was about 11 m thick. Given the above sinking rates, it would have been impossible for detached coccoliths to sink from 11m to 40m in two weeks as this would have required a minimum net sinking velocity of about 2 m d^{-1}. It is possible that the coccoliths sank while attached to cells. Had the calcite been precipitated at 20m, and sunk to 40m attached to cells, then a 1.4m d^{-1} sinking rate would have been required, close to Eppley et al.'s sinking rate for plated *E. huxleyi* cells (1.3m d^{-1}; Eppley et al. 1967). However, there are two important factors which should be kept in mind when discussing the optical impact of sinking plated cells: 1) coccolith-specific light scatter is generally thought to be greater when the coccoliths are *detached* from cells, not attached (Holligan et al. 1983). Thus, faster-sinking plated coccolithophore cells may alter the light scatter profile, but their optical impact is not as great as the slowly sinking detached coccoliths, 2) microscopic examination of water at 40m at the station given in Figure 2A revealed both detached and attached coccoliths. Fecal pellets also could have carried the coccoliths from the surface to 40m in less than a day (sinking rates >150m d^{-1} ; see Honjo 1976) but the major impact of coccolith grazing is not moving coccoliths a few meters depth, but stripping coccoliths from the euphotic zone (Honjo 1976).

Physical overturn certainly could have mixed surface coccoliths downwards to achieve the optical profiles observed in Figure 2. However, had vertical mixing been involved in transferring coccoliths to depth, then the temperature profile also should have been isothermal to 40m, which was not the case (see temperature profile in Fig. 2B).

In situ calcification and coccolith detachment remains the most likely factor affecting the profile of light scatter shown in Figure 2. Fernandez et al. (1993) demonstrated active calcification at depth in the same part of the bloom that we sampled. Given their observed calcification rates (about 1 mg m^{-3} d^{-1} at 38m; see their figure 8D) , and a carbon per coccolith of 0.25 pgC (Balch et al. 1991), then over 14d, the final coccolith concentrations should have been about $56x10^3$ coccoliths mL^{-1}. Furthermore, using the relationship between coccolith concentration and b_b' (Balch et al. 1991; their Fig. 11A &B), then

56,000 coccoliths mL^{-1} would have produced $b_b'440$ and $b_b'550$ of 1.09×10^{-2} and 8.24×10^{-3} m^{-1}, respectively This is within 25-30% of the values that we observed at 40m in Fig. 2A and 2B, reasonably close given the broad assumptions involved.

In summary, the subsurface scatter profiles probably resulted from at least two possible mechanisms: 1) plated, sinking coccolithophores shedding plates at depth (thus, the calcite originated from shallower depths) or 2) *in situ* calcification and deplating at depth by neutrally buoyant cells. Distinction between these two hypotheses will not only help elucidate the vertical distribution of calcite-dependent light scatter in the sea, but it will help in the interpretation of the complex ecology of these organisms. Moreover, the distinction is relevant to geochemical issues such as interpreting the calcite stable isotope signatures in the surface ocean, their extent of disequilibrium and resulting effect on the sedimentary isotope record (Paull and Balch 1994).

References

Ackleson, S., W. M. Balch, P. M. Holligan. 1994. The response of water-leaving radiance to particulate calcite and pigment concentration: a model for Gulf of Maine coccolithophore blooms. J. Geophys. Res. **99**: 7483-7499.

Aiken, J. and I. Bellan. 1990. Optical oceanography: An assessment of a towed method. p.39-57. *In* P. J. Herring, A. K. Campbell, M. Whitfield, and L. Maddock [eds.], Light and life in the sea. Cambridge University Press.

Aiken, J. G. F. Moore and P. M. Holligan. 1992. Remote sensing of oceanic biology in relation to global climate change. J. Phycol. **28**: 579-590.

Balch W. M., R. W. Eppley, M. R. Abbott and F. M. H. Reid. 1989. Bias in satellite-derived pigment measurements due to coccolithophores and dinoflagellates. J. Plank. Res. **11**: 575-581.

Balch, W. M. , P. M. Holligan, S. G. Ackleson, and K. J. Voss. 1991. Biological and optical properties of mesoscale coccolithophore blooms in the Gulf of Maine. Limnol. Oceanogr. **36**: 629-643.

Balch, W. M., P. M. Holligan and K. A. Kilpatrick. 1992. Calcification , photosynthesis and growth of the bloom-forming coccolithophore, *Emiliania huxleyi*. Cont. Shelf Res. **12**: 1353-1374.

Balch, W. M. and K. A. Kilpatrick. 1992. Particulate reflectance measurements of phytoplankton. J. Plank. Res. **14**: 721-735.

Balch, W.M., K.A. Kilpatrick, and P.M. Holligan. 1993. Coccolith formation and detachment by *Emiliania huxleyi* (Prymnesiophyceae). J. Phycol. **29**: 566-575.

Balch, W. M., K. A. Kilpatrick, P. Holligan, D. Harbour, and E. Fernandez. The 1991 coccolithophore bloom in the central north Atlantic. II- Relating optics to coccolith concentration. Limnology and Oceanography. submitted.

Beardsley, G. F. and J. R. V. Zaneveld. 1969. Theoretical dependence of the near-asymptotic apparent optical properties on the inherent optical properties of sea water. J. Opt. Soc. Am. 59: 373-377.

Berge, G. 1962. Discoloration of the sea due to *Coccolithus huxleyi* "bloom". Sarsia **6**: 27-40.

Birkenes, E. and T. Braarud. 1952. Phytoplankton in the Oslo fjord during a "*Coccolithus huxleyi* summer". Avhandl. Norske Videnskaps-Akad. Oslo, I. Mat. Naturv. Kl. **2**: 1-23.

Braarud, T. 1945. A phytoplankton survey of the polluted waters of inner oslo fjord. Hvalrad. Skr. **28**: 1-142.

Braarud, T. 1963. Reproduction in the marine coccolithophorid *Coccolithus huxleyi* in culture. Pubbl. staz. zool. Napoli. **33**: 110-116.

Bramlette, M. N. 1961. Pelagic Sediments.p. 345-366. *In* M. Sears [ed.], Oceanography, ed. . Am. Assoc. for the Adv. of Science, Washington, D.C..

Bricaud, A., J. R. V. Zaneveld and J. C. Kitchen. 1992. Backscattering efficiency of coccolithophorids: use of a three-layered sphere model. G. D. Gilbert [ed.], Proceedings of the Society of Photo-Optical Instrumentation Engineers.- Ocean Optics IV. **1750**: 27-33.

Brice, B. A., M. Halwer, and R. Speiser. 1950. Photoelectric light-scattering photometer for determining high molecular weights. J. Opt. Soc. Amer. **40**: 768-778.

Brongersma-Saunders, M. 1957. Mass mortality in the sea. Geol. Soc. Am. Mem. **67**: 941-1010.

Brown, C. and J. Yoder. 1993. Distribution pattern of coccolithophorid blooms in the Western North Atlantic. Cont. Shelf Res. **14**:175-198.

Brown, O. and H. Gordon. 1974. Size-refractive index distribution of clear coastal water particulates from light scattering. Applied Optics **13**: 2874-2881.

Eppley, R. W., R. W. Holmes and J. D. H. Strickland. 1967. Sinking rates of marine phytoplankton measured with a fluorometer. J. exp. mar. Biol. Ecol. **1**: 191-208.

Fernandez, E., P. Boyd, P. M. Holligan and D. S. Harbour. 1993. Production of organic and inorganic carbon within a large scale coccolithophore bloom in the north Atlantic Ocean. Mar. Ecol. Prog. Ser. **97**: 271-285.

Fukushima, H, and J. Ishizaka. 1993. Special features and applications of CZCS data in Asian waters, in press, *In* "Ocean Colour: Theory and Applications in a Decade of CZCS Experience". Kluwer Academic, Boston, MA.

Gordon, H. 1976. Radiative transfer in the ocean: A method for determination of absorption and scattering properties. Appl. Opt. **15**: 2611-2613.

Gordon, H. and A. Y. Morel. 1983. Remote Assessment of Ocean Color for Interpretation of Satellite Visible Imagery- A Review. Springer-Verlag.

Gordon, H. R., R. C. Smith, and J. R. V. Zaneveld. 1980. Introduction to Ocean Optics. in S. Duntley [ed.], Proceedings of the Society of Photo-Optical Instrumentation Engineers.- Ocean Optics IV. **208**: 14-55.

Gordon, H. R., O. B. Brown, R. H. Evans, J. W. Brown, R. C. Smith, K. S. Baker, and D. K. Clark. 1988. A semianalytic radiance model of ocean color. Journal of Geophysical Research **93**: 10909-10924.

Green, J. C., K. Perch-Nielsen and P. Westbroek. 1990. Prymnesiophyta, p. 293-317. *In* L. Margulis, J.O. Corliss, M. Melkonian and D.J. Chapman [eds.] Handbook of Protoctista, Jones and Bartlett, Boston, MA.

Groom, S., and P. M. Holligan. 1987. Remote sensing of coccolithophore blooms. Adv. Space Res. **7**: 73-78.

Halldal, P. 1953. Phytoplankton investigations from Weather Ship M in the Norwegian Sea, 1948-49. Including observations during the "Armauer Hansen" cruise July 1949. Hvalradets Skrifter Norske Videnskaps-Akad. Oslo **38**: 3-91.

Hentschel, E. 1936. Allgemeine Biologie des Sudatlantischen Ozeans. Wiss. Ergeb. deut. Exped. "Meteor" **11**: 1-344.

Hodkinson, J. R. and J. I. Greenleaves. 1963. Computations of light-scattering and extinction by spheres according to diffraction and geometrical optics and some comparisons with the Mie theory. J. Opt. Soc. Amer., 53: 577-588.

Holligan, P. M. , M. Viollier, D. S. Harbout, P. Camus, and M. Champagne-Philippe. 1983. Satellite and ship studies of coccolithophore production along a continental shelf edge. Nature **304**: 339-342.

Holligan, P. M., E. Fernandez, J. Aiken, W. M. Balch, P. Boyd, P. H. Burkill, M. Finch, S. B. Groom, G. Malin, K. Muller, D. A. Purdie, C. Robinson, C. Trees, S. Turner, and P. van der Wal. 1993. A biogeochemical study of the coccolithophore, *Emiliania huxleyi*, in the north Atlantic. Global Bio. Cycles **7**: 879-900.

Holm-Hansen, O., C. J. Lorenzen, R. W. Holmes, and J. D. H. Strickland. 1965. Fluorometric determination of chlorophyll. J. Cons. Perm. Int. Explor. Mer. **30**: 3-15.

Honjo, S. 1976. Coccoliths: production, transportation and sedimentation. Marine Micropaleontology. **1**: 65-79.

Jerlov, N. G. 1976. Marine Optics. Elsevier.

Kirk, J. T. O. 1994. Light & Photosynthesis in Aquatic Ecosystems, 2nd ed. Cambridge University Press.

Kitchen, J. and R. Zaneveld. 1990. On the noncorrelation of the vertical structure of light scattering and chlorophyll a in case I waters. Journal Geophys. Res. **95**: 20237-20246.

Kortüm, G. 1969. Reflectance Spectroscopy. Springer-Verlag, 336 p.

Kubelka, P. and Munk, F. 1931. Ein beitrag zur optik der farbanstriche. Z. Tech. Phys. 12: 593-601.

Lapota, D., C. Galt, J. R. Losee, and D. Howard. 1988. Observations and measurements of planktonic bioluminescence in and around a milky sea. J. Exp. Mar. Biol. Ecol. **119**: 55-81.

Lohmann, H. 1920. Die Coccolithophoridae, eine Monographie der Coccolithenbilenden Flagellaten. Arch. Protistenk. **1**: 89-165.

McNown, J. S. and J. Malaika. 1950. Effects of particle shape on settling velocity at low Reynolds numbers. Trans. Am. Geophys. Union. **31**: 74-82.

Mie, G. 1908. Beitrage zur Optik truber Medien, speziell kolloidalen Metall-losungen. Ann. Phys., 25: 377.

Milliman, J. 1993. Production and accumulation of calcium carbonate in the ocean: budget of a nonsteady state. Global Biogeochemical Cycles. **7**: 927-957.

Mitchell, B. G. 1990. Algorithms for determining the absorption coefficient of aquatic particulates using quantitative filter techniques (QFT). SPIE Ocean Optics X, 1302, 137-147.

Mitchell, B. G. and D. A. Kiefer. 1988. Chlorophyll a specific absorption and fluorescence excitation spectra for light-limited phytoplankton. Deep-Sea Res. **35**: 639-663.

Morel, A. 1987. Chlorophyll-specific scattering coefficient of phytoplankton, a simplified theoretical approach. Deep Sea Res. **34**: 1093-1105.

Morel, A. and Y.-H. Ahn. 1991. Optics of heterotrophic nanoflagellates and ciliates: A tentative assessment of their scattering role in oceanic waters compared to those of bacterial and algal cells. J. Mar. Res. **49**: 177-202.

Morel, A. and A. Bricaud. 1981. Theoretical results concerning light absorption in a discrete medium, and application to specific absorption of phytoplankton. Deep Sea Res. **28**: 1375-1393.

Morel, A. and L. Prieur. 1977. Analysis of variations in ocean color. Limnol. Oceanogr. **22**: 709-722.

Paasche, E. 1962. Coccolith formation. Nature **193**: 1094-1095.

Pak, H. 1970. The Columbia River as a source of marine light scattering particles. Ph.D. Dissertation. Oregon State University, 110 pp.

Paull, C. K. and W. M. Balch. 1994. Oxygen isotopic disequilibrium in coccolith carbonate from phytoplankton blooms. Deep-Sea Res. **41**: 223-228.

Petzold, T. J. 1972. Volume scattering functions for selected ocean waters. Univ. Calif. Scripps Inst. Oceanogr. Tech. Rep. 72-78.

Petzold, T. J. and R. W. Austin. 1968. An underwater transmissometer for ocean survey work. Underwater Photo-optical Instrument Applications. SPIE **12**: 133-137.

Smith, R. C. and K. S. Baker. 1981. Optical properties of the clearest natural waters (200-800 nm). Applied Optics. **20**: 177-184.

Spilhaus, A. F. Jr. 1965. Observations of light scattering in sea water. Ph.D. dissertation. Massachusetts Institute of Technology, 168 pp.

Trees, C. C., J. Aiken, H.-J. Hirche, and S. B. Groom. 1992. Bio-optical variability across the Arctic Front. Polar. Biol. **12**: 4554-4561.

Voss, K. 1992. A spectral model of the beam attenuation coefficient in the ocean and coastal areas. Limnol. Oceanogr. **37**: 501-509.

Voss, K. and R. W. Austin. 1993. Beam-attenuation measurement error due to small-angle scattering acceptance. Am. Met. Soc. **10**: 113-121.

Westbroek, P., C. W. Brown, J. van Blejswijk, C. Brownlee, G. Brummer, M. Conte, J. Egge, E. Fernandez, R. Jordan, M Knappertsbusch, J. Stefels, M. Veldhuis, P. van der Wal, and J. Young. 1993. A model system approach to biological climate forcing. The example of Emiliania huxleyi. Global and Planetary Change. **8**: 27-46.

Yentsch, C. S. and D. W. Menzel. 1963. A method for the determination of phytoplankton chlorophyll and phaeophytin by fluorescence. Deep-Sea Res. **10**: 221-231.

Yentsch, C. S. and D. A. Phinney. 1989. A bridge between ocean optics and microbial ecology. Limnol. Oceanogr. 34: 1694-1705.

Table 1- Dates (month.day), times (local) and positions (decimal degrees) of hydro-stations visited during t

DATE 1991	time (local)	JDAY	lat °N	lon °W
6.17	2.50	168.10	55.84	19.94
6.17	12.08	168.50	56.01	19.99
6.18	9.50	169.40	58.18	20.01
6.19	1.00	170.04	60.00	20.00
6.19	12.00	170.50	60.00	20.00
6.19	21.20	170.88	59.99	19.84
6.19	21.33	170.89	60.03	19.99
6.20	15.42	171.64	61.67	19.95
6.21	19.50	172.81	62.99	20.00
6.21	19.50	172.81	63.56	21.33
6.22	9.50	173.40	61.52	22.60
6.23	1.17	174.05	61.08	22.70
6.23	11.00	174.46	61.11	22.71
6.24	1.00	175.04	61.10	22.71
6.24	18.75	175.78	61.12	23.02
6.26	9.50	177.40	59.65	20.97
6.26	9.50	177.40	59.64	21.10
6.27	15.83	178.66	61.18	15.18
6.28	0.50	179.02	61.20	15.16
6.29	3.75	180.16	61.14	14.81
6.29	14.33	180.60	60.95	15.55
6.30	16.12	181.67	61.02	14.71
7.01	17.50	182.73	57.35	12.67
7.02	10.10	183.42	56.39	8.61

Table 2- List of symbols, with definitions and units . Values are given when applicable.

ap	phytoplankton absorption coefficient (m^{-1})
ap*	phytoplankton-specific absorption (m^{-2} (mg chl^{-1}))
b	Scattering coefficient (m^{-1})
b_b	Backscatter coefficient (m^{-1})
b_b'	Backscatter coefficient of calcite (m^{-1})
$\tilde{b}_b$	Ratio of scatter to backscatter, also known as backscattering probability
$\beta\theta$	Volume scatter at angle θ (m^{-1} sr^{-1})
cvlst	beam transmittance as measured with the Vis Lab Spectral Transmissometer (m^{-1})
cst	beam transmittance as measured with a Sea Tech 0.25m pathlength transmissometer (m^{-1})
cw	beam transmittance of water (m^{-1}; value used here from Gordon et al. (1980)
D	nominal diameter of an oval coccolith (1.156×10^{-6}m)
g	gravitational constant (9.8m s^{-2})
η	dynamic viscosity (1.08×10^{-3} $Kg(ms)^{-1}$ at 20°C)
K	shape factor (unitless; for flat discs at low Reynolds numbers =1.35)
Q	ratio of upwelling radiance to the upwelling irradiance toward zenith (unitless)
R	irradiance reflectance (defined as upward irradiance/downward irradiance)
ρc	density of the calcite (2700 kg m^{-3})
ρs	density of water (1025 kg m^{-3})
V	coccolith volume (1.227×10^{-18} m^3)

Table 3. Statistical summary of linear optical relationships during the BOFS cruise. Table provides the name of the independent variable (Ind. Var.), Dependent variable (Dep. Var.), number of points, least-squares fit slope, standard error (s.e.) of the slope, least-squares fit intercept (Int), standard error of the intercept, coefficient of correlation, F statistic (equal to the regression mean square/residual mean square), and P, the probability that the slope is equal to 0 (* indicates P<0.001, Type 1 error). Where regressions were performed using log transformed variables, this is shown in the first two columns.

Ind Var	Dep Var	n	Slope	s.e.	Int	s.e	r^2	F	P
Ln b_b(440)	Ln$\beta\theta$(440)	157	4.913	1.68E-2	2.71E-3	7.77E-5	0.998	85058	*
Ln b_b(550)	Ln$\beta\theta$(550)	156	3.891	1.65E-2	3.37E-3	7.07E-5	0.997	55573	*
b_b (550)	b_b(440)	156	0.762	7.99E-3	3.10E-4	1.98E-4	0.983	9124	*
b_b' (550)	b_b'(440)	154	0.766	9.06E-3	1.18E-5	1.68E-4	0.979	7148	*
ap(440)	chl a	253	0.0685	2.69E-3	2.91E-2	2.96E-3	0.721	648	*
ap(550)	chl a	253	0.0129	7.78E-4	8.15E-3	8.55E-4	0.521	273	*

Table 4- Best-fit parameters for empirical algorithm predicting $b(\lambda; m^{-1})$ from $bb(\lambda; m^{-1})$ in North Atlantic coccolithophore bloom.

λ (nm)	$b_{max}(\lambda)$	$bb_0(\lambda)$	$K_b(\lambda)$	r^2
440	4.44	4.41×10^{-3}	3.30×10^{-2}	0.84
550	3.64	4.02×10^{-3}	1.96×10^{-2}	0.86

Table 5- Data for solar zenith angle and the ratio of upwelling radiance to the upwelling irradiance toward zenith (Q) at 441 and 550nm. See text for details of measurements.

Lat (°N)	Lon (°W)	Date 1991	Time local	Stn no.	Zenith Sun Angle	Q441	Q550
59.983	19.948	19 Jun	1011	3	49.07	6.40	3.45
60.012	19.840	19 Jun	1215	4	38.33	5.98	5.98
60.030	19.817	19 Jun	1457	5	40.32	5.98	6.63
61.660	19.970	20 Jun	1400	7	38.8	4.54	5.039
63.207	21.608	21 Jun	1440	8	41.56	5.04	6.19
63.583	21.330	21 Jun	1821	9	61.85	6.19	7.60
61.517	22.598	22 Jun	0953	10	53.33	5.04	5.58
60.855	22.667	22 Jun	19.03	11	66.14	6.19	7.099
61.112	22.700	23 Jun	1058	12	45.98	5.40	5.40
61.112	22.738	23 Jun	1303	13	38.01	5.04	5.40
61.392	22.917	24 Jun	0950	14	53.48	5.21	5.21
60.917	22.900	24 Jun	1511	15	41.05	6.19	5.98
59.662	22.982	26 Jun	1043	17	46.92	6.41	6.86
59.623	21.082	26 Jun	1220	18	38.09	6.41	6.57
61.213	15.188	27 Jun	1534	19	45.78	8.14	7.10
61.158	15.230	28 Jun	0920	20	53.51	6.66	7.10
61.160	15.235	28 Jun	1216	22	37.71	6.41	6.41
61.172	15.205	28 Jun	1229	23	38.32	6.41	6.19
61.005	14.728	30 Jun	1454	26	38.82	6.41	6.41
Average						6.00	6.12

Figure Legend

Fig.1-Cruise track of the RRV Charles Darwin (cruise CD60) showing dates along the cruise track. MLML refers to the "Marine Light in the Mixed Layer" optical mooring at 59° 39' N x 20° 59' W.

Fig. 2- Vertical profiles of backscatter (bb) at two stations: A) 61°7.03' N x 23° 01.4'W, 24 June 1991, 1845h local time; data for bb at 436nm B) same station as panel (A) except data are for bb at 546nm, C) 59° 39.1' N x 20° 58.4'W, 26 June 1991, 0930h local time; data for bb at 436nm D) same station as panel (C) except data are for bb at 546nm. Note change in scales for X and Y axes between panels A and B versus C and D.

Fig. 3- Map of the study area showing surface contours of A) particulate absorption coefficient at 440nm, ap440 ($x10^{-2}$ m^{-1}), B) particulate absorption coefficient at 550nm, ap550 ($x10^{-3}$ m^{-1}), C)backscattering coefficient at 440nm, bb440 ($x10^{-3}$ m^{-1}), D)backscattering coefficient at 550nm, bb550 ($x10^{-3}$ m^{-1}), E) calcite-specific backscattering coefficient at 440nm, bb'440 ($x10^{-3}$ m^{-1}), and F) calcite-specific backscattering coefficient at 550nm, bb'550 ($x10^{-3}$ m^{-1}). Station locations are shown with *'s.

Fig. 4- Vertical section along 20°W for A) ap440 ($x10^{-2}$ m^{-1}), B) ap550 ($x10^{-3}$ m^{-1}), C)bb440 ($x10^{-3}$ m^{-1}), D)bb550 ($x10^{-3}$ m^{-1}), E) bb'440 ($x10^{-3}$ m^{-1}), and F) bb'550 ($x10^{-3}$ m^{-1}). Sample locations and depths are shown with *'s.

Fig. 5- A) Raw uncorrected beam attenuation values for two transmissometers, the VLST and Sea Tech at 8 stations where both instruments were running simultaneously. Beam attenuation of water (cw) has been subtracted from each data set. The equation relating the raw data from the two instruments was: $cvlst_{535}[0.108] = (1.05[0.072] \times cst_{660}) +$

0.207[0.071] ; r^2 = 0.97; n=8). Standard error of the dependent variable, slope and intercept are given in the square brackets. B) Same beam attenuation data as in (A) except data have been wavelength corrected to 550nm using the model of Voss (1992). The equation relating the wavelength-corrected results from the two instruments was: $cvlst_{550}$[0.112]= (0.992[0.068] x cst_{550}) + 0.215[0.074]; r^2 = 0.97; n=8). C) Same beam attenuation data as in (B) except data have been wavelength corrected for differences in optical geometry according to Voss and Austin (1993). The equation relating the wavelength-corrected results from the two instruments was: $cvlst_{550}$[0.130]= (0.910[0.062] x cst_{550}) + 0.236[0.090]; r^2 = 0.97; n=8).

Fig. 6- Total light scatter, b, versus total backscatter, bbtot; A)440nm results, B)550nm results. Values of b were calculated as the difference between beam attenuation (corrected for wavelength and instrument geometry), and the sum of particulate absorption and water absorption. Values of b_b were calculated entirely independantly using volume scatter data from the Brice Phoenix Light Scattering photometer according to Gordon(1976). Least square fits are given in the text.

Fig. 7- Same data as in Fig. 6 except $\tilde{b}_b$ is shown vs btot for A)440nm and B) 550nm.

Fig. 8- Advanced Very High Resolution Radiometer (AVHRR) image of 1991 coccolithophore bloom in the NE Atlantic Ocean. Image is from the corrected visible (channel 1) image of 19 June 1991. Regions of high reflectance appear as light areas in the image. Clouds and land were masked in each image and are black. This image was taken from NOAA 11 using the early afternoon pass for channel 1 and processed according to Groom and Holligan (1987). White contours show the same data as in figure 3f, superimposed on the image. The ship's location at the time of the image was 59° 58.9' N x 19° 59.5'W.

Fig. 9- Maps of surface reflectance calculated as described in the text. A) 440nm reflectance (%) and B) 550nm reflectance (%).

Fig. 10- Comparison of predicted irradiance reflectance and measured irradiance reflectance at seven stations. A 1:1 line is shown for reference.

A) Data at 440nm. Least squares fit to these data is:

Predicted R440[0.034]= 0.91[0.14]*Measured R440 -0.012[0.027]; r^2=0.89; n=7

B)Data at 550nm. Least squares fit to these data is:

Predicted R550[0.023]= 0.83[0.10]*Measured R550 +0.0086[0.018]; r^2=0.93

Standard errors of the slope, intercept, and predicted value are given in square brackets for both equations.

Fig. 11- $\tilde{b}_{b\,550}$ vs $\tilde{b}_{b\,440}$ for bloom calculated from bbtot and btot measurements (+ symbols). Variability of $\tilde{b}_{b\,550}$ vs $\tilde{b}_{b\,440}$ due to changes in chlorophyll concentration are shown for comparison (relationships given by Gordon and Morel,1983); the two endpoint chlorophyll concentrations are shown for reference. A 1:1 line is also shown.

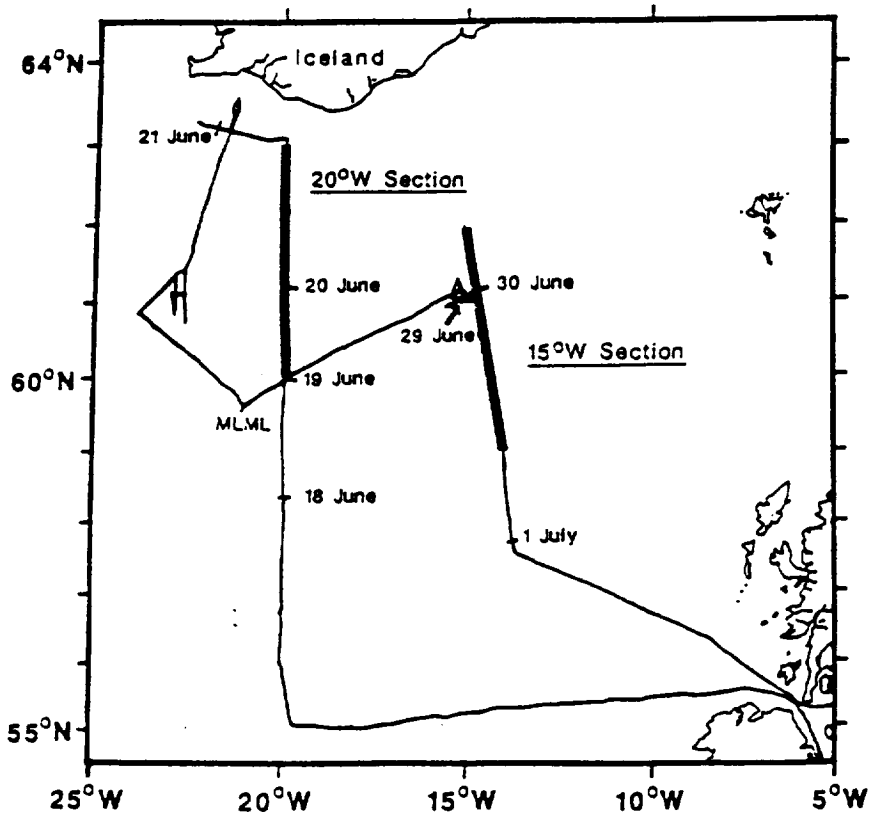
64°N
60°N
55°N
25°W
20°W
15°W
10°W
5°W
Iceland
21 June
20°W Section
20 June
30 June
29 June
15°W Section
19 June
MLML
18 June
1 July

Fig 1

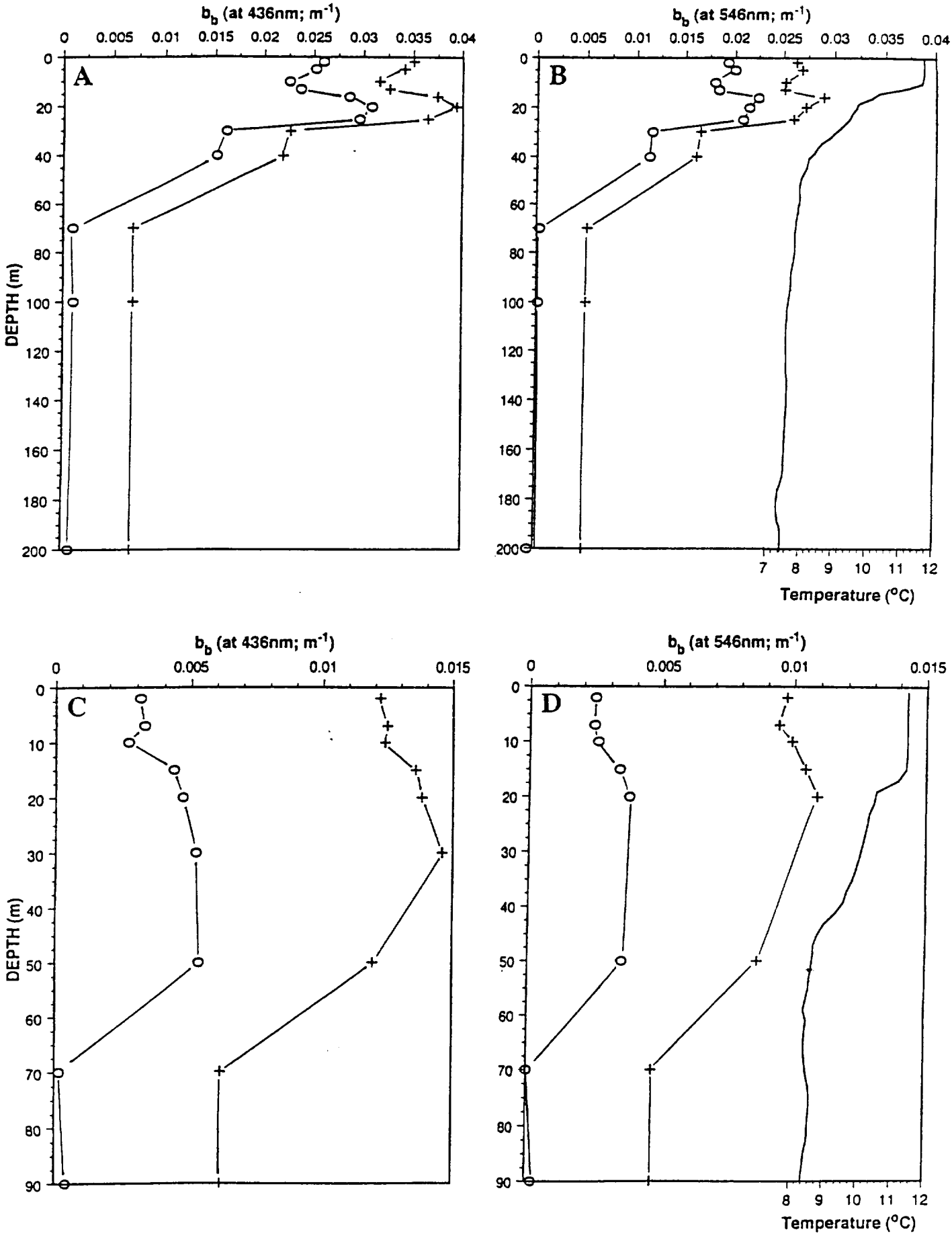
A
B
C
D
b_b (at 436nm; m^{-1})
b_b (at 546nm; m^{-1})
DEPTH (m)
Temperature (°C)
0
0.005
0.01
0.015
0.02
0.025
0.03
0.035
0.04
7
8
9
10
11
12
20
40
60
80
100
120
140
160
180
200
30
50
70
90

Fig 2

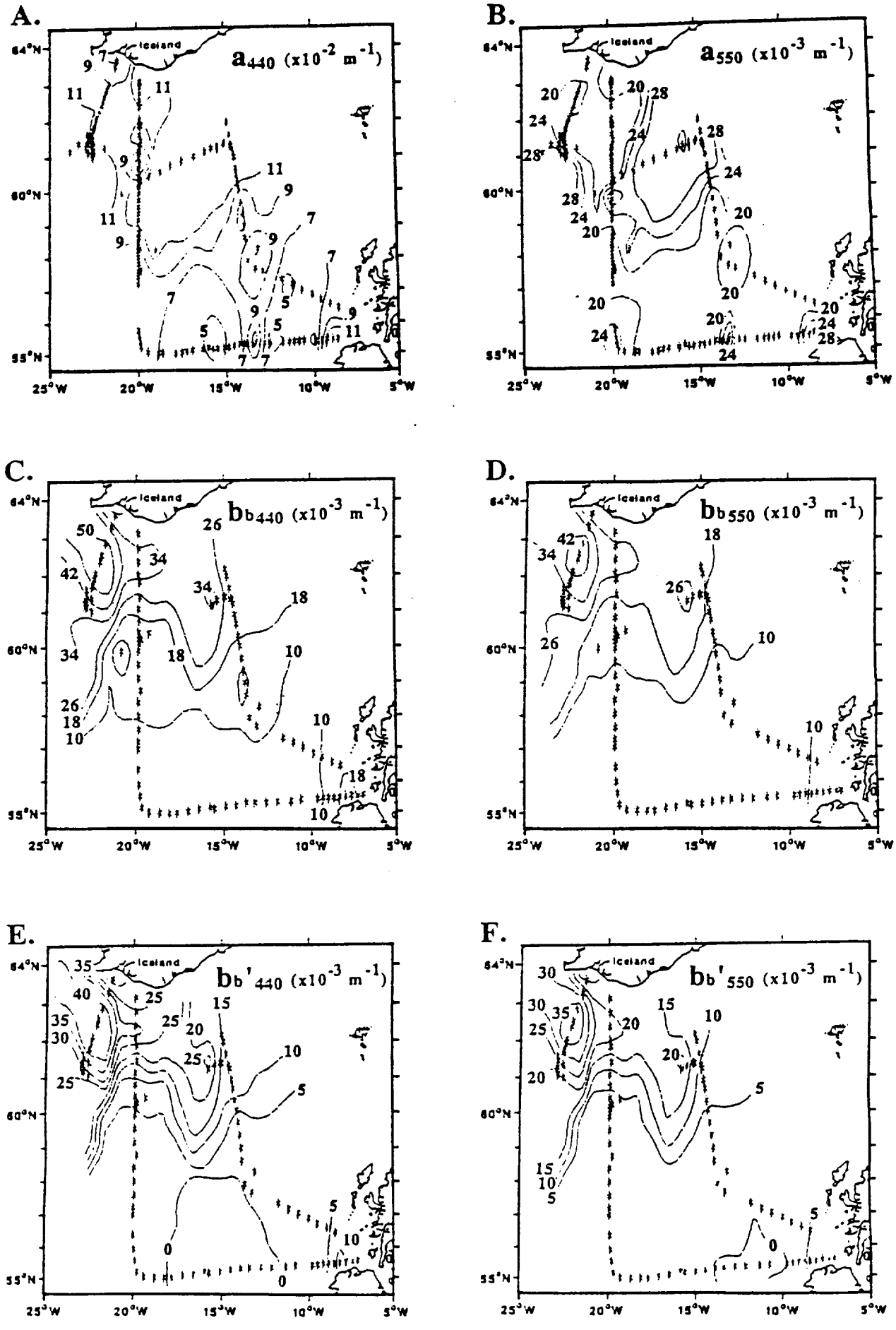
A.
a_{440} (x10^{-2} m^{-1})
B.
a_{550} (x10^{-3} m^{-1})
C.
bb_{440} (x10^{-3} m^{-1})
D.
bb_{550} (x10^{-3} m^{-1})
E.
bb'_{440} (x10^{-3} m^{-1})
F.
bb'_{550} (x10^{-3} m^{-1})
Iceland
64°N
60°N
55°N
25°W
20°W
15°W
10°W
5°W

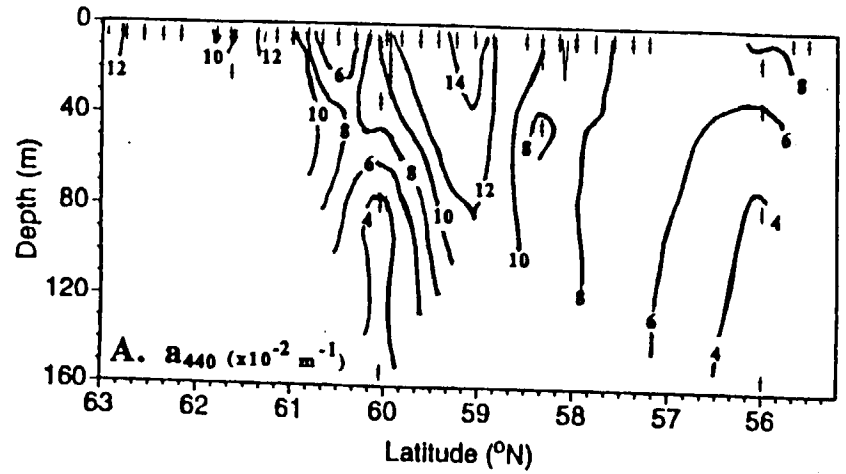
A. a_{440} (x10^{-2} m^{-1})
Depth (m)
Latitude (°N)

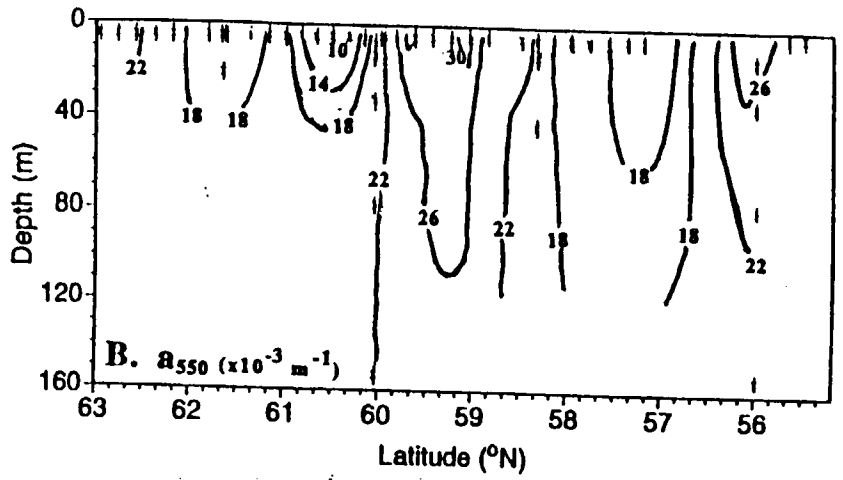
B. a_{550} (x10^{-3} m^{-1})
Depth (m)
Latitude (°N)

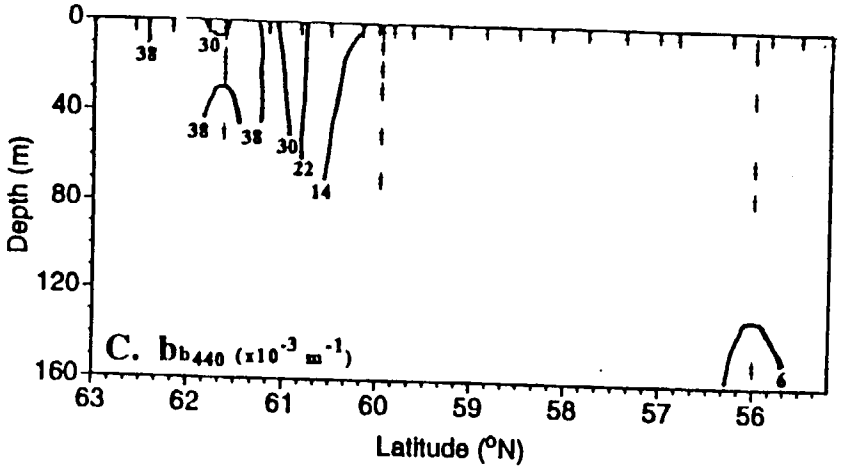
C. b_{b440} (x10^{-3} m^{-1})
Depth (m)
Latitude (°N)

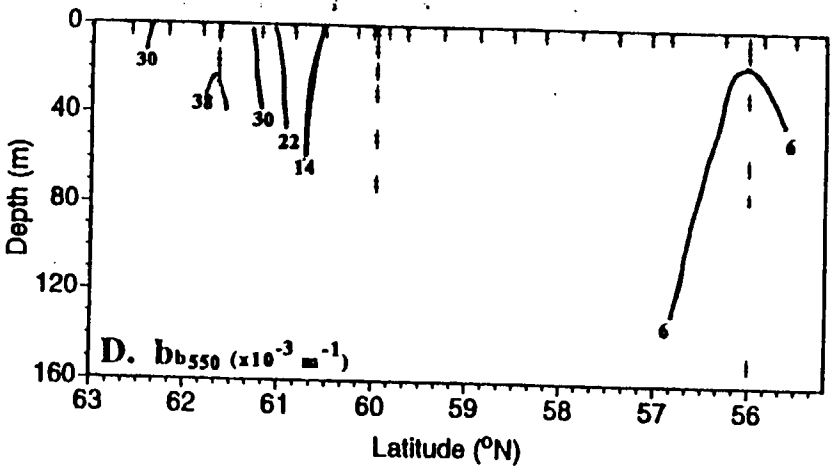
D. b_{b550} (x10^{-3} m^{-1})
Depth (m)
Latitude (°N)

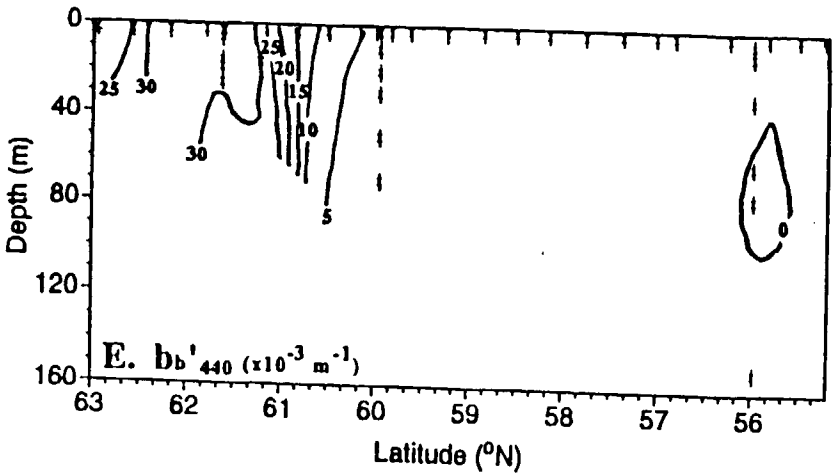
E. $b_b'_{440}$ (x10^{-3} m^{-1})
Depth (m)
Latitude (°N)

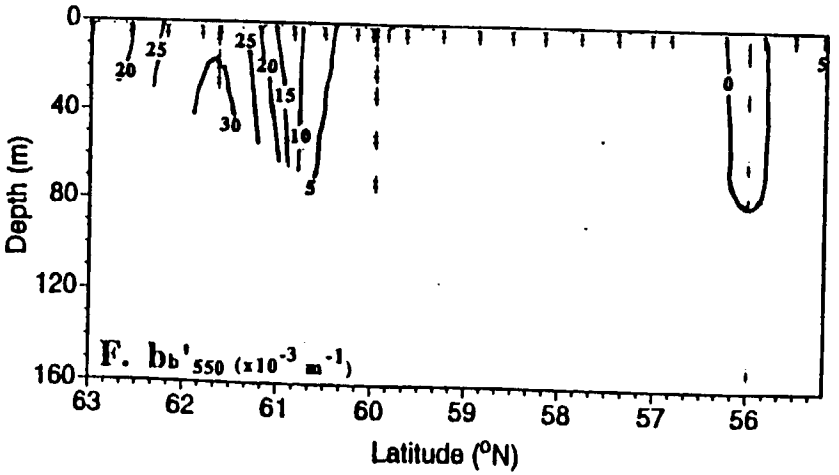
F. $b_b'_{550}$ (x10^{-3} m^{-1})
Depth (m)
Latitude (°N)

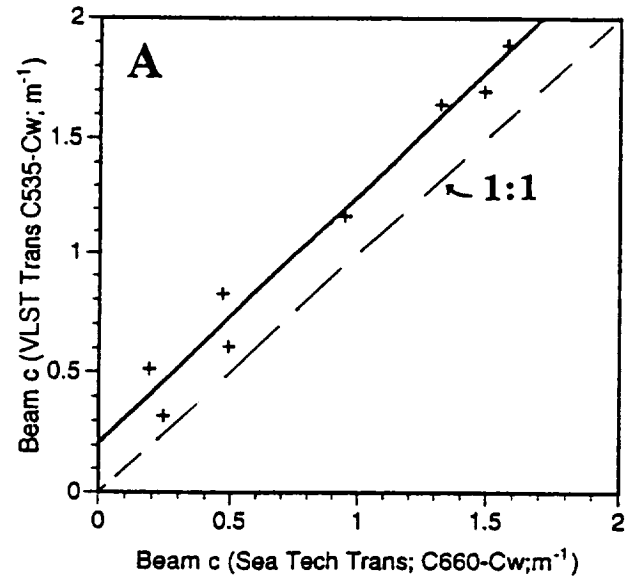
A
1:1
Beam c (VLST Trans C535-Cw; m-1)
Beam c (Sea Tech Trans; C660-Cw;m-1)
0
0.5
1
1.5
2

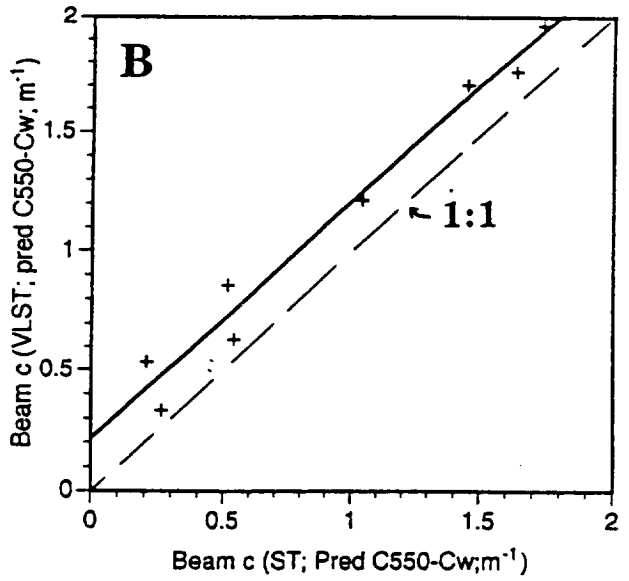
B
1:1
Beam c (VLST; pred C550-Cw; m-1)
Beam c (ST; Pred C550-Cw;m-1)
0
0.5
1
1.5
2

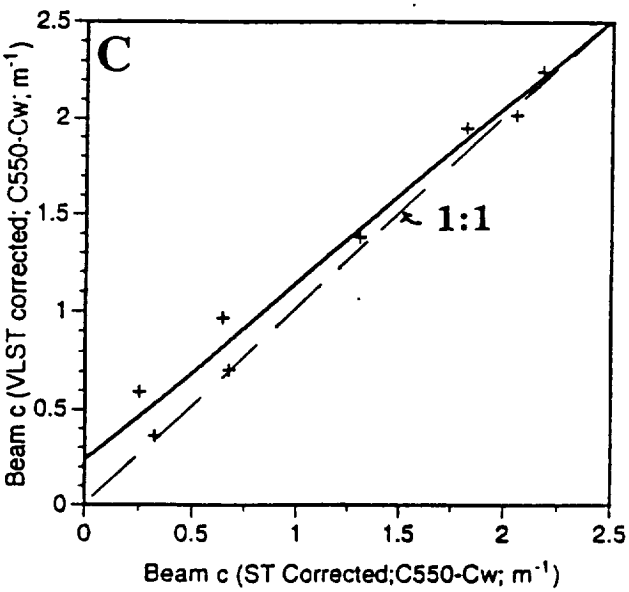
C
1:1
Beam c (VLST corrected; C550-Cw; m-1)
Beam c (ST Corrected;C550-Cw; m-1)
0
0.5
1
1.5
2
2.5

Fig 5

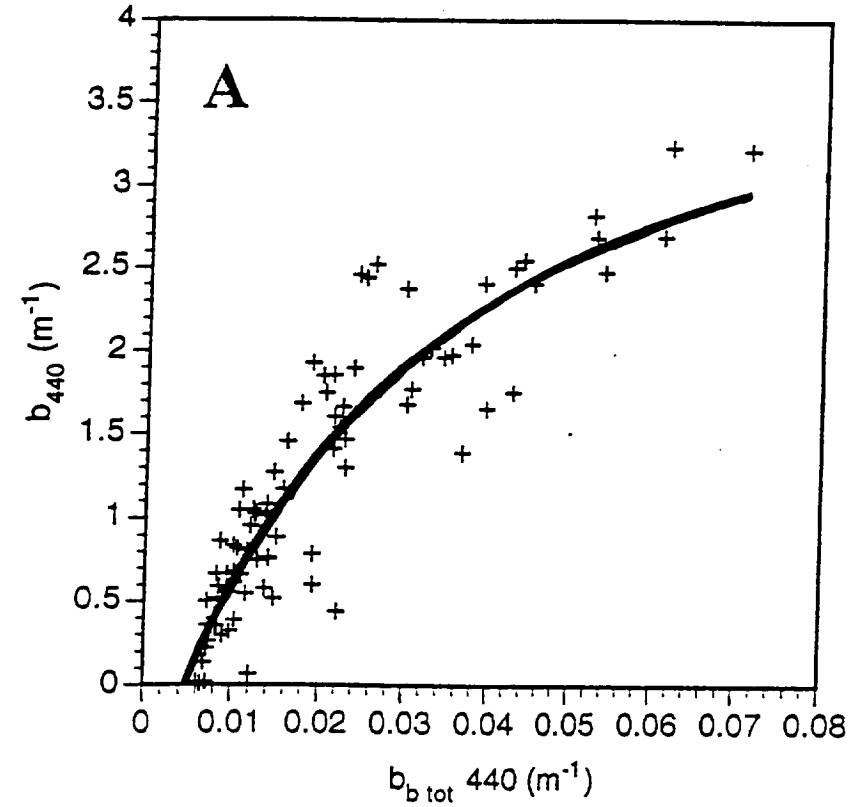
A
b_{440} (m^{-1})
$b_{b\ tot}$ 440 (m^{-1})
0
0.5
1
1.5
2
2.5
3
3.5
4
0.01
0.02
0.03
0.04
0.05
0.06
0.07
0.08

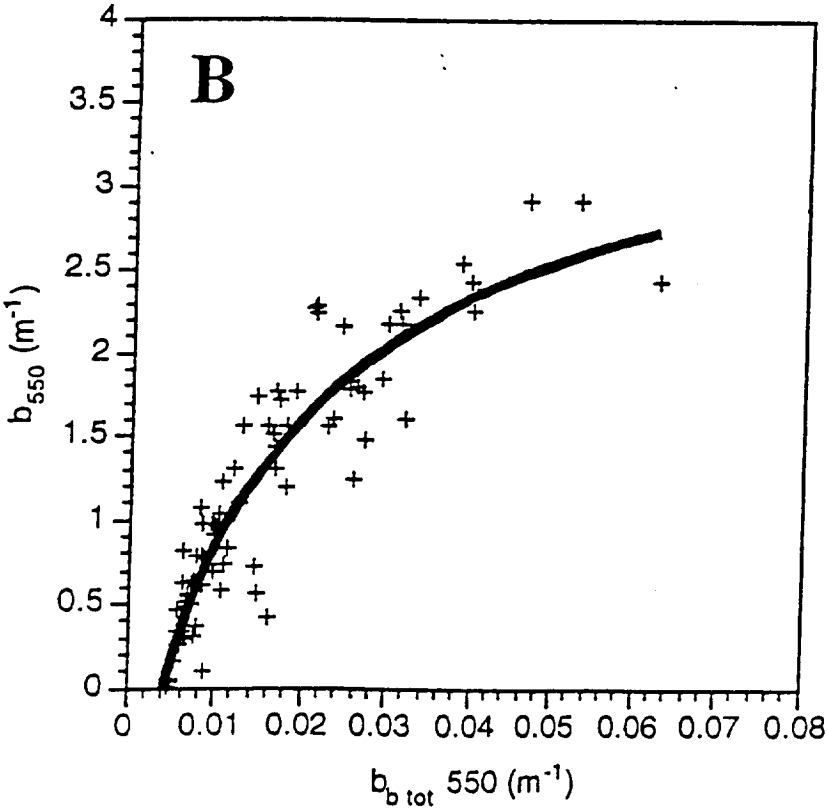
B
b_{550} (m^{-1})
$b_{b\ tot}$ 550 (m^{-1})
0
0.5
1
1.5
2
2.5
3
3.5
4
0.01
0.02
0.03
0.04
0.05
0.06
0.07
0.08

Fig 6

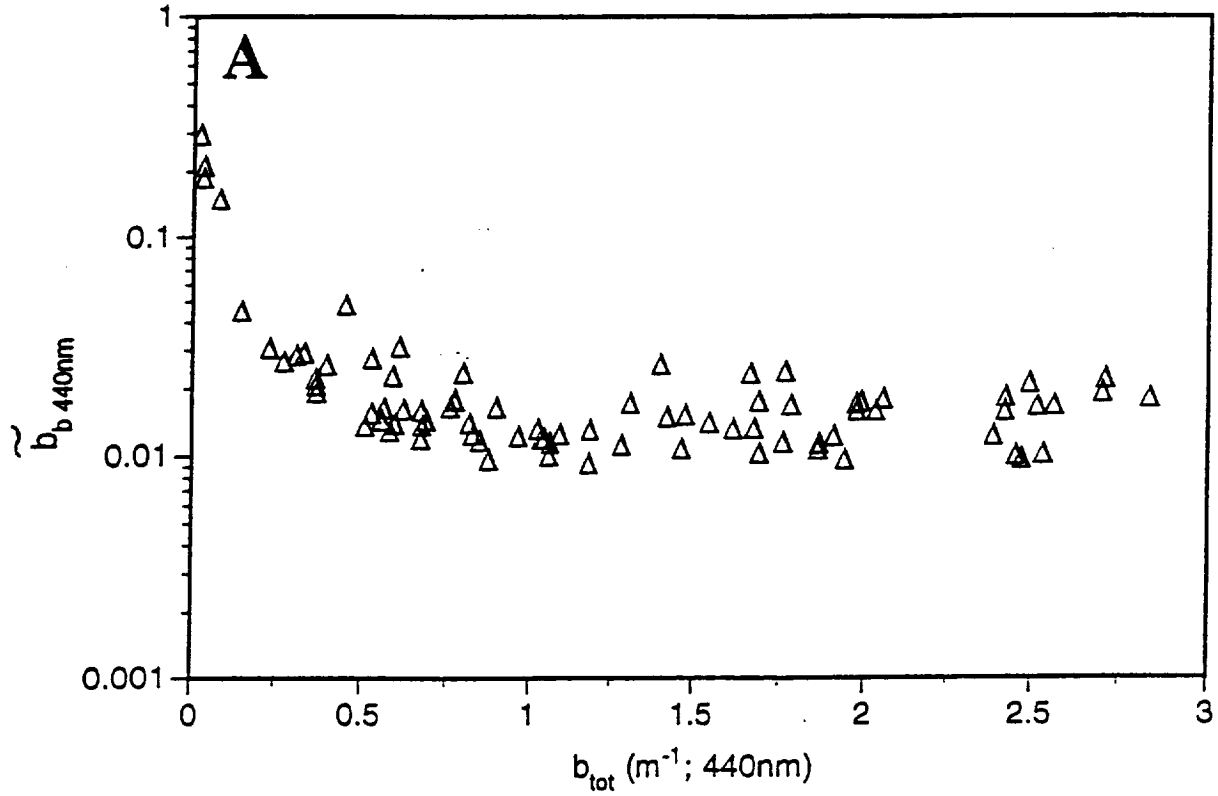
A
1
0.1
0.01
0.001
0
0.5
1
1.5
2
2.5
3
$\tilde{b}_{b\,440nm}$
b_{tot} (m^{-1}; 440nm)

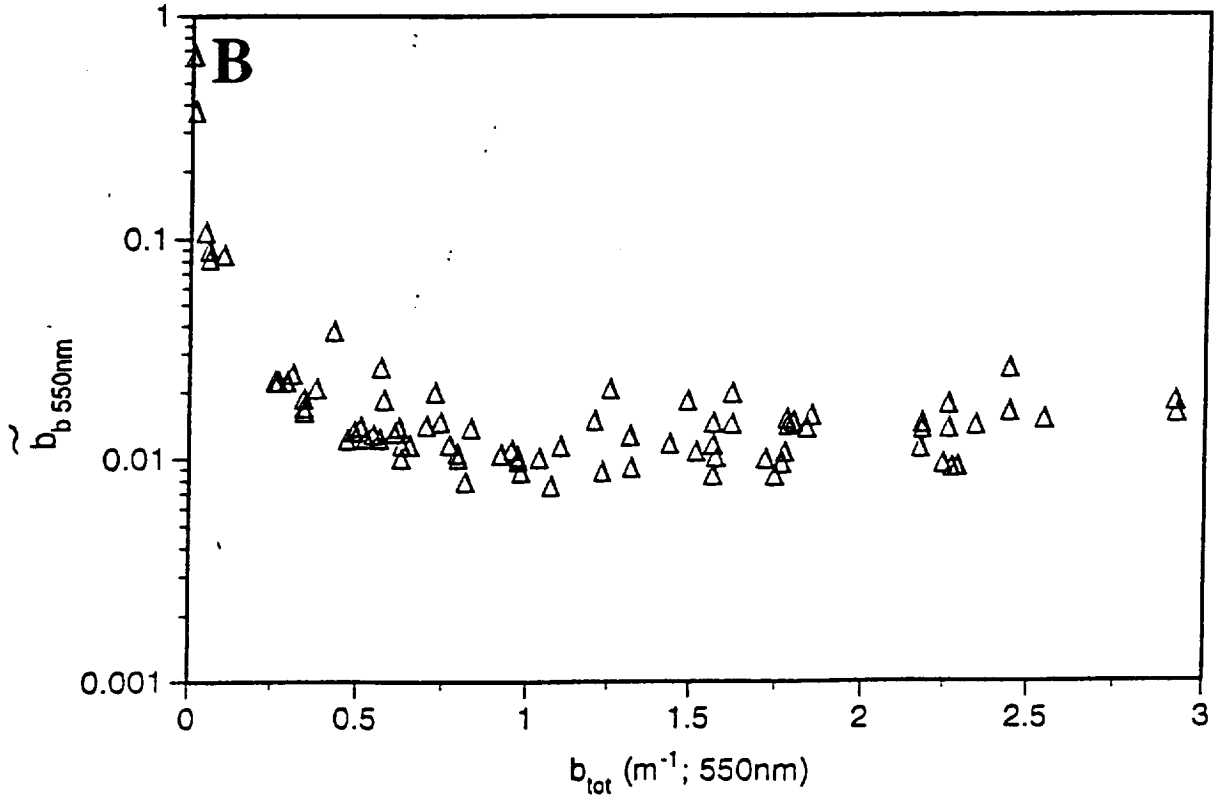
B
1
0.1
0.01
0.001
0
0.5
1
1.5
2
2.5
3
$\tilde{b}_{b\,550nm}$
b_{tot} (m^{-1}; 550nm)


Iceland
30
15
10
15
20
10
5
24 W
20 W
16 W
NOAA-11 19 June 1991 15:04 GMT

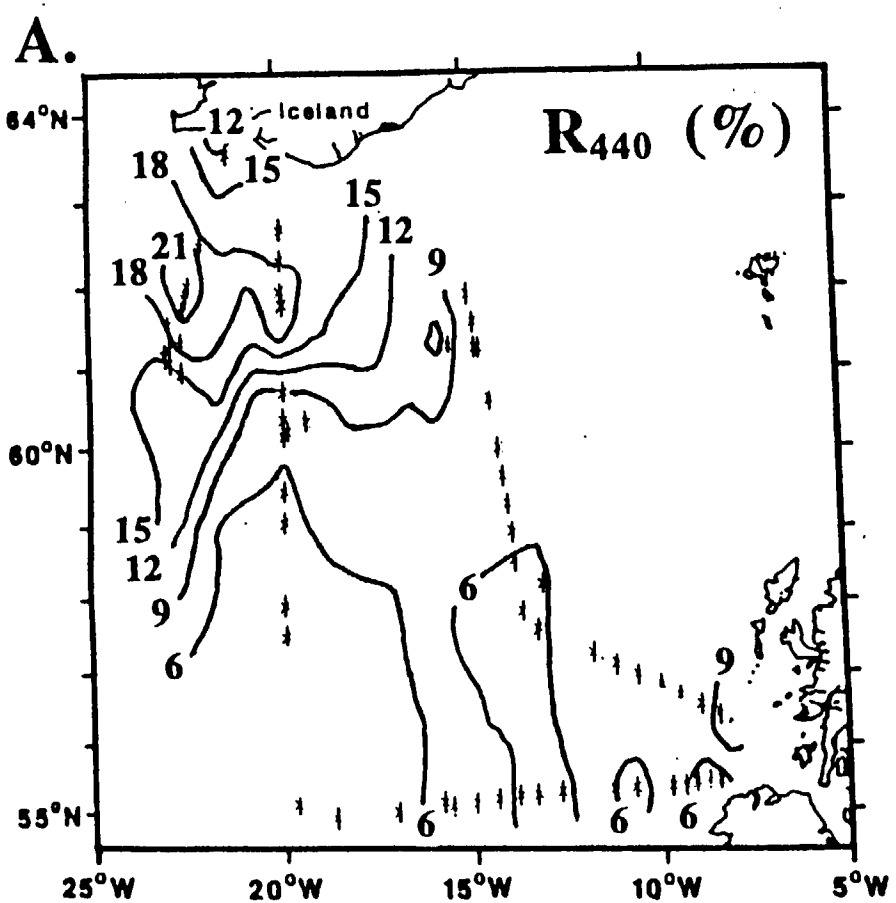
A.
Iceland
R_{440} (%)
64°N
60°N
55°N
25°W
20°W
15°W
10°W
5°W
18
15
12
21
9
6

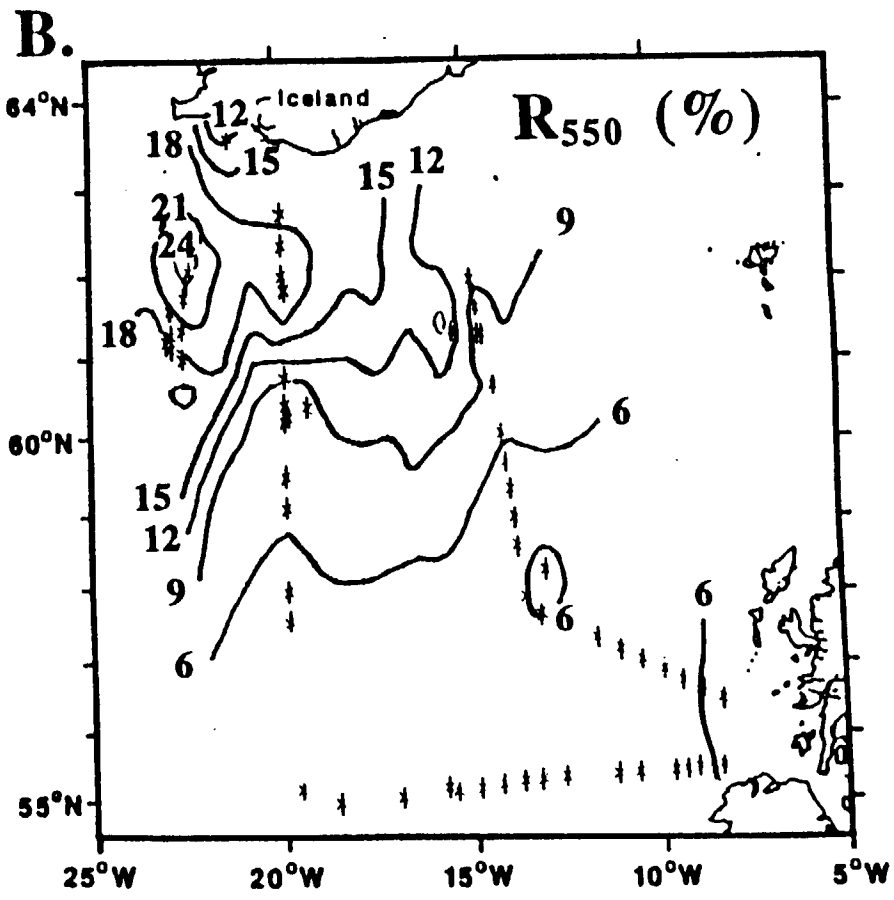
B.
Iceland
R_{550} (%)
64°N
60°N
55°N
25°W
20°W
15°W
10°W
5°W
18
15
12
21
24
9
6

Fig. 3

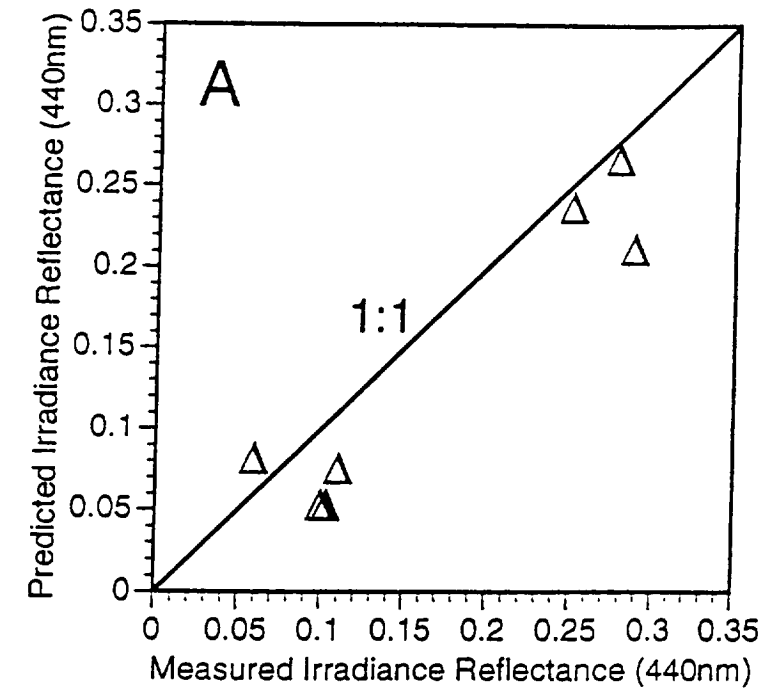
A
1:1
Predicted Irradiance Reflectance (440nm)
Measured Irradiance Reflectance (440nm)
0
0.05
0.1
0.15
0.2
0.25
0.3
0.35

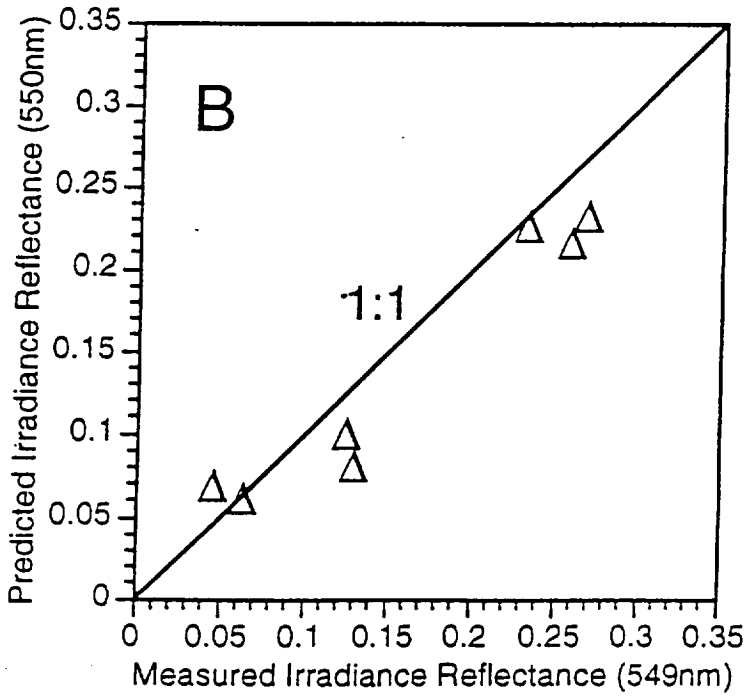
B
1:1
Predicted Irradiance Reflectance (550nm)
Measured Irradiance Reflectance (549nm)
0
0.05
0.1
0.15
0.2
0.25
0.3
0.35

FIG 10

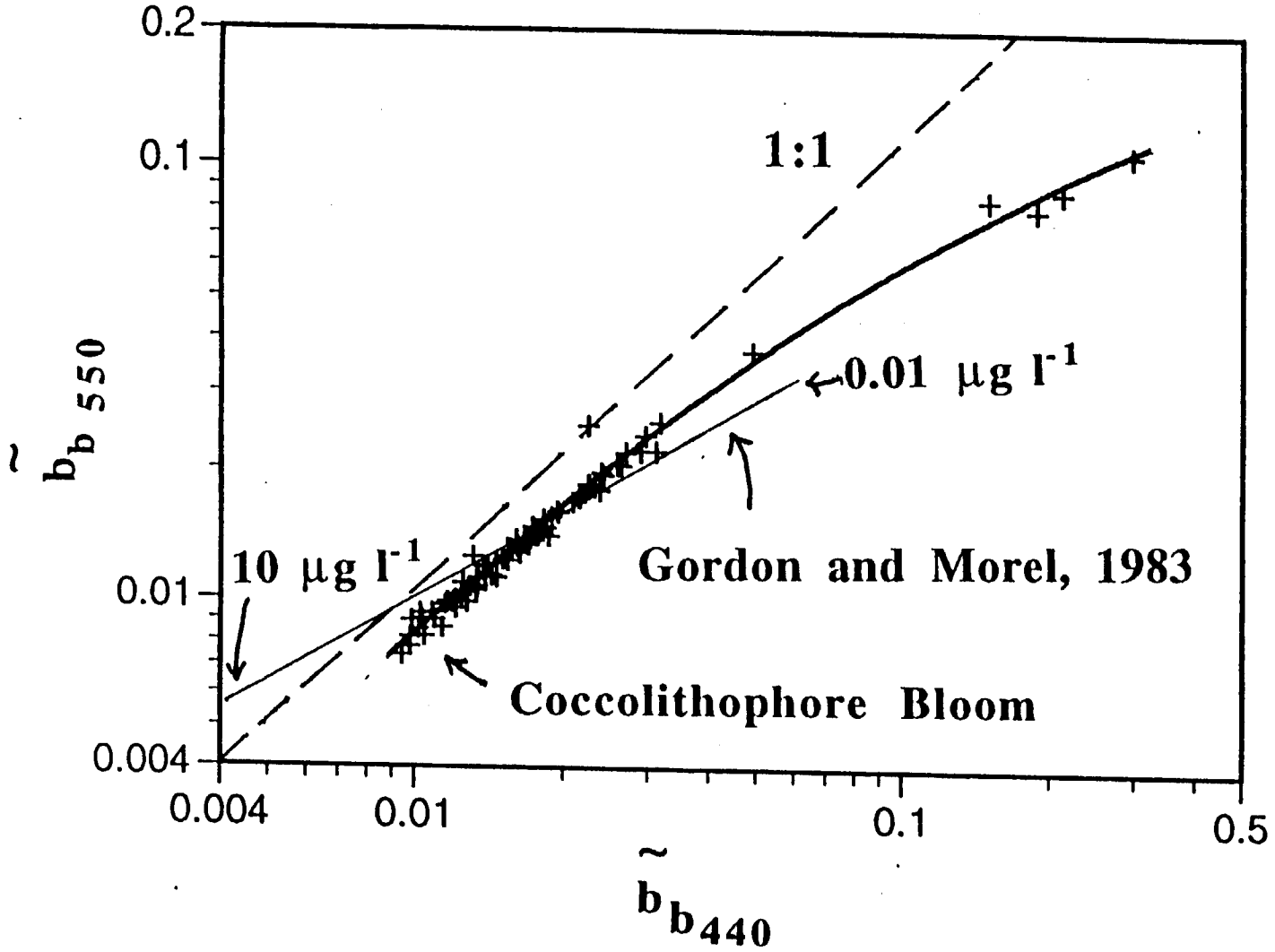
0.2
0.1
0.01
0.004
0.004
0.01
0.1
0.5
1:1
0.01 μg l-1
10 μg l-1
Gordon and Morel, 1983
Coccolithophore Bloom
b̃b 550
b̃b440

Fig 11

DRAFT 12 January 1996 In Press Revised for Limnology and Oceanography

Appendix 5

The 1991 coccolithophore bloom in the central north Atlantic

II- Relating optics to coccolith concentration

William M. Balch

Bigelow Laboratory for Ocean Sciences, McKown Point, W. Boothbay Harbor, ME 04575

Katherine A. Kilpatrick

Division of Meterology and Physical Oceanography, Rosenstiel School for Marine and Atmospheric Science, University of Miami, 4600 Rickenbacker Causeway, Miami, FL 33149-1098

Patrick Holligan

Dept. of Oceanography, University of Southampton Highfield, Southampton, S017 1BJ, U.K.

Derek
~~Derrick~~ *Harbour*

Plymouth Marine Laboratory, West Hoe, Plymouth, PL1 3DH United Kingdom

Emilio Fernandez

Depto. Recursos Naturais e Medio Ambiente, Facultad de Ciencias del Mar, Campus Lagoas-Marcosende, Universidade de Vigo, E-36200, Vigo, Spain

Running head- Coccolithophore bio-optics

Abstract

This study summarizes the relationships between various biological and optical properties of a mesoscale coccolithophore bloom observed in the north Atlantic during June 1991. The optical properties were primarily affected by the concentration of coccoliths and suspended calcite. Backscattering was positively correlated to coccolith concentration and even better correlated with the concentration of suspended calcite. The reason for this was that it was difficult to enumerate the numbers of coccoliths attached to cells using microscopy whereas atomic absorption analyses of calcite-calcium were equally accurate whether calcite was attached or detached from cells. As the bloom aged, the ratio of detached coccoliths to plated cells increased. Dilution experiments provided the most precise relationships between coccolith backscattering and coccolith abundance. The calcite-specific scattering coefficient was estimated from measurements of beam attenuation, absorption, and calcite concentration. This average coefficient was close to theoretical estimates but there was some variability; at low cell and coccolith concentrations, the calcite-specific scattering coefficient was greatest. The ratio of scattering to absorption was partially driven by the ratio of calcite to chlorophyll in the seawater. The contribution of coccolith backscattering to total scattering was modeled as a function of coccolith concentration and chlorophyll concentration. Even at lower concentrations representative of "non-blooms", coccoliths are responsible for 5-30% of the total backscattering. Anomolous diffraction theory was used to show that calcite-specific scattering is the highest for 1-3μm spheres, the diameter of *E. huxleyi* coccoliths. The calcite-specific scattering coefficients of larger calcite particles (e.g. plated coccolithophore cells, foraminifera, pteropods) would be expected to be considerably lower. These data were used to test an approach for predicting coccolith concentration from water-leaving radiance in the blue and green wavelengths.

Acknowledgments

The officers and crew of the RRS Charles Darwin are acknowledged for their expert ship handling. The staff of the Research Vessel Services, Barry, U.K. are thanked for their logistical support of these ship studies. Beam attenuation data used to calculate total scatter were kindly provided by Charles Trees (CHORS, San Diego) and Roy Lowry (British Oceanographic Data Centre, Bidston, U.K.). Howard Gordon and Ken Voss (Univ. of Miami Physics Dept.) have provided help in data interpretation. The comments of two anonymous reviewers are greatly appreciated. This work was generously supported by ONR Ocean Optics Program (N00014-91-J-1048), NASA Global Biogeochemistry (NAGW 2426), NASA EOS/MODIS (NAS5-31363) and NSF Biological Oceanography Program (OCE-8900189 and OCE-9022227) to WMB. This paper is contribution #### to the U.S. Global Ocean Flux Program and contribution #### of the Bigelow Laboratory for Ocean Sciences.

Introduction

The advent of satellite remote sensing has highlighted some classes of algal blooms that significantly modulate the water-leaving radiance of surface waters. Blue-green algae such as *Trichodesmium* can cause high reflectance, beige-colored surface "slicks" in the tropics (Borstad et al. 1992; Lewis et al. 1988). Dinoflagellates can cause blooms or "red tides" in shelf waters at frontal-scales (Pingree et al. 1975; Holligan 1984). Intense green open-ocean diatom blooms also have been observed from space at frontal scales in central ocean basins (Yoder et al. 1994). Coccolithophore blooms, first recognized in satellite images about a decade ago (Holligan et al. 1983), turn the ocean a milky turquoise color and have been observed in both coastal waters and the open ocean. Coccolithophores are members of the algal class Prymnesiophyceae which produce calcium carbonate scales called coccoliths. These range from 1-10μm in diameter and have various shapes such as rhombahedral crystals, discs (with and without a central hole and/or radial elements), and "trumpet" shapes (Reid, 1980). Coccoliths are first attached to the cells and later detach into the seawater.

The main optical impact of coccoliths is to increase the light scattering. Here, we are referring to particle scattering (as opposed to Rayleigh scattering) where the wavelength of light is less than, or equal to, the particle size. Such light scattering is mainly in the forward direction and is size dependent. That fraction of light scattered in the backwards direction per unit thickness is termed backscattering (b_b). (See Table 1 for complete list of symbols used in this work and their definitions). Volume scattering functions of homogeneous particles in the visible wavelengths (λ) are a function of 1) the spectral value of the real part of the particle's refractive index (n), the spectral value of the imaginary part of the refractive index (n', where $n' = a\lambda/4\pi$, and a is the absorption coefficient), and the particle size distribution. There are relatively few values of n and n' available in the literature for coccolithophores (but see Morel 1987 and Bricaud et al. 1992). The high index of refraction of calcite relative to water makes it an extremely efficient scatterer of

light. Given that coccoliths do not absorb light at visible wavelengths (Balch et al. 1991), then the imaginary part of their refractive index is zero.

Four features that set coccolithophore blooms apart from other monospecific blooms of non-calcifying algae are 1) the optical signature is mostly controlled by light scattering from detached inorganic coccoliths, not absorption and scattering by particulate organic matter, 2) organic biomass is often relatively low, 3) coccolithophore blooms are observed at one part of the organism's life cycle, when its plates are detaching, and 4) these blooms impact significantly larger areas than most other types of monospecific blooms. Areal extents of typical coastal coccolithophore blooms are 50,000 to 100,000 km^2 (Holligan et al. 1983; Balch et al. 1991; Brown and Yoder 1993) while open ocean blooms have been observed to have areas > 0.5 x 10^6 km^2 (Holligan et al. 1993).

Coccolithophores affect not only the optics, but also the seawater chemistry; in high abundance, they strongly modulate the alkalinity and $\Sigma CO2$ levels in surface waters (Robinson et al. 1994). Such chemical changes frequently parallel optical changes. For example, alkalinity in coccolithophore blooms has been shown to be inversely related to optical backscattering of detached coccoliths. Moreover, beam attenuation has been shown to be positively related to PCO_2 (Holligan et al. 1993).

Coccolithophore blooms also impact other aspects of biology in the euphotic zone. For example, due to their ability to survive in moderately stratified, low nutrient waters, coccolithophores can out-compete diatoms for nutrients in such conditions. Thus, they represent "transitional" species between well-mixed, diatom-dominated waters and well-stratified, dinoflagellate-dominated waters (Margalef 1979). Moreover, due to their ability to increase the light scatter of surface waters by detaching their coccoliths, they shoal the euphotic zone, which lowers the light availability for deeper algal species. In turn, this may allow the nitracline to shoal because nitrate uptake is often light-dependent (MacIsaac and Dugdale 1972).

Even though the optical scattering by coccoliths can be significant, there are still relatively few studies that define the precise relationship between the coccolith abundance and light scattering. Earlier studies showed that the relationship between coccolith concentration and light scatter was highly significant, but with variance associated with growth phase of the cells and/or coccolith detachment rates (Ackleson et al. 1994; Balch et al. 1991). The exact nature of the growth effects has remained unknown for field populations.

The first paper of this series examined the spatial variability of optical properties in a mesoscale coccolithophore bloom in the north Atlantic Ocean (Balch et al. submitted). This second paper of the series relates the optical properties (backscattering and total light scattering) to the coccolith abundance, suspended calcite concentration and particle size in this 0.5 x 10^6 km^2 bloom. We applied simple models to explain the effects of chlorophyll and calcite on inherent optical properties of absorption and scattering in seawater. Dilution experiments were used to definitively relate backscattering to coccolith concentration at a given location within the bloom. The light scattering results are compared to predictions based on calcite spheres of various sizes.

Methods

Observations were made on cruise 60 of the RRS *Charles Darwin* (CD60) from 13 June to 3 July, 1991. The cruise track can be found in Balch et al. (submitted; figure 1). Two transects were made along the 20°W and 15°W meridian. Detailed optical measurements of volume scattering and absorption were performed at 111 and 210 stations respectively. For comparative purposes, the ship visited a site well outside the bloom (59° 39' N x 20° 59' W; site of an optical mooring). Other cruise details can be found in Holligan et al. (1993). The reader is referred to Balch et al. (submitted) for details of the methodology for measuring total light scattering (b), backscattering (b_b), and particulate absorption (a_p), all at 436nm and 546nm wavelengths. Briefly, backscattering due to

calcite, hereafter called bb', was calculated as the difference between the b_b of raw seawater and the b_b of the same sample following 30s of bubbling with CO_2 (which reduced the pH to 5.5 and dissolved the calcium carbonate).

Dilution Experiments

Water was sampled using a Niskin bottle, and transferred to a 1 liter polyethylene bottle. A 100 milliliter aliquot of seawater was serially diluted with 0.2μm filtered seawater to achieve a series of coccolith concentrations. Then, volume scattering was measured and backscattering calculated for each concentration.

Total Particulate Carbon and Calcite Analyses

Total particulate carbon was measured according to Fernandez et al. (1993). The technique involved filtering 0.5 liter seawater through precombusted Whatman GFF filters and freezing at -20°C. A Carlo-Erba 1500 (series 2) CHN analyzer was used to measure the total carbon, with no pretreatment to remove calcium carbonate. Calcite was measured by first filtering seawater on pre-combusted Whatman GFF filters, then measuring the atomic absorption of calcium using the technique described by Holligan et al (1993). This technique assumes that all particulate calcium is in the form of calcium carbonate. Briefly, one liter samples were filtered through pre-combusted Whatman GFF 25mm filters, the filters were rinsed with several washes of filtered seawater before freezing at -20°C. Samples were extracted by adding 2 milliliter of 50% trace-metal-clean hydrochloric acid to tubes containing the filters. They were incubated overnight at 40 °C in a water bath. 8 milliliters of 1% lanthanum chloride was added to each tube (to remove phosphorous suppression of ionization). The supernatant was then injected into a flame photometric atomic absorption spectrometer, measuring absorption at 422.7 nm with a 10 cm air-acetylene flame. Calibration curves were prepared using commercial calcium standards. Blank filters were prepared towards the end of the cruise by mounting identical pre-

combusted filters in the filter tower apparatus, applying vacuum, and adding GFF filtered seawater to wet the filter, and identical rinsing and preparation techniques as described above. Total organic carbon was estimated as the difference between total particulate carbon and inorganic calcite carbon.

Cell and Coccolith Enumeration

Cell and coccolith enumeration was performed according to Holligan et al. (1984). Counts were performed on both buffered formalin and Lugol's iodine using an inverted microscope.

Results

Standing stocks of cells, coccoliths and carbon

There were some well-defined patterns that were observed in the cell count and particulate analyses during the meso-scale coccolithophore bloom. Coccolith concentrations [N_{cocco}] were about an order of magnitude higher than coccolithophore cell concentrations [N_{cells}]. Note, however, that the ratio of coccoliths to cells was not constant; a least-squares linear fit only explained 53% of the variance with the standard error of the dependent variable [N_{cocco}] of 45259 coccoliths/milliliter. A least-squares power fit explained considerably more variance (78%) and the relationship, plus error terms, is given in Table 2. It implies that the ratio of detached coccoliths to cells was decreasing from 26 to 17 as cell abundance increased from about 100 to 10,000 cells milliliter^{-1} (Fig. 1A). The standard error of the dependent variable (Log [N_{cocco}]) was +/- 0.31 log units or about a factor of 2.

A comparison of total particulate carbon versus calcite carbon concentrations revealed that the techniques were internally consistent; in all cases (save for one), total particulate carbon always exceeded calcite carbon. While there was not a highly significant relation between total and calcite carbon, the typical ratio of total particulate carbon:calcite

carbon varied between 2-6 with values approaching 1 as the calcite concentration increased (data not shown). Plotting calcite carbon concentration ([C_{CaCO3}] in μg liter^{-1}) versus the coccolith concentration (per milliliter^{-1}) provided an estimate of the carbon per coccolith. The least-squares relationship is given in Table 2 (Fig. 1B).

Backscattering and scattering as a function of suspended calcite

The blue and green b_b' values represent only the backscattering due to calcium carbonate, with no particulate organic carbon. Our results of comparisons between b_b' versus the numbers of coccoliths or concentration of calcium carbonate are presented in Table 2. The size of the data set for comparison of b_b' and calcite concentration was bigger than the data set for comparison of b_b' and coccolith concentration (due to the time-consuming nature of microscopic cell counts). It is not apparent that this produced any bias to the results, however, since calcite concentration and coccolith abundance were sampled throughout the bloom. Highest coefficients of determination and lowest standard errors resulted when b_b' was predicted from calcite concentration (Table 2, Fig. 2). Reasons for this will be discussed later.

The best relationships between b_b' and coccolith concentration were achieved during the dilution experiments. In seven experiments using water from the top 12m, the average coefficient of determination was 0.96 for all 436 and 546nm measurements (Table 3, Fig. 3). Moreover, the slopes of the b_b' versus coccolith relationships varied by about 4X at either wavelength, with the largest slopes observed early in the event (22, 24, and 25 June), and reduced values at the end of the bloom (6/27 and 6/29).

Beam attenuation (c) was measured along-track and in vertical profiles during the bloom (see description in Balch et al. submitted). Given that beam attenuation is the sum of scattering (b) and absorption (a), it was possible to calculate total scatter as the difference between c and a, where total absorption was taken as that due to water and particles only (Balch et al. submitted). Note, that the scatter due just to calcite (b'; m^{-1}) could not be

calculated using this technique, since the treatment to dissolve coccoliths could not be performed in situ, in the volume viewed by the transmissometer. Nevertheless, there was a positive relationship between total scatter (b_{436} or b_{546}) versus calcite concentration which was well fit by the linear relationships given in Table 2 (see also Fig. 4). For relating calcite concentration to light scatter, the green wavelengths are preferred to the blue wavelengths as the impact of chlorophyll absorption is minimized. For the b_{546} vs. $[C_{CaCO_3}]$ relationship in Table 2, the Y intercept ($0.410\ m^{-1}$) was significantly different from zero and had confidence limits of 0.29 to $0.53\ m^{-1}$. The slope of this line, $8.413 \times 10^{-3}\ m^2$ (mg calcite C)$^{-1}$ represented the calcite-specific scattering coefficient (b^*_{550}). The 95% error limits on the slope were 7.49×10^{-3} to $9.33 \times 10^{-3}\ m^2$ (mg calcite C)$^{-1}$ and there was some bias in the error, with highest b^*_{550} values at low coccolith concentrations (Fig. 5).

Scattering per unit chlorophyll was calculated for comparison to the large numbers of historical data collected by Morel (1987); such values were generally 10X greater in this coccolithophore feature than in typical non-bloom populations, and there was no correlation between chlorophyll and light scattering. A different approach for accounting for the absorption and scattering values in this coccolithophore bloom was to compare the ratio of scattering to absorption (b/a) to the ratio of the concentrations of the principal scatterer to the principle absorber (mg calcite C/ mg chlorophyll, hereafter designated γ). It should be noted, however, that the correlation was lower than expected; it was strongest at 550 nm, but still accounted for only 43% of the variance. Using only data where $b/a > 10$ (as representative of the most turbid parts of the bloom), the b/a ratio versus γ least squares fit accounted for 62% of the variance (Table 2). At 436nm, the correlations between b/a versus γ never exceeded r^2 of 0.44 (data not shown).

Discussion

From a remote sensing perspective, the time scale for the onset of turbid conditions was driven by three factors, the calcification rate, the coccolith detachment rate, and

numbers of coccoliths per coccolithophore. Numbers of coccoliths per cell have been previously estimated at about 15 for *E. huxleyi* (Paasche, 1962). Linschooten et al. (1991) also found that *E. huxleyi* in a 16:8 light dark cycle, grown on full-strength IMR medium (Eppley et al., 1967) had 15-20 coccoliths per cell at the end of the light period. They pointed out that this number of coccoliths was sufficient to cover the cells in a single layer. Our previous estimates (Balch et al. 1993) have shown that numbers of coccoliths can reach as high as 80 per cell at mid-logarithmic growth, and this decreases as cells reach stationary phase. Using just coccolith and cell size, we previously calculated that the first layer of plates consists of about 15 coccoliths. The relationship between detached coccolith abundance and cell abundance from this North Atlantic bloom was similar to previous laboratory studies (Balch et al. 1993); on average, each cell detached a maximum of 26 coccoliths, or almost two layers, during the early stages of growth and a minimum of 17 , or about one layer, towards the later stages of the bloom (Fig. 1; Table 2). Note, this should not be confused with the results of Fernandez et al. (1993; their table 1) who showed that the coccolith/cell ratio in the same bloom varied about one order of magnitude at 5 stations, from 12 to 108. The ratios cited here are the average values derived from *all* the cell counts shown in figure 1. For example, using the 95% confidence intervals for slope and intercept of the first regression in Table 2 (Log coccoliths versus Log coccolithophores) would give a range in coccoliths/cell of 11 to 65 when there were 100 cells milliliter^{-1}, and a coccolith/cell ratio of 5 to 61 when the cell concentration was 10,000 cells milliliter^{-1}. These ratios for the entire data set are a bit lower than at the five stations cited by Fernandez et al. (1993).

The fact that the ratio of detached coccoliths per cell varied, plus the observation of other phytoplankton species, undoubtedly caused large variance in ratios of total particulate carbon to calcite carbon. In the less concentrated parts of the bloom, calcite carbon represented about 16-50% of the total carbon, whereas in the densest part of the bloom, virtually all of the carbon was as calcite which leads to the question, where did the organic

carbon of the coccolithophores go? Cell lysis may have occurred but there was little evidence for unusual numbers of viruses in the late bloom stages (see Bratbak et al. 1993). It seems equally probable that the lack of organic carbon was due to highly efficient removal by grazers or sinking (Holligan et al., 1993).

The calcite concentration data, combined with coccolith count values (Fig. 1B), provided an opportunity to check the calcite carbon per coccolith for field populations of *E. huxleyi*. Previous laboratory and field studies have shown this to be variable. For example, Paasche (1962; 1963) gave a value of 0.17 pg C per coccolith for cultured cells. Linschooten et al. (1991) estimated less than half this value, 0.065-0.078 pg C per coccolith. Balch et al. (1991) estimated 0.26 pg C per coccolith based on CHN measurements of field populations. Holligan et al. (1983) saw distinctly higher values of 0.5 and 0.6 pg C per coccolith. The least squares fit to the data of Figure 1B gave 1.05 pg C per coccolith but this high value resulted from the fact that coccoliths attached to cells were not included in the coccolith count. When the coccospheres were multiplied by 20 (assuming 20 coccoliths per cell) and added to the detached coccolith concentration, the calcite per coccolith reduced to 0.47 pg C per coccolith (Fernandez et al. 1993), more reasonable, but still higher than results from previous laboratory studies. This calculation also implied that, on average, over half of the coccoliths were detached in the North Atlantic bloom of 1991. This has important ramifications for interpreting the light scatter data.

Relation of backscattering to coccolith concentration

Two fundamentally different approaches were used to understand the impact of coccolith density on calcite-dependent backscattering (b_b'). The first involved measuring b_b' of seawater samples and plotting it against coccolith concentration with no dilution (Fig. 4). Hereafter, this will be referred to as the "nondilution approach". Note, in making

these regressions, data is pooled from various locations within the bloom, regardless of growth stage.

Our past experience has shown that calcite backscattering varies not simply as a function of coccolith density. Other factors may be involved, such as the number of detached versus attached coccoliths, variance in the abundance of other calcifying algal species, coccolith size, and coccolith integrity. All of these factors may vary as a function of the growth stage of the bloom.

The second approach used in this work involved serial dilutions of individual samples and examining b_b' against coccolith abundance (hereafter called the "dilution approach"). The purpose of the dilution experiments was to examine the relationship between calcite-specific backscattering versus coccolith concentration for specific stages of bloom development. The results from the dilution experiments allowed deductions about how much variance in the b_b' versus coccolith relationship could be attributed to growth stage. The results allowed limited speculation on the cause of the variations; for example, they did *not* discern between coccolith integrity and coccolith size. Since this analysis only focused on b_b', not b_b, potentially complicating factors related to other organic particles was not invoked to interpret the results. For example, changes in refractive index would not have been expected to cause changes in b_b' (unless calcite particles had been replaced with aragonite particles, for which there was no evidence from our microscopy).

Based on the nondilution approach, 80-85% of the variance in b_b' could be accounted for by the abundance of detached coccoliths in the Gulf of Maine (Balch et al. 1991). In the North Atlantic coccolithophore bloom, only 56-63% of the variance in b_b' could be explained using the non-dilution approach (Table 2). For the BOFS expedition, use of the dilution approach increased the explained variance another 30-40% (to >95%) for 11 out of 14 individual experiments (Table 3; Fig. 3). Two exceptions with lower explained variance were at the station at 60.9°N x 23.9°W on 25 June. The results of this dilution experiment were notably curvilinear. Multiple scattering is difficult to invoke as a

reason for the curvilinear behavior since the detached coccolith concentration was not particularly high to begin with, certainly no higher than other experiments where the relationship was clearly linear. The other low r^2 value was associated with the 546nm data at the station on 27 June (61.2°N x 15.2°W; r^2=0.84). This appears to be due to one anomalous data point at 2.25 x 10^7 coccoliths $liter^{-1}$. Note, the 436nm data at the same station were highly linear (r^2=0.99) which supports the possibility that the 546 nm data had a bad data point. Overall, the dilution experiment results clearly showed the differences in the b_b' vs coccolith relationship for different parts of the bloom. We speculate that the most likely cause of the high variance between dilution experiment "slopes" were differences in the ratio of detached coccoliths to plated cells which varied with bloom age. Nevertheless, we cannot exclude changes in coccolith integrity or the size distribution of the coccoliths (the latter admittedly being one of the most important factors affecting light scattering of marine particulates).

We estimated the age of this bloom from the earliest satellite image where no high reflectance water was observed (June 10, 1991), and by the next available image (15 June, 1991) the bloom was well underway. The assumption of a 10 June start date may cause a slight overestimate in the age. For the dilution experiment data, we observed that the detached coccolith/cell ratio increased with bloom age (Table 4). Moreover, as the detached coccolith/cell ratio increased, the slopes from the dilution experiments--essentially the backscattering per detached coccolith-- decreased (Fig3).

Many of the above problems can be avoided by using the mass of calcium carbonate instead of numbers of coccoliths, to quantify coccolith abundance. Use of the non-dilution approach, but regressing bb' against calcite concentration, explained about 85% of the variance in b_b' *for all cruise samples* (Fig. 2). This tighter fit probably was due to the fact that coccoliths attached to cells were included in atomic absorption estimates but they were not included in microscope enumeration.

Calcite concentration explained 70% of the variance in total scatter (b_{546}; Fig. 4). This was due to two reasons: 1) estimates of b_{546} were based on the difference between beam attenuation and absorption, and measurement errors likely were greater for b than they were for b_b' and 2) the data included scattering from other types of non-calcite particles. Another factor which may have affected the relationship between calcite concentration and light scattering, was particle size. This will be addressed later.

Calcite, chlorophyll and b/a

Kirk (1981a &b) used a Monte Carlo approach to demonstrate that the ratio of b/a is proportional to Kd(zm)/a (vertical attenuation coefficient for downward irradiance at the mid-point of the euphotic zone divided by the absorption coefficient). Hereafter, the euphotic zone is defined as the depths where downward irradiance >1%. The relationship also included two other factors, μ_0, the cosine of the zenith angle of refracted solar photons just beneath the surface, and $G(\mu_0)$, the fraction of scattering to vertical attenuation (determined from the scattering phase function). Kirk's semi-empirical relationship is given below.

$$Kd(zm)/a = 1/\mu_0 \, [1 + G(\mu_0) \, b/a]^{1/2} \qquad (1)$$

Kirk (1991) applied a similar Monte Carlo analysis to 7 different water types of widely variable volume scattering functions (Petzold 1972). He showed that the equation 1 was generally applicable. Moreover, assuming that the incident light was vertical (μ_0=1), replacing Kd(zm) by Kd(avg) (the average Kd above the depth where downward irradiance = 1% of the surface value), he showed that G(1) was approximately constant with a coefficient of variation of 3.9%. The specific value of G(1) from San Diego Harbor based on Petzold (1972) was 0.231; this is highly relevant to this work since San Diego Harbor has been shown to have a volume scattering function very similar to a previously

observed coccolithophore bloom (Balch et al. 1991). Equation 1 therefore can be re-written.

$$Kd(avg)/a = [1 + 0.231\ b/a]^{1/2} \quad (2)$$

Equations 1 and 2 yield plots of Kd/a versus b/a that are slightly curvilinear (concave-down) up to b/a of 30. For the limit value of b/a =0 (only absorption, no scatter), Kd(zm)/a equals 1.0 (Kirk 1991; his Fig. 1). To illustrate the role of coccoliths in increasing the effective pathlength of light moving vertically through the water column, we have substituted our b/a values into equation 2. In the north Atlantic coccolithophore bloom, 87% of the b/a values at 550nm exceeded 5, and 62% exceeded 10 with the peak b/a values of 45. Therefore, we would expect that Kd(avg)/a values fell between approximately 1.5 and 3.4.

The b/a ratio in typical phytoplankton blooms is usually a function of chlorophyll, but as already discussed, b/a at 546 nm in this coccolithophore bloom was mostly a function of γ, especially in the densest parts of the bloom. The slope of the relation between γ and b/a at 550 nm in the most turbid regions (b/a>10) was about 0.06 mg Chl/mg calcite (Table 2).

To check for internal consistency between the observed inherent optical properties and the quantity of calcite and chlorophyll, the following can be written, specifically for turbid parts of this bloom where b/a>10.

$$b/a = (b^* \times CaCO_3)/(a^* \times Chl) > 10 \quad (3)$$

Equation 3 was then rearranged, substituting γ, to give equation 4, again applicable only to the turbid parts of the bloom.

$$(10a^*)/b^* < \gamma \quad (4)$$

Based on previous calculations of a* and b*, the left side of equation 4 equaled 15.33 mg calcite C/mg Chl [= (10 x 0.0129 m^2(mg Chl *a*.)$^{-1}$)/8.413x10^{-3} m^2 (mg calcite C)$^{-1}$]. As expected, γ values in the coccolithophore bloom fell above this value 97% of the time. Moreover, the slope in the plot of γ versus b546/a546 for all data where b/a>10, was 0.059 mg Chl/mg calcite C (Table 2), representing a statistical average of all of our data. The reciprocal of this slope (16.9 mg calcite C/mg Chl) fell within 10% of (10a*)/b*.

Modelling light scatter due to coccoliths

Our field results provided the means to assess the magnitude of calcite-dependent light scattering relative to the total backscatterance of seawater. The calculations were done two ways, based either on coccolith-specific backscattering or calcite-specific backscattering. There were several assumptions required, however: 1) we used 1.84x10^{-13} (m^2 coccolith)$^{-1}$ and 1.35x10^{-13} (m^2 coccolith)$^{-1}$ for the coccolith-specific backscattering coefficients at 436 nm and 546 nm, respectively (slopes in row 3 and 4, of Table 2), 2) we used the slopes from rows 5 and 6 of table 2 to calculate the calcite-specific backscattering coefficients, and 3) backscattering due to water was 2.27x10^{-3} and 0.965x10^{-3} m^{-1} for 436 nm and 546 nm, respectively (Gordon et al. 1980).

The backscattering due to chlorophyll involved two calculations. The first calculation was based on an earlier bio-optical model of Gordon (1987), designed for case I waters (that is, waters where optical characteristics are dominated by algae and their associated detritus). Particulate scattering at 550 nm (b_p(546)) was empirically predicted using a relationship from Gordon and Morel (1983; based on 550 nm light):

$b_p(550) = Bc\ C^{0.62}$

where B_C represents the scattering coefficient when the concentration of chlorophyll plus phaeopigment (C) is 1 mg m^{-3}. Typically, B_C ranges from 0.12-0.45, with an average of 0.3. Moreover, Gordon (1992) incorporated three factors into their model: 1) that detritus scatters inversely with wavelength, 2) phytoplankton scattering is much less wavelength-dependent, and 3) the wavelength-dependent effects are most pronounced at low C while at

high C, b is essentially wavelength-independent. The relationship derived to satisfy the above observations was (Gordon 1992; his eqn 14):

$$b_p(\lambda) = (0.3\ Chl^{0.62})\ ([(0.5 + (0.25 \log Chl)) + (0.5 - (0.25(\log Chl)))]\ 550/\lambda) \quad (5)$$

where λ represents the wavelength in nanometers. Next, the ratio b_b/b, or $\tilde{b}_b$, has been empirically related to chlorophyll at the two wavelengths by Gordon and Morel (1983; their p. 62).

$$\tilde{b}_b\ chl\ 436 = 1.005\ (Chl^{-0.404})\ 0.01 \quad (6)$$

$$\tilde{b}_b\ chl\ 560 = 1.009\ (Chl^{-0.262})\ 0.01 \quad (7)$$

Note that equation 7 applies to 560 nm, not 546nm but the effect of this difference will be minor. Also, both equations 6 and 7 include multiplication by 0.01 because the original equations provided $\tilde{b}_b$ values in percent (Gordon and Morel 1983). The value $b_{bchl}(\lambda)$ was taken as the product of $b_{chl}(\lambda)$ and $\tilde{b}_b\ chl\ (\lambda)$.

$$b_{bchl}(\lambda) = (b_{chl}(\lambda))\ (\tilde{b}_b\ chl(\lambda)) \quad (8)$$

The results of this modeling can be seen in figure 7 along with data from the bloom. As chlorophyll increased, chlorophyll backscattering increased according to equations 6-8. Thus, the fraction of total backscattering attributed to coccoliths would have decreased purely due to the percentage of organisms containing chlorophyll relative to those containing calcite. It is readily acknowledged that backscattering can be strongly influenced by absorption in phytoplankton (Morel and Bricaud 1980) and the two variables are not necessarily independent. To this end, the above equations relating chlorophyll to

backscattering are empirical, and therefore implicitly include effects of chlorophyll absorption. The relationship between b_b'/b_b vs. coccolith concentration or calcite concentration was curvilinear on a log-log plot with the lines converging towards higher coccolith concentrations. It can be seen that at low chlorophyll concentrations (say 0.1μg chl *a* liter^{-1}), a coccolith concentration of 2000 coccoliths ml^{-1} is sufficient to increase the calcite-dependent scatter to 10% of the total scatter at 546 nm. At a concentration of 10,000 coccoliths ml^{-1} (still considered "non-bloom"), coccoliths represent about 35% of the total b_b at both wavelengths. Values of b_b'/b_btot are 50% between coccolith concentrations of 20,000-40,000 coccoliths ml^{-1}, depending on the chlorophyll level.

The data and predictions for b_b'/b_btot showed values of 50% between calcite concentrations of 40-80 μg calcite C l^{-1}, depending on the chlorophyll level. The model predictions agreed with data mostly at high coccolith densities and there was considerable error at lowest coccolith densities. Cruise data (plotted on the same figure) often fell outside the expected range for water containing 0.01 to 10 mg chl *a* l^{-1}, especially at 436nm wavelength. Clearly, given the variance in coccolith-specific backscatterance (Fig. 3) and calcite-specific backscatterance (Fig. 2), this might account for some of the problem. Furthermore, equations 6, 7 and 8 are average relationships for predicting backscattering from chlorophyll, which also have large confidence limits. Failure of the data to fall within the bounds set by the different chlorophyll levels in figure 7, may be as much due to reduced accuracy of the chlorophyll-component of the model. Regional relationships for these equations might be one solution to this problem. This model only begins to describe the envelopes of variability of calcite-dependent scatter as a function of the concentrations of coccoliths, calcite or chlorophyll *a*. Clearly, more refinements are necessary.

As a cross-check of the scattering coefficients observed in this field study, we calculated calcite-specific scatter for calcite spheres based on anomalous diffraction theory for non-absorbing spheres of van de Hulst (1981; his p. 176). Morel (1987) defined the

attenuation efficiency factor (Qc) as a function of the dimensionless parameter ρ, which is a function of particle diameter (d), wavelength (λ), refractive indices of water (n_w=1.33; Jerlov 1976) and of calcite (n=1.583; Aas 1981). The refractive indices then were used to calculate the relative refractive index (m=n/nw=1.19 for coccoliths).

$$\rho = 2\pi\,(d/\lambda)\,(m-1) \qquad (9)$$

Next, ρ was used to approximate the efficiency of attenuation.

$$Qc(\rho) = 2 - (4/\rho)\sin\rho + (4/\rho^2)(1-\cos\rho) \qquad (10)$$

This function was derived for particles where $2\pi\,(d/\lambda) >> 1$ and the quantity $(m-1) << 1$. For coccoliths, the value of $2\pi\,(d/\lambda)$ at 550nm is 11-23. As described by van de Hulst (1981), equation 10 models light extinction not only when m is close to 1 but even up to values of m= 2 (see figure 32 of van de Hulst 1981; p. 177). Calcite is effectively non-absorbing, so its absorption efficiency, Qa, is zero and its scattering efficiency, Qb, dominates the attenuation efficiency. (That is, Qc = Qa + Qb, so with calcite particles, Qc = Qb). The calcite specific scattering coefficient was calculated by applying equations 9 and 10 to the following equation (Morel 1987):

$$b^* = (3\,\pi/c_{calcite}\,\lambda)\,nw\,(m-1)\,Qb(\rho)/\rho \qquad (11)$$

where $c_{calcite}$ was the density of calcite (2.711×10^6 g m^{-3}). These calculations were performed for calcite spheres from 0.1-1000 mm. Note, equation 10 can be used to calculate the efficiency of attenuation (or in this case the efficiency of scatter) provided that $\pi d/\lambda$ exceeds 1. For these calculations, this would occur at a diameter of 0.14 µm, thus the abscissa of Fig. 7 begins at 0.1 µm. The calcite specific scattering coefficient (b*; m^2(mg calcite C)$^{-1}$) peaked at diameters between 1-3 µm, precisely the size range of

Emiliania huxleyi coccoliths (Fig. 7). From this approach, a 2 μm calcite sphere should have a b* of 9.7x 10^{-3} m^2(mg calcite C)$^{-1}$.

The average observed calcite-specific scattering coefficient for 2 μm coccoliths (b*=8.4 x 10^{-3} m^2(mg calcite C)$^{-1}$; Fig. 4) was 13% lower than the theoretical value of b* for a 2 μm calcite sphere ($P<0.01$). This may have been related to the effect of shape on calcite scatter (discs versus spheres). Size differences also may have caused the error limits in the slopes of Fig. 4 (2 S.E. about these slopes represented +/-8%; Table 2, rows 5 and 6). As already shown, theoretical results for calcite spheres suggested that calcite-specific scatter should increase with decreasing size, peaking at a diameter of 1 μm, and declining below this size (Fig. 7).

It is also worthy of note that we observed slightly higher b* values at low calcite concentrations. This may have resulted from differences in calcite particle size or shape when the concentration of suspended calcite was low versus high (see also Aas 1984). It is important to caution, however, that there was a cluster of b^*_{550} values at early bloom stages (2 x 10^{-2} m^2 (mg calcite C)$^{-1}$) which were *above* the theoretical value for calcite spheres. This may have been due to other calcite-containing species contributing a significant fraction of the total scattering, such as *Coccolithus pelagicus*, but this remains speculative.

The peak of the theoretical b* vs size relationship of Fig. 7 was about 1.25 μm (b*= 1.19x10^{-2} m^2(mg calcite C)$^{-1}$). This has interesting ramifications towards understanding which calcite particles cause the most scatter in the sea. Most coccoliths, including those of *E. huxleyi*, are 1-2 μm in diameter which, provided their scattering behavior is similar to that of calcite spheres, would give them high calcite-specific scattering efficiency. Moreover, one would expect lower calcite specific scattering coefficients for calcite particles <1 μm and > 3 μm, which implies that, per unit mass, coccoliths are likely more important modulators of ocean scatter than plated coccolithophore cells, or the larger calcite tests of foraminifera or pteropods (>100 μm diameter). Fig. 7

shows the size ranges of these other calcium carbonate particles found in the sea for comparison, .

Heretofore, it has been difficult to ascribe any significance to the morphology of coccoliths. We only can speculate from these results that producing turbid conditions may be somehow selectively advantageous to coccolithophores. If so, natural selection may have resulted in calcite scales with peak light scatter per unit mass. We previously hypothesized (Balch et al. 1991) that shedding highly scattering plates into the water increases the effective pathlength of light within surface waters, increasing the probability of photon capture by the coccolithophores and decreasing the probability of photon capture for deeper species of the chlorophyll maximum. The results here further support this hypothesis.

The results presented in this work also aid attempts to estimate the concentration of calcite coccoliths from space. Water-leaving radiance (Lw) and reflectance are strongly related (Gordon and Morel 1983) and reflectance is a function of $b_b/(a+b_b)$ (Gordon et al. 1988). Thus, bb/(a+bb) is a good proxy for Lw. We therefore plotted $b_b/(a+b_b)546nm$ versus $b_b/(a+b_b)436nm$ and contoured isopleths of coccolith density and chlorophyll *a* (Fig. 8). The results showed that the isopleths of coccolith concentration were almost horizontal while the chlorophyll isopleths ran more diagonally. In other words, calcite was principally driving the $b_b/(a+b_b)546nm$ through scatter effects and chlorophyll was affecting both $b_b/(a+b_b)436nm$ and $b_b/(a+b_b)546nm$ through absorption and scatter effects. Gordon (personal communication) has modeled the impact of coccoliths and chlorophyll on Lw436 and Lw546 at varying coccolith concentrations and has shown similar behavior to our results. This information will be important for the correction of remotely-sensed images of phytoplankton pigments which are contaminated by high calcite abundance. Conceptually, Lw546 can be used to derive an estimate of coccolith abundance, accurate to about 25,000 coccoliths milliliter^{-1}, while both Lw436 and Lw546 are used to calculate pigment concentration, accurate to +/- 30%. Simultaneous retrieval of

surface pigments and suspended calcite will allow a new level of understanding of the cycling of organic and inorganic carbon in the sea.

References

Aas, E. 1981. The refractive index of phytoplankton. Institute Report Series, Universitetet i Oslo. 46: 61pp.

Aas, 1984. Influence of shape and structure on light scattering by marine particles. Institute Report Series, Universitetet i Olso. 53: 112pp.

Ackleson, S., W. M. Balch, P. M. Holligan. 1994. The response of water-leaving radiance to particulate calcite and pigment concentration: a model for Gulf of Maine coccolithophore blooms. J. Geophys. Res. 99: 7483-7499.

Balch, W. M., K. A. Kilpatrick, and C. R. Trees. The 1991 Coccolithophore Bloom in the Central North Atlantic I. Optical Properties and Factors Affecting Their Distribution. Limnol. Oceanogr. submitted.

Balch, W. M. , P. M. Holligan, S. G. Ackleson, and K. J. Voss. 1991. Biological and optical properties of mesoscale coccolithophore blooms in the Gulf of Maine. Limnol. Oceanogr. 36: 629-643.

Balch, W.M., K.A. Kilpatrick, and P.M. Holligan. 1993. Coccolith formation and detachment by *Emiliania huxleyi* (Prymnesiophyceae). J. Phycol. 29: 566-575.

Berger, W. H. 1976. Biogenous deep sea sediments: production, preservation and interpretation. p. 266-326. In J. P. Riley and R. Chester [eds.], Chemical Oceanography, Vol. 5. Academic Press.

Borstad, G. A., J. F. R. Gower and E. J. Carpenter. 1992. Development of algorithms for remote sensing of marine *Trichodesmium* blooms In E. J. Carpenter [ed.] Marine Pelagic Cyanobacteria: *Trichodesmium* and other diazotrophs. Kluwer.

Bratbak, G., J. K. Egge, and M. Heldal. 1993. Viral mortality of the marine alga Emiliania huxleyi (Haptophyceae) and termination of algal blooms. Mar. Ecol. Prog. Ser., 93: 39-48.

Bricaud, A, J. R. V. Zaneveld, and J. C. Kitchen. 1992. Backscattering efficiency of coccolithophorids: use of a three-layered sphere model. SPIE- The International Society for Optical Engineering, Ocean Optics XI. 1750: 27-33.

Brown, C. and J. Yoder. 1993. Distribution pattern of coccolithophorid blooms in the Western North Atlantic. Cont. Shelf Res. 14:175-198.

Eppley, R. W., R. W. Holmes, and J. D. H. Strickland. 1967. Sinking rates of marine phytoplankton measured with a fluorometer. J. Exp. Mar. Biol. Ecol. 1: 191-208.

Fernandez, E., P. Boyd, P. M. Holligan and D. S. Harbour. 1993. Production of organic and inorganic carbon within a large scale coccolithophore bloom in the north Atlantic Ocean. Mar. Ecol. Prog. Ser. 97: 271-285.

Gordon, H. R. 1987. A bio-optical model describing the distribution of irradiance at the sea surface resulting from a point source embedded in the ocean. Applied Optics 26: 4133-4148.

Gordon, H. R. 1992. Diffuse reflectance of the ocean: influence of nonuniform phytoplankton pigment profile. Applied Optics. 31: 2116-2129.

Gordon, H. and A. Y. Morel. 1983. Remote Assessment of Ocean Color for Interpretation of Satellite Visible Imagery- A Review. Springer-Verlag.

Gordon, H. R., R. C. Smith, and J. R. V. Zaneveld. 1980. Introduction to Ocean Optics. in S. Duntley [ed.], Proceedings of the Society of Photo-Optical Instrumentation Engineers.- Ocean Optics IV. 208: 14-55.

Gordon, H. R., O. B. Brown, R. H. Evans, J. W. Brown, R. C. Smith, K. S. Baker, and D. K. Clark. 1988. A semianalytic radiance model of ocean color. Journal of Geophysical Research 93: 10909-10924.

Holligan, P. M. , M. Viollier, D. S. Harbout, P. Camus, and M. Champagne-Philippe. 1983. Satellite and ship studies of coccolithophore production along a continental shelf edge. Nature 304: 339-342.

Holligan, P. M., R. P. Harris, R. C. Newell, D. S. Harbour, R. N. Head, E. A. S. Lindley, M. I. Lucas, P. R. G. Tranter, and C. M. Weekley. 1984. Vertical distribution and partitioning of organic carbon in mixed, frontal and stratified waters of the English Channel. Mar. Ecol. Prog. Ser. 14: 111-127.

Holligan, P. M., E. Fernandez, J. Aiken, W. M. Balch, P. Boyd, P. H. Burkill, M. Finch, S. B. Groom, G. Malin, K. Muller, D. A. Purdie, C. Robinson, C. Trees, S. Turner, and P. van der Wal. 1993. A biogeochemical study of the coccolithophore, *Emiliania huxleyi*, in the north Atlantic. Global Bio. Cycles 7: 879-900.

Jerlov, N. G. 1976. Marine Optics. Elsevier Scientific Publishing Company.

Kirk, J. T. O. 1981a. Monte carlo study of the nature of the underwater light field in, and the relationships between optical properties of, turbid yellow waters. Aust. J. Mar. Freshwater Res., 32: 517-532.

Kirk, J. T. O. 1981b. Estimation of the scattering coefficient of natural waters using underwater irradiance measurements. Aust. J. Mar. Freshwater Res., 32: 533-539.

Kirk, J. T. O. 1991. Volume scattering function, average cosines, and the underwater light field. Limnol. Oceanogr. 36: 455-467.

Lewis, M. R., O. Ulloa and T. Platt. 1988. Photosynthetic action, absorption, and quantum yield spectra for a natural population of *Oscillatoria* in the North Atlantic. Limnol. Oceanogr. 33: 92-98.

Linschooten, C., J. D. L. van Bleijswijk, P. R. van Emburg, J. P. M. de Vrind, E. S. Kempers, P. Westbroek, and E. W. de Vrind-de Jong. 1991. Role of the light-dark cycle and medium composition on the production of coccoliths by Emiliania huxleyi (Haptophyceae). J. Phycol. 27: 82-86.

MacIsaac, J. J. and R. C. Dugdale. 1972. Interactions of light and inorganic nitrogen in controlling nitrogen uptake in the sea. Deep-Sea Res. 19: 209-232

Margalef, R. 1979. Life-forms of phytoplankton as survival alternatives in an unstable environment. Oceanologica Acta, 1: 493-509.

Morel, A. 1987. Chlorophyll-specific scattering coefficient of phytoplankton, a simplified theoretical approach. Deep Sea Res. 34: 1093-1105.

Morel, A. and A. Bricaud 1980. Theoretical results concerning the optics of phytoplankton, with special reference to remote sensing applications. in Oceanography From Space. J. F. R. Gower ed. Plenum Press: New York. 313-321.

Paasche, E. 1962. Coccolith formation. Nature 193: 1094-1095.

Paasche, E. 1963. The adaptation of the Carbon-14 method for the measurement of coccolith production in *Coccolithus huxleyi,* Physiologia Plantarum, 16: 186-200.

Petzold, T. J. 1972. Volume scattering functions for selected ocean waters. Scripps Inst. Oceanogr. Ref. 72-78.

Pingree, R. D., P. R. Pugh, P. M. Holligan and G. R. Forster. 1975. Summer phytoplankton blooms and red tides along tidal fronts in the approaches to the English Channel. Nature. 258: 672-677.

Reid, F. M. H. 1980. Coccolithophorids of the North Pacific Central Gyre with notes on their vertical and seasonal distribution. Micropaleontology. 26: 151-176.

Robinson, J. E., C. Robinson, D. R. Turner, P. M. Holligan, A. J. Watson, P. Boyd, E. Fernandez, and M. Finch. 1994. The impact of a coccolithophore bloom on oceanic carbon uptake in the N. E. Atlantic during summer 1991. Deep Sea Research. 41: 297-314.

Seibold, E. and W. H. Berger. 1982. The Sea Floor. Springer-Verlag.

van de Hulst, H. C. 1981. Light scattering by small particles. Dover Publications, Inc.

Winter, A. and W. G. Siesser. 1994. Coccolithophores. Cambridge University Press.

Yoder, J. A., S. G. Ackleson, R. T. Barber, P. Flament, and W. M. Balch. 1994. A line in the sea. Nature. 371: 689-692.

Table 1- List of symbols, with definitions and units . Values are given when applicable.

a	absorption coefficient (m^{-1})
ap	particulate absorption coefficient (m^{-1})
a*	Chlorophyll *a*-specific absorption (m^{-2} (mg chl^{-1}))
b	Scattering coefficient (m^{-1})
b_{chl}	scattering due to chlorophyll *a* (m^{-1})
$b^*\lambda$	calcite-specific scattering coefficient (m^2 (mg calcite C)$^{-1}$)
b_b	backscattering coefficient (m^{-1})
b_b'	calcite-specific backscattering coefficient (m^{-1})
b_{bchl}	chlorophyll *a*-specific backscattering coefficient (m^{-1})
B_C	scattering coefficient when chlorophyll *a* +phaeopigment =1 mg m^{-3}
$\bar{b}_b$	b_b/b (dimensionless)
$\bar{b}_{b\,chl}$	b_{bchl}/b_{chl} (dimensionless)
C_{CaCO3}	concentration of calcite as carbon (μg $liter^{-1}$)
c	beam attenuation coefficient (m^{-1})
$c_{calcite}$	density of calcite (2.711×10^6 g m^{-3})
C	concentration of chlorophyll plus phaeopigment (mg m^{-3})
Chl	concentration of chlorophyll (mg m^{-3})
d	particle diameter (m)
γ	ratio of calcite:chlorophyll by mass (mg calcite C/ mg chlorophyll *a*)
$G(\mu_o)$	fraction of scattering to vertical attenuation
Kd	vertical attenuation coefficient for downward irradiance (m^{-1})
Kd(zm)	vertical attenuation coefficient for downward irradiance at mid-point of euphotic zone (m^{-1})
Kd(avg)	average Kd in euphotic zone (m^{-1})
λ	wavelength (nm)
Lw	water-leaving radiance (W m^{-2} sr^{-1})

n	index of refraction (=1.58 for calcite)
n_w	index of refraction of water (=1.33)
n'	imaginary part of the refractive index
N_{cocco}	concentration of coccoliths (per milliliter^{-1})
N_{cells}	concentration of coccolithophore cells (per milliliter^{-1})
μ_o	cosine of the zenith angle of refracted solar photons just beneath the surface
m	relative refractive index (n/n_w)
Qa	absorption efficiency
Qb	scattering efficiency
Qc	attenuation efficiency
ρ	dimensionless parameter relating the size of particles to the wavelength of light and their relative refractive index $[2\pi (d/\lambda) (m-1)]$

Table 2. Statistical summary of linear optical relationships found during the BOFS cruise. Table provides the name of the independent variable (Ind. Var.) and its associated standard error of prediction, Dependent variable (Dep. Var.), number of points, least-squares fit slope, standard error (s.e.) of the slope, least-squares fit intercept (Int), standard error of the intercept, coefficient of determination, F statistic (equal to the regression mean square/residual mean square), and P, the probability that the slope is equal to 0 (* indicates $P<0.001$, Type 1 error). When regressions were performed using log transformed variables, this is shown in the first two columns. The units of the variables are N_{cell} (cells milliliter^{-1}), N_{cocco} (coccoliths milliliter^{-1}), C_{CaCO3}(mg C liter^{-1}), b_b'(m^{-1}), b (m^{-1}), b/a (dimensionless), and γ (mg calcite C/mg chlorophyll a).

Ind Var	s.e. Y	Dep Var	n	Slope	s.e.	Int	s.e	r^2	F	P
Log[N_{cell}]	0.31	Log[N_{cocco}]	172	0.91	3.72E-2	1.60	1.21E-1	0.779	600	*
[C_{CaCO3}]	51.69	[N_{cocco}]	102	1.05E-3	6.93E-5	48.27	7.41	0.690	231	*
b_b'436	9.61E-3	[N_{cocco}]	61	1.84E-7	1.82E-8	3.36E-3	1.82E-3	0.634	102	*
b_b'546	8.35E-3	[Ncocco]	61	1.35E-7	1.58E-8	3.06E-3	1.58E-3	0.556	74	*
b_b'436	5.24E-3	[C_{CaCO3}]	118	1.76E-4	6.33E-6	-4.67E-3	7.17E-4	0.866	775	*
b_b'546	4.33E-3	[CCaCO3]	118	1.36E-4	5.23E-6	-3.61E-3	5.92E-4	0.849	674	*
b436	0.552	[C_{CaCO3}]	140	9.37E-3	5.28E-4	4.42E-1	7.23E-2	0.695	315	*
b546	0.492	[C_{CaCO3}]	143	8.41E-3	4.64E-4	4.10E-1	6.28E-2	0.700	328	*
b546/a546	7.70	γ	135	6.69E-2	6.63E-3	7.62	1.03	0.433	102	*
b546/a546†	5.28	γ	83	5.94E-2	5.20E-3	13.09	0.943	0.617	130	*

† for data where b546/a546 >10 only.

Table 3-Results of dilution experiments at various locations within the mesoscale coccolithophore bloom.

Date 1991	Lat	Lon	Depth (m)	n	Slope x10^{-10}	Int x10^{-3}	r^2	Slope x10^{-10}	Int x10^{-3}	r^2
					436nm			546nm		
6/22	61.5	22.6	12	7	5.34	1.76	0.99	3.72	1.3	0.99
6/24	60.9	22.9	2	6	2.58	0.31	0.98	1.82	-3.01	0.97
6/25	60.9	23.9	2	7	4.66	0.97	0.91	3.56	0.59	0.91
6/27	61.2	15.2	2	5	1.35	0.50	0.99	1.01	1.5	0.84
6/29	61.1	15.0	2	7	1.58	-0.98	0.95	1.22	-0.80	0.97
6/29b	61.0	15.6	2	5	2.65	0.33	0.99	2.07	0.036	1.00
6/30	62.0	15.2	2	6	1.96	1.19	0.99	1.54	0.43	0.99

Table 4- Detached coccoliths per plated coccolithophore and coccolith-specific backscattering (m^{-1} per coccolith) as a function of bloom age (d). Column 2 assumes that the bloom began on June 10, 1991, the date of the last clear satellite image (Balch et al., submitted). Data are only given for stations where b_b' was measured. This table demonstrates how normalization of b_b' by the number of detached coccoliths, not including those attached to cells, can cause an increase in the coccolith-specific backscattering at early stages of bloom development.

Date June '91	Bloom Age Days	Detached coccoliths per plated coccolithophore	b_b^* $x10^{-13}$ m^2/det. coccolith
22	12	7.65	3.72
24	14	11.94	1.82
25	15	9.07	3.56
27	17	19.49	1.01
29	19	18.48	2.07
29	19	28.29	1.22
30	20	36.99	1.54

Figure Legends

Fig. 1A) Relationship between detached coccolith concentration and numbers of *E. huxleyi* coccoliths per liter. Line drawn is a least squares fit. B) Suspended calcite concentration versus coccolith concentration. Line represents a least-squares fit to the data. See text for equation.

Fig. 2- Calcite-specific backscattering at A) 436nm and B) 546nm, as a function of concentration of suspended calcite. Lines represent least-squares fits to the data (see Table 2 for equations).

Fig. 3- Results of seven dilution experiments in which seawater (containing coccolithophores and detached coccoliths) was serially diluted, and calcite-dependent backscattering was estimated at A) 436nm and B) 546nm wavelengths. The least squares fit is shown for each experiment along with the date. See Table 3 for the slope and intercept values for each experiment. Note, the ordinate scales are different. The symbols represent the following sample dates (during 1991) : +=6/22, Δ=6/24, O=6/25, ●=6/27, ▼ = 6/29, ❑ =6/29b, X=6/30.

Fig. 4- Scatter at 436 nm and 546 nm versus the concentration of calcite carbon. Lines represent least-squares fits; the fitted slopes and intercepts are given in Table 2.

Fig. 5- Calcite-specific scatter at 546nm versus coccolith concentration showing trend towards low b* values at high detached coccolith concentrations. The solid line represents the slope in Fig. 4b. The dashed line represents the theoretical maximum b* calculated using anomalous diffraction theory (van de Hulst 1981). See discussion for details of the calculation.

Fig. 6- Modeled ratio for b_b'/b_btot at 436 nm as a function of A) coccolith concentration and B) calcite concentration. Modeled ratio for b_b'/b_btot at 546nm as a function of C) coccolith concentration and D)calcite concentration. Each line assumes a chlorophyll *a* concentration, from top to bottom, of 0.01, 0.03, 0.1,0.3, 1.0, 3.0, 10.0 μg/liter. Data points from the mesoscale coccolithophore bloom are shown as Δ's.

Fig. 7- Theoretical calcite-specific scatter coefficient for calcite spheres versus sphere diameter, calculated using the anomalous diffraction theory (van de Hulst 1981). See text for details of this calculation. The size ranges of various calcium carbonate particles found in the sea are shown for reference (see Berger 1976, Seibold and Berger 1982, Winter and Siesser 1994).

Fig. 8- Values of $b_b/(a+b_b)$ at 546 nm plotted versus $b_b/(a+b_b)$ at 436 nm. Concentrations of coccoliths contoured which show high dependence of $b_b/(a+b_b)$ 546 on coccolith abundance and relative independence of $b_b/(a+b_b)$ at 436 nm to coccolith abundance. The values $b_b/(a+b_b)$ are expected to act similarly to reflectance and water-leaving irradiance at the respective wavelengths.

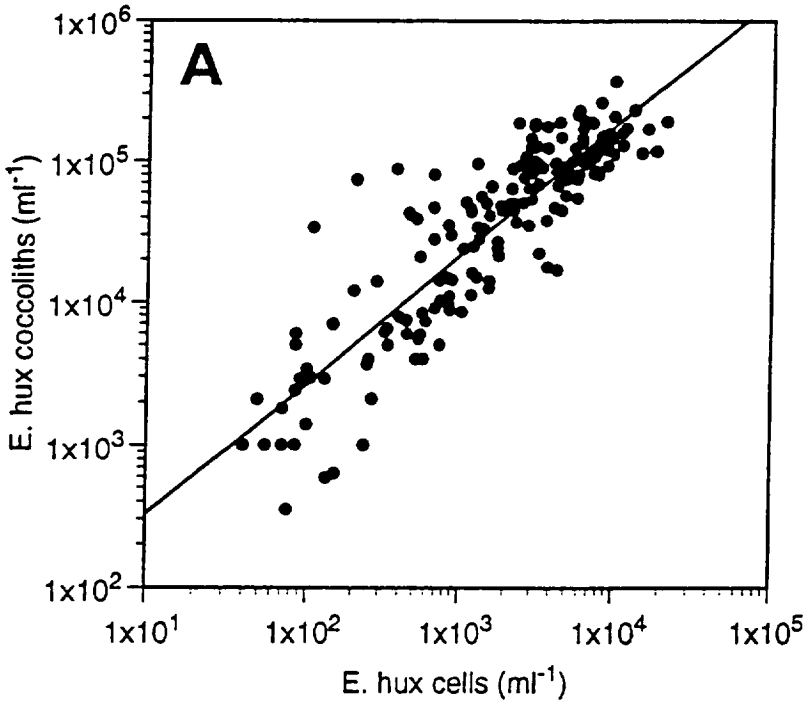
A
1x10^6
1x10^5
1x10^4
1x10^3
1x10^2
E. hux coccoliths (ml^-1)
1x10^1
1x10^2
1x10^3
1x10^4
1x10^5
E. hux cells (ml^-1)

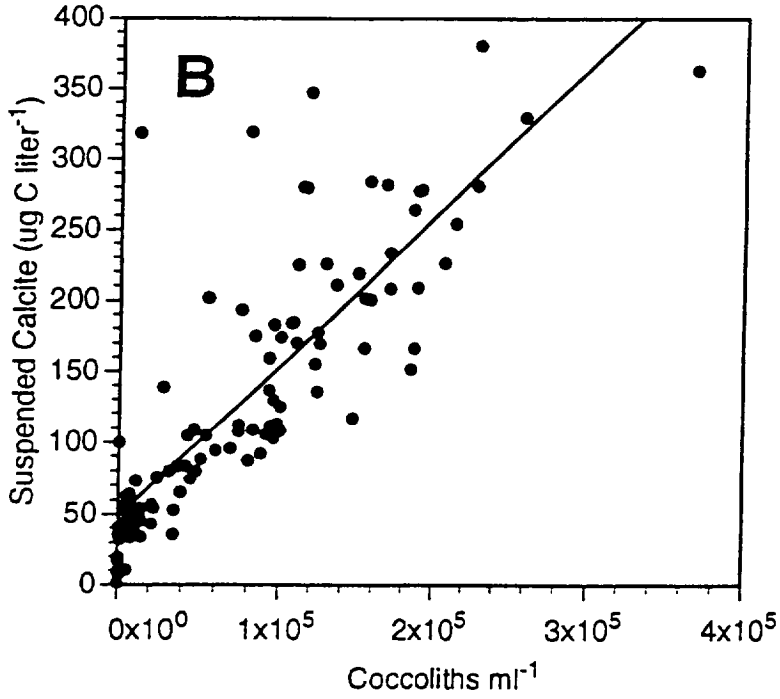
B
400
350
300
250
200
150
100
50
0
Suspended Calcite (ug C liter^-1)
0x10^0
1x10^5
2x10^5
3x10^5
4x10^5
Coccoliths ml^-1

Fig 1

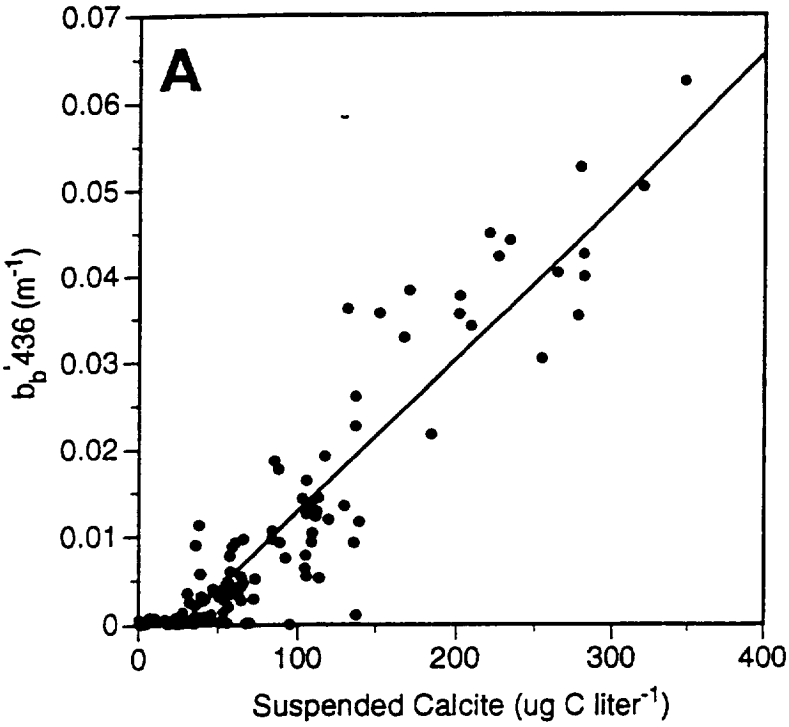
A
0.07
0.06
0.05
0.04
0.03
0.02
0.01
0
b_b'436 (m^{-1})
0
100
200
300
400
Suspended Calcite (ug C $liter^{-1}$)

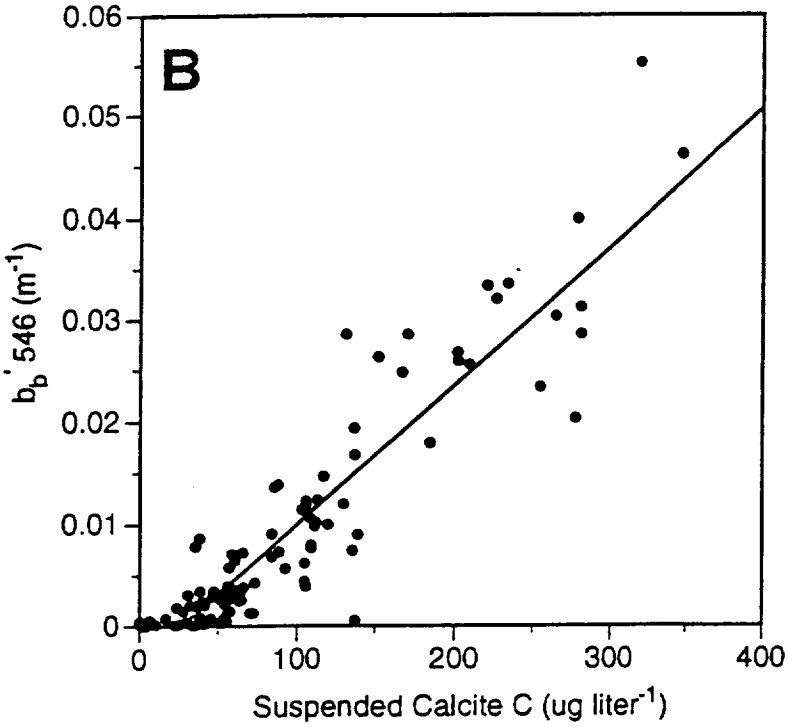
B
0.06
0.05
0.04
0.03
0.02
0.01
0
b_b'546 (m^{-1})
0
100
200
300
400
Suspended Calcite C (ug $liter^{-1}$)

Fig 2

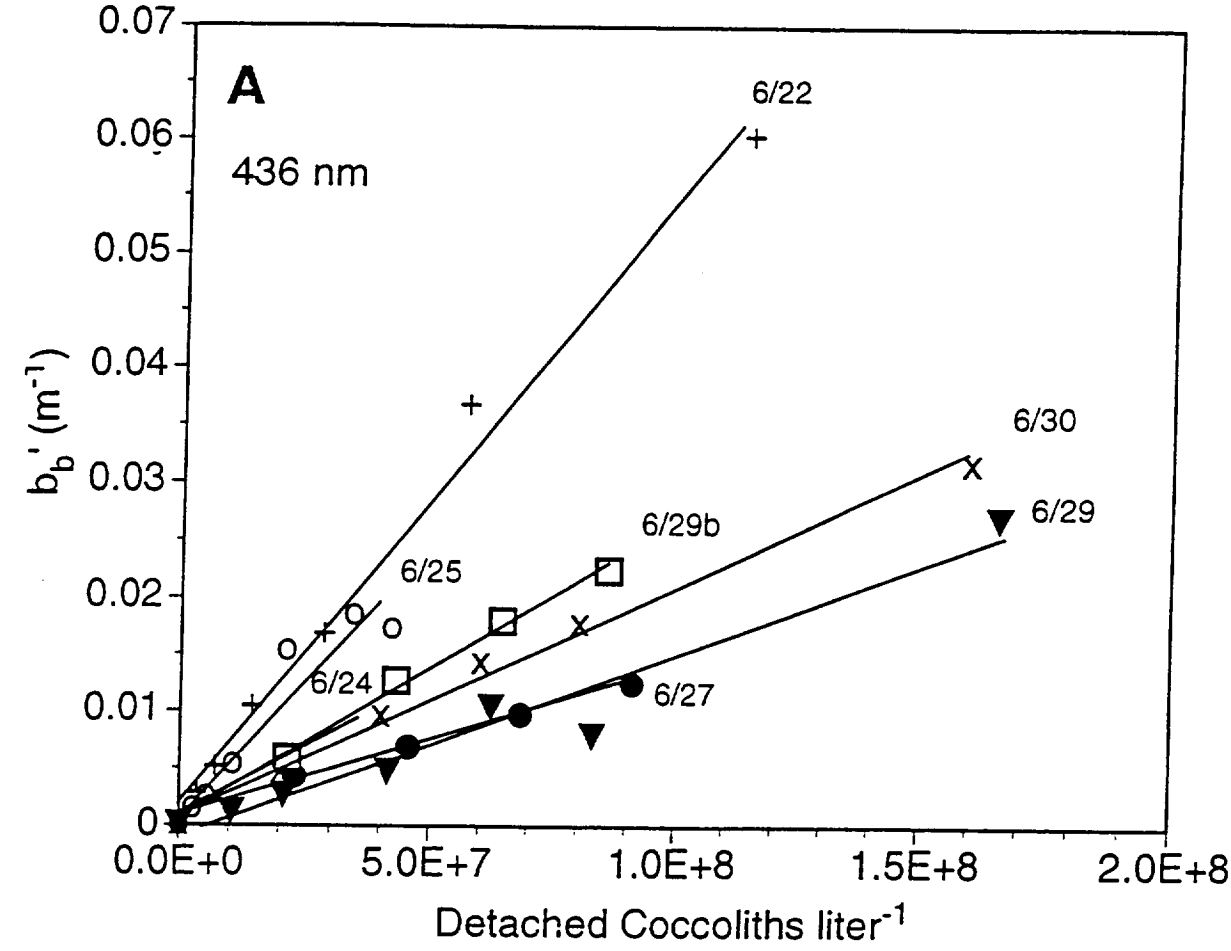
A
436 nm
6/22
6/30
6/29
6/29b
6/25
6/24
6/27
0.07
0.06
0.05
0.04
0.03
0.02
0.01
0
b_b' (m^{-1})
0.0E+0
5.0E+7
1.0E+8
1.5E+8
2.0E+8
Detached Coccoliths $liter^{-1}$

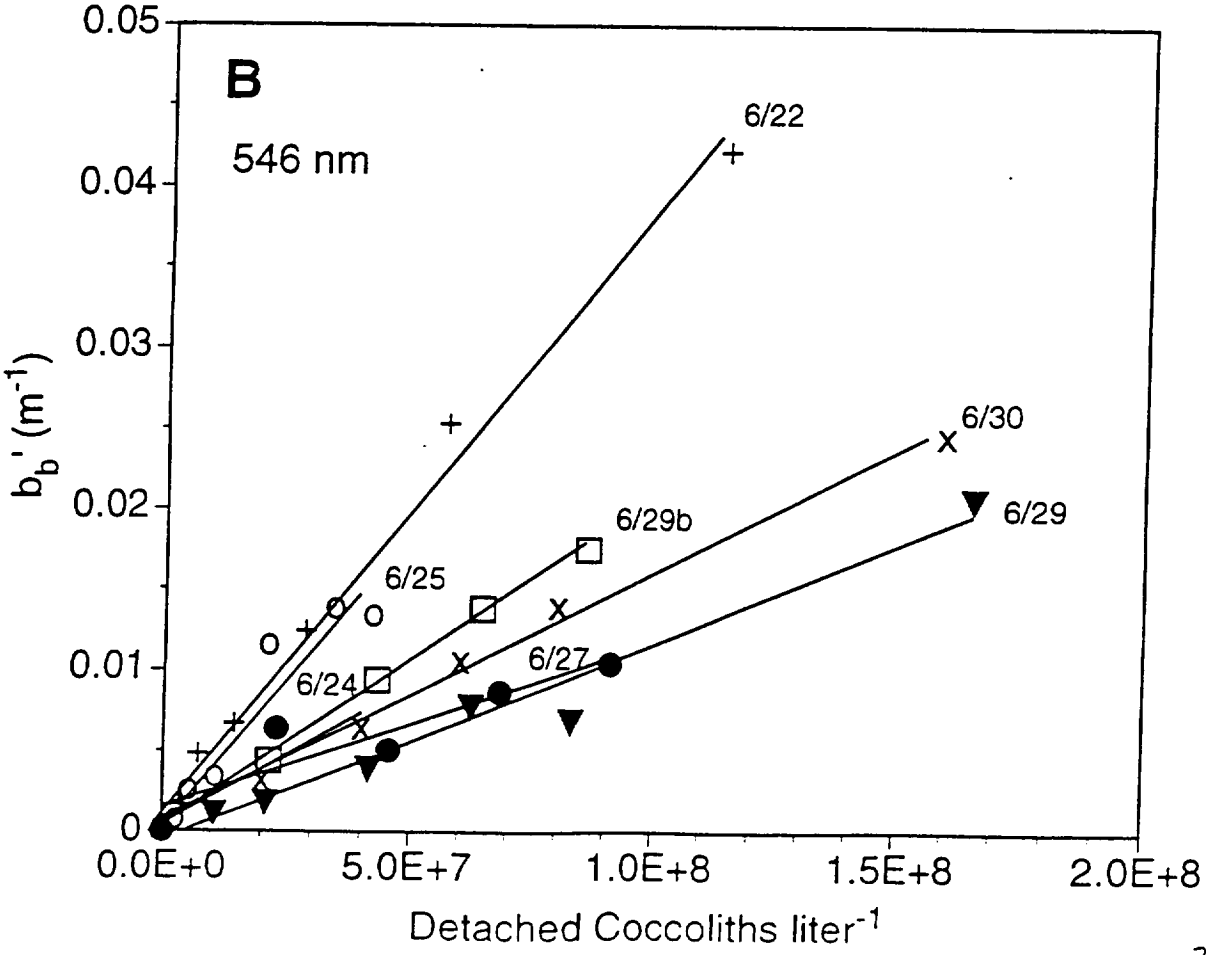
B
546 nm
6/22
6/30
6/29
6/29b
6/25
6/24
6/27
0.05
0.04
0.03
0.02
0.01
0
b_b' (m^{-1})
0.0E+0
5.0E+7
1.0E+8
1.5E+8
2.0E+8
Detached Coccoliths $liter^{-1}$

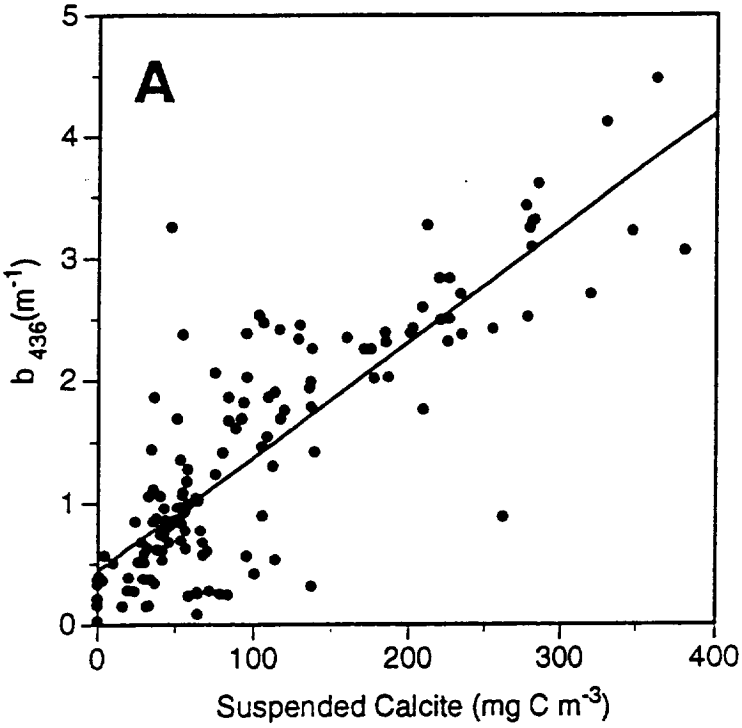
A
$b_{436}(m^{-1})$
Suspended Calcite (mg C m^{-3})
0
1
2
3
4
5
0
100
200
300
400

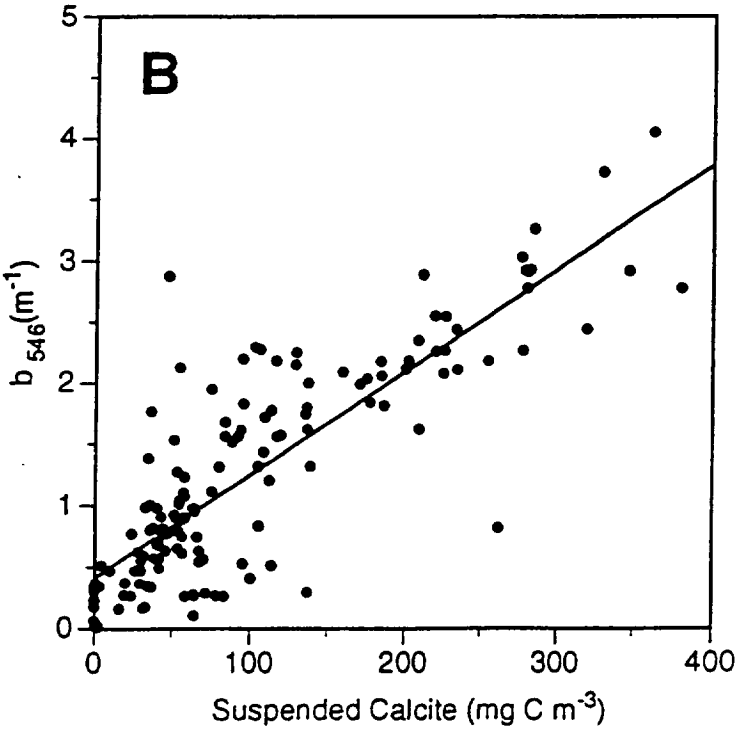
B
$b_{546}(m^{-1})$
Suspended Calcite (mg C m^{-3})
0
1
2
3
4
5
0
100
200
300
400

Fig 4

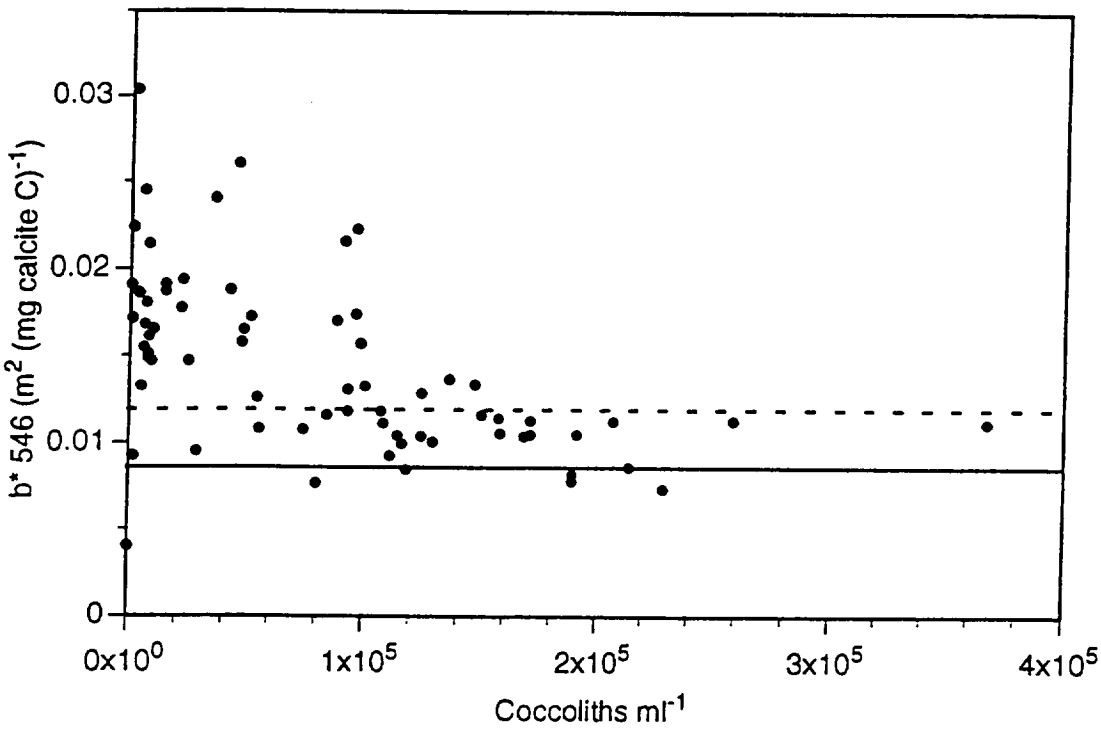
0.03
0.02
0.01
0
b* 546 (m^2 (mg calcite C)$^{-1}$)
0x10^0
1x10^5
2x10^5
3x10^5
4x10^5
Coccoliths ml^{-1}

Fig 5

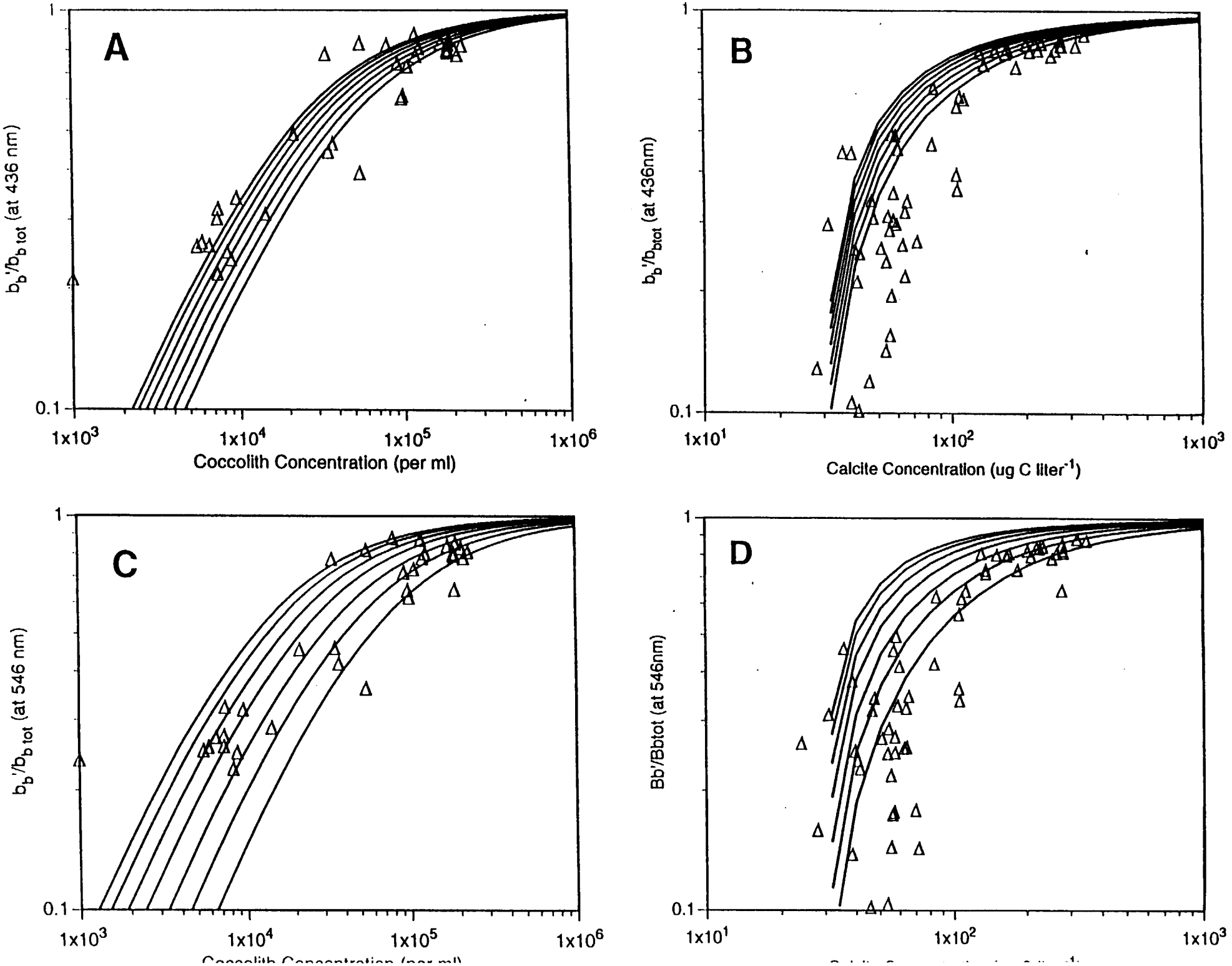
A
B
C
D
1
0.1
$b_b'/b_{b\,tot}$ (at 436 nm)
b_b'/b_{btot} (at 436nm)
$b_b'/b_{b\,tot}$ (at 546 nm)
Bb'/Bbtot (at 546nm)
1x10^3
1x10^4
1x10^5
1x10^6
1x10^1
1x10^2
1x10^3
Coccolith Concentration (per ml)
Calcite Concentration (ug C liter^-1)

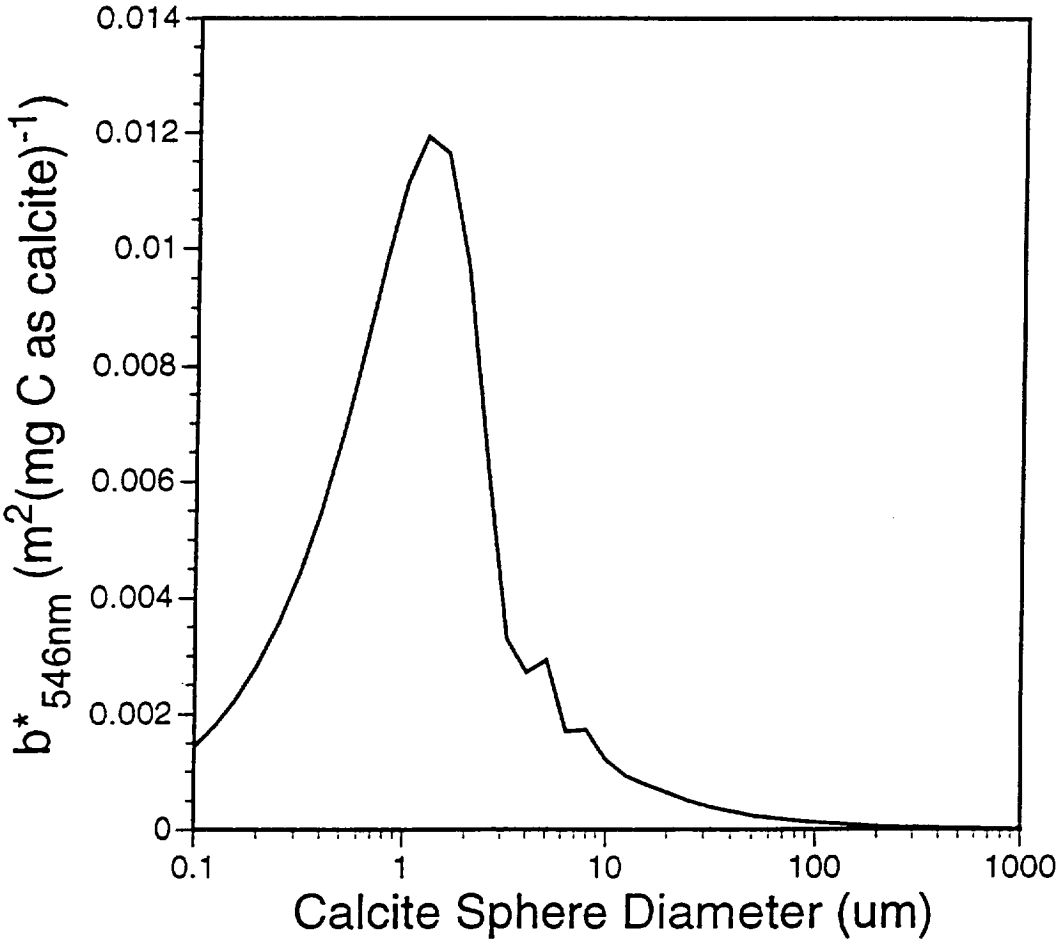

Range in diameter of E. huxleyi coccoliths

Range in diameter of foraminifera tests

Range in diameter of most coccoliths

Pteropod shells and oolites ~1-3mm in diameter

Size range of coccospheres

Range in Length of Aragonite Needles

Fig 7

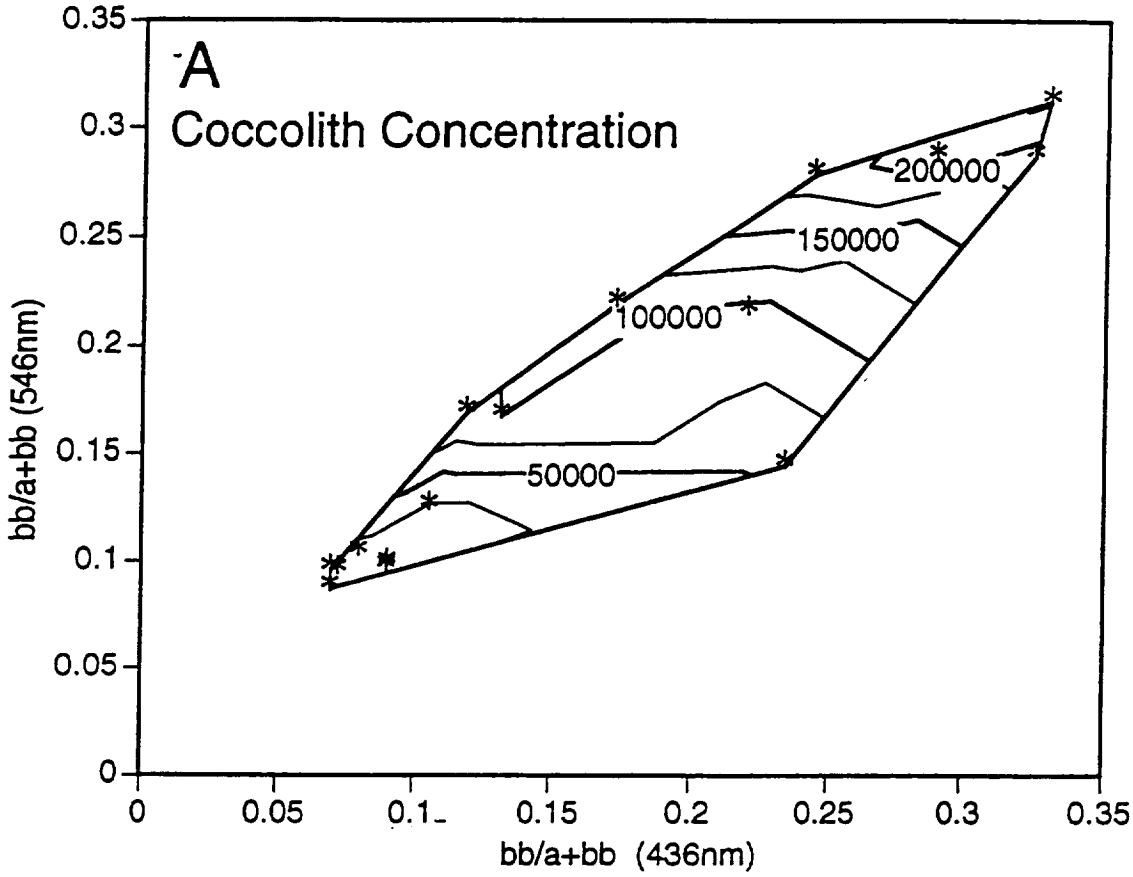
A
Coccolith Concentration
200000
150000
100000
50000
bb/a+bb (546nm)
bb/a+bb (436nm)
0.35
0.3
0.25
0.2
0.15
0.1
0.05
0
0
0.05
0.1
0.15
0.2
0.25
0.3
0.35

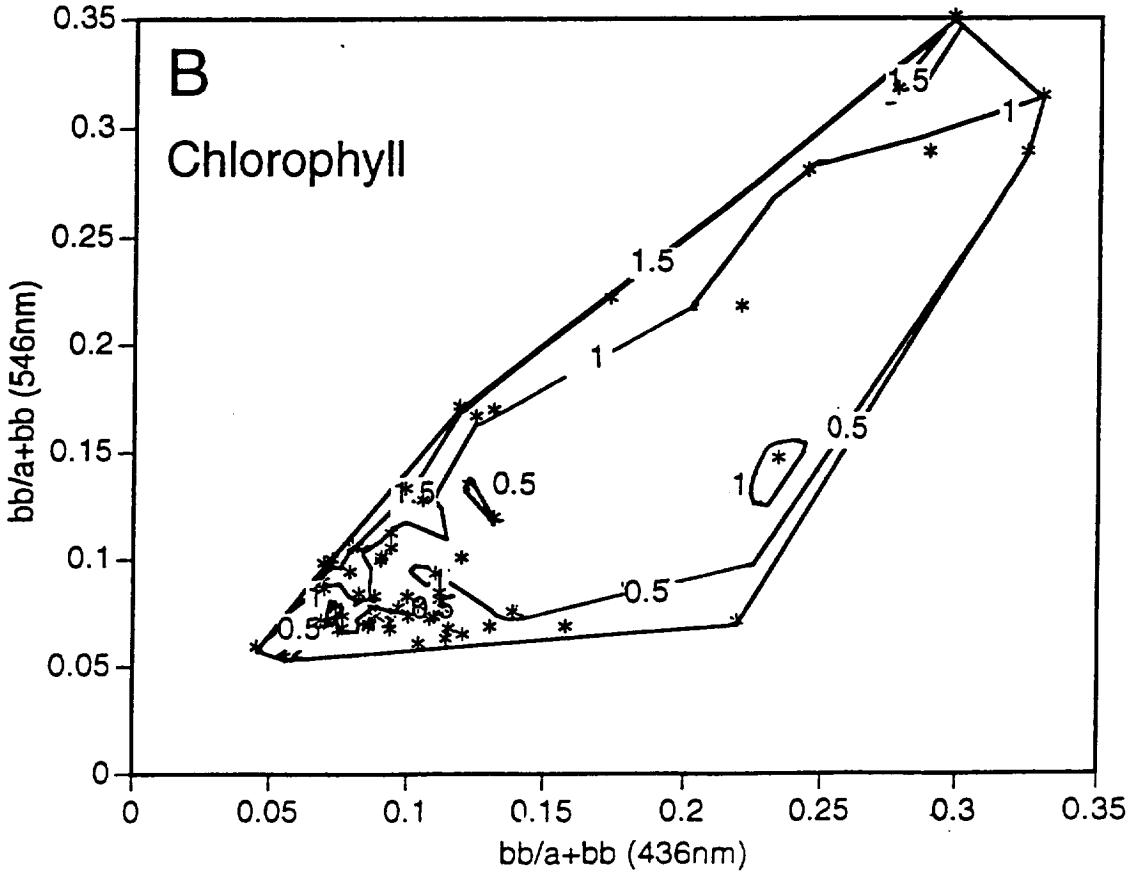
B
Chlorophyll
1.5
1
0.5
bb/a+bb (546nm)
bb/a+bb (436nm)
0.35
0.3
0.25
0.2
0.15
0.1
0.05
0
0
0.05
0.1
0.15
0.2
0.25
0.3
0.35

Fig 8

Deep Sea Research in press 6 March, 1996

Appendix 6

Calcification Rates in the Equatorial Pacific along 140°W

William M. Balch
Bigelow Laboratory for Ocean Sciences
P.O. Box 475
McKown Point
W. Boothbay Harbor, ME 04575

Katherine Kilpatrick
Division of Meteorology and Physical Oceanography
Rosenstiel School for Marine and Atmospheric Sciences
University of Miami
4600 Rickenbacker Causeway
Miami, FL 33149-1098

Running Head: Calcification in the Equatorial Pacific

Abstract

The calcite standing stock, calcification rate, concentrations of detached coccoliths and plated coccolithophore cells were determined in the equatorial Pacific along 140°W, between 12°N and 12°S latitude, during August and September 1992. Continuous surface optical and fluorescence measurements also were taken along this transect. Integrated calcification ranged between 3 and 12% of the total carbon fixed into particulate matter. Calcification exceeded 50% of the total fixed carbon (per unit volume) at specific depths from the northern-most oligotrophic stations. A pronounced subsurface peak in suspended calcite was noted near the equator. Calcification was considerably more patchy than photosynthesis. Normalizing the calcification rates to the surface area of calcite-producing species provided an estimate of the extracellular calcite flux rates. These results showed that the populations from the equator to 3°N at 60m depth, and near the surface from the equator to 9°S were the most active calcite producers. Underway estimates of light scattering showed the importance of upwelling for bringing cold, clear, relatively particle-free water to the surface, followed by growth and calcite production as the water warmed. When temperatures reached their upper range (about 28.8°C), light scattering decreased again, presumably as growth slowed and particles sank. Integrated calcification estimates averaged over the equatorial region were compared to sediment trap data; the results suggest significant disappearance of calcite particles in the top 1000m, above the lysocline. One hypothesis to explain this is that dissolution occurred in microzones where decomposition of reduced organic matter lowered the pH sufficiently to dissolve calcite.

Introduction

Calcification in open ocean systems is poorly understood from ecological and biogeographical perspectives. Most calcification studies have been performed on calcifying macroalgae and corals due to their easy access from shore (e.g. Wefer, 1980; Kawaguti and Sakumoto, 1948). Studies of foraminiferal calcification, an important source of calcite for some course-grained sediments, are more difficult due to problems in laboratory culturing, lack of knowledge about life cycles, as well as finding sufficient material at sea (Be et al., 1977; ter Kuille and Erez, 1987). Coccolithophore calcification, a major source of calcite sediments in the world ocean (Milliman, 1993), has been well studied in the laboratory (e.g. Paasche, 1963) but direct, field estimates of calcification are few.

It has long been recognized that coccoliths contribute a major portion of the calcite content of pelagic sediments (Lohmann, 1908; Bramlette, 1958) and the distribution of many coccolithophores in surface waters matches their sediment distribution (McIntyre and

Be, 1967) except when preservation is poor. Atlantic waters are characterized by low dissolved CO_2, a deep calcium compensation depth (CCD) and good calcium carbonate preservation. However, the Indian and Pacific deep waters are generally characterized by relatively high dissolved CO_2 concentrations, high alkalinities, a shallow CCD, and low $CaCO_3$ preservation (Berger, 1971). In regions of high carbonate supply, the CCD can be depressed (the equatorial Pacific is such an example). Arrhenius (1952) first described significant variability in the calcite content of sediments, either due to changes in productivity or changes in dissolution (see also Cwienk and Leinen, 1985 and Sarnthein et al., 1988 for discussion of burial of biogenic phases). Broecker and Peng (1982) globally set the ratio of deposited calcite to surface-produced calcite as about 1:7, although this value will vary regionally as a function of the lysocline depth relative to the bottom depth. It is generally thought that calcite represents a progressively larger fraction of the total carbon flux as particles sink into deep water (see figure 1 from Westbroek, 1993).

Broecker and Peng (1982) estimate that, on a global basis, 1 mole of calcium carbonate is formed for about every 4.5 moles of organic carbon (i.e. 18% C is as calcium carbonate). In practice, any carbon fixed into calcium carbonate during bottle incubations is usually dissolved by acid fuming during analysis (Parsons et al., 1984); thus, information about this large carbon fraction is not included in production estimates. Moreover, little is known about coccolithophore patchiness scales in the horizontal and vertical dimensions. While large-scale variability (biogeography) is of more applicability to interpreting the sedimentary record, smaller scales of variability are important for understanding the physiological ecology of coccolithophores. Taxonomic studies have revealed vertical scales of variability in coccolithophore standing stock with resolution of about 20m (e.g. Okada and Honjo, 1973; Okada and McIntyre, 1977; Reid, 1980) . Few data are available concerning horizontal variability of coccolithophores in surface waters, at scales smaller than 100 km. Basin scale variability can be inferred from sedimentary distributions in the Atlantic (MacIntyre and Be, 1967) and the same probably applies to other ocean basins. Based on cell counts, Okada and Honjo (1973) showed in the Pacific Basin that coccolithophore biomass is highest at high latitudes, decreasing in temperate and subtropical regions, and then increasing again in the equatorial zone. Mesoscale blooms of coccolithophores also have been observed from space, allowing estimates of their scales of variability with resolution down to length scales of kilometers (Holligan et al., 1983; Balch et al., 1991; Aiken and Bellan, 1990; Holligan et al., 1993; Brown and Yoder, 1994a&b). Note, these bloom studies provided mostly information about the concentration of suspended coccoliths of *E. huxleyi*, not its biomass. This is because calcite coccoliths are highly visible from space due to their unique light scattering properties. Rates of

production of these suspended calcite particles also are not well understood in nature (but see examples in Balch et al., 1992 and Fernandez et al., 1993).

Geological studies of the equatorial Pacific have shown it to be a region of significant calcite sedimentation (Van Andel, 1975). Calcite represents >50% of the sediments by weight west along the equator to 158°W, with a zonal distribution from about 7°N to more than 15°S. The region of >70% calcite sediments is more restricted longitudinally, extending from 125°W to 157°W, then diminishing eastward along the East Pacific Rise. The latitudinal extent of the >70% calcite sediments is greatest at 135°W to 140°W (5°N to 15°S). Clearly, in the Equatorial Pacific, the majority of the sinking flux of biogenic carbon is being buried as calcium carbonate, not organic carbon (Van Andel, 1975).

Geochemical estimates of calcification

Most of the open ocean estimates of calcification in surface waters are indirect estimates by geochemists. They are based on measurements of inorganic carbon and nitrate over vertical length scales of hundreds of meters, and time scales of months (e.g. Broecker and Peng, 1982). Such data, combined with estimates of upwelling velocities allow estimation of the rates of photosynthesis and calcification. Alkalinity represents the extra positive charge that is balanced with HCO_3^- and $CO_3^=$ to achieve electrical neutrality. The production of organic matter in photosynthesis is associated with a *decrease* in total carbon dioxide (ΣCO_2), and an *increase* in alkalinity (due to the uptake of NO_3^-). Calcification on the other hand, *reduces* the ΣCO_2, and removal of Ca^{++} also removes 2 equivalents of positive charge. The net result is that during calcification, the decrease in alkalinity is twice the decrease in ΣCO_2. This appears in the equation for calculating calcification (Broecker and Peng, 1982):

$$\Delta C_{CaCO3} = (\Delta Alk + \Delta NO_3)/2 \qquad (1)$$

where ΔC_{CaCO3} represents the change in calcite carbon from the deeper water to the euphotic zone (μmol kg^{-1}), ΔAlk (mEq kg^{-1}) represents the vertical decrease in alkalinity from the deep water to the euphotic zone and ΔNO_3 (mM kg^{-1}) represents the vertical decrease in nitrate from the deep water to the shallow water. This is to be contrasted with the geochemical production of organic carbon which is calculated using equation 2:

$$\Delta C_{org} = \Delta \Sigma CO_2 - \Delta C_{CaCO3} \qquad (2)$$

where ΔC_{org} represents the production of organic matter in surface waters, and $\Delta \Sigma CO_2$ represents the decrease in total inorganic carbon going from deeper water to shallow water as primary production occurs. Note that primary production and calcification have opposing effects on the dissolved inorganic carbon supply; photosynthesis consumes CO_2, calcification consumes two bicarbonate molecules, and produces one molecule of calcium carbonate and one molecule of CO_2.

As an example of calcification rates predicted by the above equation 1, we have applied the GEOSECS data from station 334 in the Equatorial Pacific (0° 3'N x 124° 34'W; 27 May 1974). An upwelling rate of about 1 m d^{-1} has been reported in this region but it is confined to the top Ekman layer (about 50-100m in this region) with significant deep meridional geostrophic flow from the north and south (Wyrtki, 1981). Therefore, we base euphotic estimates of calcification on geochemical changes in this vertical depth range. The value of ΔC_{CaCO3} at the equator, based on equation 1, is 17.08 μmol l^{-1} after normalizing for salinity differences and correcting for density. Multiplying these values by the average regional upwelling velocity gives integral calcification values of 17.08 mmol C m^{-2} d^{-1} or 6.24 mol m^{-2} y^{-1}. These data, applied to equations 1 and 2, predict that over 10% of the carbon fixed into particles in this highly productive region would be as calcium carbonate. There are no direct measurements of calcification to verify this, however.

Calcite production does not require nitrogen, hence, calcification technically should not be included in new production (sensu strictu Eppley and Peterson, 1979). Calcite does represent a large fraction of the export carbon, however. The new production "f" ratio (fraction of total production associated with nitrate uptake) from the tropical Pacific is about 0.14 (Pena et al., 1994) , which is about the same as estimates of carbon fixed into calcite in this specific region. The importance of the calcite production over new production becomes even more obvious, when one considers that most of the new production is never buried in sediments, but is remineralized enroute to the sea floor. If the global average primary production is between 20-30 gt carbon y^{-1}, and organic production is 4.5 times the calcite production (Broecker and Peng, 1982), then global calcite production will range from 4.4 to 6.7 gt carbon y^{-1}. This spans the global calcite production estimate of Milliman (1993; 5.2 gt carbon y^{-1}). In the Equatorial Pacific box described by Wyrtki (1981; 1.1 x 10^{13} m^2), the geochemical estimate of total calcification would be about 0.8 gt carbon y^{-1}, which represents 12-19% of global calcite production, and is of the same order of magnitude as new production in the equatorial Pacific (Chavez and Barber, 1987).

The rationale for this Equatorial Pacific study was based on the importance of sinking calcite to 1)export carbon fluxes, and 2) the total global calcification burial. Clearly, little is known about the factors that affect calcification by coccolithophores in

space and time. Better knowledge of the rate of crystalization of this mineral, coupled with mass balance, indirectly provides limits for the euphotic loss terms, sinking and dissolution. The following study represents the first direct measurements of surface calcification rates in the equatorial Pacific, a region where calcification is an important fraction of the flux of carbon from surface waters to deep sediments.

Methods

Cruise Details

All measurements were made during the 1992 Survey II cruise aboard the R/V Thompson (5 August-18 September, 1992) from Hawaii to Tahiti. Fifteen stations along 140° W were occupied, stopping at 12° N, 9° N, 7° N, 5° N, 3° N, 2° N, 1° N, 0° , 1° S, 2° S, 3° S, 5° S, 7° S, 9° S, 12° S. A description follows of the measurements made at each station (as vertical profiles). These measurements were also made on surface underway samples every 1-2 hours of the transit.

Calcification Measurements

Water for vertical profiles was sampled using a trace-metal clean rosette, equipped with eight 30 liter GO-FLO sampling bottles. Samples for calcification were generally taken between midnight and 0300 local time to avoid light shock to the phytoplankton. Water from each depth was poured into two 250 ml polycarbonate bottles after 5 bottle rinses. Gloves were used during all sampling and handling. Calcification was measured using the technique of Paasche (1962, 1963). 40μCi of ^{14}C bicarbonate (radiochemical purity>99.9999% as determined in our laboratory) was added to each sample afterwhich the bottle was incubated in situ or in incubators on the ship's deck. Subsamples of 100μl were taken from two bottles of each series for total 14C counts, and mixed with 100μl of phenethyl amine, mixed, and 7ml Ecolume scintillation cocktail was added. For in situ incubations, two bottles were placed in each of eight nylon monofilament bags, attached to a floating spar buoy. They were incubated at 1, 12, 21, 34, 45, 60, 79, and 118m (approximately the 100, 50, 30, 14, 7, 3, 1, and 0.1% light depths) for 24 hours. Simulated in situ incubations were done in a series of Plexiglas tanks on the fantail of the ship with temperature matched to the in situ temperature within 1°C. The tanks had blue Plexiglas walls and tops to mimic the spectral quality of the water. Light quantity was controlled by neutral density screen bags around the bottles. After 24h, all samples were retrieved. Four 50 ml samples from each 250 ml bottle were filtered through 0.4 μm Nuclepore filters, rinsed 5 times with filtered sea water with low vacuum, then the filter tower was removed and the filter given a careful "rim rinse" to wash off any radiolabeled

bicarbonate activity, being careful that all the rim rinse was drawn through the filter. All filter manipulations were done using acid-cleaned/seawater-rinsed forceps to avoid contamination. For every four replicate filters, two were added directly to 7mL of Ecolume scintillation cocktail. The other two were placed in a desiccator containing 25ml of concentrated HCl for 4 minutes, then removed and placed in a scintillation vial with 7 ml of scintillation cocktail. Previous studies have shown that this fuming process was sufficient to remove any calcite on the filter (Balch et al., 1992). Radioactivity was measured using the external channels ratio method. All samples were counted for 5 minutes. The equations of Parsons et al. (1984) were used to calculate the uptake rate of carbon into organic matter/calcite, isotope discrimination was assumed to be 5%.

Suspended Calcite Analyses

Suspended calcite was measured on pre-combusted GFF filters using the technique described by Holligan et al (1993). One liter samples were filtered through pre-combusted Whatman GFF 25mm filters, the filters were rinsed several washes with filtered seawater. Then one rinse of 20mM borate buffer, pH 8.0 to remove any calcium ions in sea water before freezing the filters at -20^{o}C. Samples were extracted by adding ml -50% trace-metal clean hydrochloric acid to tubes containing the filters. They were incubated overnight at 40 ^{o} C in a water bath. 8 ml of 1% lanthanum chloride was added to each tube, followed by centrifugation to remove any filter fragments. The supernatant was then injected into a Perkin Elmer model 2380 flame photometric atomic absorption spectrometer, measuring absorption at 422.7 nm with a 10 cm flame. Calibration curves were prepared using commercial calcium standard from Fisher Scientific. Blank filters were prepared towards the end of the cruise by mounting identical pre-combusted filters in the filter tower apparatus, applying vacuum, and adding GFF-filtered seawater to wet the filter, and identical rinsing and preparation techniques as described above.

Chlorophyll

Chlorophyll concentration was measured as described by Yentsch and Menzel (1963) subsequently modified by Holm-Hansen (1965). For all samples, 250 ml was filtered through GFF filters, the filters were extracted in 90% acetone in scintillation vials overnight at 4^{o}C, the acetone was decanted into a cuvette and chlorophyll fluorescence measured with a Turner Designs fluorometer.

Continuous along-track measurements

A flow-through system was attached to the ship's clean stainless steel seawater supply. The underway system consisted of a Turner 111 fluorometer with flow-through door, an Interoceans model 541 temperature/conductivity probe. Water passed through a continuous 90° light scattering detector described elsewhere by Kilpatrick et al (1994). Basically, 90° light scattering was monitored over 3 minute cycles as a peristaltic pump moved water through a flow-through cuvette at a rate of 11 ml min^{-1}. During half the cycle, a second pump injected 1% glacial acetic acid to lower the pH to 5 and dissolve any suspended calcium carbonate. When the signal stabilized, the acidified reading was subtracted from the unacidified, raw reading. The difference in readings represented acid-labile scatter which was calibrated to suspended calcite in the laboratory. At a steaming speed of 11 knots (required for other towed instruments) , the underway system sampled about once every kilometer.

Cell Counts

Samples for cell counts were taken at every station and preserved with 3 ml buffered Lugols solution in 60ml brown glass bottles. Samples were stored up to 1.5 years before enumeration; bottles were taken at random for counting and the bottle identification numbers were not known to the microscopist until after the count. Ten ml of each sample was poured into a settling cylinder which rested over a Palmer Maloney counting chamber (the cylinder was lightly greased with silicon grease to seal it to the counting slide. Particles were allowed to settle onto the counting slide for 24 hours. Then the upper cylinder was removed by slowly sliding if across the Palmer Maloney slide and draining it into an underlying beaker. The settled sample was examined with an Olympus BH2 microscope equipped with polarization optics which allowed the enumeration of calcite birefringence. Detached coccoliths and 3 sizes of plated coccolithophores were counted (<10um, 10-20um, 20-30um diameter). The total numbers of coccoliths ml^{-1} were calculated based on the counts of single, detached coccoliths as well as estimates of coccoliths on cells and in aggregates. Cells and aggregates were binned according to the size categories given above for cells. Approximate numbers of coccoliths were estimated for cells or aggregates based on microscopic examination: <10μm =16 coccoliths, 10-20μm = 100 coccoliths, and 20-30μm =200 coccoliths. Each particle type was enumerated in the chamber up to a maximum count of 200 particles, otherwise the entire chamber was counted. Naked coccolithophores were difficult to identify using this technique, and were not included in the counts. In order to relate the physiological measurements to the microscopic counts, an extracellular calcite flux was calculated by dividing the calcification

rate by the plated coccolithophore cell surface area assuming spheres of the diameter given above (units of m^2 cell surface area $(m^3$ seawater$)^{-1}$).

Results

Distributions of detached coccoliths and plated coccolithophores covaried with highest concentrations observed between the equator and 3°S (highest at 1°S) and at 7°N and 7°S (Fig. 1). In general, highest concentrations within the euphotic zone were shallower than 50m. The concentration of both coccoliths and cells varied over 3 orders of magnitude in the study area ; the least squares relationship between detached coccoliths and plated cells was: Log coccoliths = 0.93 * Log Plated Coccolithophores + 0.95 (r^2=0.61; Fig. 2). Based on this relationship, the ratio of detached coccoliths to plated coccolithophores varied between 5 and 8. This did not include clumps of detached coccoliths which sometimes were abundant, but impossible to count accurately. Unidentified 0.5um birefringent particles were extremely abundant (up to 75,000mL^{-1}) at about 40-50 meters between 5°S and 4°N as well as some deeper at 100m from 10°S to 4°N (Fig. 3). Attempts to examine them using scanning electron microscopy were fruitless as they proved to be extremely fragile.

Photosynthesis rates showed a broad, asymmetrical maximum centered at 2°N. Meridional gradients in primary production were considerably stronger north of the equator, with the steepest gradient observed between 2°N and 3°N, at the "Great Front" (Fig. 4a). This was an open-ocean front, associated with the convergence between the westward-flowing south equatorial current, and the eastward-flowing north equatorial counter current (Yoder et al., 1994). Calcification did not show the same pattern as primary productivity, and was considerably more patchy. Highest values were seen at the equator. The lowest calcification rates were observed north of about 7°N (Fig. 4b). Suspended calcite was highest near the equator, just below the depth of peak calcification (Fig. 4c). Calcite data from 7°-12°N were lost.

It should be noted that the estimates of suspended calcite concentrations using water from Niskin bottles tended to be higher than water sampled from in situ pumps. Suspended calcite concentrations measured by large-volume pumps were about a factor of 2-5 times less than values from discrete bottles (J. Bishop, personal communication). This was also true of the particulate organic carbon samples (Ducklow, personal communication). We cross-checked the precision of our atomic absorption technique by running sub-samples from the large volume filtration system of J. Bishop, and our results were within 10%. Thus, the discrepancy between large-volume samplers and Niskin bottles rests in how the samples were taken, rinsed or stored. Given that the absolute

accuracy of either method is poorly defined, it is impossible to resolve this difference and we report our results from the Niskin bottles.

A plot of calcification versus photosynthesis for in situ and simulated in situ incubations showed that calcification rates were equal or greater than photosynthesis rates in the most oligotrophic water. In higher productivity water, calcification was generally about 10% of photosynthesis, with maximum calcification rates of about 0.25 μmol C m^{-3} d^{-1} (Fig. 5).

Calcification, photosynthesis, and suspended calcite concentrations were integrated to the 0.1% light depth using trapezoidal integration. General patterns of integrated calcification and photosynthesis showed that calcification was usually about 5-10% of total carbon production, which was highly latitudinally dependent. Integrated calcification and photosynthesis were highest at 2°N (Fig. 6a) with a gradual decrease south of the equator, and steeper decline north of the equator. Integrated calcite standing stocks were greatest at 1°S (Fig. 6b). Turnover, estimated by dividing the calcite standing stock by its rate of production, was almost always less than about 10d except for the data calculated from the in situ incubations at 1°S (Fig. 6c). Integrated calcification was between 3% and 12% of the integrated photosynthesis (Fig. 7).

The abundance of detached coccoliths was compared with the surface area of the plated coccolithophore cells that presumably generated them (Fig. 8). The expected relationship for coccoliths of different radius was generated assuming that all detached coccoliths originated from the plated coccolithophores, and that those coccoliths originally completely covered the cells in a single layer. Calcification rates were also normalized to the surface area of plated cells (calculated from the cell counts). The results showed that the greatest rates (> 2 mol C m^{-2} cell surface area d^{-1}) were found between the equator and 3°N at about 60m, and also at 9°S at the surface (Fig. 9). Most of the study region had rates <0.25mol C m^{-2} cell surface area d^{-1}. Calcification rates normalized to the numbers of plated cells showed no trends, probably due to the large range of cell sizes seen in the samples.

Underway transect results

The underway data (figure 10) showed that salinities increased along the transect from 12°N to 12°S, with a pronounced low of 34.75 associated with the "great front" and a broad region of 35.25-35.5 salinity from the equator to 5°S associated with the south equatorial current. Lowest salinities of about 34.25 were seen from 9-12°N. Underway temperature values were highest at 7-9°N, and coolest south of the convergence front at 2°N (lowest temperature of the transect was ~24.5°C) . A temperature drop of about 1°C

was observed at 9°N. Surface temperatures warmed from 2°N to 8-9°S, then cooled about one degree at 12°S. Chlorophyll fluorescence a) increased from 6°N to 5°N, b) had a sharp maximum just north of the 2°N convergence front, and c) had lesser peaks at 1.5°N and the equator. From the equator to 6°S, chlorophyll values ranged from 0.1-0.2 mg m^{-3} and the beginning chlorophyll value from one transect rarely matched that from the end of the previous transect; this indicated that conditions were changing while the ship was on station for 2-3d. Small, well-defined chlorophyll peaks of 0.15 mg/m^3 were observed at 6°S and 9°S. Trends in total 90° volume scattering generally covaried with temperature, with the exception of two regions at 2°N and 8°N. For interpretation of the total 90° scattering signal, it is important to caution that an impeller pump supplied the water to the flow-through system and extremely large cells such as the diatom, *Rhizosolenia castracanei,* from the "great front" (Yoder et al., 1994) may have not survived intact. The difference between total and acidified 90° volume scattering (calcite-dependent scattering) was highly variable from 12°N to 5°N. At 2°N and 2°S, large peaks of acid-labile light scatter were observed. In the southern part of the transect (6°S-12°S), the acid-labile scatter values were slightly negative (~-0.01V).

The same underway data were plotted on temperature/salinity coordinates in figure 11 to relate the observations to specific water masses. The surface waters between 12°N and 12°S had sigma-T values ranging from 21.5 to 23.5 respectively (Fig. 11a). The same data, with isopleths of latitude showed the low density water in the north part of the transect, and coldest water observed just north of the equator (~1°N; Fig. 11b). The chlorophyll data, superimposed on the temperature/salinity space showed the presence of the intense *Rhizosolenia castrecanii* bloom at 2°N (Yoder et al., 1994) as well as a minor peak in the cool, $\sigma_{t23.5}$ water upwelled at the equator. Acid labile 90° volume scattering data, plotted in temperature/salinity space again were extremely patchy, but several peaks were observed well within the upwelled equatorial water at 1°N, and some patches at about 12°S (Fig. 11d). Total 90° volume scattering showed an unexpected pattern, almost inverse to the chlorophyll pattern, with values lowest at the great front and equator, and higher in more oligotrophic parts of the transect (Fig. 11e).

A different way to examine the total 90° light scattering was to plot it against temperature (Fig. 12). The results showed lowest 90° scattering in the cold upwelled water, reaching a maximum at about 28.8°C, then abruptly declining up to 29°C. A line, drawn by eye, illustrates this trend.

The above results have been submitted to the U.S.-JGOFS data system.

Discussion

Horizontal and Vertical Distribution of Coccoliths and Coccolithophores

Two aspects of the spatial distribution of coccoliths are worthy of note. The absolute abundance of detached coccoliths (plus plated coccolithophores) peaked in the waters south of the equator, which was recently upwelled and of moderately low chlorophyll (Fig. 11). This was in agreement with the observations of Okada and Honjo (1973). Furthermore, the locations of the highest coccolith abundance and calcite concentration generally, but not always, corresponded to the locations of peak calcification (compare Figs. 1a, 1b, 4b and 4c). Patches of water with high calcite-dependent, 90° volume scattering were observed in regions of moderate chlorophyll between 1°N and 2°N, south of the "great front" (Fig. 10). While coccolithophores are usually thought to tolerate low nutrient, low iron water (Kramer and Ryther ,1960), our data showed patches clearly associated with recently upwelled water (Fig. 11d). This might be explained using the mandala derived by Margalef (1978) in which he placed coccolithophorids between the dinoflagellates (selected for low turbulence, low nutrient environments) and the diatoms (selected for high turbulence, high nutrient environments). The flagellated life stage of coccolithophores appears to be a relatively minor part of its overall life cycle, and most of the time, cells are covered by calcite plates giving them high sinking rates. Thus, Margalef rationalized that coccolithophores require moderate turbulence to remain aloft in the water column. Recently upwelled water, in the process of stratifying, might provide just such conditions.

The optical data indicated fairly uniform but low concentrations of coccoliths in the north end of the transect and extremely low values in the southern surface waters. Slightly negative volume scattering in the south end of the transect, suggested that there may have been some fragmentation of fragile cells during the pH shift, such that the acidified volume scattering values were slightly greater than those from raw seawater. These same trends were also observed in the cell and coccolith count data (Fig. 1), albeit with considerably lower horizontal resolution (one vertical profile every 300km).

The unidentified birefringent particles (Fig. 3) may have been holococcoliths, rhombohedral crystals produced by some Prymnesiophytes. This remains unconfirmed due to lack of scanning electron micrographs, however. Most striking was the coherence in the pattern given that samples were randomly counted (and sample identities were unknown to the microscopist until after the counts). It should be noted that these particles corresponded to patches of high suspended calcite concentration (Fig. 4c), 30-50m above the core of the equatorial undercurrent.

Calcification and Photosynthesis

One of the most striking results of the calcification measurements was that there were several areas, such as at 12°N, at 20m depth, where calcification and photosynthesis were equal (Fig. 5). This was even more striking when one considers that calcification was performed by only a few species, while photosynthesis was performed by all phytoplankton. Another interesting result concerned the short turnover times of calcite in the euphotic zone (3-10d), unexpected for a non-nutritious particle (Fig. 6c). Only at 1S, was the turnover time 50d due to the very high standing stock of calcite. These data, combined with the cell counts (Fig. 1) suggest that grazing was partially responsible for the rapid calcite disappearance. We have previously observed similar rapid turnover in the central north Atlantic and Gulf of Maine (unpublished data). This interpretation was consistent with the model of Honjo (1976) which listed zooplankton fecal pellets as the major vehicle for carrying micron-sized sinking calcite particles to depth.

Calcification normalized to the area of plated coccolithophore cells provided insight into where extracellular calcite fluxes were most rapid. The scale of these measurements ranged over two orders of magnitude. Admittedly, this analysis was taxonomic in only the broadest sense, since we only enumerated the numbers and sizes of plated coccolithophores, not their species identification. Even if we had identified cells to the species level, it would have been impossible to unequivocally determine which ones were responsible for the highest flux rates because coccolithophore populations were rarely monospecific. Another limitation of this analysis was that it assumed that only calcifying cells had visible calcite birefringence. Nevertheless, there was the possibility that certain calcifying cells had not yet accreted sufficient coccoliths to make their birefringence clearly visible in the microscope, or they simply had detached all of their coccoliths. Our analysis assumed that such cells represented a small fraction of the total coccolithophore biomass.

The mean extracellular calcification flux rate at all stations was 0.24 mol C (m^2 cell membrane)$^{-1}$ d^{-1} (standard deviation= 0.44 mol C (m^2 cell membrane)$^{-1}$ d^{-1}). This average was somewhat biased by samples from a few select depths, with rates 10X higher than the average (e.g. 60m depth and 1°N). In fact, most of the study area had flux rates < 0.1mol C (m^2 cell membrane)$^{-1}$ d^{-1}. It is useful to compare these rates to data from *Emiliania huxleyi*. Our previous laboratory results showed that clone 88E of this species had an average diameter of 4.75μm (average cell surface area without coccoliths= 70.9μm^2; See table 2 from Balch et al., 1993) and calcification rates of 10-60 fmol cell^{-1} h^{-1} (Balch et al., 1992). Therefore, the range of extracellular calcification flux rates was 3.39 x 10^{-3} to 2.00 x 10^{-2} mol C (m^2 cell membrane)$^{-1}$ d^{-1}, over 10X lower than what we observed in the equatorial Pacific. As a cross check, the same analysis was done for a

coccolithophore bloom in the Gulf of Maine in 1989, at station 4, 5m (see Balch et al., 1992). The coccolithophore concentration at this station was 1550 cells ml^{-1} and the calcification rate was 1mmol m^{-3} d^{-1}. Using the same diameter for *E. huxleyi* given above, the extracellular calcite flux rate was 9.1 x10^{-3} mol C (m^2 cell membrane)$^{-1}$ d^{-1}, again much lower than the Equatorial Pacific data, yet quite similar to the data from our laboratory experiments. Our conclusion from these comparisons was that *E. huxleyi*, in laboratory cultures or monospecific blooms, can be characterized by a moderately low extracellular calcification flux rate, and probably another coccolithophore species was responsible for the higher extracellular calcite flux rates in the equatorial upwelling region. Typical coccolithophore species in this region are *E. huxleyi*, *Cyclococcolithina fragilis*, *Cyclococcolithina leptoporus*, *Gephyrocapsa oceanica*, *Umbellosphaera hulburtiana*, *Umbellosphaera irregularis*, and *Discosphaera tubifera* (see Okada and Honjo, 1973).

The estimated area of plated coccolithophore cells plotted against the number of detached coccoliths had a slope equal to the effective area per coccolith. If one assumes that the coccoliths were shaped like flattened discs, then the lower limit of the data distribution (Fig. 8) represented coccoliths of about 1μm radius, the size of the smallest coccoliths of *Emiliania huxleyi* and *Gephyrocapsa oceanica*. The high end of the distribution implied coccoliths having 8μm radii. The least-squares-fit slope to these data (Log plated cell area m-3 = (0.50 (log (detached coccolith concentration))) - 4.0) was about half of the slope of the isopleths shown in Fig. 8; while this could have been fortuitous, it could have been due to coccolith size changing as a function of coccolith concentration. That is, when the concentration of detached coccoliths was low, the mean coccolith radius was about 4μm and when the concentration was high, the mean radius was about 1μm. As stated before, such an interpretation does not take into consideration that coccoliths may have been layered on cells (Balch et al., 1993). Since the lower limit of these data closely matched the minimum size of heterococcoliths of the smallest species (see Reid (1980) or Okada and Honjo (1973) for examples of Pacific Ocean coccolithophore species) then the idea that cells were covered by one layer of coccoliths seems reasonable.

Light scattering by particles and upwelling

The results of the underway measurements showed that in the *Rhizosolenia* bloom at the "great front", the total volume scattering at 90° was unexpectedly less than in adjoining waters. To the contrary, just north of the equator, in the core of the upwelled water, a small peak in chlorophyll was associated with increased 90° volume scattering. While the large Rhizosolenia may have not survived the impeller pump, it is more likely that the 90° volume scattering was contributed mostly by very small particles, not the 400-

500μm length *Rhizosolenia* cells, and these small scattering particles were at minimal concentration at the front whereas they were more abundant in the upwelling waters. Morel and Ahn (1991) have previously shown that heterotrophic bacteria and other sub-micron particles are extremely efficient backscatterers of light, more than larger algae. Thus, 90° volume scattering could have been dominated by small particles instead of large diatoms. This interpretation was also buttressed by the fact that similar patterns were observed in the underway beam attenuation and fluorescence measurements made with the Undulating Optical Recorder (UOR; Trees and Aiken, personal communication). Their data showed the presence of the same chlorophyll features that are shown in figure 11 as well as similar behavior of beam attenuation; it *decreased* in the *Rhizosolenia* feature and increased in the non-*Rhizosolenia* feature. It is important to caution that beam attenuation is more a function of total scattering than backscattering, and Morel and Ahn (1991) have shown that algal cells influence the total scattering coefficient more than backscattering coefficient.

A plot of total 90° volume scattering versus temperature indicated an asymmetrical curve reminiscent of temperature tolerance experiments done by others (Eppley, 1972). In such experiments, populations grew increasingly fast as temperature was raised, but above a threshold temperature, growth rates declined precipitously. In our data, the coldest upwelled water was associated with water having the lowest 90° volume scattering. The only exception was a small patch of water at 8.5°N that also had low scattering and a temperature of 27.5°C; this patch may have still represented water upwelled from a shallower depth, however (Fig. 10). The surface temperature where volume scattering decreased sharply was about 28.5°C and by 29°C, the total 90° volume scattering was the same as in the newly upwelled equatorial water. Our cell counts certainly showed that the species of phytoplankton varied over the transect, thus it was not possible to attribute this behavior to any one species undergoing thermal stress. Nevertheless, from a bio-optical perspective, the evidence suggested that the upwelled water surfaced relatively free of particles, particle formation occurred in the mid-temperature ranges and stopped above 28.5°C. Subsequent sinking of remaining particles caused the 29°C surface water to reach the clarity of the upwelled water.

Synthesis: Sources and Fates of Calcite Production in the Equatorial Pacific

These results provide insight into the biogeochemistry of calcium carbonate in the equatorial Pacific. Broecker and Peng (1982) showed with GEOSECS data that in the Pacific, the average ratio of biologically produced organic matter to biogenically produced calcite was 4.4 (not much different from their global ratio of ~4.5). Integral chlorophyll values from survey cruise II (JGOFS core data of B. Bidigare and J. Newton) were used

to calculate integral phytoplankton carbon, assuming a typical carbon:chlorophyll ratio of 75. Dividing these values by our observed integral calcite standing stocks gave ratios of organic to inorganic standing stocks with a large range, between 4 and 12 (with the exception of 1°S which had an anonymously low value of 1.5).

The conceptual model of Westbroek et al. (1993) predicted that the global ratio of photosynthesis to calcification is 20-30 and they showed how organic matter is gradually remineralized enroute to the sea floor until calcite far outweighed organic carbon, and the ratio of burial rates of organic to inorganic carbon into the geological archive was about 0.18 (See also Fig. 4 from Milliman, 1993). Our data suggested that in the equatorial Pacific, surface calcite production played a more important role than suggested by Westbroek (1993). This is because the ratio of integral photosynthesis to calcification was about 7-9 in the oligotrophic regions and about 8-32 near the equator, not 20-30. The average ratio for the entire data set was about 11. Such values were similar to the ratios of the standing stocks of organic carbon to calcite carbon. The main way to incorporate increased calcification into models such as that of Westbroek et al. (1993), without changing burial fluxes, is to increase calcite dissolution, either at the bottom or enroute to the sea floor.

The cell count data demonstrated a general decrease in the concentration of calcite coccoliths and cells in equal proportion below 60m depth (with the exception of one sample at 80m at 5°N; Fig. 1). Since these particles were well above the lysocline and calcium compensation depth (Seibold and Berger, 1982), dissolution should have been minimal, but, for reasons to be discussed, this possibility still cannot be discounted.

Detached coccoliths settle at extremely slow rates of about 0.1 m d^{-1} so that incorporation into fast-sinking fecal pellets is the most likely vertical transport mechanism (Honjo, 1976). Two potential causes for the loss of coccoliths and coccolithophores below 60m are: 1) incorporation into fast-sinking fecal pellets by grazers or 2) dissolution. If the sinking pellet hypothesis is true, then our data do not suggest much discrimination by grazers between coccolithophores and their coccoliths since the ratio of coccoliths to plated cells (about 10:1; Fig. 2) did not change with depth. Had the ratio increased with depth, then one could have hypothesized that the plated cells were preferentially grazed. Lack of a vertical change in this ratio could also be attributed to dissolution, which presumably is the same for coccoliths detached or attached to cells.

It is reasonable to assume that grazing was the process repackaging coccoliths and transporting them downwards in fecal pellets, given that the estimated turnover time of the calcite was several days. However, calcite in fecal pellets should have been caught in sediment traps. The sediment trap data of Newton (in preparation) and Honjo et al.

(submitted) showed that a large fraction of the calcite flux disappeared in the top 3000m of the water column, which can be attributed to dissolution or horizontal advection of calcite particles from the trap sites. For example, the sediment trap data that most corresponded to the period of survey cruise II are from 10 -27 September, 1992 (time periods 14 and 15; Table 3 of Honjo et al., submitted). Note, as suggested by these investigators, this time period allowed 17d for the particles to sink from the surface to the traps. Averaging the Honjo et al. (submitted) flux data for all traps between 2000m and 3800m, within 5°N and 5°S, gave calcite flux rates of 535μmol m^{-2} d^{-1} (s.e.=43.3, n=11). Our average integrated calcification rates within 5°N and 5°S were 2750μmol m^{-2} d^{-1} (s.e.=11.5; n=9). If our assumption was correct, that is, that the calcification we measured was caught in the traps between 10 and 27 September, then some 4/5 of the calcite disappeared above the CCD (4700-5000m; Van Andel, 1975). At the equatorial station reported by Honjo et al. (submitted) their shallowest trap was deployed at 800m. The flux of calcite into this trap was 332 μmol m^{-2} d^{-1}, not significantly different from the trap at 2284m (490μmol m^{-2} d^{-1}). This argues that any calcite loss was occurring in the top 1000m of the water column.

One obvious explanation for the above results was that there was a mis-match of time and space scales; that is, the calcite that was caught in the sediment traps was not the same that we measured in surface waters. Milliman (1993) discussed the potential problems when comparing fluxes and accumulation rates of sediment traps and sediment cores due to the different time scales involved; the same could apply to comparisons of surface incubations and sediment trap data. Obviously, given the potential problems with sediment trap efficiencies, such data should be interpreted carefully. Nevertheless, the data of Honjo et al.(submitted) convincingly showed minimal temporal offset (<17d) between the surface and deep sediment trap collection rates, suggesting rapid settling fluxes. If dissolution indeed were occurring above the CCD, then one explanation was that calcite dissolved in microzones, perhaps where decomposition of reduced organic matter lowered the pH sufficiently to dissolve calcite (analogous to Emerson and Bender's (1981) model of calcite dissolution at the sediment-water interface). Obviously, there are some historical data contrary to this hypothesis (e.g. Berger et al., 1982), but if the hypothesis is true, then the role of calcification in transferring bicarbonate to the deep sea (Westbroek et al., 1993) should be reevaluated in the equatorial Pacific since much of the carbonate never reaches the CCD.

The importance of dissolution in the benthos is also addressed by Berelson et al. (1990). They showed deep water calcium carbonate dissolution rates in the equatorial Pacific (135-140°W) of about 300-500 μmol m^{-2} d^{-1}. Berelson's measurements from the EqPac cruises (Berelson et al., in press) ranged from 450-650 μmol m^{-2} d^{-1} with highest

rates at 2°N. Such rates essentially are identical to the rates of delivery calculated by Honjo et al. (submitted). Thus, while most dissolution happened in shallow waters through some unknown mechanism, deep sedimentation of calcite balanced benthic dissolution. This would imply that no net accumulation of calcium carbonate currently is occurring in this region.

A final aspect of carbonate cycling that has arisen during this analysis relates to the fraction of calcite production that sinks to the sea floor. As mentioned above, the overall average integral calcification between 5°N and 5°S over the 32 days that those samples were taken was about 2750 μmol m^{-2} d^{-1}. The ratio of calcite production to sedimentation was ~5, smaller than the global ratio of 7 cited by Berger (1971) and Broecker and Peng (1982). Clearly, if calcite dissolution was occurring in the upper water column instead of the deep sea, and one part in five reached the sediments instead of one part in seven, then equatorial Pacific carbon flux models need to be adjusted accordingly. The ramifications of such a difference would mean that, assuming the same surface calcification rate, 1) most of the bicarbonate produced during calcite dissolution would remain in the top 1000m instead of the deep sea, and 2) the larger fraction of surface calcification reaching the benthos would help maintain the balance between calcite sedimentation and burial in this important part of the world ocean.

Acknowledgments- The captain and crew of the R/V Thomas Thompson provided expert ship handling and logistical support. James Murray and two anonymous reviewers provided comments on an earlier draft. Susan Kadar provided vital pre- and post-cruise logistical support. This is contribution number 220 of the U.S. JGOFS program and contribution number 96003 of the Bigelow Laboratory for Ocean Sciences. This work was generously supported by the National Science Foundation (OCE-9022227), the Office of Naval Research (N00014-91-J-1048) and NASA (NAGW-2426 and NAS5-31363).

References

Aiken, J. and I. Bellan (1990) Optical oceanography: An assessment of a towed method, In: *Light and Life in the Sea*, P. J. Herring, A. K. Campbell, M. Whitfield, and L. Maddock, editors. Cambridge University Press, New York, pp. 39-57.

Arrhenius, G.O. (1952) Sediment cores from the East Pacific. *Swedish Deep-Sea Expedition Reports, 1947-48.*, **5**, 189-201.

Balch, W.M., P.M. Holligan, S.G. Ackleson, and K.J. Voss (1991) Biological and optical properties of mesoscale coccolithophore blooms in the Gulf of Maine. *Limnology and Oceanography*, **36**, 629-643.

Balch, W. M., P. M. Holligan and K. A. Kilpatrick (1992) Calcification, photosynthesis and growth of the bloom-forming coccolithophore, *Emiliania huxleyi.*, Continental Shelf Research, **12**, 1353-1374.

Balch, W.M., K.A. Kilpatrick, and P.M. Holligan (1993) Coccolith formation and detachment by *Emiliania huxleyi* (Prymnesiophyceae), *Journal of Phycology*, **29**, 566-575.

Be, A. W. H., C. Hemleben, O. R. Anderson, M. Spindler, J. Hacunda, and S. Tuntivate-Choy (1977) Laboratory and field observations of living planktonic foraminifera, *Micropaleontology*, **23**, 155-179.

Berelson, W. M., D. E. Hammond, and G. A. Cutter (1990) In situ measurements of calcium carbonate dissolution rates in the deep-sea sediments, Geochimica et Cosmochimica Acta, **54**, 3013-3020.

Berger, W. (1971) Sedimentation of planktonic foraminifera, *Marine Geology*, **11**, 325-358.

Berger, W., M., -C. Bonneau, and F. L. Parker. (1982) Foraminifera on the deep-sea floor: Lysocline and dissolution rate. Oceanol. Acta, **5**, 249-258.

Bramlette, M.N. (1958) Significance of coccolithophorids in calcium carbonate deposition, *Bulletin of the Geological Society of America*, **69**, 121-126.

Broecker and Peng (1982) *Tracers in the sea.* Lamont-Doherty Geol. Obs., Columbia University , New York. 690 pp.

Brown, C. and J. Yoder (1994a) Distribution pattern of coccolithophorid blooms in the Western North Atlantic. Cont. Shelf Res., **14**, 175-198.

Brown, C. W. and J. A. Yoder (1994b) Coccolithophorid blooms in the global ocean. J. Geophys. Res. **99**, 7467-7482.

Chavez, F. P. and R. T. Barber (1987) An estimate of new production in the equatorial Pacific. *Deep-Sea Res.*, **34**, 1229-1243.

Cwienk, D. and M. Leinen (1985) Expression of global sediment component fluxes in surface sediment accumulation rates, *EOS, Transactions of the American Geophysical Union*, **66**, 930.

Emerson, S., and M. Bender (1981) Carbon fluxes at the sediment-water interface of the deep-sea: calcium carbonate preservation, *Journal of Marine Research*, **39**, 139-162.

Eppley, R. W. (1972) Temperature and phytoplankton growth in the sea. *Fisheries Bulletin*, **70**, 1063-1085.

Eppley, R. W. and B. Peterson (1979) Particulate organic matter flux and planktonic new production in the deep ocean. *Nature*, **282**,677-680.

Fernandez, E., P. Boyd, P. M. Holligan, and D. S. Harbour (1993) Production of organic and inorganic carbon within a large scale coccolithophore bloom in the North Atlantic ocean. Mar. Ecol. Prog. Ser., 97, 271-285.

Holligan, P. M. , M. Viollier, D. S. Harbour, P. Camus, and M. Champagne-Philippe (1983) Satellite and ship studies of coccolithophore production along a continental shelf edge, *Nature*, **304**, 339-342.

Holligan, P. M., E. Fernandez, J. Aiken, W. Balch, P. Boyd, P Burkill, M. Finch, S. Groom, G. Malin, K. Muller, D. Purdie, C. Robinson, C. Trees, S. Turner, and P. van der Wal (1993) A biogeochemical study of the coccolithophore, *Emiliania huxleyi*, in the north Atlantic, *Global Biogeochemical Cycles*, **7**, 879-900.

Holm-Hansen, O., C. J. Lorenzen, R. W. Holmes, and J. D. H. Strickland (1965) Fluorometric determination of chlorophyll. *J. Cons perm. int. Explor. Mer*, **30**, 3-15.

Honjo, S. (1976) Coccoliths: production, transportation and sedimentation. Mar. *Micropaleontology*, **1**, 65-79.

Honjo, S, J. Dymond, R. Collier, and S. J. Manganini (submitted) Export production of particles to the interior of the equatorial Pacific Ocean during the 1992 EqPac experiment, *Deep-Sea Research*.

Kawaguti, S. and D. Sakumoto (1948) The effect of light on the calcium deposition of corals. *Bulletin of the Oceanographic Institite of Taiwan*, **4**, 65-70.

Kilpatrick, K., W. M. Balch, Y. Ge, and K. J. Voss (1994) A photometer for the continuous measurement of calcite-dependent light scatter in seawater. *Proceedings of the Society of Photo-Optical Instrumentation Engineers*, in press.

Kramer, D. D. and J. H. Ryther (1960) The iron requirement of some marine plankton algae. *Biological Bulletin*, **119**, 324.

Lohmann, H. (1908) On the relationship between pelagic deposits and marine plankton (in German), *Int. Rev. Ges. Hydrobiol. Hydrogr.*, **1**, 309-323.

Margalef, Ramon (1978) Life-forms of phytoplankton as survival alternatives in an unstable environment, *Oceanologica Acta*, **1**, 493-509.

McIntyre, A. and A.W.H. Be (1967) Modern coccolithophoridae of the Atlantic Ocean-I. Placoliths and cyrtoliths. *Deep Sea Research*, **14**, 561-597.

Millero, F. J. and A. Poisson (1981) International one-atmosphere equation of state of sea-water, *Deep-Sea Research*, **28A**, 625-629.

Milliman, J. D. (1993) Production and accumulation of calcium carbonate in the ocean: budget of a nonsteady state. Global Biogeochemical Cycles, **7**, 927-957.

Morel, A. and Y. Ahn (1991) Optics of heterotrophic nanoflagellates and ciliates: A tentative assessment of their scattering role in oceanic waters compared to those of bacterial and algal cells. *Journal of Marine Research*, **49**, 177-202.

Okada, H. and S. Honjo (1973) The distribution of oceanic coccolithophorids in the Pacific. Deep-Sea Research, **20**, 355-374.

Okada, H. and A. McIntyre (1977) Modern coccolithophores of the Pacific and North Atlantic Oceans. Micropaleontology, **23**, 1-55.

Paasche, E. (1962) Coccolith formation. *Nature*, **193**, 1094-1095.

Paasche, E. (1963) The adaptation of the Carbon-14 method for the measurement of coccolith production in *Coccolithus huxleyi*, *Physiologia Plantarum*, **16**, 186-200.

Parsons, T. R., Y. Maita and C. M. Lalli (1984) *A manual of chemical and biological methods for seawater analysis*. Pergamon Press Inc., New York, 173 pp.

Pena, M. A., M. R. Lewis, and J. J. Cullen (1994) New production in the warm waters of the tropical Pacific Ocean. *Journal of Geophysical Research*, **99**, 14255-14268.

Reid, F (1980) Coccolithophorids of the North Pacific Central Gyre with notes on their vertical and seasonal distribution. *Micropaleontology*, **26**, 151-176.

Sarnthein, M., K. Winn, J.-C. Duplessy and M.R. Fontugne (1988) Global carbon variations of surface ocean productivity in low and mid-latitudes: influence on CO2 reservoirs of the deep ocean and atmosphere during the last 21,000 years. *Paleo-oceanography*, **3**, 361-399.

Seibold, E. and W. H. Berger (1982) *The sea floor- An introduction to marine geology*. Springer-Verlag, New York, 288pp.

ter Kuile, B. and J. Erez. (1987) Uptake of inorganic carbon and internal carbon cycling in symbiont-bearing benthonic foraminifera, *Marine Biology*, **94**, 499-509.

Van Andel, T. H. (1975) Cenozoic history and paleoceanography of the central equatorial Pacific Ocean, *Geological Society of America Memoirs*, **143**, 1-134.

Wefer, G. (1980) Carbonate production by algae *Halimeda, Penicillus* and *Padina. Nature*, **285**, 323-324.

Westbroek, P, C. W. Brown, J. van Bleijswijk, C. Brownlee, G. Jan Brummer, M. Conte, J. Egge, E. Fernandez, R. Jordan, M. Knappertsbusch, J. Stefels, M. Veldhuis, P. van der Wal and J. Young (1993) A model system approach to biological climate forcing. The example of *Emiliania huxley*i, *Global and Planetary Change*, **8**, 27-46.

Wyrtki, K. (1981) An estimate of equatorial upwelling in the Pacific. *Journal of Physical Oceanography*, **11**, 1205-1214.

Yentsch, C. S. and D. Menzel (1963) Method for the determination of phytoplankton chlorophyll and phaeophytin by fluorescence. *Deep-Sea Research*, **10**, 221-231.

Yoder, J. A., S. G. Ackleson, R. T. Barber, P. Flament and W. M. Balch (1994) A line in the sea. Nature, **371**, 689-692.

Figure Legend

Fig. 1. (a) Vertical section of detached coccolith concentration from 12°N to 12°S, from the surface to 120m depth, along 140^0 W. Contour levels are 50, 100, 200, 400, and 600 ml^{-1}. Counts are made as described in text. (b) Vertical section of total plated coccolithophores, showing contours of 5,10, 20, 40, and 60 ml^{-1}. Sample locations and depths are shown with an asterisk in both panels.

Fig. 2. Plot of detached coccoliths versus total plated coccolithophores (log axes). Formula for the least-squares fit line is given in the text.

Fig. 3. Vertical section along 140^0 W for unidentified, 0.5μM diameter, birefringent particles (possibly holococcoliths). Other details of the section are described in Fig. 1. Contour interval is 0.4×10^4, 2.0×10^4, 3.6×10^4, 5.2×10^4, 6.8×10^4 particles per mL.

Fig. 4. (a) Vertical section of photosynthesis along 140^0 W. Other details of section are described in Fig. 1. Contour intervals are: 0.15, 0.40, 0.65, 0.90, 1.15, 1.40, 1.65, 1.90, 2.15 mmol C m^{-3} d^{-1}. (b) Vertical section of calcification from same samples as in panel a above. Contour intervals are: 8.3×10^{-3}, 16.7×10^{-3}, 33.3×10^{-3}, 66.7×10^{-3} mmol C m^{-3} d^{-1}. Peak calcification values (above 66.7×10^{-3} mmol C m^{-3} d^{-1}) are designated. (c) Vertical section of suspended calcite carbon showing contours of 0.17, 0.25, 0.33, 0.67, 1.33 mmol calcite C m^{-3}.

Fig. 5. Calcification rate (mmol C m^{-3} d^{-1}) versus photosynthesis (mmol C m^{-3} d^{-1}) for all data from TT011. The 1:1 line is shown for reference. It can be seen that in some cases, calcification rates were equal to photosynthesis rates but generally, they were about 10% of the photosynthesis rates and this fraction varied considerably. Symbols on the figure are: + and * = in situ replicates, Δ and o = simulated in situ replicates.

Fig. 6. (a) Integrated photosynthesis and calcification versus latitude along 140°W. (Symbols are: + = in situ photosynthesis, * = simulated in situ photosynthesis, o = in situ calcification and Δ= simulated in situ calcification; units are mmol C m^{-2} d^{-1}). (b) Integrated suspended calcite (molC m^{-2}). Results were integrated to 120m depth for both plots. Samples from 7° N-12° N were lost. (c) Turnover time of euphotic zone calcite carbon (days) versus latitude. Values calculated by dividing the standing stock of calcite by

the calcification rate. Symbols are: + = simulated in situ incubations and o= in situ incubations.

Fig. 7. Integral calcification as a percent of the total carbon fixed, based on integrals of the simulated in situ incubation data.

Fig. 8. Plot of the concentration of detached coccoliths versus the estimated surface area of plated coccolithophores. The coccolith concentration does not include those attached to cells or in loose clumps. The cell surface area was calculated by binning the counts of plated cells into nominal size categories, then calculating surface area assuming spherical cells. See text for details. The expected relationship for 1 μm, 2μm, 4μm, and 8μm radius coccoliths is shown, which assumes that the coccoliths were shed as a single layer, that they were round discs, and that the detached plates originally completely covered the cells. These data suggest calcite particles of 1-8μm in radius. It was not possible to accurately include "clumped" coccoliths into this calculation which would have shifted the data to the right on the plot.

Fig. 9. Vertical section along 140° W of the extracellular calcite flux, as determined from the ^{14}C incorporation data and binned cell counts (units are mol C (m^{-2} cell surface area) d^{-1}).

Fig. 10. Surface transect data along 140° W for (a) salinity and chlorophyll, (b) temperature and total β_{90} volume scatter and (c) calcite-dependent β_{90} (acid labile). Each plot contains 2726 measurements between 12° N and 12° S (no data were collected between 5° N and 3° N due to instrument problems). The average data collection rate was 1.1 points per kilometer.

Fig. 11. Surface transect data plotted on 2 dimensional temperature-salinity diagrams to allow better water mass discrimination. (a) Temperature-salinity data showing isopleths of density calculated from equations of Millero and Poisson (1981). (b) Same data as in panel a showing contours of latitude. (c) Distribution of chlorophyll within the various water masses surveyed, also showing isopleths of latitude as in panel b. (d) Distribution of calcite-dependent β_{90} within the various water masses surveyed, also showing isopleths of latitude as in panel b. (e)Distribution of total β_{90} within the various water masses surveyed, also showing isopleths of latitude as in panel b.

Fig. 12. Surface transect data for total β_{90} versus temperature. Upper and lower dashed lines were drawn by eye to illustrate curvilinear data envelope.

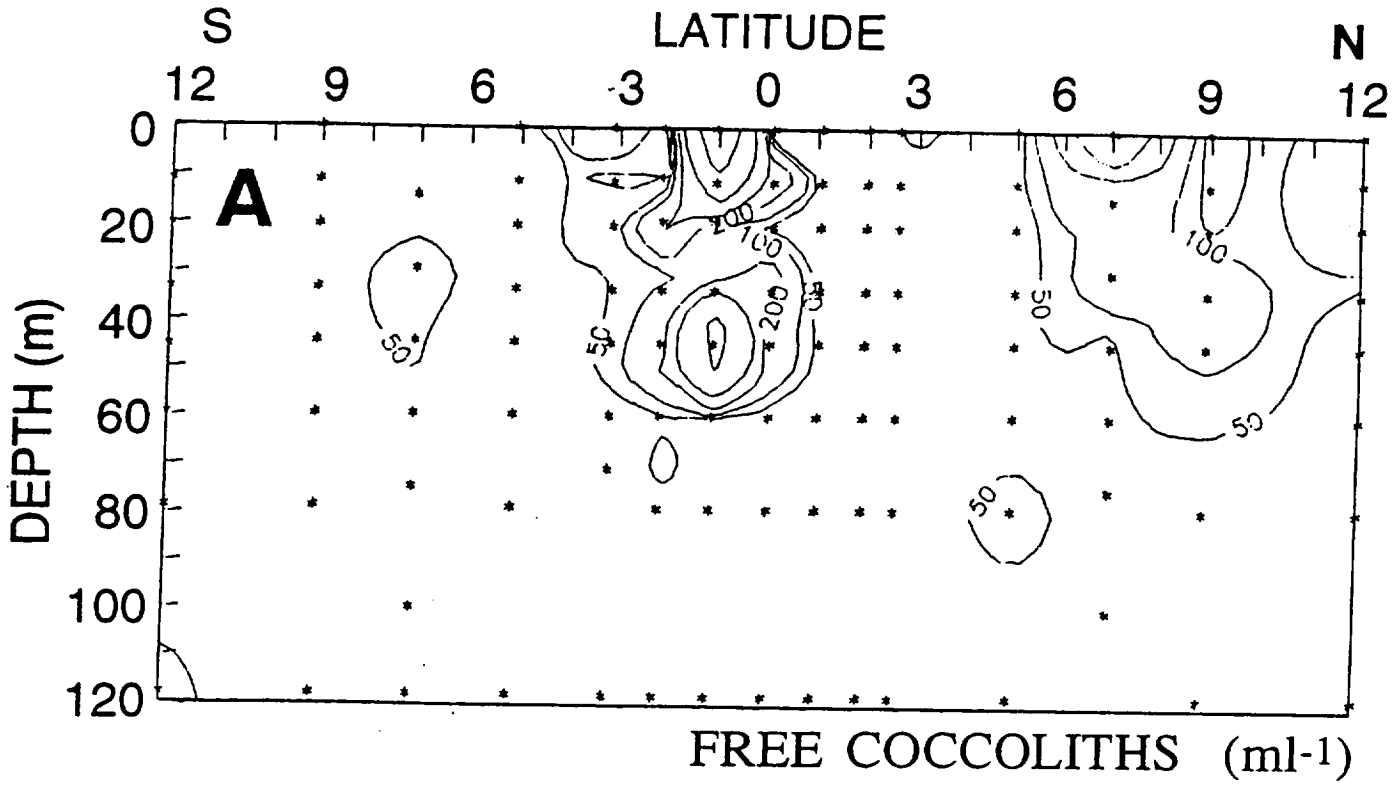
S
LATITUDE
N
12 9 6 3 0 3 6 9 12
A
DEPTH (m)
0 20 40 60 80 100 120
50
100
200
FREE COCCOLITHS (ml-1)

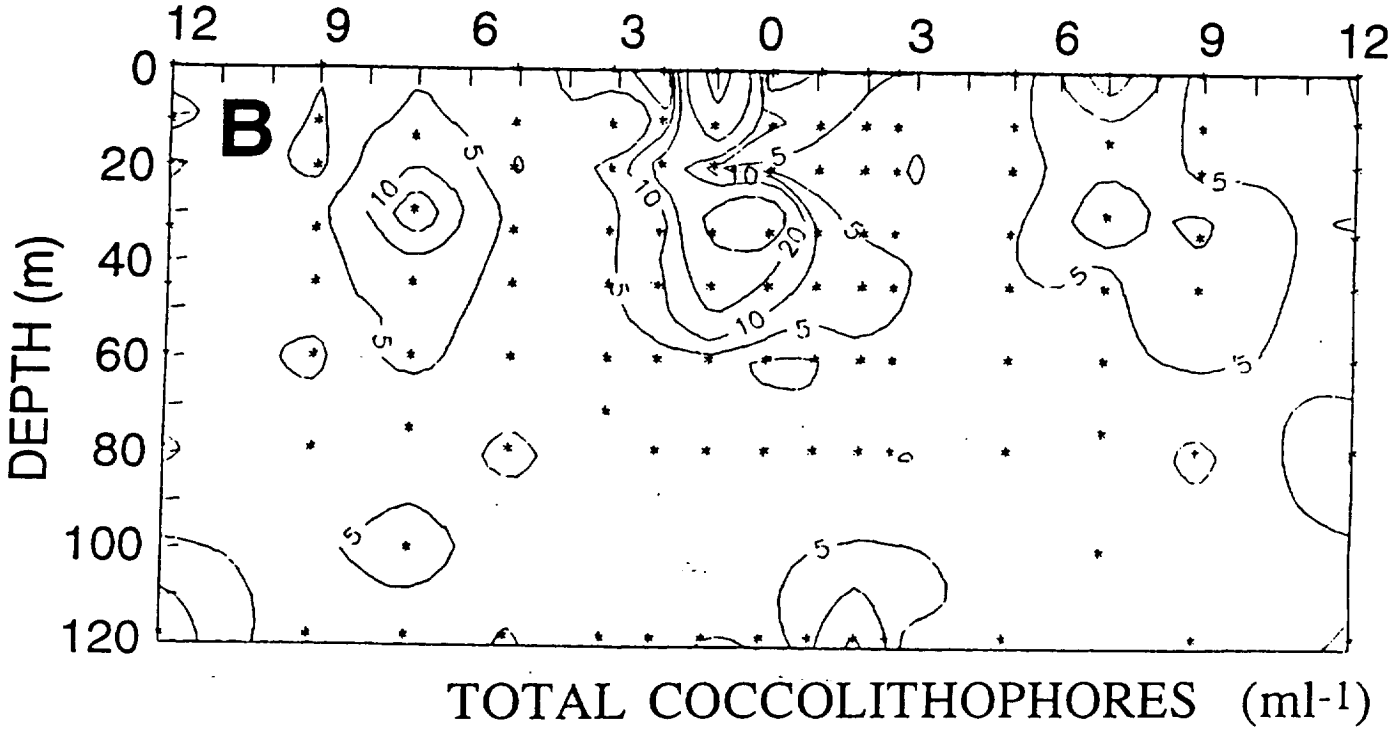
12 9 6 3 0 3 6 9 12
B
DEPTH (m)
0 20 40 60 80 100 120
5
10
20
TOTAL COCCOLITHOPHORES (ml-1)

Fig 1

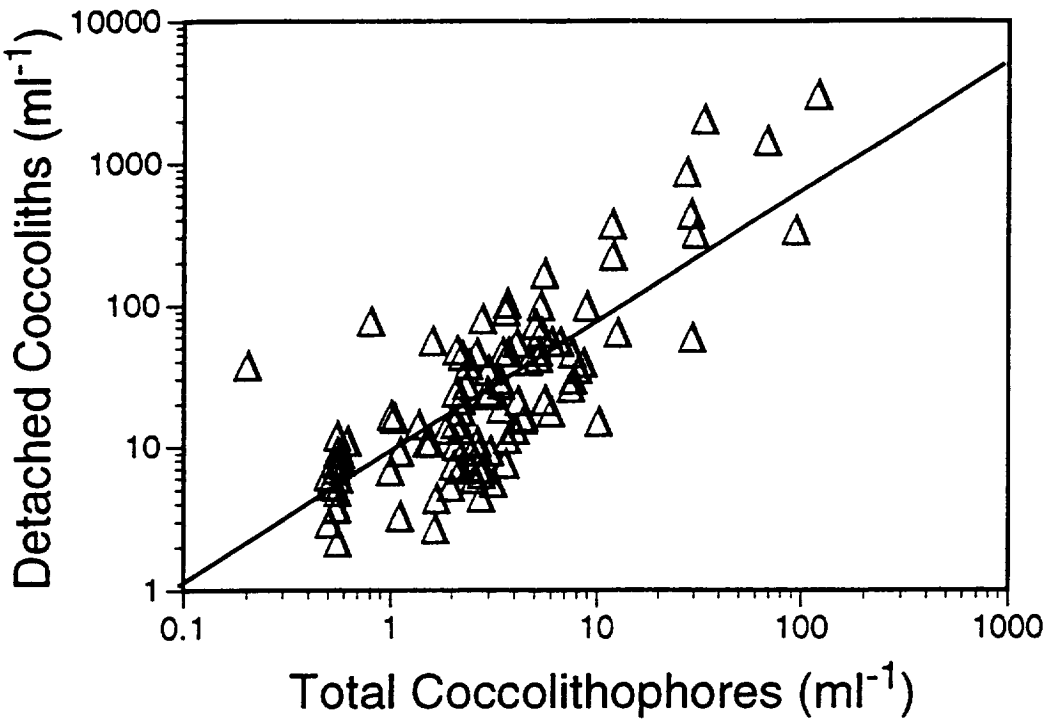
Detached Coccoliths (ml-1)
10000
1000
100
10
1
0.1
1
10
100
1000
Total Coccolithophores (ml-1)

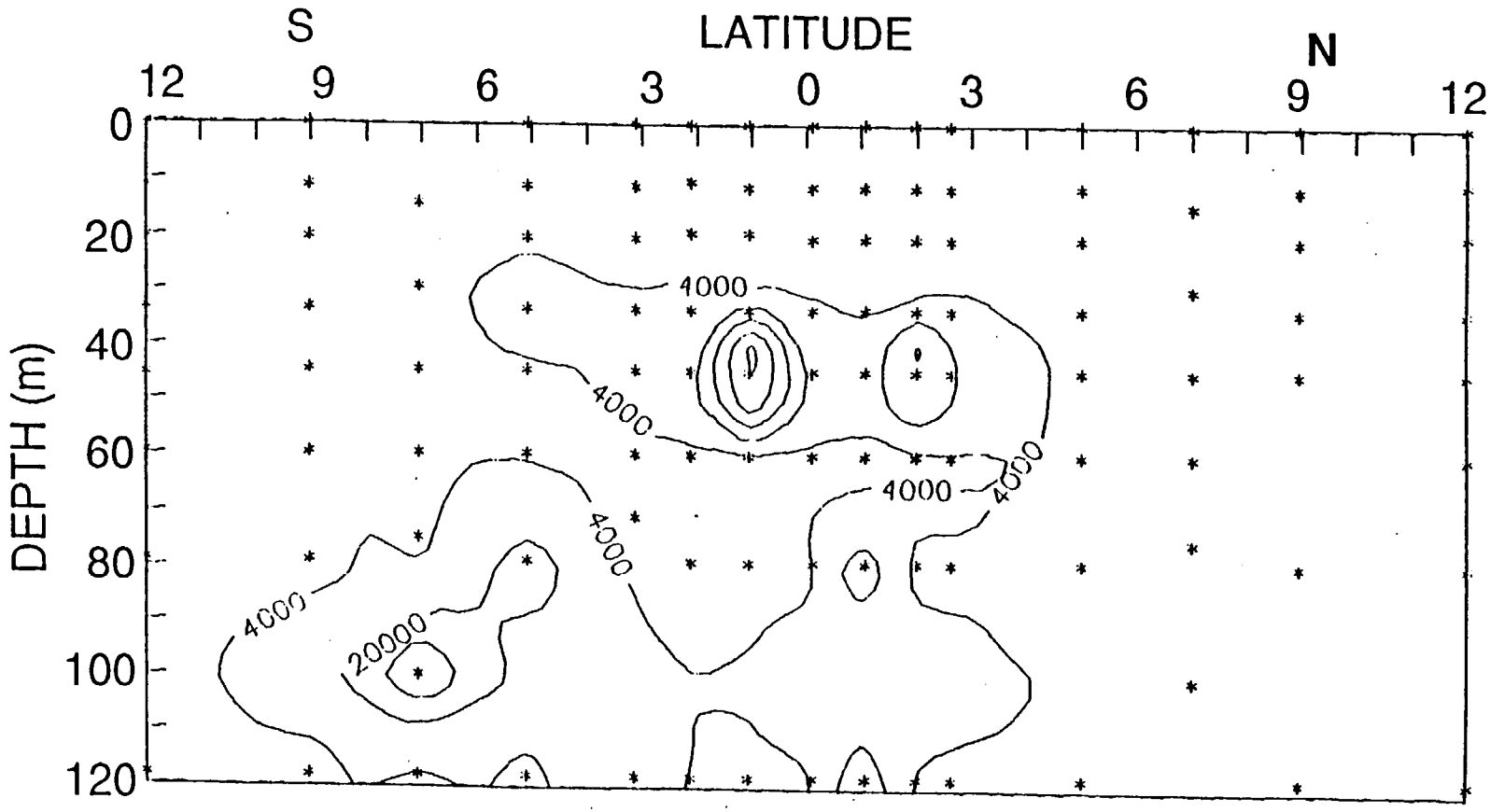
S
LATITUDE
N
12
9
6
3
0
3
6
9
12
0
20
40
60
80
100
120
DEPTH (m)
4000
4000
4000
4000
4000
20000

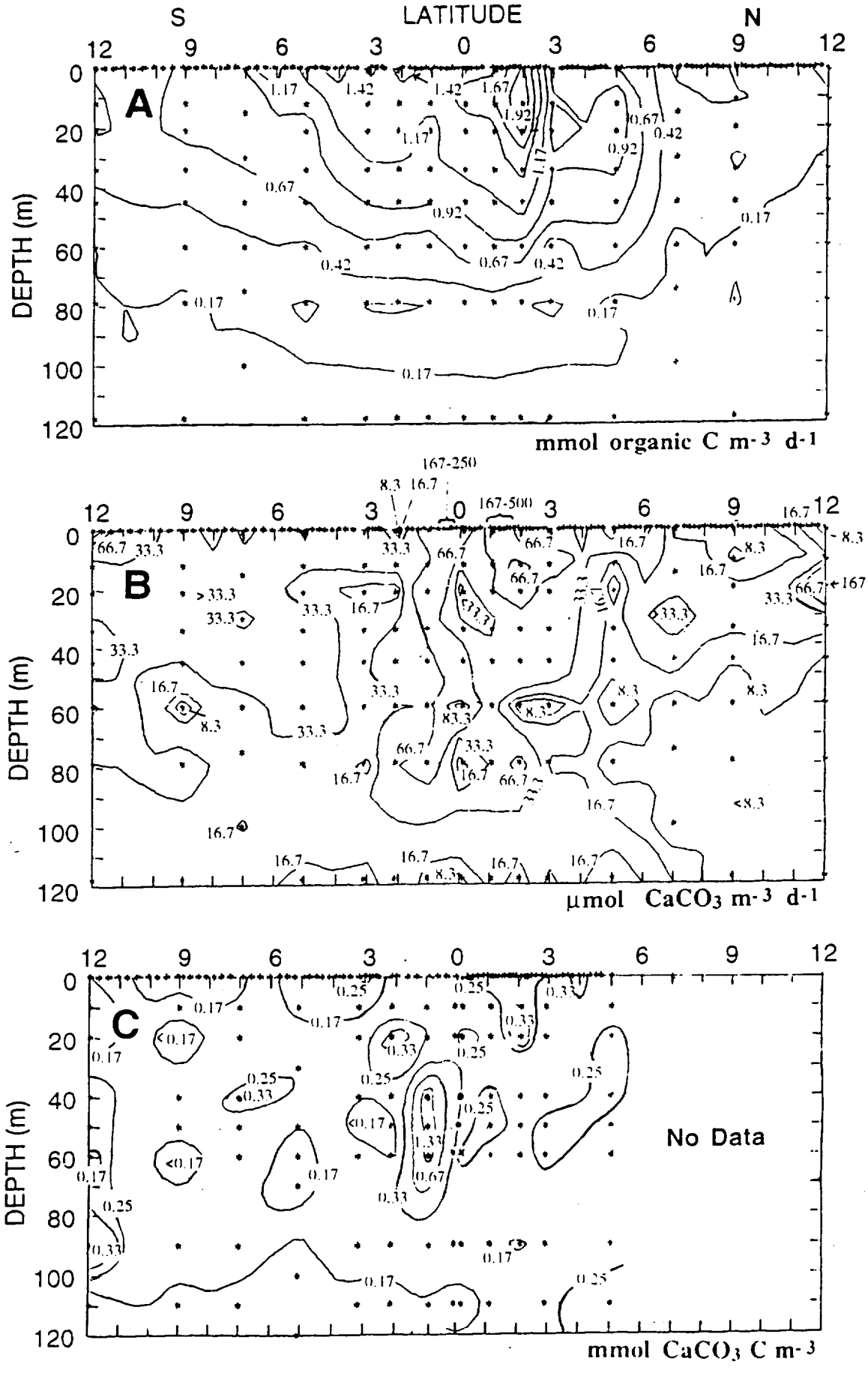
S
LATITUDE
N
12 9 6 3 0 3 6 9 12
DEPTH (m)
0 20 40 60 80 100 120
A
mmol organic C m-3 d-1
B
167-250
167-500
µmol CaCO3 m-3 d-1
C
No Data
mmol CaCO3 C m-3

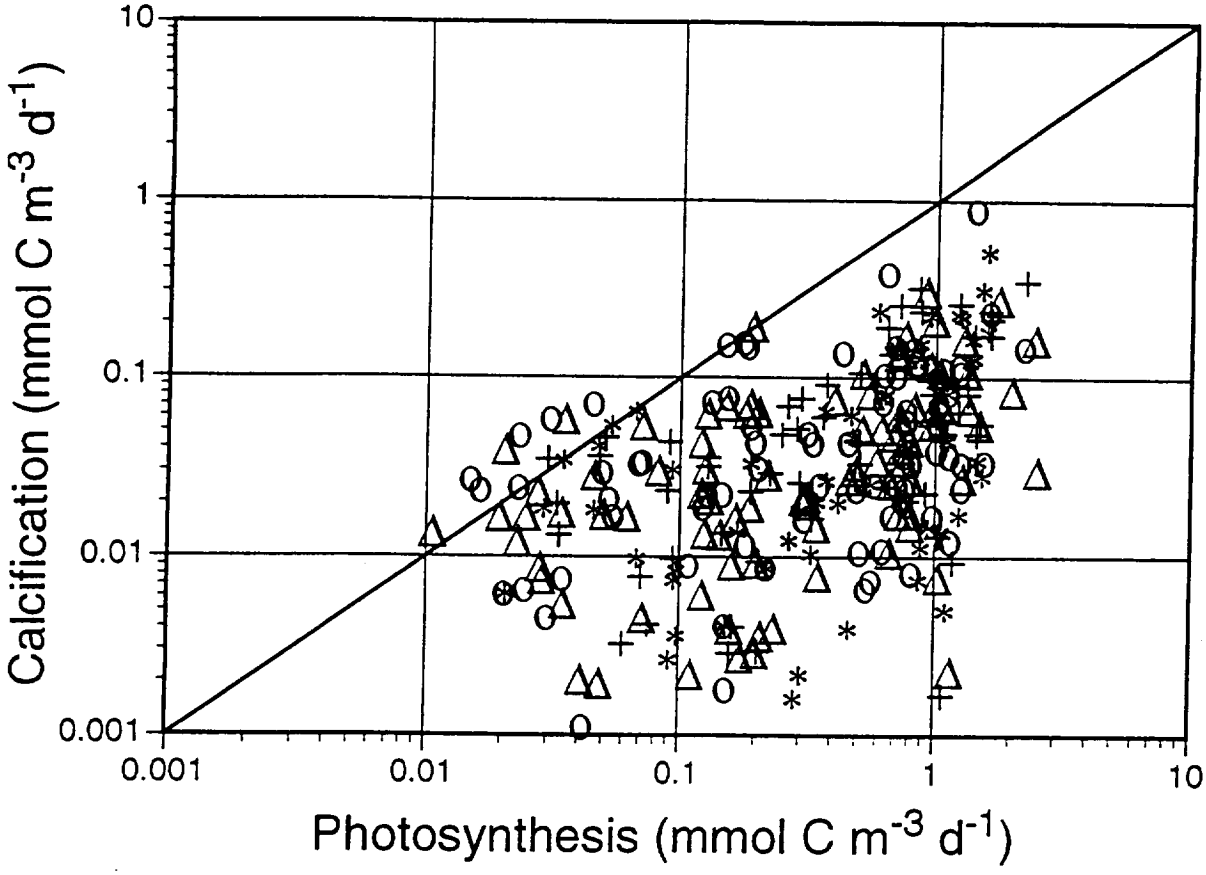
Calcification (mmol C m-3 d-1)
Photosynthesis (mmol C m-3 d-1)
10
1
0.1
0.01
0.001
0.001
0.01
0.1
1
10

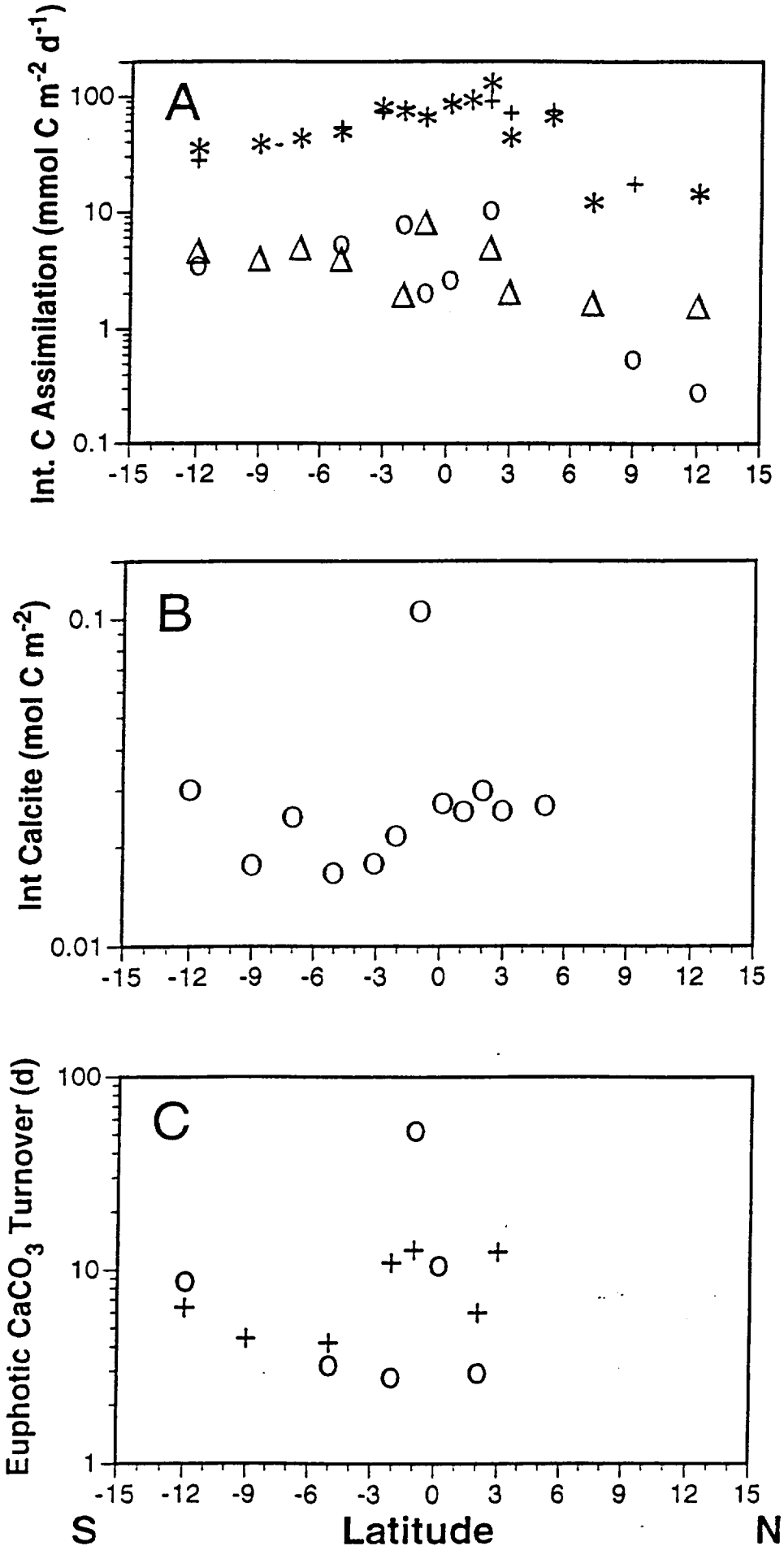
A
Int. C Assimilation (mmol C m-2 d-1)
100
10
1
0.1
-15 -12 -9 -6 -3 0 3 6 9 12 15
B
Int Calcite (mol C m-2)
0.1
0.01
-15 -12 -9 -6 -3 0 3 6 9 12 15
C
Euphotic CaCO3 Turnover (d)
100
10
1
-15 -12 -9 -6 -3 0 3 6 9 12 15
S
Latitude
N

Fig 1

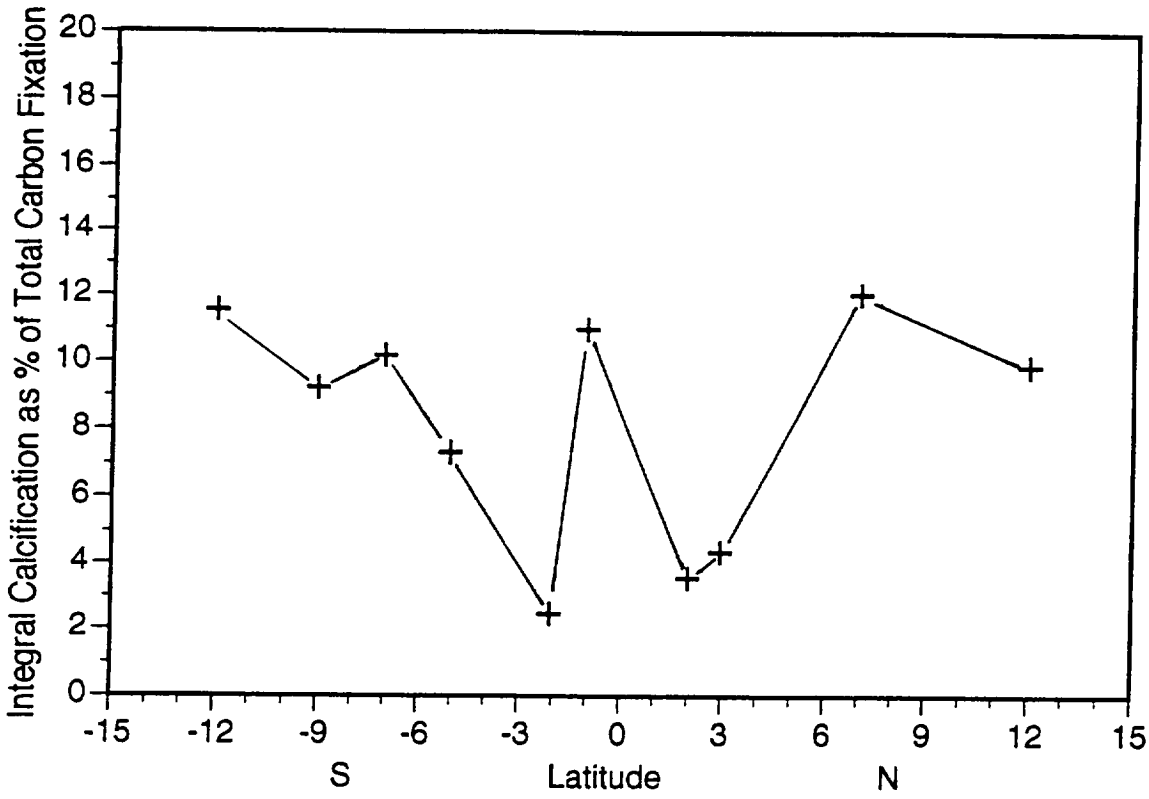

Simulated In Situ Data

Fig 3

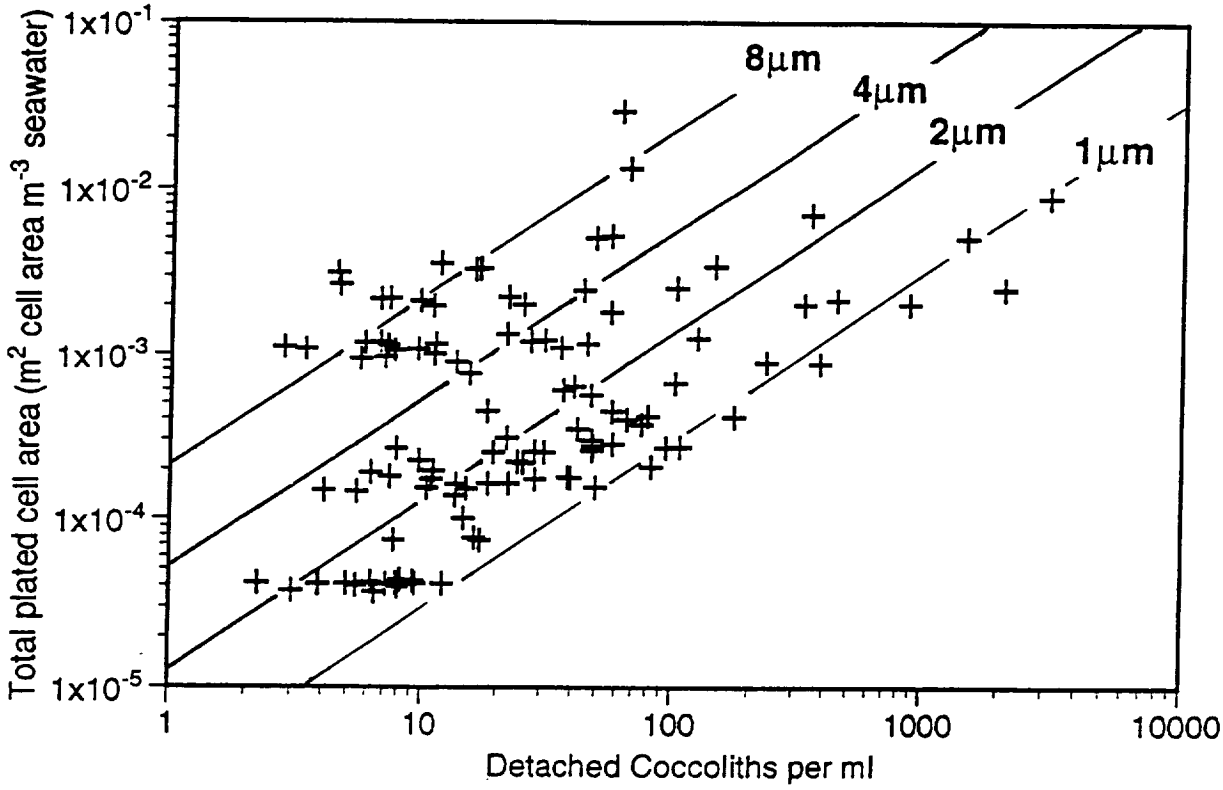
8μm
4μm
2μm
1μm
1x10-1
1x10-2
1x10-3
1x10-4
1x10-5
Total plated cell area (m2 cell area m-3 seawater)
1
10
100
1000
10000
Detached Coccoliths per ml

Fig 8

Extracellular Calcite Flux

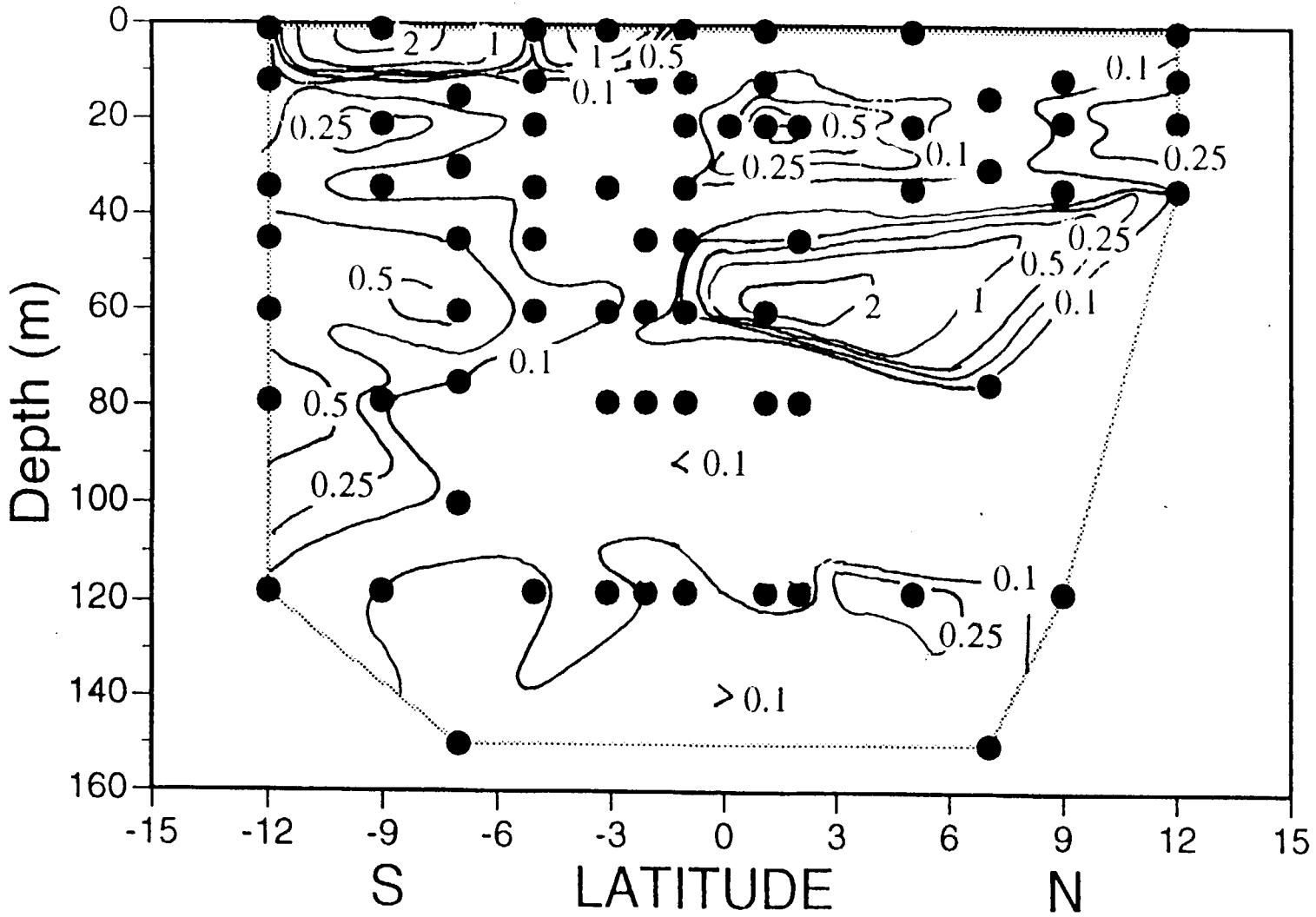

Fig 9

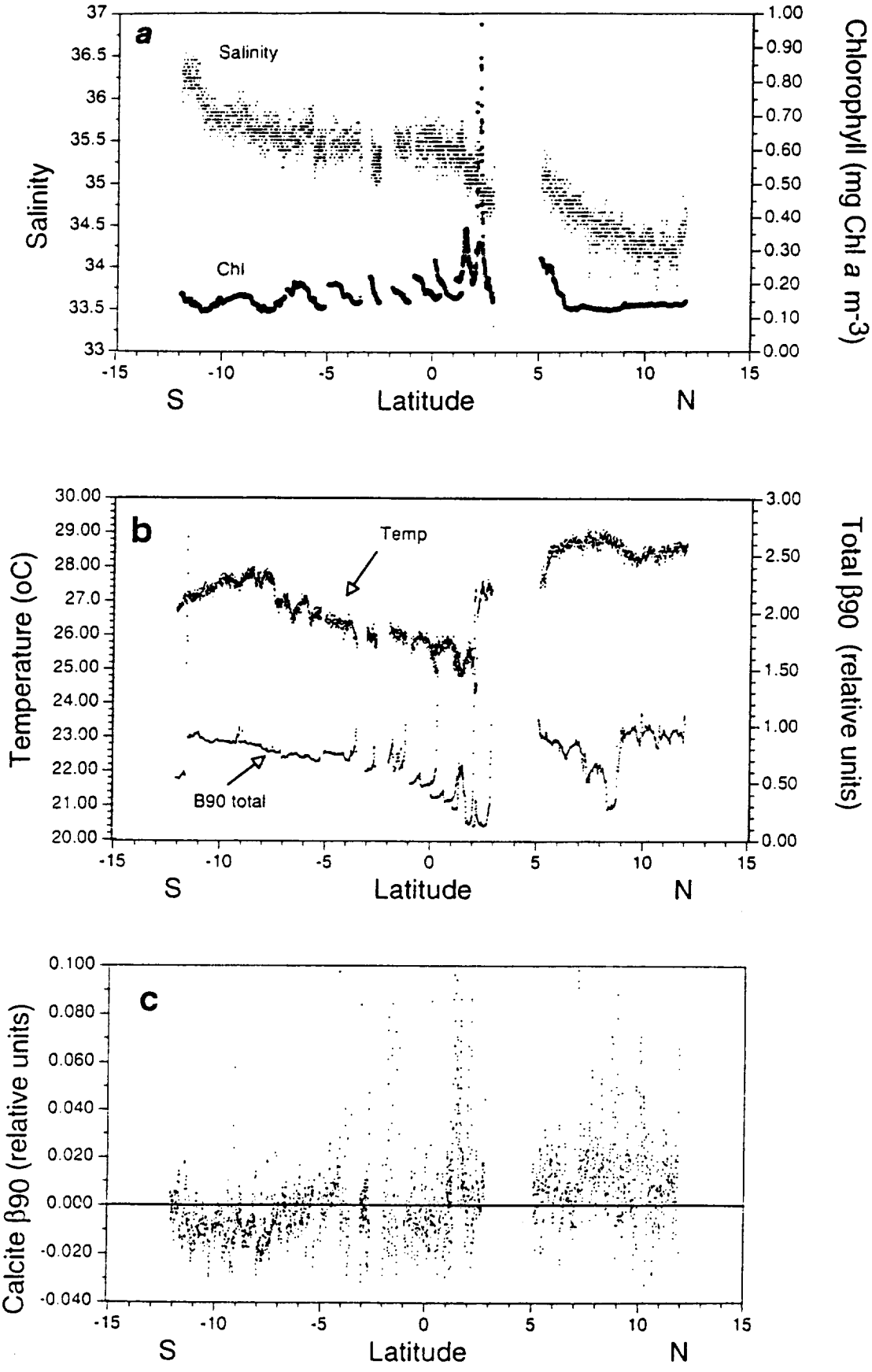
a
Salinity
Chl
Salinity
Chlorophyll (mg Chl a m-3)
37
36.5
36
35.5
35
34.5
34
33.5
33
1.00
0.90
0.80
0.70
0.60
0.50
0.40
0.30
0.20
0.10
0.00
-15
-10
-5
0
5
10
15
S
Latitude
N
b
Temp
B90 total
Temperature (oC)
Total β90 (relative units)
30.00
29.00
28.00
27.0
26.00
25.00
24.00
23.00
22.00
21.00
20.00
3.00
2.50
2.00
1.50
1.00
0.50
0.00
c
Calcite β90 (relative units)
0.100
0.080
0.060
0.040
0.020
0.000
-0.020
-0.040

Fig 10

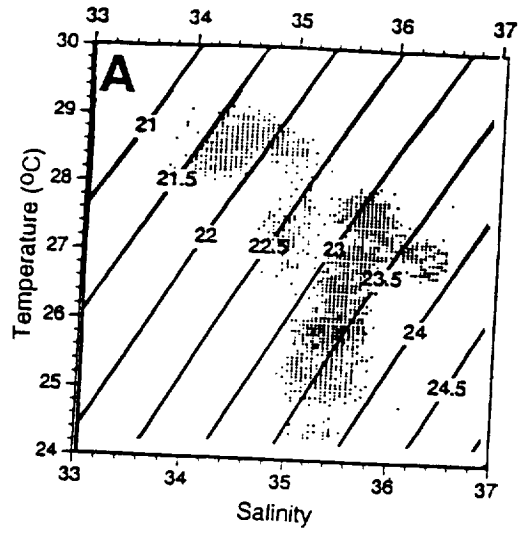

Volume Scatter Due to Calcite (90°; volts)

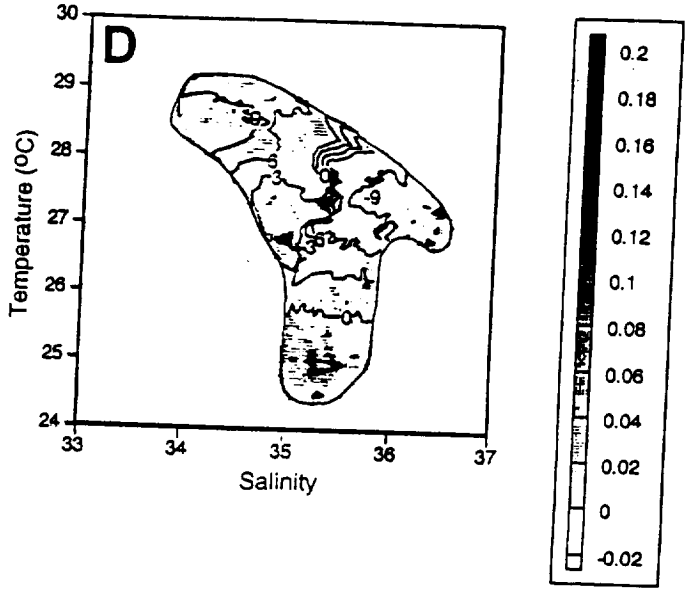

Total Volume Scatter (90°; volts)

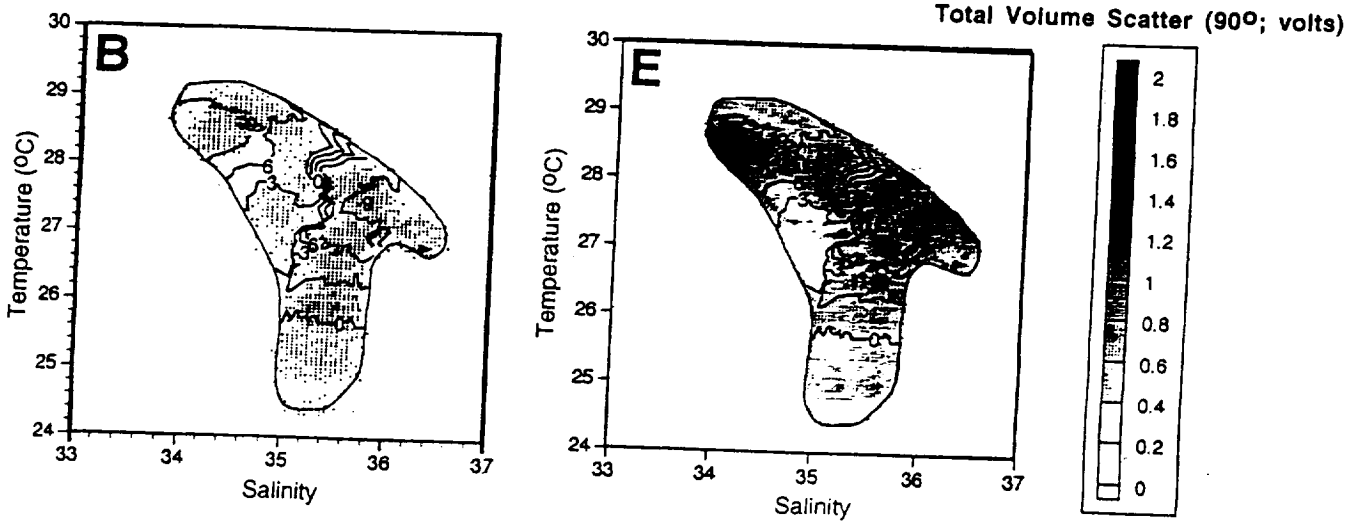

Chlorophyll (mg m^{-3})

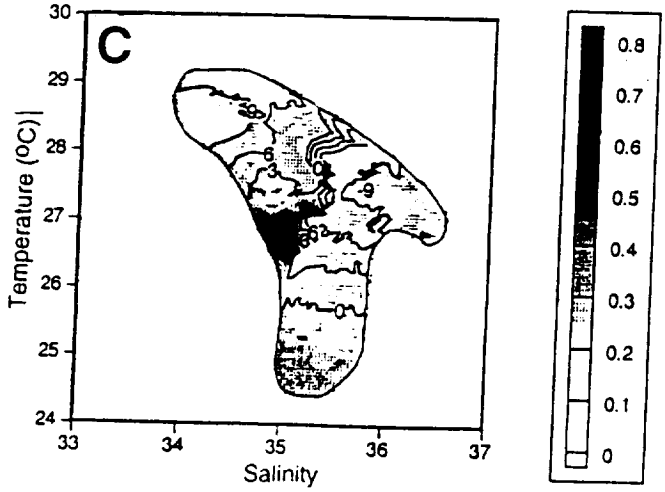

Fig 11

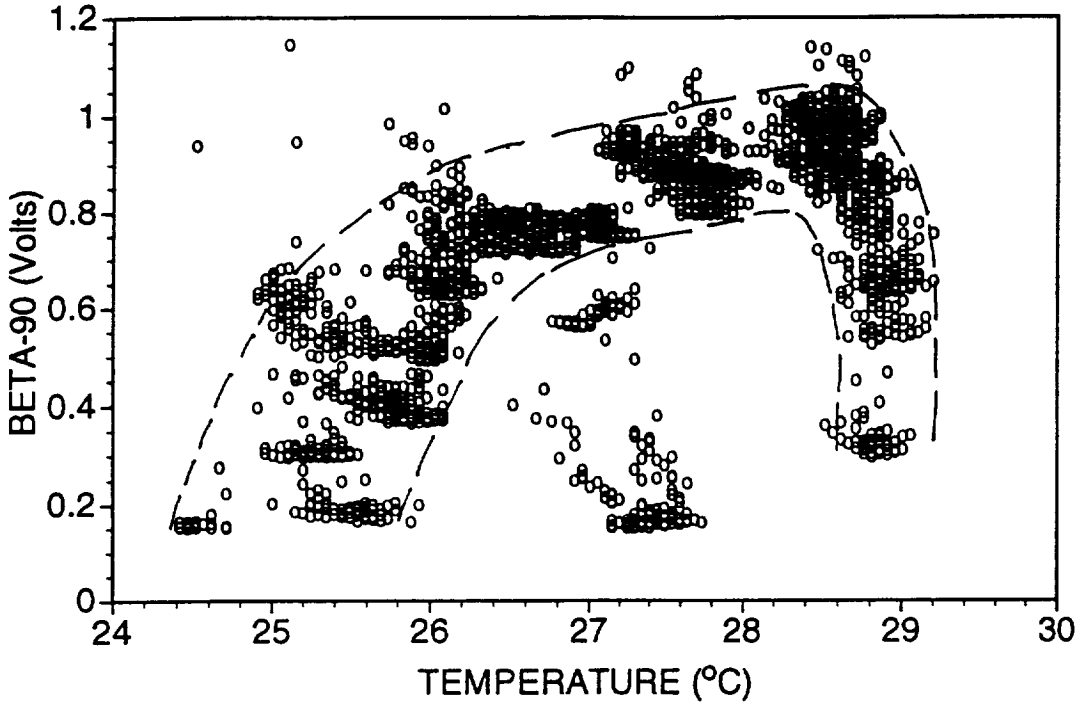

Fig 12

Appendix 7

WHITECAPS: SPECTRAL REFLECTANCE IN THE OPEN OCEAN AND THEIR CONTRIBUTION TO WATER LEAVING RADIANCE

Karl D. Moore, Ken J. Voss, Howard R. Gordon

Physics Dept., University of Miami
Coral Gables, FL 33124

Abstract: The reflectance of white water (foam) generated by whitecaps in the open ocean is obtained with a 6-channel spectral radiometer, extended from the bow of a ship, measuring the upwelling radiance from the water surface. Simultaneously, a 6-channel cosine collector measures the downwelling irradiance at the same wavelengths (410, 440, 510, 550, 670 and 860 nm). In addition to reflectance data, air / water temperature, wind speed and direction are obtained as well as GPS (global positioning system) information in order to characterize ocean surface conditions. A visual reference for sea surface conditions measured by the radiometer is recorded using a video camera mounted along side the radiometer. By measuring a small area of the water surface over time, the presence and spectral influence of whitecaps can be quantified. Using this technique the spectral reflectance of individual whitecaps can be measured and tracked through their complete life cycle. Also, integration over larger time series of ocean surface reflectance data provides a measurement of the augmented or extra contribution from white water reflectance to the water leaving radiance observed by ocean color satellites. Estimates of the augmented reflectance is subsequently correlated to sea surface state, and includes the frequency of occurrence and spectral contribution from various levels of white water reflectance as whitecaps grow and decay.

The effects of sky reflectance, sun glitter and specular reflectance are investigated in terms of setting the threshold between white water and non white water events and the consequences in accurately determining the augmented reflectance contribution. A brief discussion is provided of the impact of sky conditions (overcast/clear) during the measurement process and the implications of solar zenith angle on the water leaving radiance during whitecap conditions from nadir observing platforms.